ELECTRON AND ION BEAM SCIENCE AND TECHNOLOGY

FIFTH INTERNATIONAL CONFERENCE

Edited by

Robert Bakish
Bakish Materials Corporation
Englewood, New Jersey

ELECTROTHERMICS AND METALLURGY DIVISION
THE ELECTROCHEMICAL SOCIETY, INC., P.O. Box 2071, Princeton, New Jersey 08540

The Electrochemical Society, Inc.

POST OFFICE BOX 2071 • PRINCETON, NEW JERSEY 08540

Office of the
EXECUTIVE SECRETARY

November 29, 1972

I am pleased to transmit your personal copy of the Symposium Volume entitled "Electron and Ion Beam Science and Technology - Fifth International Conference."

This publication was the result of the symposium which was held in Houston, Texas, May 7-11, 1972 during the 141st meeting of the Society. You were a contributor to this symposium. The combined contributions of all participants resulted in a most stimulating symposium. Again, thank you for your participation.

Sincerely,

Ernest G. Enck
Executive Secretary

EGE/maf

Enclosure

TELEPHONE: (609) 924-1902

ELECTRON AND ION BEAM SCIENCE AND TECHNOLOGY

FIFTH INTERNATIONAL CONFERENCE

Edited by

Robert Bakish

Bakish Materials Corporation

Englewood, New Jersey

ELECTROTHERMICS AND METALLURGY DIVISION

THE ELECTROCHEMICAL SOCIETY, INC., P.O. Box 2071, Princeton, New Jersey 08540

Library of Congress Catalog Card Number: 71-120300
Printed in the United States of America

PREFACE

This volume contains the papers presented in the Vth International Conference on Electron and Ion Beams in Science and Technology. Only the 3 papers in the plenary presentation are in their original order. I have taken the liberty to rearrange the remaining papers in the hope of making this volume more coherent. These have been arranged into 2 groups using the electron or ion beam power level as an approximate basis for this division.

The first group deals with low energy electron and ion beams and is essentially, but not exclusively, related to the microelectronics field. It contains the papers dealing with physical aspects of the electron and ion beams with beam material interactions and devices. This group also contains all the ion implantation related papers which present an important compilation of points of view by some of the leading companies using the technique. I believe ion implantation is the most important recent development affecting microelectronics, and I am certain that it will materially change the art of device and IC manufacture.

The second group contains the papers dealing essentially, but not exclusively, with high power electron beams. The majority of the papers here are devoted to electron beam welding and consider both mechanism and applications related work.

While this meeting did not plan to exclude from consideration papers dealing with electron beam recording and information storage and electron beam irradiation processing, no papers dealing with either of these topics were submitted for consideration. It is well known however that activities of considerable interest are progressing in both of these areas.

As has been the case in the past, we would hope that this conference continues in the future with its objective to bring together those with competence in the field and those who wish to learn together and to assure diffusion of information on the subject matter of "Electron and Ion Beams in Science and Technology." In this spirit we are proceeding with plans for the VIth event which will take place in May of 1974 in San Francisco. We would hope at that time to be able to schedule sessions on: (1) Physics of Electron and Ion Beams, (2) Beams Materials Interaction, (3) Electron Beam Welding, (4) Electron and Ion Beams in Microelectronics including Ion Implantation and a session devoted to Electron Beam Irradiation Processing.

Since its inception, this event has been sponsored by the Electrothermics and Metallurgy Division of the Society. To give the event a broader base in the Society and to improve its organizational support, the next meeting will be jointly sponsored by the Electrothermics and Metallurgy and the Electronics Divisions of the Society

It is my sincere hope that all who made this event a possibility will continue to work with us at the Society to further the objectives of the conference.

R. Bakish
Englewood, New Jersey

CONTENTS

Page

Electron and Ion Probes
A. N. Broers..... 3

Electron-Energy Dissipation in Solids
R. F. Herzog and T. E. Everhart..... 26

Nanoelectronics
J. E. Picquendar..... 31

Electron Beam Exposure Profiles in Thin Polymer Films
R. J. Hawryluk and H. I. Smith..... 51

Submicron-Mask Making by Electron Beam
N. Saitou and S. Nonogaki..... 68

X-Ray Replication of Scanning Electron Microscope Generated Patterns
D. L. Spears, H. I. Smith, and E. Stern..... 80

Automatic Control of an Electron Beam Pattern Generator
O. Cahen, R. Sigelle, and J. Trotel..... 92

Direct Formation by Electron Beam of Passivating and Phosphosilicate Glass Film Patterns
E. D. Roberts..... 102

Polyvinyl Siloxane (PVS), A Highly Sensitive Electon-Beam Resist
J. C. Dubois and M. Gazard..... 112

Fabrication of Micron Sized Permalloy Circuit Elements Suitable for Magnetic "Bubble" Propagation Using Electron Beam Lithography
R. C. Henderson, W. B. Suiter, and T. A. Weber..... 123

Hologram Recording with Electron Beam
A. Maekawa, S. Yonezawa, H. Itoh, and Y. Kando..... 134

Electron Irradiation of MIS Capacitors - Annealing and Bias-Temperature Stress Studies
L. R. Thibault and K. A. Pickar..... 148

Profiling a High Power Density Electron Beam for Precision Thermal Machining
W. W. Koste and W. Bojman..... 162

Advances of Thermal Electron Beam Machining of Thin-Films
S. Schiller, U. Heisig, S. Panzer, and J. Henneberger..... 171

Page

A Telefocus Ion Gun with Variable Beam Profile
K. Wittmaack and F. Schulz..... 181

Possibilities of the Ion Microprobe in Surface Analysis
L. Habraken, V. Leroy, and J. P. Servais..... 196

The Challenges for Ion Implantation Technology
R. G. Wilson..... 217

Semiconductor Device Production-A Challenge to Ion Implantation
C. M. Pleass..... 225

Production Machine Requirements for Ion Implantation Processing in the Semiconductor Industry
M. R. MacPherson..... 235

Ion Implantation Equipment for Semiconductor Manufacturing
W. J. Kleinfelder..... 241

Concentration Profiles of Ion-Implanted Ions in Silicon
S. Namba, K. Masuda, K. Gamo, M. Iwaki, S. Ishihara, and I. Kimura..... 254

Fast, Low Power Switching Integrated Circuits Made by Electron Beam Pattern Generation and Ion Implantation
A. Bobenrieth, O. Cahen, and R. Lyon-Caen..... 265

Luminescence of GaSe under Intense Excitation by an Electron Beam
T. Ugumori, K. Masuda, and S. Namba..... 281

An Experimental Analysis of Penetration Mechanism of High Power Density Electron Beam
T. Miyazaki and N. Taniguchi..... 291

Direct Observation of the Penetration Mechanism of Partial Penetration Electron Beam Welding
C. M. Weber..... 307

Effects of Electrode Alignment of a Pierce Type Gun on Beam Current Density Distribution
H. Tong, W. H. Giedt, and Z-C Hong..... 321

Power Density as a Control Parameter in Electron Beam Welding
D. J. Sandstrom..... 341

Page

Some Improvements in Beam Quality for High Voltage Electron Beam Welders
G. S. Lawrence..... 354

A Systems Approach to Electron Beam Production Welding Equipment
F. D. Seaman..... 372

High-Power Electron Guns for Evaporation (Axial Systems)
S. Schiller, H. Foerster, P. Lenk, and G. Jaesch..... 399

Index..... 413

ACKNOWLEDGMENT

As the Society's representative I wish to acknowledge the Society's and my own gratitude for the assistance rendered to the Conference by the following individuals for serving on the conference committee and as session organizers and chairmen. These individuals and the speakers whom they brought together made the Vth International Electron and Ion Beam Conference a reality.

Dr. K. Amboss, Hughes Research Laboratories, Malibu, California
Prof. M. von Ardenne, Institute von Ardenne, 8051 Dresden, East Germany
Dr. E. Bas, Swiss Federal Polytechnic Institute, Zurich, Switzerland
Dr. F. Benesowski, Metalwerk Plansee, Reutte/Tyrol, Austria
Mr. M. Boston, Torvac Ltd., Histon, Cambridge, England
Dr. A. Broers, IBM Research Laboratories, Yorktown Heights, New York
Prof. L. Habraken, CNRM, Liege, Belgium
Dr. C. Hayashi, Ulvac Corporation, 2500 Hagisono, Chigasaki City, Kanagowa, Japan
Prof. A. E. Jenkins, University of New South Wales, NSW, Australia
Prof. H. Koch, Schweistechnische und Versuchanstalt, Manheim, West Germany
Dr. S. Namba, The Institute of Physical and Chemical Research, Tokyo, Japan
Dr. W. C. Nixon, Cambridge University, Cambridge, England
Prof. N. A. Olshanski, Moscow Power Institute, Moscow, U.S.S.R.
Academician B. Paton, Director, Institute for Electro-Welding, Kiev, U.S.S.R.
Dr. R. F. Pease, Bell Telephone Laboratories, Murray Hill, New Jersey
Dr. F. D. Seaman, Sciaky Brothers, Chicago, Illinois
Dr. J. Siekman, Philips Research Laboratories, Eindhoven, Holland
Prof. G. Slodzian, University of Paris, South Center d'Orsay, 91-Orsay, France
Prof. W. W. Smeltzer, McMaster University, Hamilton, Ontario, Canada
Dr. J. Smith, Westinghouse Electric, Bettis Plant
Dr. J. A. Stohr, Centre d'Etudes Nucleaires, Saclay, France
Dr. O. Winkler, Balzers AG, Balzers, Lichtenstein

I also wish to thank all at the Society's Headquarters for their help and understanding in the months preceeding the Conference and for their responsiveness to the need of the hour during the event itself.

R. Bakish

INTRODUCTORY REMARKS

Ladies and gentlemen, it gives me a great pleasure to welcome you here in Houston on the occasion of the Vth Jubilee Meeting of the International Conference on Electron and Ion Beams in Science and Technology. It is indeed a happy occasion to see many more faces than was the case some two years ago in Los Angeles. We are seemingly getting out of the clutches of the rather troublesome economic recession, and hopefully we are at the beginning of a shift to an expanding economy. While it does not appear that the seventies will surpass the "Golden Sixties" in terms of opportunities for the scientific and engineering profession, I would like to hope that the level of activities will at least be such as to sustain a healthy scientific and technological climate which we certainly need.

Let me come back to our conference. The lingering economic slow down has apparently affected the number of presentations submitted to this meeting, as they are somewhat fewer than we have had on prior occasions. Nevertheless I do believe that they are more than sufficient to assure an interesting and informative program, and they do permit you to obtain an accurate estimate of the level of progress in the technology since the last conference. I hope that as in the past the conference which you and your managements have placed in the event by your presence here will be well rewarded by the professional and personal benefits which you will derive from it.

I will say no more but turn the podium to my friend, Dr. Fabian Pease who will chair the plenary session.

Robert Bakish
Houston, Texas, May, 1972

INVITED PAPERS

ELECTRON AND ION PROBES

A. N. Broers

IBM Thomas J. Watson Research Center
Yorktown Heights, New York 10598

ABSTRACT

The optical parameters that determine the performance of some of the electron and ion beam systems used for microscopy, microanalysis and microfabrication are discussed. In the case of electron probes, tungsten, lanthanum hexaboride, and field emission cathodes are considered.

INTRODUCTION

The most important parameters that determine the on-axis performance of electron and ion probes are, source brightness, source energy spread, variation of source brightness with aperture, the on-axis aberrations of the lens or lenses used to focus the beam, and diffraction. When the beam has to be scanned through relatively large angles ($> 10^{-2}$ radian) deflection coil aberrations and, when the beam is scanned before the final lens, the off-axis aberrations of the final lens must also be considered. This paper discusses how these optical parameters affect the performance of the most common probe systems. The applications for which the probes are built are only discussed in so far as they determine the optical characteristics required of the probe.

ELECTRON PROBES

In this section electron probes for transmission scanning electron microscopes (SEM's), surface SEM's, x-ray microanalyzers, and beams suitable for electron beam microfabrication are considered. The performance to be expected in each case when field emission, lanthanum hexaboride, and tungsten hairpin cathodes are used, is reviewed.

Scanning Electron Microscopes

In SEM's the smallest available beam diameter is needed. The minimum useful beam current falls between 10^{-12} amperes and 10^{-10} amperes

depending on the contrast in the image, the quality of the image, and the time available to obtain the image. There are two distinct types of SEM, the surface SEM which uses the secondary electrons emitted from the sample surface to form an image of a surface, and the transmission SEM which forms an image of a thin sample by collecting the high energy electrons transmitted through the sample. The contrast in the latter case is similar to that obtained in conventional transmission electron microscopes and is generally higher than in surface microscopes. Higher contrast allows smaller beam current to be used.

In surface SEMs the final lens has to have a relatively long focal length (15-20mm) so that the specimen can be kept outside the magnetic field of the lens and the low energy secondary electrons needed to form a high resolution image collected efficiently. This also allows the specimen to be tilted and manipulated with ease, but it means the lens has relatively large aberrations, (C_s = 10-30mm, C_c = 10-30mm. The large C_c makes beam energy spread important. In transmission SEM's the specimen can be immersed in the magnetic field and a final lens similar to the objective in a conventional EM can be used. (focal length = 0.5 - 1.0mm, C_s = 0.4-1mm, C_c = 0.4-1mm). Chromatic aberration is not nearly so important in this case.

Because the beam diameter and current are very small in all SEM's, effective loss of brightness at larger currents is not important and field emitters are capable of fully illuminating the lens apertures used for optimum performance. This is not the case, as explained later, when larger beam diameters and currents are needed.

The diameter (d) of the final focused beam is obtained by summing in quadrature the disks of confusion due to the final lens aberrations, diffraction, and the Gaussian image of the source. The aberrations of earlier lenses, when used, can generally be ignored because of the demagnification of the final lens. The beam aperture (α_{opt}) which gives the best compromise between lens aberrations, diffraction, and beam current is obtained by differentiating the expression for (d) with respect to α.

Thermal Electron Sources

With thermal electron sources the following well known expressions for d and α_{opt} are obtained.[1] d is the diameter which contains 80% of the beam current.

$$d^2 = P/\alpha^2 + c\,\alpha^6 + Q\,\alpha^2 \qquad (1)$$

and

$$\alpha_{opt}^4 = [(Q^2 + 12CP)^{1/2} - Q]/6C \qquad (2)$$

$$P = i/B + (0.9\lambda)^2$$

$$B = 5.6V\ J_c \times 10^3 / T = 1.51\beta$$

$$C = (1/2\ C_s)^2$$

$$Q = (C_c \delta V/V)^2 + Za^2$$

where

i beam current (amp)

δV axial energy spread(volt)

V accelerating potential(volt)

λ wavelength of electrons $(\sqrt{\frac{150}{V}}\ \text{Å})$

J_c cathode emission density (amp/cm^2)

T cathode temperature (°K)

β electron brightness of source (amp/cm^2. steradian)

Za distance between line foci when lens is astigmatic (cm)

If the aberrations of the final lens are assumed to be constant, the electron optical performance of an SEM is set by the brightness (current density per unit solid angle) of the electron gun. If space charge effects are negligible, brightness in thermal source guns is given by the following expession derived by Langmuir.[2]

$$\beta = Jc\ \frac{11{,}600V}{\pi T} \qquad (3)$$

In practical guns, however, space charge makes the electrons diverge as they leave the cathode surface and the beam angle becomes greater than that taken by Langmuir who assumed that the beam divergence was set by the initial lateral thermal energy of the electrons alone. In order to obtain the highest brightness, therefore, the electric field at the cathode surface must be maximized so that the electrons are accelerated as fast as possible, and diverge as little as possible. The field at the cathode surface depends on the Wehnelt geometry, the cathode shape, the anode-cathode field, and the degree to which the cathode is immersed in the accelerating field - (i.e. the gun bias conditions). The sharper the cathode, and the more the cathode is immersed in the accelerating field the higher the surface field. Plane or conical Wehnelts give higher fields than those with reentrant apertures.

The degree to which the cathode is immersed in the accelerating field is limited by two factors; hollow beam formation, and excessive energy spread due to Boersch effect.[3] As mentioned above chromatic aberration is important in surface SEMs and energy spread generation is therefore particularly detrimental in this type of instrument. Pfeiffer[4] has shown that energy spread is proportional to $\sqrt{\beta r}$ where r is the radius of the gun cross-over. Immersing the cathode further in the accelerating field increases the surface field but at the same time increases the emitting area of the cathode and therefore the crossover size. Measurements indicate that energy spread of 4-5 eV can occur with tungsten hairpins at a brightness of 1.5×10^5 A/cm^2 steradian (20kV) and 3-4 eV with LaB_6 cathodes (20μ tip) at a brightness of 1×10^6 A/cm^2 steradian.[5] Sharper LaB_6 cathodes allow higher brightness at lower energy spread because they do not have to be immersed so far into the accelerating field to produce a given field at the cathode surface.

In summary for high brightness, both high emission density and high surface accelerating fields are needed. For these reasons LaB_6 cathodes give higher brightness than tungsten hairpins. Higher current density is available at reasonable life (100-200 A/cm^2 compared with 5-10 A/cm^2) and the LaB_6 cathodes can be formed with sharper points. (1-20 micron compared with 125-500μ).

Pointed tungsten hairpins also give higher brightness than standard tungsten hairpins, but lifetime becomes inconveniently short at emission densities above 10 A/cm^2. If pressures of 10^{-7} - 10^{-8}mmHg are available, tip diameters below a micron may be used, and the tip field increased to the extent that the emission density is increased by Schottky effect. In these cases, brightnesses of 5×10^5 A/cm^2 str (25kV) can be obtained.

The electron optical performance - beam diameter versus beam current - for electron probes using a lens suitable for surface SEMs is given in Fig. 1. The final lens is assumed to have C_s = 1.8cm, C_c = 1cm, and negligible astigmatism. The following brightnesses are taken for the different cathodes. It is assumed that a planar grid electrode is used.

Tungsten hairpin
- Brightness 1.5×10^5 A/cm^2 ster. (25kV)
- Life 10-15 hrs.
- Maximum acceptable pressure 10^{-4}mmHg

LaB_6 (20 micron ciameter tip)
- Brightness 1.1×10^6 A/cm^2 ster (25kV)
- Life 100-200 hrs.
- Maximum acceptable pressure 10^{-5}mmHg (25kV)

LaB_6 (1 micron diameter tip)
- Brightness 5×10^6 A/cm^2 ster (25kV)

Life 50-100 hrs.
Max. acceptable pressure 10^{-6}mmHg

The solid lines show the performance that will be obtained if the energy spread is that due to the initial thermal energy alone (0.25 volt for tungsten, and 0.2 volt for LaB_6). The dotted lines show the performance that will be obtained if the axial energy spread is increased by Boersch Effect to 4 eV for the tungsten hairpin and 3 eV for the LaB_6 cathodes.

Field Emission Cathodes

The highest electron brightness available today comes from single crystal tungsten field emitters. The emission density available is very great (up to 10^6 A/cm^2) and the field gradient at the cathode surface is so high (10^7v/cm) that space charge divergence does not occur. The main difficulty with field emission cathodes is that stable emission can only be obtained in a vacuum of about 10^{-10}mmHg. This is because emission depends strongly on the work function of the surface and the shape of the tip, both of which can be altered by surface contaminants and/or cathode sputtering. Emission densities of about 10^4 A/cm^2 can be obtained at pressures up to about 10^{-9}mmHg with sufficient stability for microscopy. The brightness is therefore between 50-100 times greater than with thermal LaB_6 cathodes.

Because the current depends strongly on the applied field, two anodes are generally used in field emission guns. The first anode controls emission, and the second sets the overall accelerating potential. Because the effective source is very much smaller than with thermal cathodes more attention has to be paid to reducing the aberrations in the gun so that the gun 'sees' the source as close to its actual size, Several low aberrations guns have been designed, the first by Butler.[6]

Because the source size is very small in field emission guns (30-50 Å diameter) very small probes can be obtained using the gun alone. The minimum beam size in this case is set by the chromatic aberration of the gun and diffraction. Unlike the situation in an SEM using a thermal source and two or more lenses, the size of the Gaussian image of the source cannot be varied once the gun geometry is fixed, so the current in the beam is determined only by the operating aperture of the gun and the tip current. The following expressions for d_G, α_{Gopt} and I describe the performance of this type of gun. (see Fig. 2)

$$d_G^2 = A\,\alpha_G^6 + B\alpha_G^2 + \frac{C}{\alpha_G^2} + D \qquad (4)$$

$$\alpha_{Gopt}^4 = \frac{[B^2 + 12\,AC]^{1/2} - B}{6A} \qquad (5)$$

$$I = \pi \alpha_s^2 I_o = \pi M_G^2 V_r \alpha_G I_o$$

where

$$A = (0.5\, C_{sG} M_G^4 V_r^{3/2})^2$$

$$B = (C_{cG} \frac{\delta V}{V_1} M_G^2 V_r^{1/2})^2$$

$$C = (0.9\lambda)^2$$

$$D = (M_G d_o)^2$$

C_{sG} Spherical aberration coefficient of gun referred to the source

C_{cG} Chromatic aberration coefficient of gun referred to the source

α_s Beam angle at source (see Fig. 2)

α_G Beam angle at image (see Fig. 2)

M_G Magnification of gun

V_1 First anode potential

V Second anode potential

$V_r = V_o/V_1$

δ_V Energy spread of emitted electrons

I_s Total source current, I Final beam current.

d_o Diameter of source (60 Å used in Fig. 3 and 10)

It is assummed that the current is emitted into a solid angle of 1 steradian.

Figure 3 shows the beam diameter and beam current obtained as the operating aperture is varied in such a field emission gun. Three operating conditions are given. (Aberration data obtained from Crewe[7,8]). A is that used in the typical field emission gun microscope. The dotted curve shows the performance if the energy spread in the emitted beam increases from 0.2eV, the theoretical spread set by tunnelling, to 0.5eV. Such an increase can occur when the emitter surface becomes contaminated. B is close to the optimum practical operating limit if maximum current is to be obtained at larger spot sizes. More current

still can be obtained if V_r is increased further, but this leads to smaller V_1 for a given accelerating potential (less than 1700 volts for V_o = 25kV). V_r = 15 is already very optimistic compared with the normal values employed which range between 3 and 6. Smaller V_1 means that smaller tip diameters are needed for a given emission density, and greater difficulty is encountered in maintaining stability. C is close to the optimum practical limit when the smallest beam diameter is needed. The limit is set in this case by the need to have sufficient space between the gun and the image for a deflection unit to scan the beam, and a stigmator to correct for beam asymetries. 2.5 cm is considered here to be the minimum practical working distance. The gun operating conditions for the three cases are given in Table I.

Field Emission Gun and Lens

In order to take full advantage of the potential of field emission cathodes for scanning electron microscopy, a demagnifying lens or lenses must be used in conjunction with the gun. When this is done the minimum beam diameter in effect becomes limited only by the aberrations of the final lens, and diffraction. The aberrations of the gun are rendered insignificant by the demagnification of the lens. In practice for microscopy neither the exact location of the lens, nor the particular operating conditions of the gun are critical provided they are correctly adjusted with respect to each other. That is, the lens must provide only sufficient demagnification to reduce the Gaussian image of the gun crossover, whether real or virtual, to a small but finite fraction of the overall beam diameter. This is similar to the situation with thermal cathodes where beyond a certain point demagnification only reduces beam current without appreciably decreasing beam diameter. The exact operating conditions and lens location become more important when larger beam currents and spot sizes are needed. In these cases, which are discussed further later, care must be taken to transfer all the current available from the source into the final beam.

As with the simple field emission gun, the current available in the beam is set by the operating aperture subtended at the source and the total emitted current, according to the following expression.

$$I = \pi \alpha_s^2 I_o \qquad \text{(See Fig. 4)}$$

This assumes again that the current is emitted into 1 steradian. α_s can be calculated from α_L using the relation

$$\alpha_s = \frac{M_G}{M_L} \sqrt{V_r} \alpha_L$$

where M_G is the magnification of the gun, and M_L the demagnification provided by the lens. α_L is chosen to give the best compromise between lens aberrations (predominantly spherical aberration) and diffraction. The minimum beam diameter considering lens aberrations alone

$$d_{limit} = 1.03\, C_s^{1/4} \lambda^{3/4}$$

This beam diameter will only be obtained if the gun crossover diameter is zero or if infinite demagnification is provided by the lens. In practice this is approximately the case for beam currents below about 10^{-10} amps when the demagnification can be kept relatively large. This can be seen in Figs. 5-7 which show the performance of gun lens combinations.

In calculating the performance of all the gun-lens combinations shown in Figs. 5-7 except curve D, it is assumed that the optimum lens demagnification (M_{Lopt}) is used for each beam current. M_{Lopt} is calculated in a similar way to α_{opt} for thermal cathodes. That is by differentiating the expression for overall beam diameter with respect to M_L. The following expressions are used for the overall beam diameter (d), the beam current (I), and M_{Lopt}.

$$d^2 = AM_L^6 + BM_L^2 + \frac{C}{M_L^2}$$

$$M_{Lopt}^4 = \left\{ (B^2 + 12AC)^{1/2} - B \right\} / 6A$$

$$A = \left(.5 C_{sL} \frac{P^3}{M_G^3} \right)^2$$

$$B = \left(C_{cL} \frac{\delta V}{V} \frac{P}{M_G} \right)^2$$

$$C = \left(M_G V_r^{3/2} .5 C_{sG} P^3 \right)^2 + \left(M_G V_r^{1/2} C_{cG} \frac{\delta V}{V_1} P \right)^2 + \left(0.9\lambda \frac{M_G}{P} \right)^2 + \left(M_G d_o \right)^2$$

where $$P = \left\{ \frac{I}{V_r I_o \pi} \right\}^{1/2}$$

$$\alpha_L = M_L \alpha_G = \frac{M_L}{M_G V_R^{1/2}} \alpha_s$$

$$I = \pi \alpha_s^2 I_o = \pi \left(\frac{M_G}{M_L} V_r^{1/2} \alpha_L \right)^2 I_o$$

where the parameters are those given in Fig. 4. d_o is taken as 60 Å.

The operating conditions for the field emission gun, and the aberrations for the final lenses are given in Table II.

The gun operating conditions for D and E are close to optimum when maximum current is required at all beam diameters. Higher current still is available if the source distance is reduced and V_r increased. Smaller source distance can lead however to instability due to outgassing from the anode. The difficulty in increasing V_r has already been discussed. D shows the performance when the lens demagnification is fixed at 30 and the beam current altered by varying the beam aperture. E is the performance if the optimum demagnification is used for all beam diameters and currents.

If the gun and lens are fixed mechanically both in their own configurations and in relation to each other, the current in the beam can only be altered by altering I_o or α_L. In either case the optimum operating conditions with regard to gun performance or demagnification are lost. This inflexibility can be overcome with a second demagnifying lens. The overall demagnification can then be altered without significantly interfering with the performance of the gun or the final lens. Fortunately the "effective brightness" (it is very difficult to talk in terms of conventional brightness with field emission sources because of the strong variation of brightness with operating aperture) is so high that when only one lens is available, small losses of performance through excessive demagnification can be tolerated without reducing the beam current to an unacceptable level. Excessive demagnification is preferable to insufficient demagnification because in the latter case the spot diameter is increased.

When two lenses are employed care has to be taken to keep the demagnification provided by the final lens high enough to render the aberrations of the first lens insignificient, and also to avoid increasing the spherical aberration of the final lens.

Figures 8 and 9 show how beam diameter and current vary with lens demagnification when a single lens is used. For the surface microscope case (Fig. 8) a demagnification of about 35 is sufficient to reduce the beam diameter to within 10% of the limit set by the aberrations of the final lens. For the transmission case (Fig. 9) a demagnification of 100 is required.

In Fig. 10 the performance of thermal and field emission cathodes with a surface microscope lens are superimposed for comparison. For beam diameters up to about 300 Å the field emission gun plus lens combination provides superior performance. It is therefore the best choice for surface microscopy. For beam diameters between about 130 Å and 800 Å the performance of the simple field emission gun exceeds that of a conventional column using a tungsten hairpin cathode. Above and below this range the tungsten hairpin is better. For beam diameters between

about 130 Å and 200 Å the simple gun has approximately the same performance as a conventional column with a 20 micron LaB_6 cathode. An LaB_6 cathode with a 1μ tip provides superior performance to the simple gun for all beam diameters.

Figures 6 and 7 show the performance of probes suitable for transmission SEMs. The final lens is assumed to have a focal length of 0.4mm (C_s = 0.4mm, C_c = .4mm) at 30kV, and a focal length of 1mm (C_s = 1mm, C_c = 1mm) at 100kV. The difference between thermal and field emission cathodes is less for transmission microscopy than for surface microscopy particularly when higher accelerating potentials are used. This is because chromatic aberration becomes less important, and also because the "effective brightness" of field emission sources does not increase as much as the brightness of thermal cathodes at higher accelerating potentials.

X - RAY MICROANALYZERS

The resolution in electron probe x-ray microanalyzers is limited to 0.2 - 1 micron by the volume from which x-rays are emitted. The resolution is improved with thin samples but there is still no point in using beam diameters smaller than about 0.1 micron. The maximum possible current is useful, however, particularly when small quantities of material are to be detected and the x-ray count is low.

Microanalyzer final lenses have focal lengths similar to the focal length of surface SEM lenses and the performance can be obtained, therefore, from Fig. 1. For the larger beam diameters (0.1μ and above), it can be seen that chromatic aberration is not significant even for the large energy spread obtained with thermal cathodes. This means that when thermal cathodes are used the choice of gun operating conditions need not be influenced by the need to minimize energy spread. Stability is a primary requirement so the gun should run with the cathode well immersed in the accelerating field (see discussion above). The highest brightness can be obtained in this way and the larger emitting area reduces variation in brightness due to both emitter position and variations in emission density across the cathode surface.

As can be seen in Fig. 1 the current that can be focussed into a 0.1 micron beam using an LaB_6 cathode can be more than 20 times greater than with a tungsten hairpin. In addition LaB_6 cathodes offer better stability if a stable vacuum environment of 10^{-5}mmHg or below can be maintained in the gun. They would appear therefore to be the obvious choice for microanalyzers.

Figure 10 shows that the performance obtained from a field emission gun used with or without a lens deteriorates below that of thermal cathodes for beam diameters of 0.1μ and above. It should be noted, however, that the field emission curves assume a source current of 10 microamps. If this current is increased, the current in a given beam size will

be increased by the same amount. For example, if 1mA can be drawn stably, the performance of a field emission gun with a lens will be greater than with the brightest LaB_6 cathode for all beam sizes up to about 3000 Å. The major difficulty at higher currents is that the field emitted current becomes less stable. Stability is very important in microanalyzers because of the need to obtain exact relative x-ray counts.

MICROFABRICATION

Most electron beam microfabrication systems suitable for making semiconductor devices are required to build structures with minimum dimensions between 0.25-1 micron. If a small round electron beam is to precisely delineate these structures the beam diameter has to be approximately five times smaller than the minimum dimension, that is .05 - .02 micron. This is similar to the beam size required in an x-ray microanalyzer. There is an important difference however. In the microanalyzer, as in an SEM, the resolution of the display CRT limits the size of the field that can be resolved to approximately 10^3 times the spot size. This is not the case for most high performance fabrication systems where much larger fields have to be scanned if the mechanical stepping time between fields is not to dominate exposure time. For example, a standard integrated circuit chip may be several thousand times larger than the minimum dimension, and more than 10,000 times larger than the beam. In general the field size is limited to about 2000 times the minimum dimension by the stability of the electronics used to scan and control the beam.

Because beam growth due to deflection aberrations is very much more important than in scanning microscopes and microanalyzers, smaller beam apertures and beam deflection angles must be used for microfabrication. This means using lenses with longer focal length. Figures 11 and 12 compare the performance to be expected when a field emission gun and a standard LaB_6 thermal cathode are used with two such lenses. The performance of the field emission gun alone is also included. In Fig. 11 the field emission gun is assumed to be operating at a 4cm working distance, and in Fig. 12 at a working distance of 8cm. The focal length of the lens in Fig. 11 is about 5cm and in Fig. 12 about 10cm. The dotted lines show the performance that will be obtained if the optimum beam aperture set for the on-axis aberrations of the final lens alone is used for each beam current. As mentioned above with the simple field emission gun there is no "optimum" aperture for every current. The aperture itself determines the current.

The solid lines show the performance that will be obtained if the beam aperture is held at .006 radian and not increased for larger beam sizes. .006 radian is a conservative limit for the beam half angle if the beam is to be scanned over fields 10,000 times larger than the beam diameter with only dynamic focus correction. Dynamic astigigmatism correction will probably be necessary if larger field sizes are to be covered.

If a total deflection angle of 4×10^{-2} radian is used, the 10cm focal length lens will allow a 4mm diameter field. The 5cm focal length lens will allow half this field size. In both cases the field emission gun plus lens will give better performance than the simple gun, or the LaB_6 thermal cathode, for beam sizes up to about 1500 Å. For beam sizes greater than 1500 Å the LaB_6 cathode is superior. The simple field emission gun when operated at $\alpha = .006$ radian is superior to the LaB_6 cathode only up to beam diameters of about 600 Å for the 5cm focal length lens, and 800 Å for the 10cm focal length lens.

ION PROBES

Ion Beam Microanalyzer

The technology of producing high resolution ion probes has been explored for several years, mainly for ion beam microanalzers. The minimum useful beam current in these instruments falls between 10^{-10} - 10^{-9} amperes. Beam diameters below 1 micron are needed. The ion optical column generally consists of a duoplasmatron ion source and one or more electrostatic lenses. The performance of the focussed beam is given by the same relationships given for electron probes using thermal cathodes (Eqs. 1 and 2).

For typical electrostatic lenses $C_s = 30\ f$ where f is the lens focal length. For ion probe microanalyzers a focal length of at least 3cm has to be used so that the ions sputtered from the sample surface can be collected efficiently and passed through a mass spectometer.

The major limitations to probe performance are the spherical aberration of the final lens and brightness. The following brightnesses have been measured from duoplasmatrons.

$90\ A/cm^2$. steradian Protons 60 kV Von Ardenne[9]

$100 - 200\ A/cm^2$. steradian Argon 12 kV Liebl[10]

A certain degree of confusion arises in the definition of the brightness of ion sources. Many workers with ion beam systems use "normalized brightness", which is brightness as it is usually defined in electron optics, that is current density per unit solid angle, multiplied by the factor $\frac{mc}{P}$ where P is the axial momentum of the particle, m_o the rest mass, and c the velocity of light. This factor can be considered as "normalizing" the brightness with respect to changes in particle velocity and therefore particle mass and accelerating potential. When the optical performance of an ion beam system is to be calculated, conventional brightness must be used, and not normalized brightness. Normalized brightness is only useful for comparing the performance of ion sources operating with different ions at different

accelerating potentials. The lower curve in Fig. 13 is the current versus beam diameter characteristic for an ion probe system suitable for an ion beam microanalyzer. A brightness of 250 A/cm^2 . ster at 25 kV is assumed, together with a final lens spherical aberration coefficient of 100 cm, a lens chromatic aberration coefficient of 7cm, and an axial energy spread of 2 eV. As can be seen at a current of 10^{-10} ampere, a beam diameter of 0.7 micron is obtained.

Ion Beam Microfabrication

A focused ion beam can be used to "write" diffusion patterns into semiconductor wafers without the need for the normal SiO_2 or metal surface barrier masks. This technique can in principle[2] simplify semiconductor device production and perhaps reduce cost. As with electron beam apparatus, a range of ion optical systems can be considered for device production. A simple round beam system suitable for this purpose is considered here.

In order to dope a semiconductor to a density of 10^{15} ions/cm^2 (typical of the dose required for the active region of transistors) a charge density of 1.4×10^{-4} coulomb/cm^2 has to be deposited. This is approximately ten times the electron charge density needed to expose electron resist materials. The greater charge density plus the much lower brightness available from ion sources combine to make ion beam systems approximately 10^4 times slower than their electron beam counterparts in fabricating over a given area at a given resolution. Considerable savings in complexity and cost may be realized with direct ion beam implantation through the elimination of diffusion furnaces, oxide growth furnaces, and resist coating and oxide etching equipment, however, resist processes are still required for metallization and the additional complexity of the ion beam system will offset these advantages.

Figure 13 shows the beam current versus beam diameter characteristic for an ion beam system suitable for fabrication. A lens with a focal length of approximately 5cm is considered. (C_s = 200cm). A Brightness of 10^3 A/cm^2. steradian (100kV) is taken which is the highest brightness that might be expected from a duoplasmatron under these circumstances. It should be noted, however, that the brightnesses quoted above for duoplasmatrons are measured with protons or inert gas ions. Presently available data indicates that less than 5% of this brightness is available when ions useful for doping semiconductors are used.

As with the electron beam systems the solid line shows the case where the beam half angle is limited to 0.006 radian. The dotted line is the performance when the optimum aperture set by the on-axis aberrations of the lens alone is employed for all beam currents.

REFERENCES

1. Smith, K. C. A., PHD Thesis, Cambridge University (1956).

2. Langmuir, D. B., Proc. IRE, 25, p. 977 (1937)

3. Boersch, H. Z. Physik 139, p. 115 (1954).

4. Pfeiffer, H. C. Record of 11th Symposium on Electron Ion and laser Beam Technology, Boulder, R. F. M. Thornley (Ed). p. 239 (1971).

5. Broers, A. N. and Pfeiffer, H. C., Record of 11th Symposium on Electron Ion and Laser Beam Technology, Boulder, R. F. M. Thornley (Ed) p. 205 (1971).

6. Butler, J. W. Proc. 6th Int. Congr. Electron Microscopy, Rome, p. 191 (1966).

7. Crewe, A. V., Quarterly Reviews of Biophysics 3, p. 137-175 (1970).

8. Crewe, A. V. J. Mol. Biol. 48, p. 375-393 (1970).

9. Von Ardenne, M. "Tabellen fur Electronen, Ionenphysik und Ubermikroskopie", VEB Deutscher Verlag der Wissenschaften, Berlin (1956).

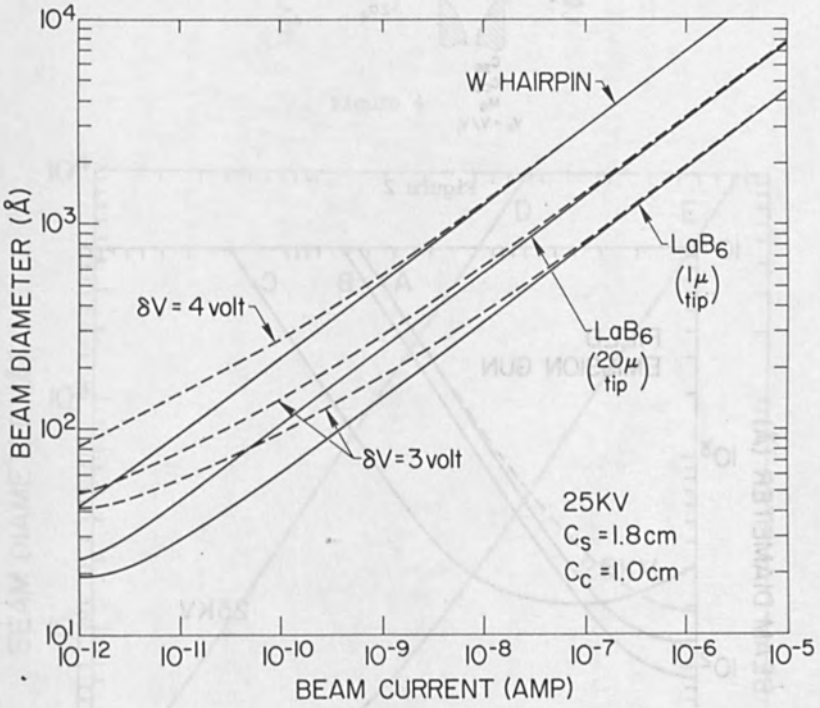
W HAIRPIN
LaB6 (1μ tip)
LaB6 (20μ tip)
δV = 4 volt
δV = 3 volt
25KV
Cs = 1.8cm
Cc = 1.0cm
BEAM DIAMETER (Å)
BEAM CURRENT (AMP)
10^4
10^3
10^2
10^1
10^-12
10^-11
10^-10
10^-9
10^-8
10^-7
10^-6
10^-5

Figure 1

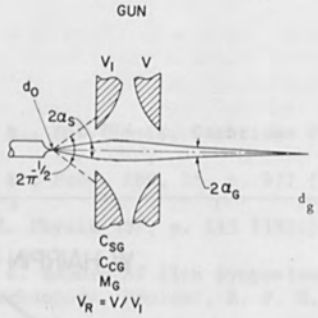

Figure 2

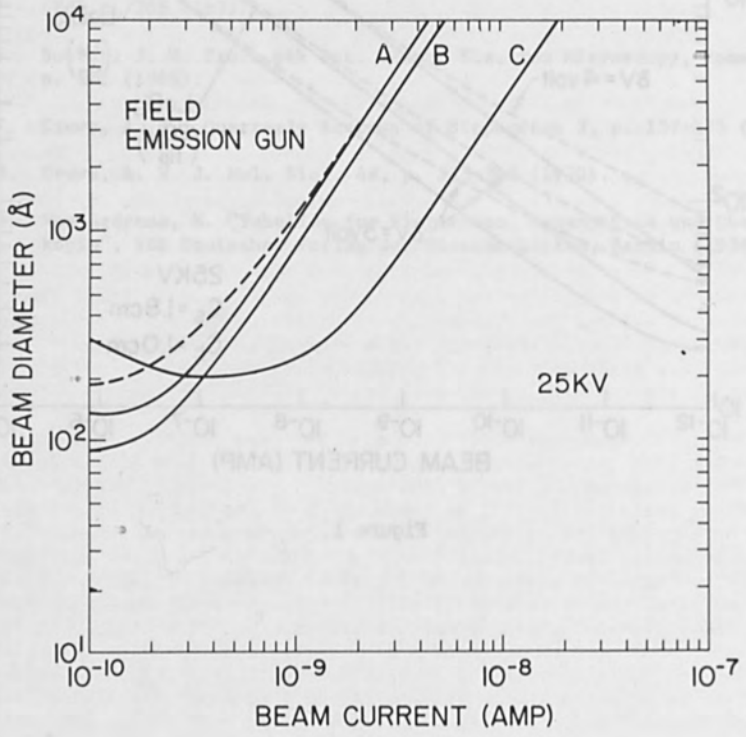

Figure 3

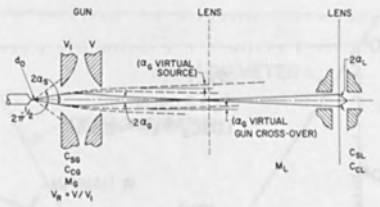

Figure 4

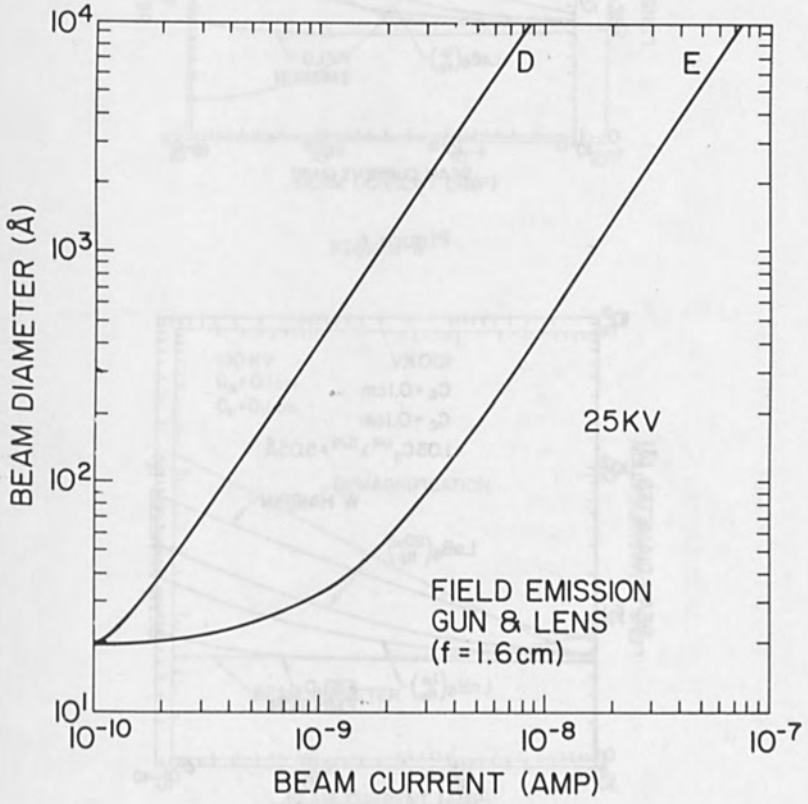

Figure 5

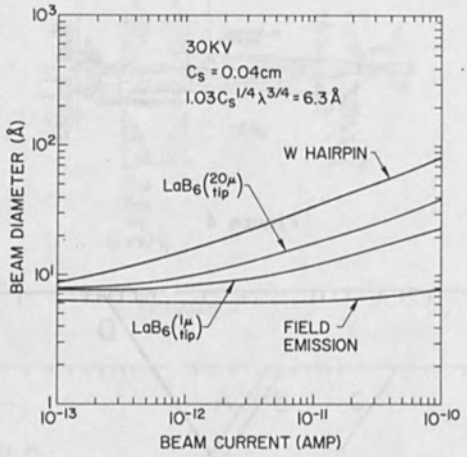

Figure 6

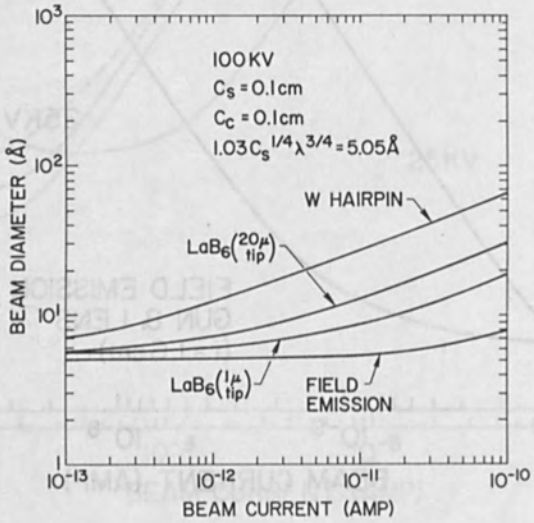

Figure 7

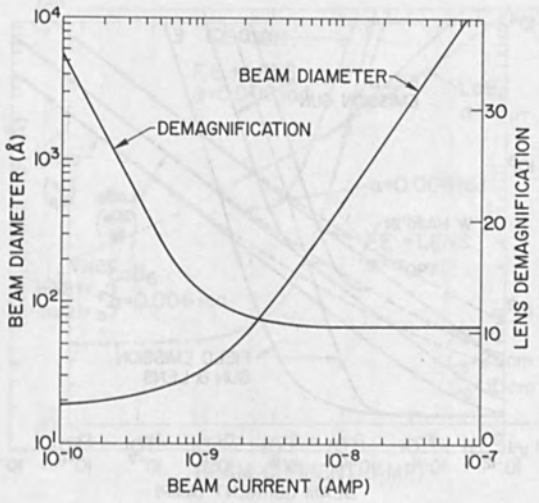

Figure 8

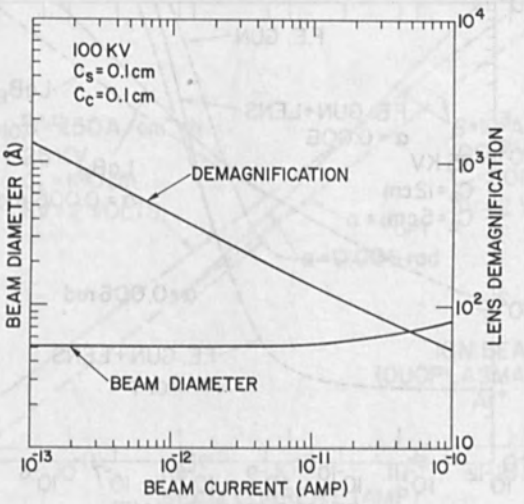

Figure 9

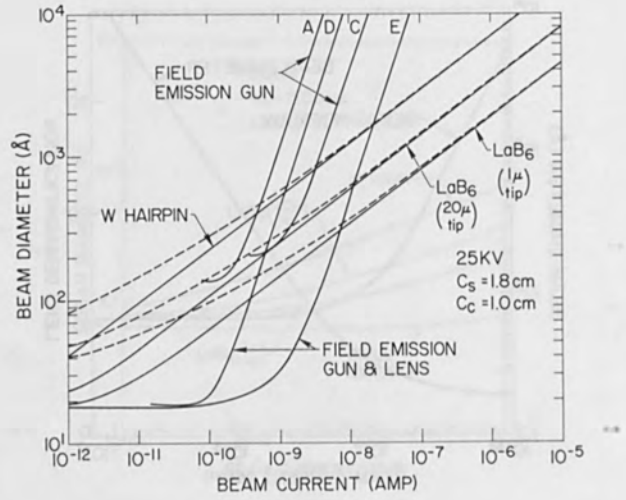

Figure 10

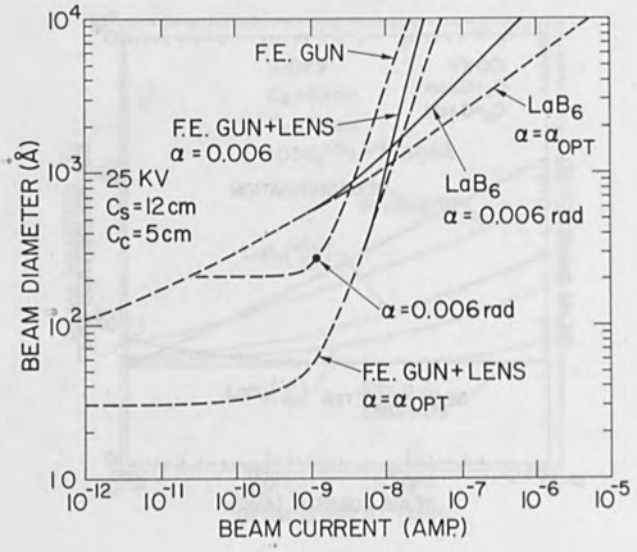

Figure 11

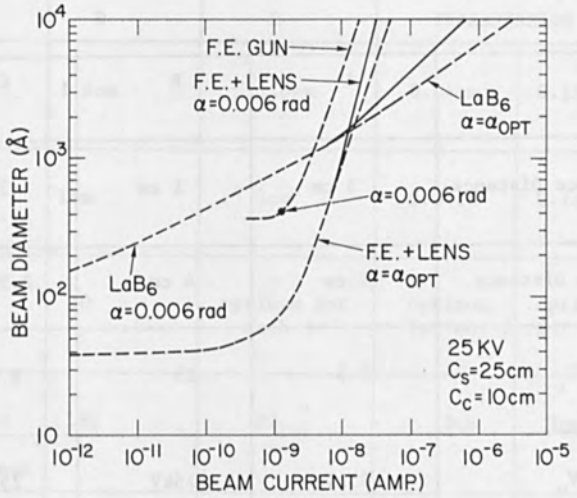

Figure 12

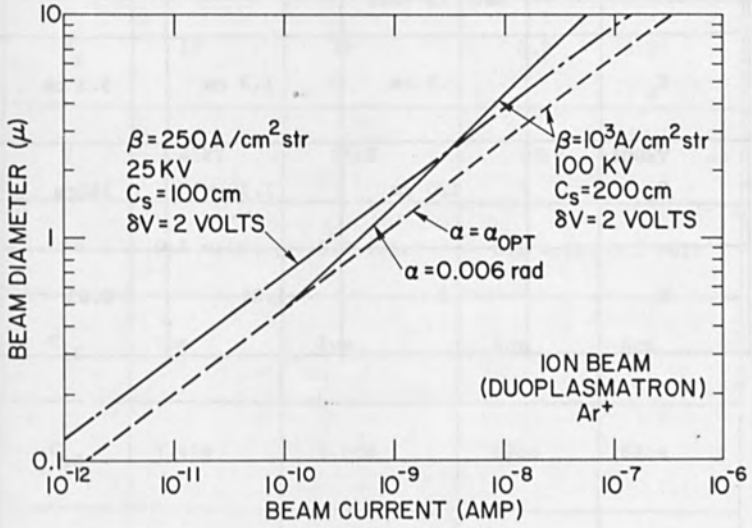

Figure 13

TABLE I

	A	B	C
Source Distance	3 cm	1 cm	3 cm
Image Distance	4 cm	4 cm	2.5 cm
V_r	7.5	15	8.6
V_o	25kV	25kV	25kV
δ_V	.2 volt and .5 volt	0.2 volt	0.2 volt
C_c	.5 cm	1.3 cm	5.3 cm
C_s	120 cm	7.2 cm	142cm
M	3	1.85	0.63

TABLE II -

		D	E	TRANSMISSION	
LENS	C_{sL}	1.8cm	1.8cm	0.04cm	0.1cm
	C_{cL}	1cm	1cm	0.04cm	0.1cm
	M_L	50	optimum for each I	optimum for ea. I	optimum for ea. I
	Source Distance	.82	.82	3cm	3cm
	Image Distance	8cm	8cm	25cm	25cm
	V_r	15	15	5.2	5.2
GUN	V	25kV	25kV	30kV	100kV
	δV	0.2 volt	0.2 volt	0.2 volt	0.2 volt
	C_{cG}	1cm	1cm	4cm	4cm
	C_{sG}	4.4cm	4.4cm	69cm	69cm
	M_G	3.5	3.5	4.3	4.3

ELECTRON-ENERGY DISSIPATION IN SOLIDS

R. F. Herzog and T. E. Everhart
Electronics Research Laboratory
University of California
Berkeley, California 94720

Electron beam interactions with matter must be understood if maximum information is to be derived from finely focussed probes such as those used in scanning electron microscopes, or if optimum resist exposure is to be used to fabricate modern electronic circuits. Ideally, for a given material with density ρ, atomic number Z, gram atomic weight A, and for a given incident beam energy E, we should like to know the energy dissipated per unit volume in the material as a function of position (x,y,z) from the beam's point of entry, taken as (0,0,0). Let this energy dissipation/unit volume be $g_3(x,y,z)$. Semi-empirical formulas can be used to estimate g_3,[1] or we can rely on Monte-Carlo calculations for a few cases determined thus far.[2] Alternatively, we could perhaps determine g_3 experimentally. A related parameter is the energy dissipated per unit depth z, which is given by

$$g_1(z) = \int_{-\infty}^{\infty}\int g_3(x,y,z)\, dx\, dy \qquad (1)$$

An experimental determination of $g_1(z)$ has been reported recently[3], and a promising method of determining $g_3(x,y,z)$ based on an improved resist development scheme was reported last year[4]. The purpose of this paper is to report on progress since that time.

Briefly, an electron beam is scanned in a line pattern with eight different exposure dosages (measured in Coulombs/meter) and four different lines at each dosage. This allows a measure of reproducibility to be determined for the data. Since lines are used, and the cross-section of these lines are examined to determine profiles of constant energy dissipation, we are measuring

$$g_2(x,z) = \int_{-\infty}^{\infty} g_3(x,y,z)\, dy = \text{constant} = g_{2c} \qquad (2)$$

Here g_{2c} is the critical energy dissipation/unit area required before the exposed resist is developed away.[4] For $g_2 < g_{2c}$, no resist is removed by the development procedure. The boundary has proven quite sharp in practise for the resist (polymethylmethacrylate) and the developer (ethyl alcohol) used. A set of sample profiles are shown in Fig. 1, illustrating this. Each successively larger profile was produced by a higher charge/unit length. If line a was produced by a charge/unit length Q_ℓ, line b was produced by $K\, Q_\ell$, etc. to line h, which was produced by $K^7\, Q_\ell$. K can be varied at will, and is usually 1.5 to 1.7.

We reduce these profiles by knowing the energy dissipated inside the area of profile a, A_a, is greater than $g_{2c} A_a$. The energy dissipated inside the area of profile b, A_b, is greater than $g_{2c}(A_b - A_a) + K A_a$, etc. To complete this calculation for many exposures and for many profiles at each exposure (in order to obtain a good measure of experimental reproducibility) is very laborious if done by hand. Hence we have digitized and stored each profile in a computer disk file, for automatic processing. Numerical results of the computer processing will be reported later. Briefly, we presently calculate the maximum depth, maximum width, neck width, profile area, and the profile center of gravity for each digitized stored profile, and also compute the average of each of these quantities for all profiles processed at the same exposure charge/unit length and beam voltage. By comparing each stored profile with this weighted average, we determine which stored profile fits the data best, and then display the family of best fit profiles for each beam energy, as shown in Fig. 2. Figures 3, 4, and 5 are similarly determined families of profiles for different incident beam energies. Clearly, as the beam energy decreases, large angle scattering becomes more appreciable compared to electron energy dissipation per unit depth, as would be predicted from the ratio of the Rutherford scattering probability p(Q,E) to the fractional energy loss in a thickness dz[3].

$$\frac{p(Q,E)}{\Delta E/E} = \frac{1}{32\,\pi} \frac{Z}{\ln \frac{aE}{I} \sin^4(\frac{\phi}{2})} \qquad (3)$$

Note that as aE/I decreases large angle scattering becomes much more pronounced compared to $\Delta E/E$. However, we have not ruled out the possibility that charging in the plastic deflects the incoming electrons more at the lower energies. This possibility becomes more important for two reasons: first, the charge is deposited nearer the surface, so the charge density available goes up, and second, the incoming electrons are slower, and more easily deflected. These possibilities are presently under investigation. We are extending these experiments to additional voltages. The examples presented here show that the shape of energy dissipation profiles are sensitive functions of the beam voltage for the low mean atomic number material investigated.

Acknowledgments: The authors are grateful to T. Scott for many scanning electron micrographs of developed profiles. This work was supported by NIH grant USPHS-GM-17523.

References:

1. see for example C. A. Klein, Appl. Optics 5, 1922 (1966).
2. H. E. Bishop, Brit. J. Appl. Phys. 18, 703 (1967).
   R. Shimizu and K. Murata, J. Appl. Phys. 42, 387 (1971).
   L. Reimer, Optik 27, 86 (1968).

3. T. E. Everhart and P. H. Hoff, J. Appl. Phys. 42, 5837 (1971).
4. R. F. Herzog, J. S. Greeneich, T. E. Everhart and T. Van Duzer, Record of 11th Symposium on Electron, Ion, and Laser Beam Technology (R.F.M. Thornley, ed. San Francisco Press, Inc., 1972) pp. 483-494, also IEEE Trans. Electron Device EO-19, 635 (1972).

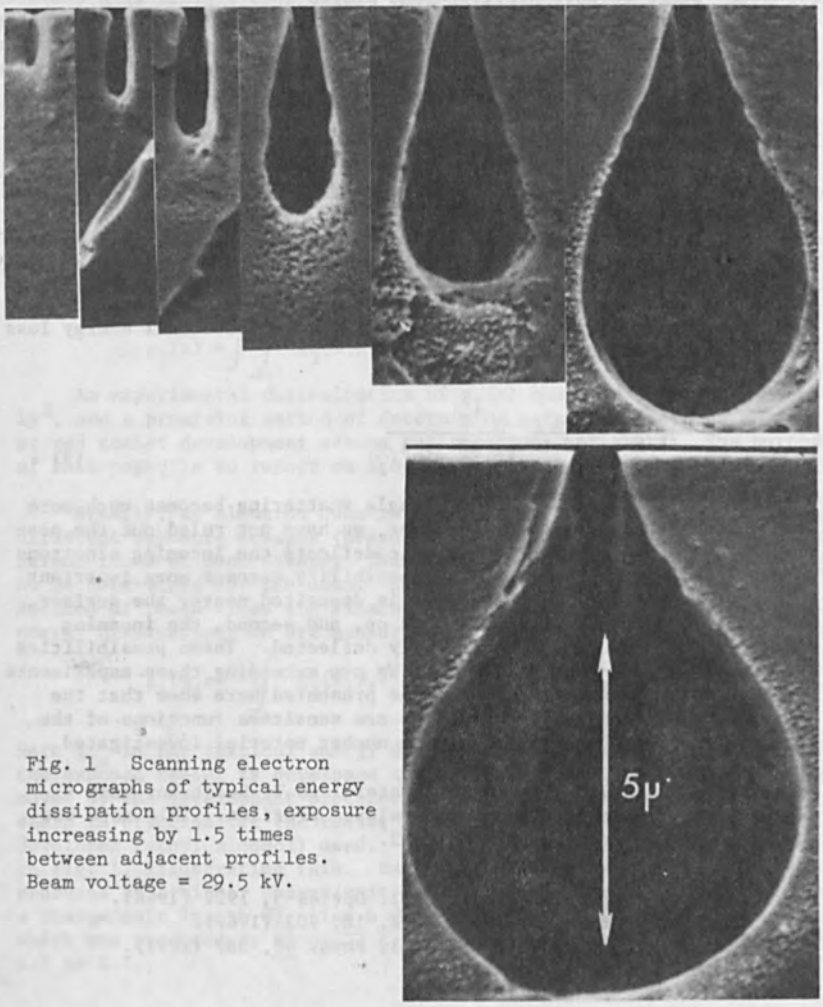

Fig. 1 Scanning electron micrographs of typical energy dissipation profiles, exposure increasing by 1.5 times between adjacent profiles. Beam voltage = 29.5 kV.

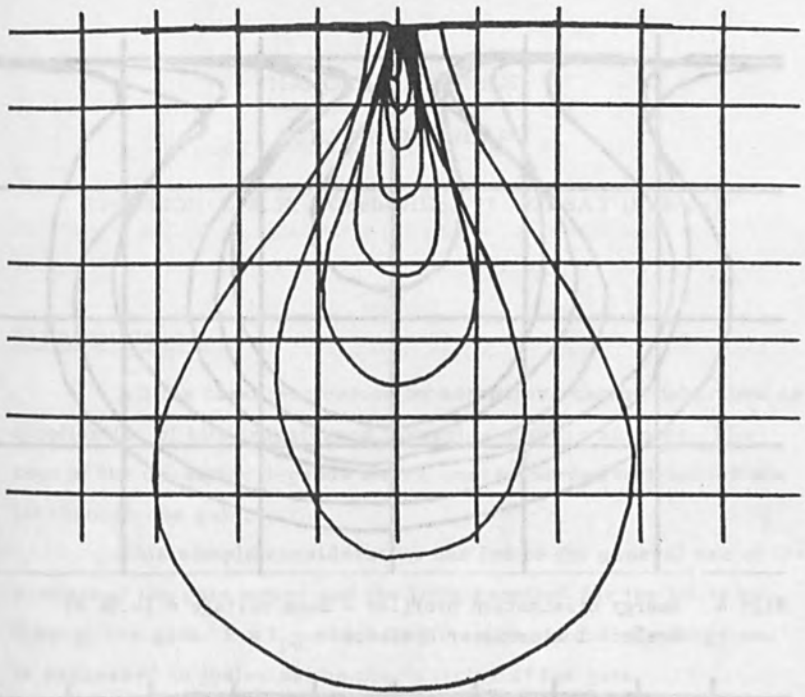

Fig. 2 Energy dissipation profiles - Beam voltage = 29.5 kV
Scale: 1 micrometer/division

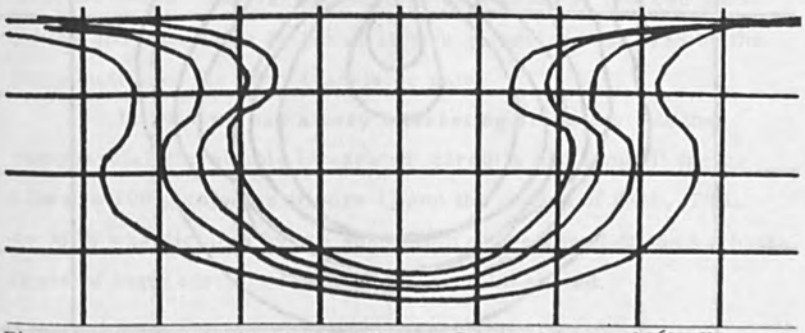

Fig. 3 Energy dissipation profiles - Beam voltage = 9560 V.
Scale: 1 micrometer/division

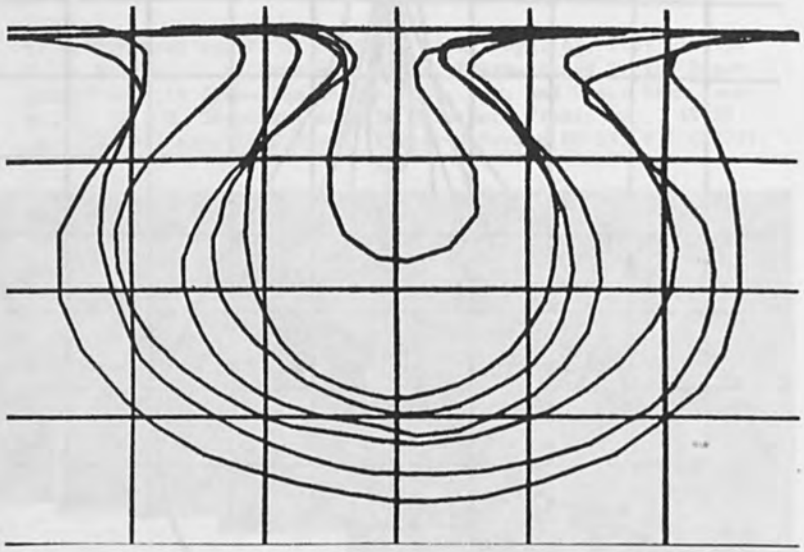

Fig. 4 Energy dissipation profiles - Beam voltage = 14.86 kV
Scale: 1 micrometer/division

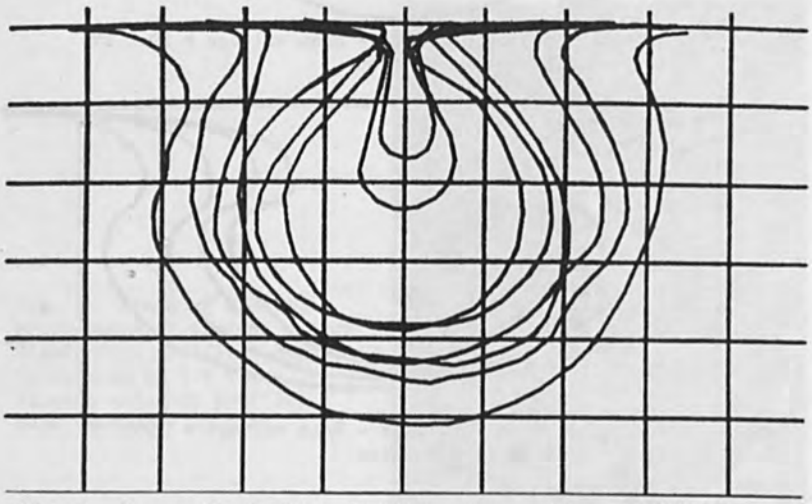

Fig. 5 Energy dissipation profiles - Beam voltage = 17.7 kV
Scale: 1 micrometer/division.

NANOELECTRONICS

J. E. PICQUENDAR

THOMSON-C. S. F., Corbeville, 91 - ORSAY (France)

INTRODUCTION.

All the tasks performed by computers can be described as a collection of bits transferred through a number of gates. The cost of the operation depends on the energy needed to transfer one bit through one gate.

This simple consideration has led to the general use of the product of the gate power and the time required for the bit to go through the gate, $P \times t_{pd}$ which has the dimensions of energy and is expressed in joules as the merit factor of the gate.

In figure 1, one can see the evolution of this merit factor with the years. The vacuum tube gates started at 100,000 picojoules and a decisive factor of 10 was gained around 1955 by the introduction of the alloy transistor gate.

In 1967 we had a very interesting situation : all the commercially available integrated circuits had a merit factor close to 100 picojoules (figure 1) and the choice of ECL, TTL, or MOS was dictated by the adaptation of the speed of the various types of logic circuits to the problem to be solved.

LIMITS OF INTEGRATED CIRCUIT PERFORMANCES.

Let us estimate the amount of energy spent in a simple gate to switch it on and off : the gate consists of a transistor, a

load resistor R and, of course, a parasitic capacitance C. Switching time is roughly T = RC.

If the voltage is V, the stand-by power dissipation is $\frac{V^2}{R}$.

The energy dissipated per cycle for the charge and discharge of the capacity is $E = CV^2$. If the circuit works at its top speed $F = 1/T$, then $E_{total} = 2\ CV^2$ per cycle (figure 2). The energy is proportional to the merit factor $P.t_{pd}$. To reduce this energy, one can act on C and/or V.

The capacitance C is, of course, proportional to the area of the circuit so one way to reduce it is to reduce the dimensions of the circuit ; this is the original nanoelectronic concept.

Since C is mainly a capacitance between an ohmic conductor and a semiconductor substrate, it also depends on the square root of the carrier concentration in the semiconductor.

The voltage V is proportional to the supply voltage and since it appears to the second power, much can be gained by reducing the supply voltage.

Many efforts have been made over the past several years to reduce C by going to finer geometries.

Since all the standard I. C. technologies use photolithography, they are limited in the race toward smaller dimensions by the diffraction of light which places a practical limit on these dimensions of about 1 micron.

Refinement of techniques has recently led to the reduction of the $P.t_{pd}$ product by about one order of magnitude towards the 10 picojoule region.

ELECTRON AND ION BEAM TECHNOLOGY.

To go through the optical diffraction barrier, one has to rely on other physical processes ; i.e., replace low energy (a few electron volts) photons by high energy (several KeV) electrons and ions.

At several KeV all associated wavelengths for charged particles are no longer in the micrometer range but are in the nanometer range, so there is no longer a practical influence due to diffraction.

In IC technology there are three fundamental operations : lithography, thin film etching and doping. As the years have passed a coherent set of technologies has been developed - coherent in the sense that an accuracy compatible with the limitation of photolithography can be achieved.

If we switch from photolithography to electrolithography we must develop a new coherent set of technologies for the three basic operations aiming at submicron geometry.

ELECTRON BEAM PATTERN GENERATOR.

Electrons have much the same effects on resists as photons but electron beams make much finer spots in the nanometer range. Many people have made narrow lines in the Laboratory and a few have also made some circuits. This can be done with commercially available laboratory apparatus : the scanning electron microscope.

The problem is not to make the first circuits but to develop the apparatus for low-cost processes in industrial applications.

The direct exposure of a silicon wafer is convenient for developing new types of circuits or for special applications like microwave transistors ; direct exposure is not suitable for mass production, even with automatic registration.

Due to the sequential nature of operation of an EBPG the time required to cover a 2" x 2" area is greater than one hour. Therefore the EBPG can be used only for production of master masks. Two more conditions must be met for mask production :

1. - to be able to generate a 2" mask with absolute step and positioning accuracy of .1 micron.

2. - to develop a fast large area projection system with the same accuracy.

A master mask fully automated EBPG machine with an absolute position accuracy of .1 micron is presented in another paper at this conference.

DUPLICATOR.

Several projection schemes have been proposed -- among them the Westinghouse scheme (ELIPS system), the Radiant Energy system machine, the X-ray projection scheme, etc...

The main problems to be solved here can be stated as follows :

- keep the resolution within .1 micron,
- insure a practical alignment process accurate to .1 micron which could be automated,
- keep the resolution even if the mechanical prepositioning is in the normal mechanical precision range of 10 microns.

THIN FILM ETCHING.

The chemical etching normally used is non-directional and sensitive to crystal grains. The fuzziness of the edge and the undercutting are tolerable for standard microcircuits using 5 microns lines.

For nanoelectronic circuits one must use a directed ion beam for etching which provides straight , sharp edges with a fuzziness less than 50 nanometers and practically no undercutting.

DOPING OF SEMICONDUCTORS.

We want to preserve the lateral precision so we can no longer use isotropic thermal diffusion.

Ion implantation is a normal and practical solution to this problem.

It leads also to side benefits ; the annealing temperature after implantation is low enough to allow the use of semi-insulating material without risking carrier type-inversion.

These first steps in ion and electron beam technology give a reduction of linear dimensions by a factor of 10.

NANOELECTRONIC CIRCUITS DESIGN.

How do we make the best use of these new possibilities of electron and ion beam technology ? What type of active devices are best suited now for this purpose... Bipolars ? Mosfets ? Mesfets ? (figure 3). After careful study we have selected as the first generation of nanoelectronic circuits the field effect transistor with ion implanted source, channel and drain and Schottky

gate.

We have coined the name ASTEC from them. Let us first consider the relations between the performances of mesfets devices and their size.

The supply voltage V used with the device is proportional to the pinch off voltage $Vp = q \frac{Na\ 2}{2\varepsilon}$ which does not depend on the lateral dimensions of the device.

To optimize the merit factor of the device we can show that there is an optimum ratio of a to L. If Vp is too small for a given L the electric field in the channel is low ; the electrons are slow and t_{pd} is great. However, after a certain value it does not pay anymore to increase Vp : the field in the channel becomes larger than the drift saturation field and t_{pd} does not decrease further whereas P increases rapidly.

It is possible to compute this optimum ratio so the choice of L determines the best operating voltage V.

One then can show that the power of the device is proportional to L^2 and Z. The propagation delay time is proportional to C.

Then the merit factor of the device is proportional to the fourth power of the linear dimensions, whereas for bipolars the merit factor varies only as the second power of the linear dimensions (figure 4).

We may also remark that the mesfet technology requires fewer masks and operations than bipolar technology. Mesfets are somewhat simpler to make than mosfets and presently have lower operating voltages and t_{pd}.

As explained in another paper presented at this conference the possibility of doping the channel and contacts by ion implanta-

tion allows the use of semi-insulating substrates and reduces the parasitic capacitance of connections.

We can also see that the power dissipated per square centimeter of silicon decreases linearly with the dimensions of the mesfet gate.

NANOELECTRONIC CIRCUITS OF TODAY.

Up to this date two basic nanoelectronic circuits have been made.

- a threeport NAND circuit was designed with a trigate mesfet as described in another paper. Its size was determined by the fact that a direct measurement of t_{pd} was desired thereby fixing the power of the output emitter follower transistor (1 mA in a 50 ohm line).

This circuit was measured and exhibited a t_{pd} of around 100 picoseconds and a power consumption of .7 mW.

The $P.t_{pd}$ product is under 100 femtojoules.

- the second circuit has normal nanoelectronic sized elements and its purpose is to ascertain the $P.t_{pd}$ factor.

The circuit consists of four gates with 3 gates connected in an oscillating ring (figure 5).

Circuits have been made but not yet dynamically tested up to this date. Simulation and computations lead us to expect a $P.t_{pd}$ factor of less than 10 femtojoules.

Figure 6 shows a comparison of the sizes of a two gates TTL circuits and a 4 gates ASTEC circuit.

Figure 7 shows a high magnification optical photograph of the ASTEC circuit. It looks fuzzy because it is impossible to correctly observe this circuit; and consequently impossible to

make by optical means.

Figure 8 (magnification x 1500) shows a SEM micrograph of the same circuit. At the start of the nanoelectronic project in 1968 we shot for a picojoule circuit. We have already measured less than 100 femtojoules and we are expecting very shortly less than 10 femtojoules (figure 9).

INDUSTRIAL DEVELOPMENT OF MACHINES.

It is nice to make wonders in the Laboratory -- it is better to be able to manufacture and sell them at sensible prices.

It all depends on :

- the availability of Ion and Electron Beam Machines,
- their initial cost,
- their normal output rate.

Let us review the status of these machines :

ELECTRON BEAM PATTERN GENERATOR

We have now fully developed an automated CAD compatible EBPG.

Its characteristics are as follows :

- size of mask 2" x 2"
- data input by magnetic tape
- standard time per mask 2 hours
- minimum line width .2 micron
- absolute precision .1 micron
- price comparable to the price of the equipment needed to make the same size (2") microelectronic ($>$ 1 micron) optical mask.

Units are under construction to be delivered to customers (figure 10).

DUPLICATOR.

- All the desired characteristics have been obtained,
- The prototype is under final testing,
- The machine will be fully automated,
- We plan to fit it with a loading magazine and expect a yield of one 2" wafer every 2 minutes (figure 11).

ION ETCHING.

- The "Microetch" was the first machine of this series to be put in the market. More than 50 units have already been sold.

We have a new high capacity machine under development for line production. It will be equipped with the same loading magazine as the duplicator and we expect a yield of one 2" wafer per minute (figure 12).

ION IMPLANTATION MACHINE.

We have developped a production machine as have many other people. For ASTEC the yield is one 2" wafer each five minutes (figure 13).

FUTURE FOR NANOELECTRONIC CIRCUITS.

As we have seen, the machines are, or are about to be, commercially available. Their production rates, i.e. the number of wafers produced per hour and per dollar invested, is comparable to standard microelectronics, and we therefore expect the price per square centimeter of silicon area to remain at a comparable level.

The ASTEC gates use very-low power transistors and cannot drive outgoing transmission lines. On the other hand

their dimensions are so small that one can put several thousand of them per square millimeter of silicon. To make the best use of their speed one wants to put them as close as possible to each another.

This leads to the concept of NSI circuits (Normal Scale Integrated Circuits) using a piece of silicon a few millimeters square with ASTEC gates in the middle surrounded by a row of larger mesfets to connect the NSI to the output gates.

CONCLUSION.

We have reported in this paper the Ion and Electron Beam Technology aspects of the nanoelectronic project. The first phase of this project covers the years 1968 to 1973 and will lead to the demonstration of NSI feasibility. Much more is involved in this project than mere technologies.

The whole project is a great challenge but will lead to a revolution in the semiconductor business.

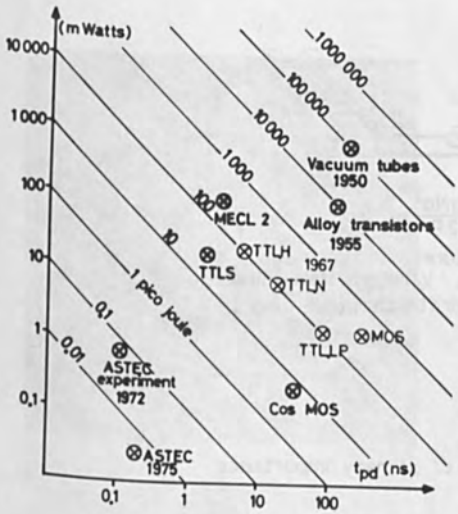

1950 – 1975

Figure 1

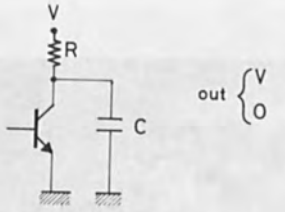

DELAY TIME $t_{pd} = RC$

STATIC POWER $P_S = \frac{V^2}{R}$

DYNAMIC ENERGY / CYCLE $E_D = CV^2$

TOTAL ENERGY/CYCLE AT THE LIMIT FREQUENCY F $E_T \simeq CV^2 + t_{pd} P_S$

$= 2CV^2$

$2C = \lambda S$

$$\boxed{E_T = \lambda S V^2}$$

Figure 2

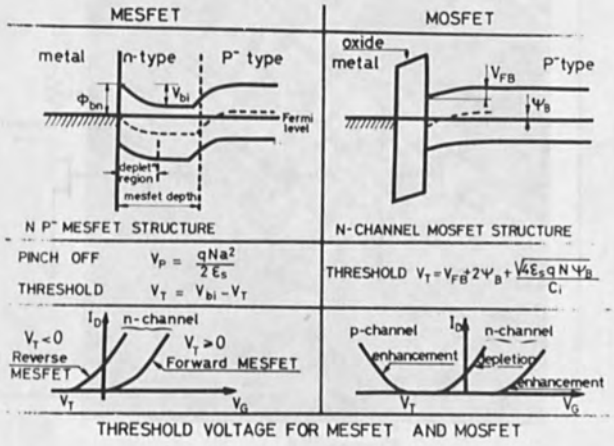

Figure 3

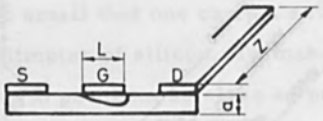

Pinch off: $V_p = \frac{qNa^2}{2\varepsilon}$

Optimized structure:
where L / V_p ratio is determined
by the drift saturation field

Power : $\sim L^2 \times Z$

t_{pd} : $\sim L$

$P \times t_{pd}$: $\sim L^3 \times Z$

Gate length L is of primary importance

MESFET PERFORMANCE

Figure 4

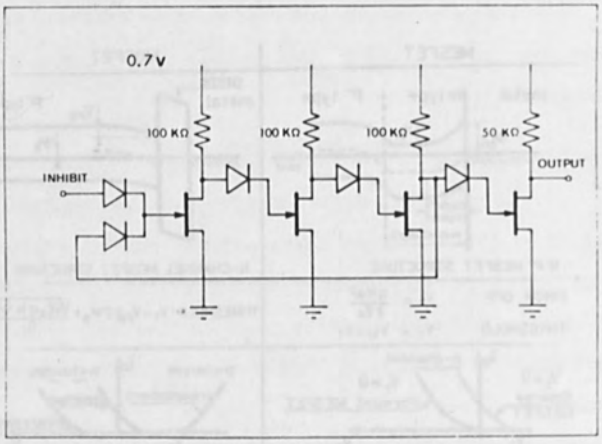

Figure 5

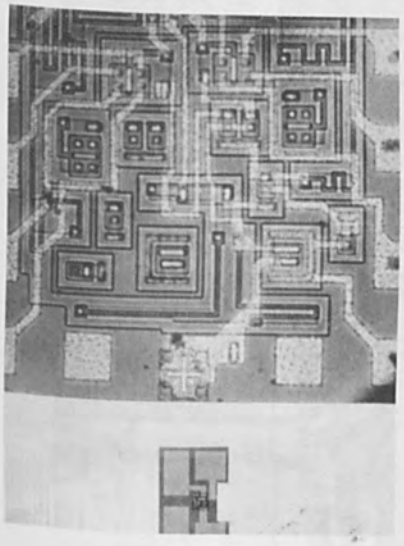

Figure 6

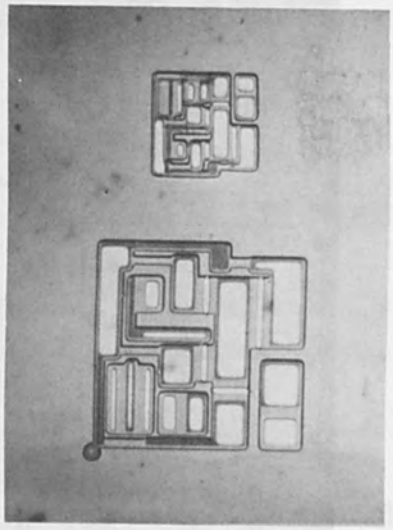

Figure 7

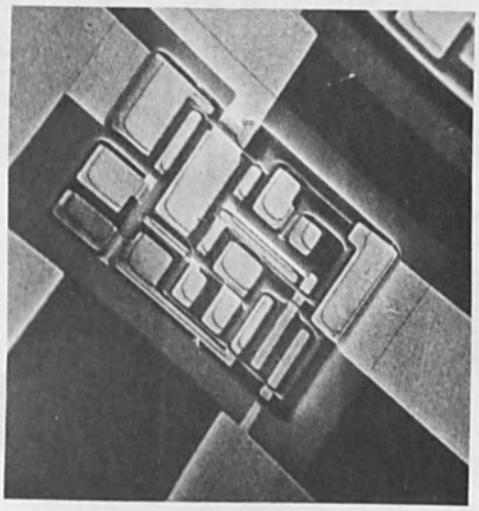

Figure 8

LOGIC GATES IN DIFFERENT TECHNOLOGIES

	POWER mWatts	t_{pd} nano secondes	$P \cdot t_{pd}$ pico joules
TUBES	1000 filament power +300 (100V•3mA)	100	$\sim 10^5$
ALLOY TRANSISTORS	100 (10V•10mA)	100	$\sim 10^4$
TTL	10 (5V•2mA)	10	10^2
ASTEC	0.05 (1V•0.05mA)	0.5	10^{-2}

Figure 9

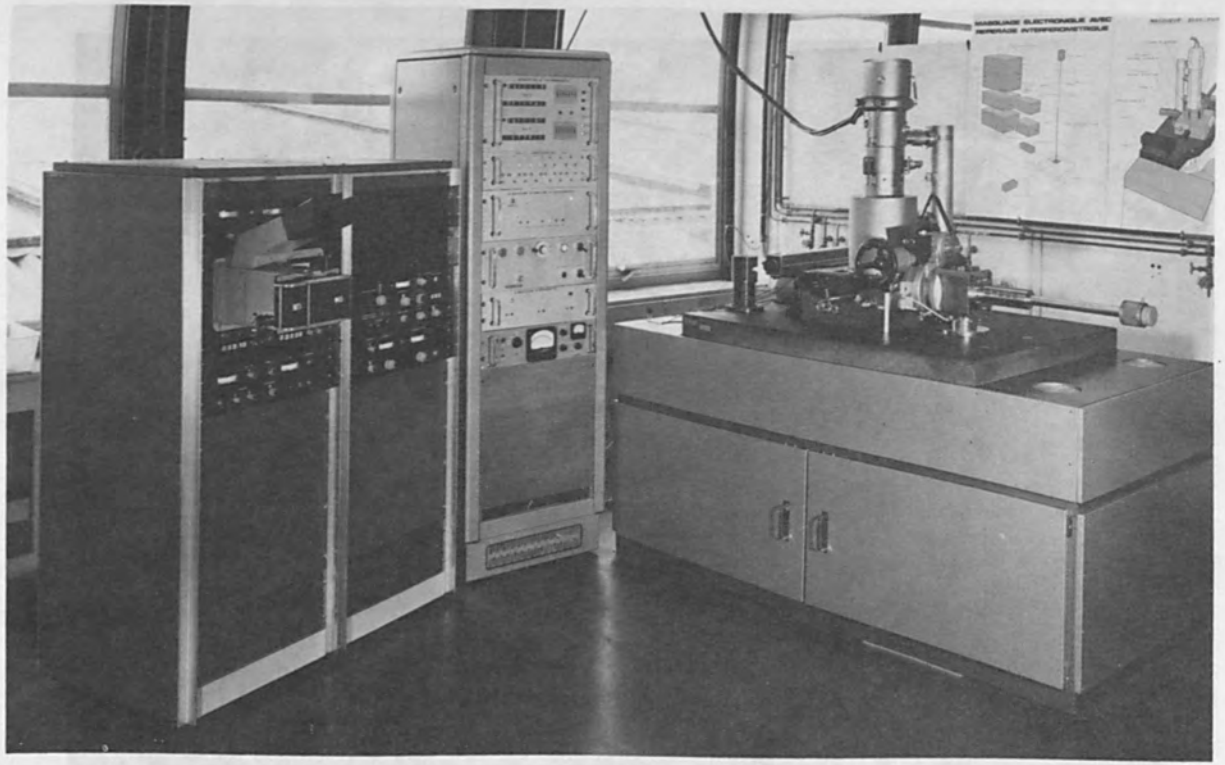

Figure 10

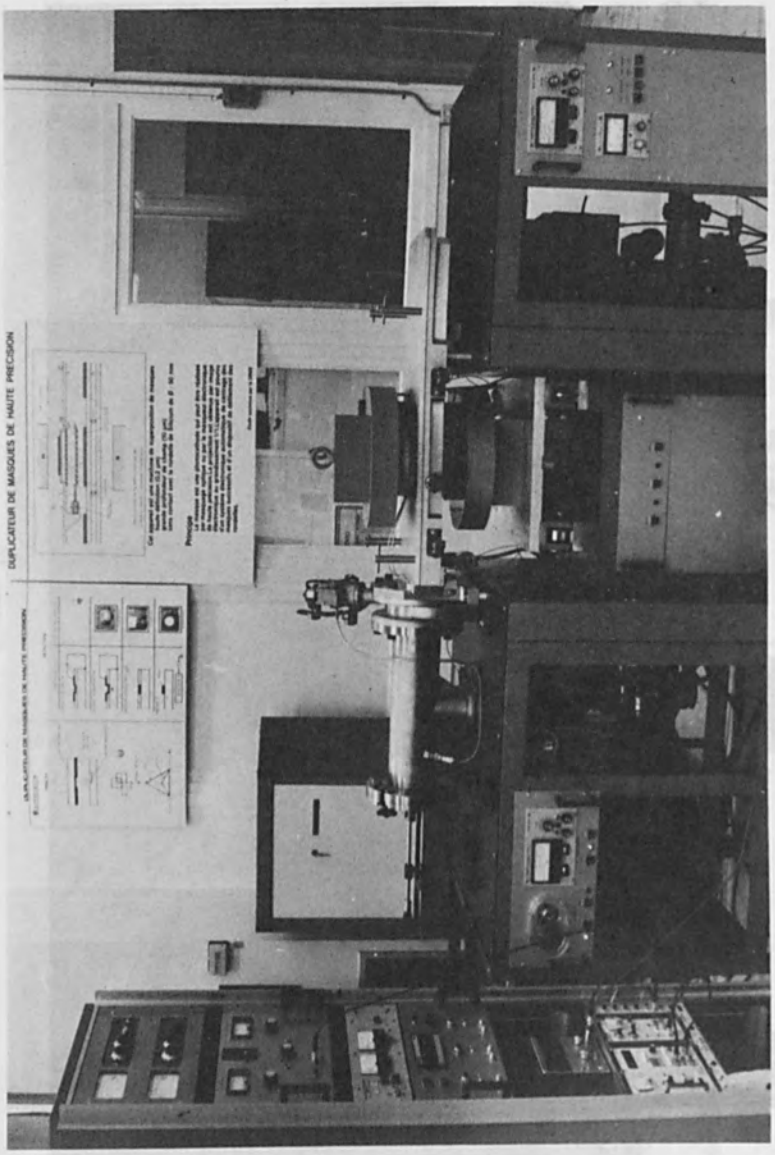

Figure 11

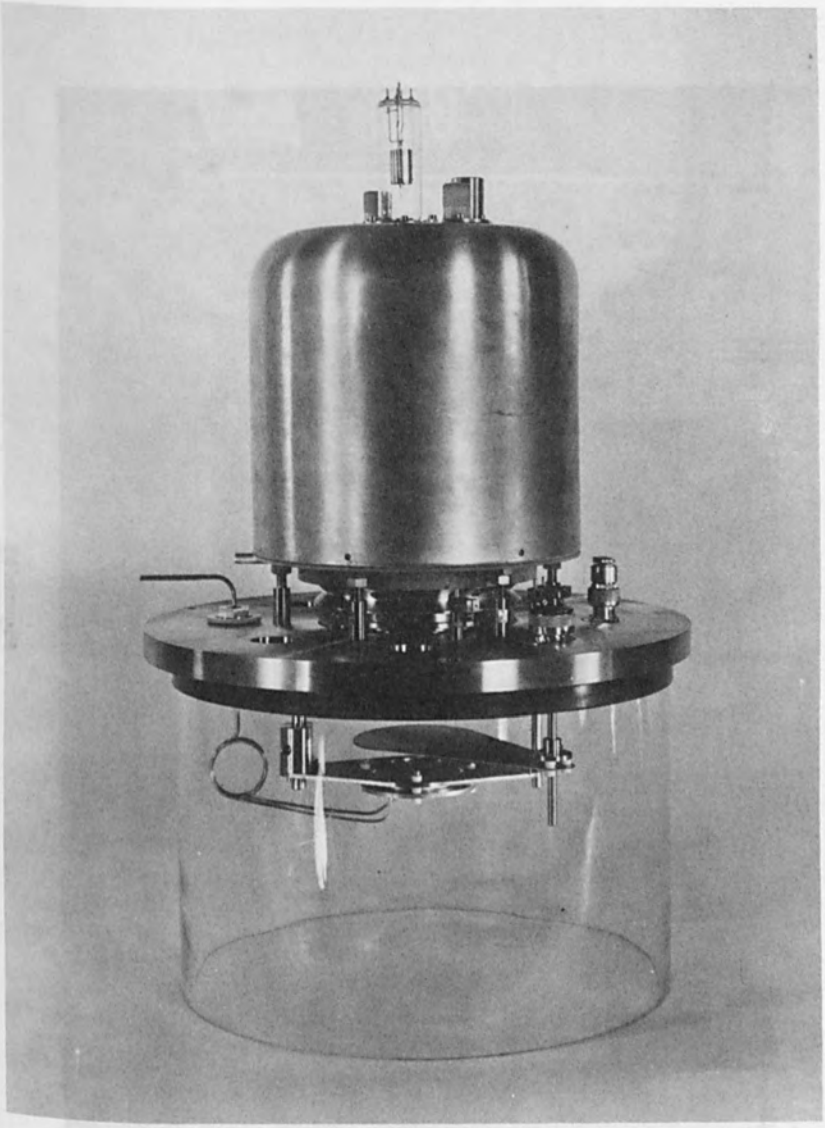

Figure 12

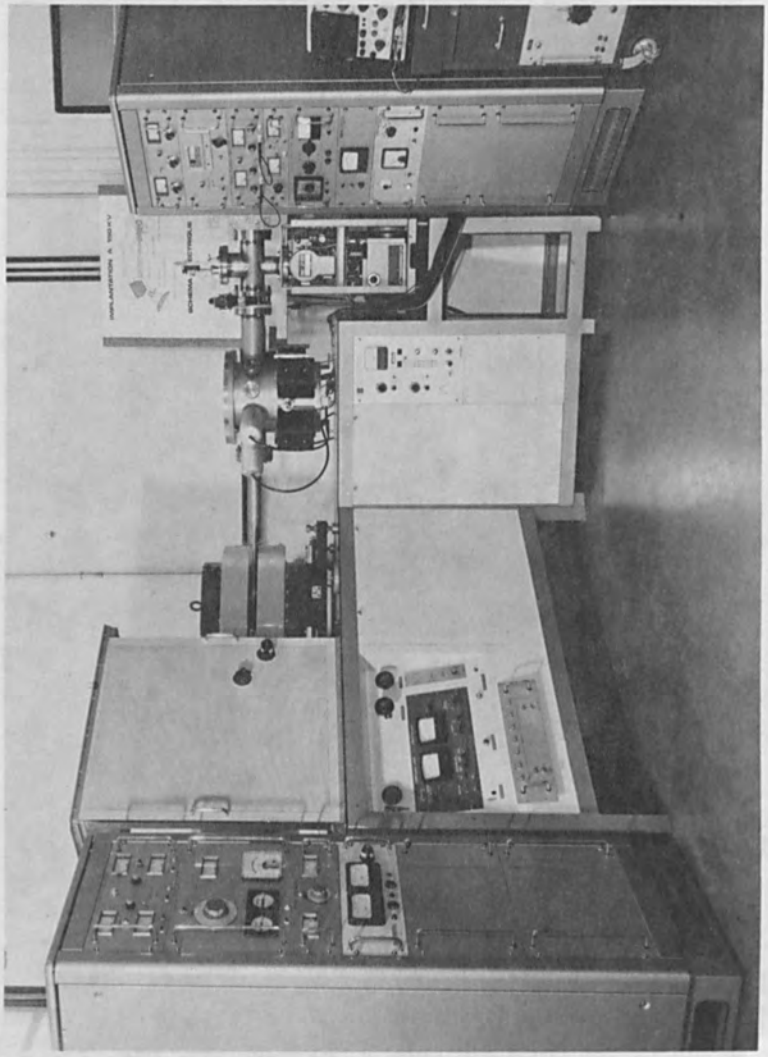

Figure 13

PRESENTED PAPERS

GROUP I

ELECTRON BEAM EXPOSURE PROFILES IN THIN POLYMER FILMS

R. J. Hawryluk

Department of Physics and Research Laboratory of Electronics
Massachusetts Institute of Technology
Cambridge, Massachusetts 02139

and

Henry I. Smith

Lincoln Laboratory
Massachusetts Institute of Technology
Lexington, Massachusetts 02173

ABSTRACT

High resolution electron beam lithography depends on producing an undercut profile in an electron sensitive polymer film. We have constructed a theoretical model of the electron scattering and dissipation of energy in such polymer films. The study incorporates film thickness, beam diameter, voltage, and substrate material as parameters. A comparison with experiment is made. The model indicates that large angle back-scattering plays the dominant role in producing the familiar undercut profile.

I. INTRODUCTION

The high resolution capability of electron beam lithography was demonstrated several years ago[1,2,3]. However, this early work did not provide practical device fabrication techniques. In 1968, Haller et al[4], working with thin polymer films on substrates, developed a new approach to electron beam lithography, which took advantage of the fact that in certain polymers irradiated with moderate doses of low energy electrons, the mechanism of chain scission predominates over cross linking. In the irradiated regions, the average molecular weight is reduced, and this material can be selectively removed by an appropriate mixture of solvent and non-solvent. Polymethyl methacrylate (PMMA) was considered the preferred polymer material by virtue of its ease of synthesis, its high resolution capability, and its resistance to chemical etchants. In analogy to the term photoresist, electron sensitive polymer

This work is sponsored by the Department of the Army.

films are frequently called electron resists, even though resistance to chemical etchants is probably of limited utility at sub-micron resolutions.

For microelectronic device fabrication, producing a pattern in a polymer film is only the first step. This pattern is then used as a mask either for chemical etching, sputter etching, ion implantation, or metal film lift-off. The last refers to a technique developed by Hatzakis[5] wherein a metal is evaporated onto a developed PMMA film, after which the polymer is removed by a solvent, and a metal film pattern corresponding to the pattern in the PMMA is left behind on the substrate. It was found that the success of the Hatzakis lift-off technique depended on producing an undercut profile in the PMMA film so as to prevent continuity between the metal on the substrate and that on top of the PMMA, as depicted in Figure 1.

The width and shape of the profile produced in an electron resist film depend on the combined effects of the incident electron beam and electrons scattered back from the substrate. For a fixed beam diameter, the profile can be varied by changing either the voltage or the charge per unit length laid down by the beam. This is shown in Figure 2 taken from Wolf, et al[6]. The present theoretical investigation was undertaken in order to determine the factors which contribute to the undercut profile so essential to the Hatzakis technique. Earlier work by Nosker[7] had concluded that only the forward scattering of the incident electron beam was important in determing profile (his Figure 13). The present study takes into account a number of factors overlooked by Nosker and comes closer to accord with experimental observations.

II. THEORETICAL MODEL

It will be assumed that the development rate of an electron resist depends on the energy dissipated per unit volume[8], and thus the profiles produced can be identified as energy dissipation profiles. Following Nosker [7], we will treat forward and back-scattering separately.

We will be considering only the configuration of thin polymer films ($\lesssim$5000 Å) on semi infinite substrates, and normal incidence electron beams in the 10 - 30 keV range. These conditions are compatible with high resolution patterns.

Multiple Forward Scattering

When the electron beam enters the film, it undergoes many small angle scattering events before entering the substrate. The effect of this is to increase the diameter of the beam. The average energy lost per electron in passing through the film is small and, for the purpose of calculating the beam spreading, inelastic collisions will be ignored. So also will large angle backscattering events. Both will be accounted for at a later point.

Following the work of Massey[9], Bethe, et al[10], and Rossi and Greisen[11] the following expression is obtained for the probability per unit area an electron will be scattered to a radial distance r after penetrating a vertical distance z

$$H(r,z) = \frac{3\lambda}{4\pi z^3} \exp\left[-\frac{3}{4}\left(\lambda r^2/z^3\right)\right] . \qquad (1)$$

This expression is actually from unpublished work of Fermi[11], and represents a steady state solution for the small angle scattering approximation to the Boltzman equation. λ in equation (1) is the momentum loss mean free path which depends on the differential scattering cross sections of the atoms composing the polymer[10]. Following Nosker[7] and Massey[9] the differential scattering cross-sections were obtained using the Born approximation to the Schroedinger equation and a Hartree-Fock corrected Thomas-Fermi model for the atomic scattering potential[12,13]. For PMMA ($C_5H_8O_2$) with a density of 1.18 gm/cm^3 we obtained the following values for λ:

$$\lambda_{PMMA} = 4.727 \cdot 10^4 \text{ Å} \quad @ \text{ 10 keV}$$
$$= 1.009 \cdot 10^5 \text{ Å} \quad @ \text{ 15 keV}$$
$$= 1.729 \cdot 10^5 \text{ Å} \quad @ \text{ 20 keV.}$$

Equation (1) is known as the delta function response since it corresponds to a single electron entering the film at r = 0 and z = 0.

A real electron beam will, of course, have a finite radius and some distribution. We assume this distribution is azimuthally symmetric and Gaussian,

$$N(X) = N_o \exp(-aX^2), \qquad (2)$$

where X is a radial distance from the beam axis, and the total number of electrons is $I = \pi N_o / a$. The resulting density distribution of electrons in the polymer film as a function of r_o and z is given by

$$D(r_o, z) = \int_0^{2\pi} \int_0^{\infty} H(r, z)\, N(X) X dX d\varphi$$

$$= \frac{N_o b \exp\left(-b r_o^2\right)}{a+b} \left\{ 1 + \pi^{-1/2} \int_0^{\pi} d\varphi \, \frac{r_o b \cos\varphi}{\sqrt{a+b}} \right.$$

$$\left. \cdot \exp\left(\frac{b^2 r_o^2 \cos^2\varphi}{a+b} \right) \operatorname{erf}\left(\frac{r_o b \cos\varphi}{\sqrt{a+b}} \right) \right\} \qquad (3)$$

where $b = 3\lambda / 4z^3$ and $r^2 = r_o^2 + X^2 - 2 r_o X \cos\varphi$. Figure 3 illustrates the coordinate system and the relation among r, X, φ, and r_o. Equation (3) must be evaluated numerically, and this was done by a computer subroutine called DENS.

Energy Loss

For the purpose of calculating $D(r_o, z)$, we ignored inelastic collisions. We will now take into account the energy loss of the incident beam in passing through the polymer film. The energy dissipated by an electron in passing through a material of density ρ, atomic number Z, and atomic weight A is obtained from the expression[14]

$$-\frac{dE}{ds} = \frac{4\pi N_A e^4 Z \rho}{m v^2 A} \ln\left(\frac{m v^2}{I} \right), \qquad (4)$$

where N_A is Avagadro's number and I is the so-called average ionization energy. The usually accepted value in electron volts is $I = 11.5Z$. The weighted average of Z for PMMA is 3.76 so that

$$I_{PMMA} = 41.4 \text{ eV}$$

It was found that if I was varied over a wide range, no significant changes were observed in the corresponding energy dissipation profiles.

Energy dissipation profiles corresponding to forward scattered incident beams of small initial cross sections are shown in Figures 4-6. They are obtained by multiplying $D(r_o, z)$ by the energy loss factor obtained from equation (4). These do not correspond to the profiles shown in Figure 2 and it is clear that large angle backscattering is responsible for most of the details of these profiles.

In earlier work, Nosker using a broad Gaussian beam reached the conclusion that backscattering from the substrate increased the exposure level but had negligible effect on linewidth[7]. From this he concluded that only forward scattered electrons were important in determining profile (his Figure 13 for Ge). This conclusion does not follow and is at variance with experimental work. In Figure 2, taken from Wolf et al, the polymer profiles have a minimum width (neck) near their top surfaces which is generally many times greater than the incident beam diameter. This cannot be explained by forward scattering along. Similarly, in our own laboratory, we have used beam diameters in the range 100 Å to 800 Å, in conjunction with the Hatzakis lift-off technique[5], to produce metal lines with widths ranging from 2000 Å to 10,000 Å (Figure 7).

Backscattering

Nosker's conclusion resulted from his model which calculated the energy dissipated by the backscattered electrons only at the substrate-thin film interface and ignored its variation with depth in the polymer. We have extended the work of Everhart[15], Archard[16] and Nosker[7] with respect to the backscattered electrons and explicitly taken into account the continued energy loss of the electrons as they pass back through the polymer film, and the increase in interaction as a function of the angle of emergence.

The coordinate system is shown in Figure 8. We obtained the following expression for the energy dissipation per unit volume in the polymer film by electrons backscattered from the substrate as a function of the depth in the polymer (t) and the distance from the beam axis (r):

$$E(r,t) = \left[\frac{4\pi N_A e^4 Z_2 \rho_2}{m v_o^2 A_2}\right] \frac{\beta n_o}{\pi R^2} \int_o^{y_{max}} \frac{(1-y)^{\beta-1}}{(y+d)^2} \left[1+\frac{\sqrt{(y+d)^2+b^2}}{y+d}\right]^{-2} \cdot \frac{\ln\left\{\frac{mv_o^2}{I}\left[1-y-\frac{y}{y+d}\sqrt{b^2+(y+d)^2} - \frac{\rho_2}{\rho_1}\frac{d}{y+d}\sqrt{b^2+(y+d)^2}\right]^{1/2}\right\}}{\left[1-y-\frac{y}{y+d}\sqrt{b^2+(y+d)^2} - \frac{\rho_2}{\rho_1}\frac{d}{y+d}\sqrt{b^2+(y+d)^2}\right]^{1/2}} dy. \quad ,(5)$$

where N_A is Avagadro's number, and ρ_1 is the density of the substrate. Z_2, ρ_2, and A_2 are the atomic number, the density and the atomic weight of the polymer film, respectively. n_o is the number of electrons incident at $x=0$. β is a parameter which is set equal to 0.045 Z, as was done by Everhart[15] in order to obtain a good fit to the experimental reflection coefficient as a function of substrate atomic number. R is the electron range for the substrate material as given by the Thomson - Whiddington law[15]. And

$$y = x/R$$
$$d = t/R$$
$$b = r/R \qquad (6)$$

Everhart[15] and Nosker[7] chose y_{max} from the condition that no electron could travel a distance greater than R. They thus calculated the effect of all electrons which emerge from the substrate. In contrast to this, we will choose y_{max} in such a way as to account only for those electrons which emerge from the substrate with "directionality". This follows from our assumption that if through inelastic collisions the velocity of an electron decreases to the point where it should be described by plural scattering, then its effect to first order is to contribute only to a background of energy dissipation. From Massey[9] and Bethe et al[10], the criterion

for the onset of plural scattering is that the mean energy E_p is given by

$$\int_{E_p}^{E_o} \frac{dE}{\lambda \left| dE/ds \right|} = \frac{1}{2}, \qquad (7)$$

where $E_o = 1/2\ mv_o^2$, λ is the momentum loss mean free path referred to earlier, and dE/ds is obtained from equation (4). In this calculation the effect of the overlayer film is negligible so that λ and dE/ds refer to the substrate material. From the Thomson - Whiddington law [15],

$$\frac{v^4}{v_o^4} = 1 - \frac{\text{distance in substrate}}{R}$$

$$= 1 - \left[y + \frac{y}{y+d} \sqrt{b^2 + (y+d)^2} \right], \qquad (8)$$

and y_{max} is obtained from

$$1 - \left(E_p / E_o \right)^2 = y_{max} + \sqrt{y_{max}^2 + \left(\frac{b\, y_{max}}{y_{max} + d} \right)^2}. \qquad (9)$$

Equation (5) was evaluated numerically by a computer subroutine known as EXPO.

From equation (5) another equation can be obtained which evaluates the contribution to the energy dissipation of large angle backscattering within the polymer film itself which occurs during the initial passage of the incident beam; a contribution which was ignored earlier. To do this, equation (5) is modified by letting

$$d = 0$$

$$n_o = \pi N_o / a \quad \text{(see equation (2))}$$

$y_{max} = t/R$, when y_{max} as given by plural scattering is greater than t/R, and Z, R, and ρ take on the values characteristic of the polymer. The result is

$$E'(r_o, z) = \left[\frac{4\pi N_A e^4 Z_2 \rho_2}{m v_o^2 A_2}\right] \frac{N_o}{a R_2^2} \int_o^{t/R} \frac{\ln\left[\frac{m v_o^2}{I}\left(1-y-\sqrt{y^2+b^2}\right)\right]^{1/2}}{\left(1-y-\sqrt{y^2+b^2}\right)^{1/2}} \cdot \left[y+\sqrt{y^2+b^2}\right]^{-2} \left[\beta\,(1-y)^{\beta-1}\right]_{poly} dy \qquad (10)$$

where the factor $[\beta\,(1-y)^{\beta-1}]_{poly}$ is a weighted average of the contributions from the atoms making up the polymer. For the case of PMMA ($C_5H_8O_2$) and making use of Everhart's[15] result, $\beta \simeq 0.045Z$, this factor is given by

$$\left[\beta\,(1-y)^{\beta-1}\right]_{PMMA} = 0.045\left[\left(\frac{5Z_C}{15}\right)(1-y)^{0.045Z_C-1} + \left(\frac{8Z_H}{15}\right)(1-y)^{0.045Z_H-1} + \left(\frac{2Z_O}{15}\right)(1-y)^{0.045Z_O-1}\right]. \qquad (11)$$

Equation (5) gives the energy dissipated by the backscattered electron when the beam incident at the substrate-film interface is of negligible width. Equation (3) gives the distribution of electrons at the film-substrate interface when the input beam is Gaussian, and this can be convoluted with a normalized E(r, t) to give the energy dissipated by the backscattered electron when the input beam is Gaussian and has a finite beam radius:

$$E''(r_o, z) = \frac{1}{n_b} \int_0^{2\pi} \int_0^{\infty} D(X, T)\, E(r, T-z)\, X\, dX\, d\varphi\,, \qquad (12)$$

where $r^2 = X^2 + r_o^2 - 2Xr_o \cos\varphi$ and $1/n_o$ normalizes $E(r, T-z)$ to one incident electron. Equation (12) was also evaluated numerically. It was found that for small beam diameters (~250 Å) the resulting energy dissipation differed from that predicted by equation (5) only at very small values of r_o, where the energy dissipated by the multiple scattered electrons is much larger than the energy dissipated by the backscattered electrons. Thus, for small beam diameters the total energy dissipated in the polymer film is given with sufficient accuracy by the following simpler expression:

$$\mathcal{E}(r_o, z) = \left[\frac{4\pi N_A e^4 Z_2 \rho_2}{mv_o^2 A_2} \ln\left(\frac{mv_o^2}{I}\right)\right] D(r_o, z)$$

$$+ \frac{E(r_o, T-z)}{n_o} \frac{\pi N_o}{a} + E'(r_o, z)\,. \qquad (13)$$

III. DISCUSSION

Equation (13) gives the total energy dissipated per cm^3 in the polymer as a function of r_o and z. The function $\mathcal{E}(r_o, z)$, which we call "total", was evaluated numerically. Figure 9, shows the polymer profiles predicted by the theory for a PMMA film thickness of 4000 Å on a silicon substrate for a beam voltage of 20 keV. Note that in contrast with the case of multiply scattered electrons(Figures 4-6), there is appreciable widening at the neck as well as the undercut profile. In Figure 10, profiles are shown for a beam voltage of 15 keV. Note that Figures 9 and 10 show good qualitative agreement with Figure 2. A quantitative comparison has not been made because the profiles of Figure 2 were produced by a line scan, whereas our calculations are for a stationary beam. The additional convolution required in order to obtain profiles for the scanned beam case has not been done here.

Figure 7 shows experimental line width versus exposure data. For the denser $LiNbO_3$ substrate ($\rho = 4.64$), less exposure is required than on a silicon substrate in order to obtain a given linewidth. A similar result can be obtained from the theory if it is assumed that linewidth can be equated to the width of the neck in the polymer profile. In Figure 11 the exposed radius at the top surface of a 4000 Å thick PMMA film is plotted versus exposure. The latter is in arbitrary units, proportional to the number of input electrons, since to assign an absolute exposure number would necessitate assumptions about the PMMA sensitivity and development conditions. Figure 11 shows that fewer electrons are required on the titanium substrate ($\rho = 4.5$ $Z = 22$) than on the silicon substrate ($\rho = 2.33$ $Z = 14$) in order to obtain a given exposed radius.

Figure 12 is a plot similar to Figure 11 except that here the substrate is silicon and the beam voltage is varied. As the voltage is increased the number of electrons needed to obtain a given exposed radius must likewise be increased. This is borne out be results such as shown in Figure 2 for voltages greater than 10 keV.

Figure 13 shows the predicted dependence of exposed radius on film thickness. The effect predicted here has been observed experimentally, and illustrates the role of large angle backscattering both in the PMMA and the substrate.

IV. CONCLUSIONS

The above model has delineated those factors which contribute to the formation of profiles in electron sensitive polymer films when exposed by a finely focused electron beam. Figures 14, 15, and 16 are intended to illustrate these contributions by plotting $\mathcal{E}(r_o, z)$ as a function of r_o along with the three contributions to it namely: (1) the energy dissipated by multiply scattered electrons, (2) the energy dissipated by electrons backscattered from the substrate and (3) the energy dissipated by electrons backscattered from the PMMA. Figures 14, 15, and 16 are for $z = 0$, 2000 Å, 4000 Å, respectively. Figure 14 illustrates that the previously neglected effect of large angle backscattering in the PMMA is not insignificant in the formation of the polymer neck. Hence it may also be desirable to include intermediate angle scattering events in the PMMA.

In calculating the effect of backscattered electrons, the onset of plural scattering served as the criterion for determining the upper limit of integration, y_{max}. It is expected that this assumption and hence the entire model would begin to break down when the maximum total distance an electron can travel in the substrate, as given by the plural scattering criterion, is on the order of the radius of exposure at the polymer-substrate interface. As a result, for $r_o \sim 7000$ Å the model breaks down for beam voltage less than ~12 keV with silicon substrates and for beam voltage less than ~20 keV for substrates whose atomic number and density are greater than those of titanium.

ACKNOWLEDGMENT

The authors wish to thank E. D. Wolf for providing Figure 2 and A. Soares for carrying out the electron beam lithography experiments.

References

1. G. Mollenstedt and R. Speidel, Physikalische Blatter 16, 192 (1960).

2. A. N. Broers, Microelectronics and Reliability 4, 103 (1965).

3. T. H. P. Chang and W. C. Nixon, J. Sci. Instr. 44, 321 (1967).

4. I. Haller, M. Hatzakis and R. Srinivasan, IBM J. Res. Develop. 12, 251, (1968).

5. M. Hatzakis, J. Electrochem. Soc. 116, 1033 (1969).

6. E. D. Wolf, F. S. Ozdemir, W. E. Perkins, and P. J. Coane, "Response of the Positive Electron Resist, Elvacite 2041, to Kilovolt Electron Beam Exposure", Record of the Eleventh Symposium on Electron Ion and Laser Beam Technology, Boulder, Colorado, May 12-14, 1971, R. F. M. Thornley, Ed. (San Francisco Press, San Francisco, 1971).

7. R. W. Nosker, J. Appl. Phys. 40, 1872 (1969).

8. Mikitishin, S. I., Tinnie, A. N., and Bazilevich, Z. A., Fiz-Khim Mekh. Mater., 1968, 4, pp. 459-462.

9. H. S. W. Massey, Advances in Electronics IV, 1-68 (1952).

10. H. A. Bethe, M. E. Rose, and L. P. Smith, Proc. Am. Phil. Soc. 78, 573 (1938).

11. B. Rossi and K. Greisen, Rev. Mod. Phys. 13, 241 (1941).

12. V. Bush and S. H. Caldwell, Phys. Rev. 38, 1898 (1931).

13. L. Marton and L. I. Schiff, J. Appl. Phys. 12, 759 (1941).

14. R. D. Birkhoff, vol 34, p. 53, Handbuch der Physik, edited E. Flugge, Springer, Berlin 1958.

15. T. E. Everhart, J. Appl. Phys. 31, 1483 (1960).

16. G. D. Archard, J. Appl. Phys. 32, 1505 (1961).

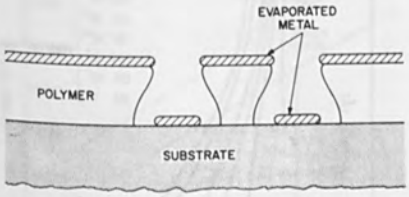

HIGH-RESOLUTION ELECTRON BEAM FABRICATION

Fig. 1. This illustrates how the undercut profile prevents continuity between the metal on the substrate and that on top of the polymer.

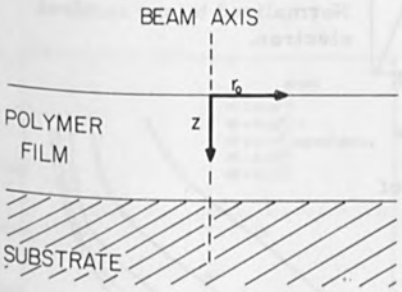

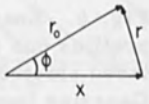

$$r^2 = r_o^2 + x^2 - 2xr_o \cos\phi$$

Fig. 3. Coordinate system.

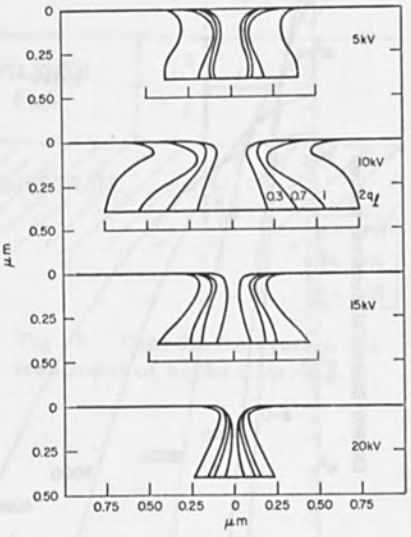

FAMILY OF PROFILES FOR 5, 10, 15, AND 20kV EXPOSURES

Fig. 2. $q_\ell = 1 \times 10^{-8}$ coulombs/cm is a line charge density, see reference 6. Figure provided through the courtesy of E. D. Wolf.

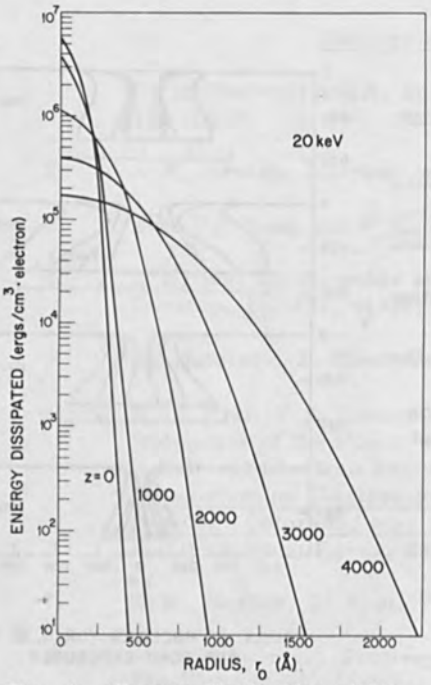

Fig. 4. Energy dissipation of the multiply scattered electrons as a function of r_o for various values of z, normalized to one incident electron. Gaussian input beam has a diameter of 250 Å and an energy of 20 KeV.

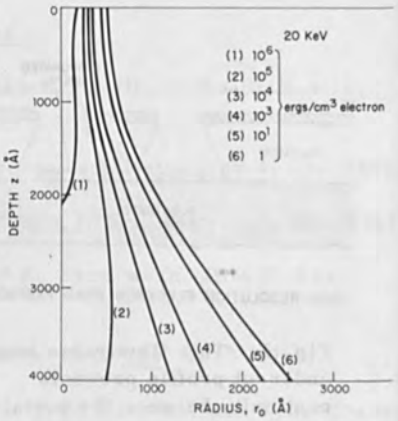

Fig. 5. Energy dissipation profiles due to multiply scattered electrons for a 20 KeV Gaussian input beam of 250 Å diameter. Normalized to one incident electron.

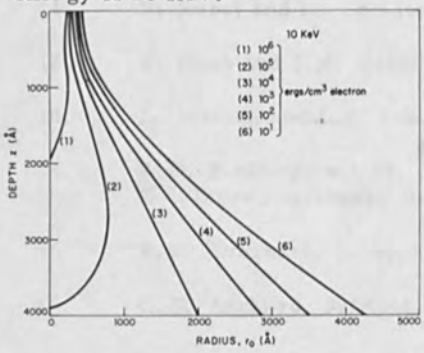

Fig. 6. Energy dissipation profiles due to multiply scattered electrons for a 10 KeV Gaussian input beam of 250 Å diameter. Normalized to one incident electron.

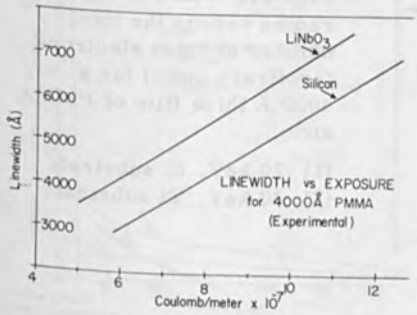

Fig. 7. Experimental linewidth versus exposure for 20 keV, ~250 Å diameter beam, and 4000 Å PMMA on $LiNbO_3$ and silicon substrates.

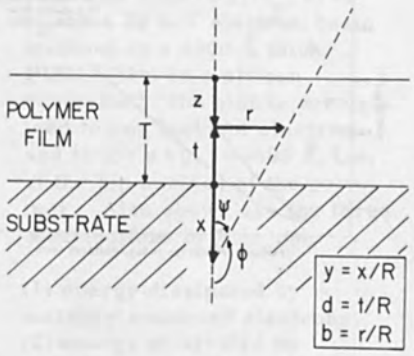

Fig. 8. Coordinate system for treatment of backscattering.

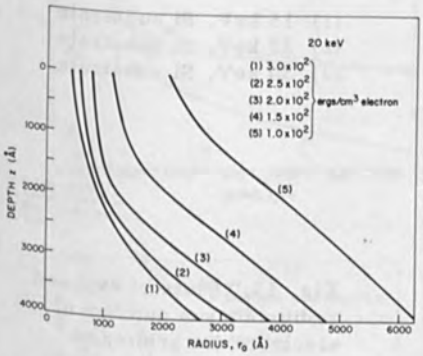

Fig. 9. Profiles of equal total energy dissipation ($\mathcal{E}(r_o, z)$) for a 20 keV electron beam incident on a 4000 Å thick PMMA film on a silicon substrate. Plots are normalized to one incident electron

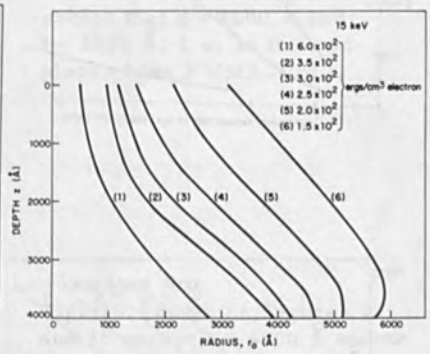

Fig. 10. Same as Figure 9 except the beam energy is 15 keV.

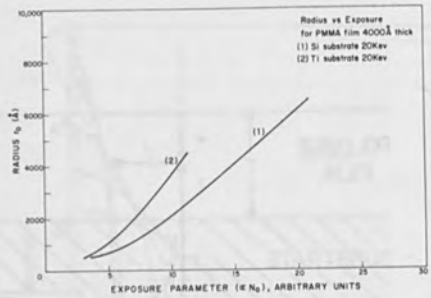

Fig. 11. Plots of exposed radius versus the total number of input electrons (arbitrary units) for a 4000 Å thick film of PMMA and:

(1) 20 keV, Si substrate
(2) 20 keV, Ti substrate

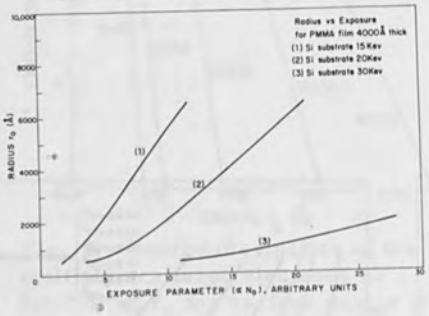

Fig. 12. Plots of exposed radius versus the total number of input electrons (arbitrary units) for a 4000 Å thick film of PMMA and:

(1) 15 keV, Si substrate
(2) 20 keV, Si substrate
(3) 30 keV, Si substrate

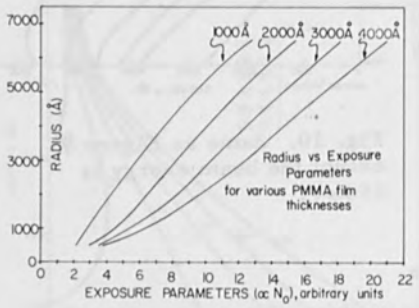

Fig. 13. Plots of exposed radius versus number of electrons (in arbitrary units) for several values of PMMA thickness. Silicon substrate, 20 keV beam.

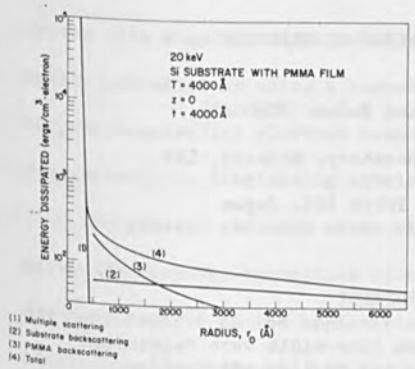

Fig. 14. Plot of $\mathcal{E}(r_o, z)$ vs r_o for a 20 keV electron beam incident on a 4000 Å thick PMMA film on a silicon substrate. The plot is normalized to one incident electron and is for z = 0, t = 4000 Å, i.e. at the top surface of the polymer. Also shown are the three contributions to $\mathcal{E}(r_o, z)$:

(1) energy dissipated by multiply scattered electrons,
(2) energy dissipated by electrons backscattered from the substrate,
(3) energy dissipated by electrons backscattered from the PMMA film.

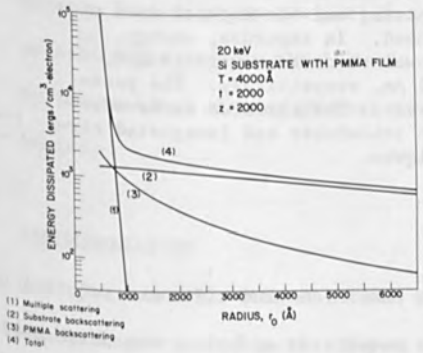

Fig. 15. Same as Figure 14 except that z = 2000 Å and t = 2000 Å, i.e. in the mid-plane of the PMMA film.

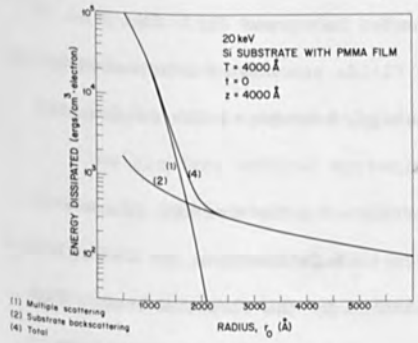

Fig. 16. Same as Figures 14 and 15 except z = 4000 Å and t = 0, i.e. at the substrate-PMMA interface.

SUBMICRON-MASK MAKING BY ELECTRON BEAM

Norio SAITOU and Saburo NONOGAKI

Central Research Laboratory, Hitachi, Ltd.,

Kokubunji, Tokyo 185, Japan

ABSTRACT

Chromium masks with submicron line-width were fabricated by chemical etching process, not by lift-off process, using a fine electron beam. The electron beam exposure was done in a computer-controlled scanning electron microscope (SEM). Polymethyl-methacrylate resist (PMMA) was coated on a chromium-clad glass plate by using spinning technique. After electron irradiation the samples were developed by suitable processing and the exposed area of chromium was chemically etched. In exposure, energy, current and diameter of the electron beam were 15 keV, 0.1 nA and smaller than 0.1 μm, respectively. The post-baking process was unnecessary. The chromium masks were obtained for a surface wave transducer and integrated circuits by using those techniques.

INTRODUCTION

Recently, fine patterns with submicron line-width are required in such various field as large scale integrated circuits, superhighspeed-integrated circuits, computer-generated holograms etc. The fine patterns which are required in the fields can not be fabricated by the conventional optical masking technology, because of the fundamental limitation arising from diffraction.

As the wave length of the electron of a few ten keV is much shorter than that of light, the effect of diffraction can be neglected in the fabrication of submicron patterns by the electron beam. The beam diameter can be made smaller than 0.1 μm. The electron beam

system with its deflection and blanking capabilities, moreover, can be easily automated by using a computer. According to Brewer[1], the computer-controlled electron beam exposure is one of the most promissing method for fabricating submicron patterns.

The present chromium masks with submicron line-width were made by using the computer-controlled electron beam apparatus. Though there are many reports on the application of a fine electron beam to microelectronics[1], there has not yet been reported on submicron mask-making. Hatzakis[2] has made IC masks by the similar technique of lift-off process using the positive type electron resist, where the minimum line-width in the pattern is, however, 1 μm or larger. The present paper reports the IC masks with submicron line-width fabricated by the chemical etching process using the positive type electron resist.

INSTRUMENTATION

The schematic diagram of the computer-controlled electron beam system is shown in Fig. 1. Figure 2 is the photograph of the system. It is composed of two parts: the electron optical column and the electron control system.

(a) Electron optical column

The electron optical system is originally a scanning electron microscope (SEM) developed at Hitachi Central Research Laboratory[3]. The column is constructed with the electron gun at the bottom and the specimen chamber at the top. The electron beam is produced by a conventional tri-electrode electron gun. Two electromagnetic lenses

focus the beam into a spot smaller than 0.1 μm over scanning area of 300 μm square. The electron beam whose energy is 15 keV is scanned by double deflection coils in synchronism with the cathode-ray tubes which serve as viewing monitors. The Wehnelt electrode is usually set at the beam cut-off voltage by using the fixed bias method. The electron beam is emitted from the gun when a 5 MHz pulse voltage is applied to the Wehnelt electrode[4]. In order to stabilize the emission current, it is necessary to keep the clearance between filament and Wehnelt constant[5]. For the purpose a quartz spacer is set[6] in the electron gun as shown in Fig. 3. The change of the emission current became smaller than $\pm$10 % for an hour using the structure[7]. Maximum specimen current is about 300 pA.

(b) Electron control system

The electron beam is deflected in two scanning mode. One is a raster mode as a scanning electron microscope and another is a random positioning mode as a pattern generator connected with a digital computer. The details of the control system have been described elsewhere[8]. The beam scanning speed is from 1 ms to 10 s/0.3 mm in case of a random positioning mode.

MASK FABRICATION

Preliminary experiment

Polymethyl-methacrylate (PMMA), obtained by polymerizing the monomer with potassium persulfate, was generally used as an electron resist. This resist, firstly developed at IBM Research[9], is a positive working resist. The sensitivity towards electron beam is

much lower than those of the commercially available photoresists. But, PMMA is suitable for high-resolution work as it gives sharp edges of resist patterns. Figure 4 shows the exposure characteristics for PMMA and an epoxide-containing polymer developed at Hitachi[10].

Figure 5 shows the mask fabrication processes where PMMA is used. In order to obtain submicron masks, it is important to establish the best condition in each process. In this work, the effect of the postbaking temperature was carefully evaluated[11]. It has been suggested that postbaking process before etching has a decisive effect upon etching width. Certainly, electron exposed KPR or KTFR are stripped in etching process without postbaking process. In the present study, samples were postbaked at temperatures varying from room temperature (no postbaking) to 170 °C for 20 min (The melting point of PMMA is about 120 °C).

Simple patterns such as crossing or parallel lines were fabricated by using the raster scanning mode. Samples to be exposed to the electron beam were prepared as follows: PMMA was coated on chromium-clad glass plate by using spinning technique. The layer thicknesses of the resist and chromium were about 0.2 μm and 0.1 μm, respectively. The plate was then baked at 170 °C for 30 min in the air. After electron beam irradiation (8×10^{-5} C/cm^2) the samples were developed in a 3 : 2 mixture of isopropyl alcohol and methyl isobutyl ketone for 2 min and sprayed for 30 sec with the same solution. After drying, the samples were postbaked at various temperatures. Subsequently those samples were etched in Kodak etch bath EB-5 ($NaOH : K_3Fe(CN)_6 : H_2O = 1 : 2 : 8$).

Etched patterns were observed in the same SEM. Figure 6 shows the etched chromium patterns for four postbaking temperatures. The dark parts in the pictures are electron beam exposed lines at which chromium is washed away by etching process. The pitch of the crossing lines is about 2.1 μm. Without postbaking process, the resist was not stripped and the line width which is 0.3 μm in Fig. 6(a) was the narrowest of all the samples. When the postbaking temperature is higher than 130 ^{o}C the flow of the resist line edge appears. In the case of postbaking at 170 ^{o}C, the pattern of crossing lines disappeared completely. At the postbaking temperature lower than 90 ^{o}C the line widths were the same as those at 110 ^{o}C. The cross sections of the lines were not observed.

Mask patterns

Many patterns of chromium masks were fabricated through proper processes as mentioned in previous section. The pattern signals were obtained from a digital computer. Figure 7 shows a chromium mask for a surface wave transducer. White parts in the picture correspond to the electron beam exposed lines, where chromium is etched away. The line-width is 0.4 μm. Figure 8 shows an example of serial set of IC chromium masks. Drafting times are shown in the parentheses. Side lengthes are about 270 μm. The minimum line-width is 1.2 μm.

The masks can be used as master masks for IC by using an electron beam projection system[12]. This method of mask fabrication can be also applied to high density recording or computer hologram recording[13-15].

CONCLUSION

A scanning electron microscope was connected with a digital computer. The chromium patterns with 0.3 μm has constantly been obtained not by lift-off process but by chemical etching process. The postbaking process of PMMA was found to be unnecessary for etching the chromium layer when the resist layer was about 0.2 μm. The chromium masks were obtained for a surface wave transducer and integrated circuits.

ACKNOWLEDGEMENTS

The authors wish to thank Drs. Y. Yamada, T. Tomura and A. Maekawa for encouragements and useful discussions throughout this study. They are also indebted to Messrs. H. Morishita, H. Itoh, Y. Miura and Y. Honda for their assistance in the experiment.

REFERENCES

1) G. R. Brewer: IEEE Spectrum 8 (1971) 23.

2) M. Hatzakis: J. Electrochem. Soc. 116 (1969) 1033.

3) T. Tomura et al.: Septieme Congress International de Microscopie Electronique, Grennoble (1970) 213.

4) H. Itoh: Japan. J. appl. Phys. 11 (1972) 412.

5) C. Munakata: Int. J. Electronics. 27 (1969) 221.

6) P. Holl: Optik. 28 (1968) 76.

7) C. Munakata: Int. J. Electronics: to be published.

8) A. Maekawa et al.: Proc. 4th Intern. Conf. Electron and Ion Beam Sci. and Technology (Bakish Materials Corp., Englewood 1970) p.503.

9) I. Haller et al.: IBM Journal of Research and Development 12 (1968) 251.

10) T. Hirai et al.: J. Electrochem. Soc. 118 (1971) 669.

11) N. Saitou et al.: Japan. J. appl. Phys. 10 (1971) 1486.

12) T. W. Okeeffe et al.: Solid-State Electronics 12 (1969) 841.

13) A. Maekawa et al.: Japan. J. appl. Phys. 10 (1971) 810.

14) S. Yonezawa et al.: ibid. 10 (1971) 1279.

15) A. Maekawa et al.: ibid. 10 (1971) 1658.

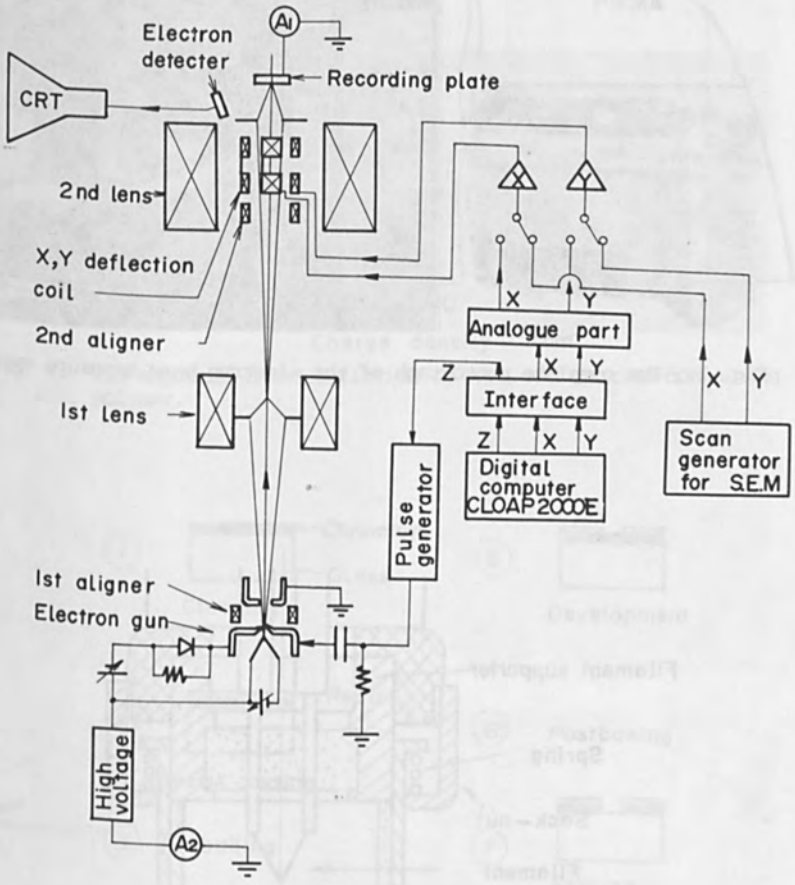

Fig. 1. The schematic diagram of the electron beam exposure system.

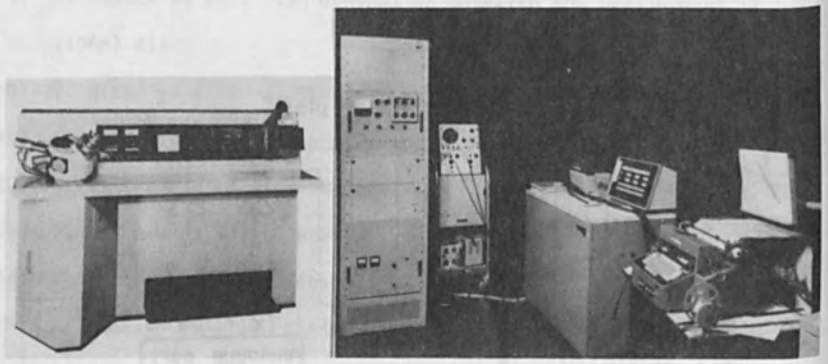

Fig. 2. The complete photograph of the electron beam exposure system.

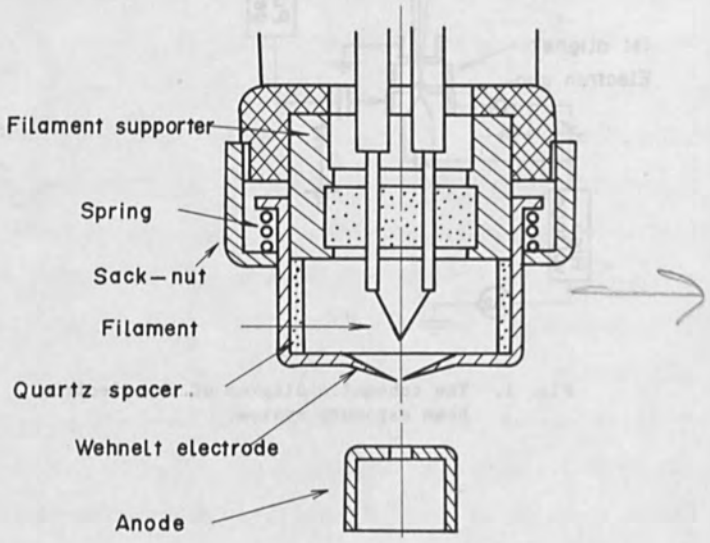

Fig. 3. The structure of the new type of electron gun. The emission current is stabilized.

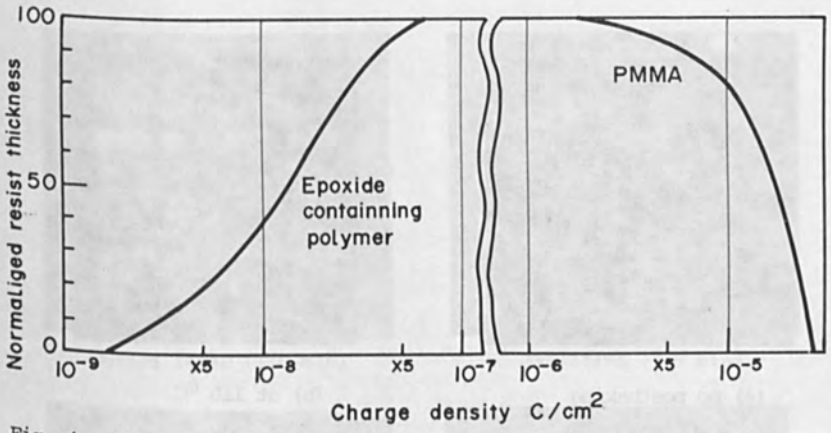

Fig. 4. The exposure characteristics of PMMA and epoxide-containing polymer.

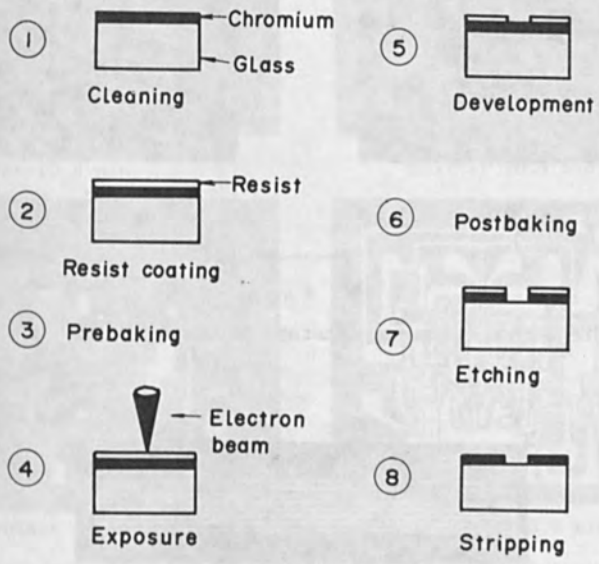

Fig. 5. The fabrication processes of chromium mask in case of using positive electron resist.

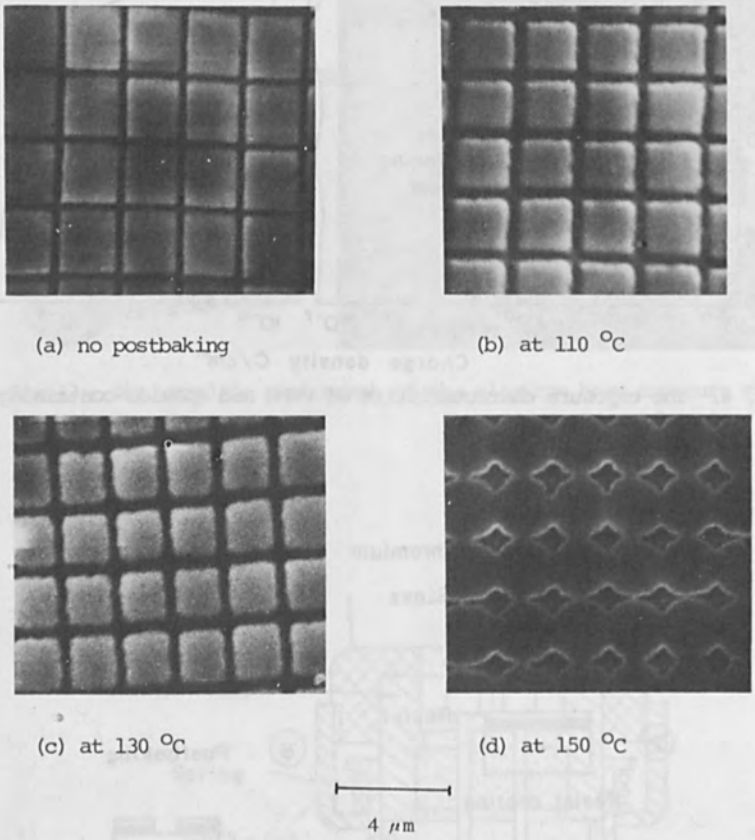

Fig. 6. The etched chromium patterns for four postbacking temperatures.

Fig. 7. A chromium mask for a surface wave transducer.

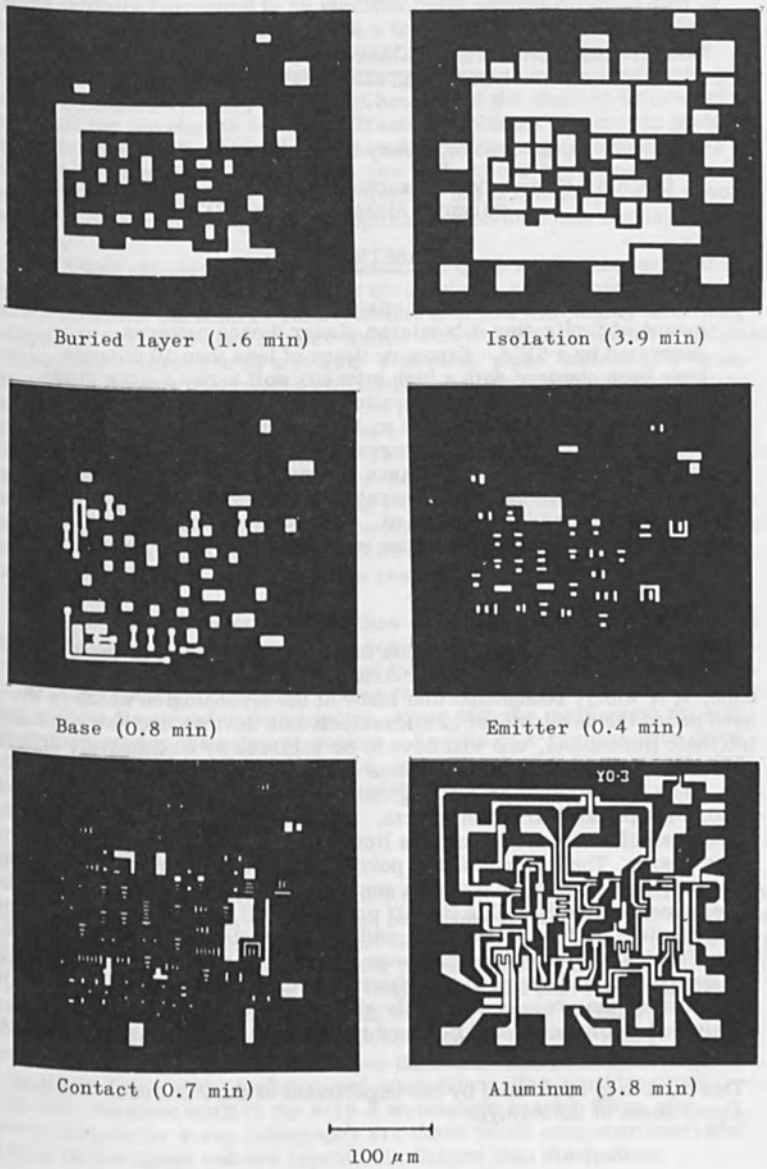

Fig. 8. A serial set of IC chromium mask.

X-RAY REPLICATION OF SCANNING ELECTRON MICROSCOPE GENERATED PATTERNS

D. L. Spears, Henry I. Smith and E. Stern

Lincoln Laboratory, Massachusetts Institute of Technology
Lexington, Massachusetts 02173

ABSTRACT

Soft x-ray shadow printing has been investigated as a means of replicating sub-micron planar device patterns generated by a SEM. Exposure times of less than 10 minutes have been obtained with a high intensity soft x-ray source made from an electron beam evaporation gun. Special exposure masks have been developed for the 4 to 14 Å wavelength region. Acoustic surface wave transducer patterns with 1.3 μm electrode spacings were fabricated onto such masks and successfully replicated. Imperfections in the SEM generated mask less than 0.2 μm in size were faithfully reproduced. Both positive and negative resists have shown sub-micron resolution with x-ray exposure.

INTRODUCTION

It is a widely held expectation in the microelectronics field that devices will evolve towards smaller geometries and higher frequencies. At the same time, it is widely recognized that many of the technologies which in the past have paced the development of microelectronic devices are now encountering intrinsic limitations, and will have to be replaced by qualitatively different ones. Photolithography is an obvious example, but certainly not the only one. The limitation of photolithography is its spatial resolution which is related to optical diffraction effects. Scanning electron beam lithography techniques offer a way around this limitation, as has been recognized for many years. The introduction of polymethyl methacrylate (PMMA) as an efficient, high resolution electron sensitive recording medium (1) and the development of the Hatzakis lift-off procedure (2) provided a practical means of fabricating devices. However, wide scale implementation of electron beam fabrication techniques has been hindered by the cost and complexity of the equipment, and the need to sequentially expose each part of a pattern, which makes the process inherently slow. These problems could be eliminated if a means could be found to precisely replicate patterns once

This work was sponsored by the Department of the Air Force and the Department of the Army.

they were initially fabricated in an electron beam system on some sort of mask. In this paper, we describe such a technique which is new and has already demonstrated the capability of replicating sub-micron resolution patterns (3). Soft x-rays are passed through the mask in a manner analogous to photolithographic contact printing but, because of the shorter wavelength (~ 10 Å), all the wavelength related diffraction problems inherent in photolithographic contact printing are eliminated and a finite gap between mask and sample is permitted. We call this new technique x-ray lithography. It bears the same relation to scanning electron beam lithography that photolithographic contact printing bears to optical projection mask making.

The x-ray exposure scheme is shown in Fig. 1 and is quite similar to contact microradiography (4). The mask consists of a semitransparent substrate on which the desired pattern exists in a thin film highly absorbing to x-rays. It is placed over a wafer coated with a radiation sensitive polymer film commonly referred to as a resist. A distant "point" source of x-rays, produced by a focused electron beam, illuminates the mask, thus projecting the shadow of the x-ray absorber onto the polymer film. This is the only feasible exposure scheme since efficient x-ray lenses and mirrors for collimation purposes cannot be made. The finite size of any real x-ray source leads to some blurring of the image, as illustrated by the inset in Fig. 1. However, the mask-to-wafer spacing s, the source diameter d, and distance D can always be chosen so that the penumbral width δ is small compared to the minimum linewidth to be replicated. Diffraction can generally be neglected since for $\lambda = 10$ Å, 1/4 μm lines can be resolved for s as large as 60 μm.

X-rays with wavelengths longer than 4 Å must be used to achieve submicron resolution, which places some constraints on the construction of the x-ray source (5). The fabrication of the special soft x-ray mask also involves some unusual problems. These two key elements of x-ray lithography will be discussed in detail below, along with the mechanism through which x-rays expose the polymer resists. Results of x-ray exposure tests are presented and discussed. A simple, precision registration scheme for multiple maskings will be discussed elsewhere (6).

SOFT X-RAY SOURCE

If reasonable exposure times (a few minutes) are to be obtained with an x-ray source small enough to allow high resolution replication, the source must have the maximum possible brightness. Generally, if the energy of electrons striking a target exceeds the threshold for production of characteristic K or L radiation by a factor of about two, the intensity of this characteristic line radiation is greater than that of the total bremsstrahlung spectrum. Thus, although a monochromatic source is not necessary for x-ray lithography, it provides the highest intensity, and hence the shortest exposure times. It will be shown below that resolution and mask fabrication considerations dictate that one must work in the 4-14 Å wavelength range. Thus, the optimum targets for x-ray lithography are those which emit characteristic radiation in this range and are capable of efficient heat dissipation.

Molybdenum, aluminum and copper with characteristic x-rays of 5.4, 8.3, and 13.3 Å respectively are the most promising materials.

The x-ray power flux a distance D from a target small compared to D is given by

$$\Phi = \frac{I\epsilon}{D^2} \quad \frac{h\nu}{q} \qquad (1)$$

where I is the electron beam current, ϵ is the fluorescence efficiency/steradian of the target, $h\nu$ is the photon energy and q is the electron charge. The fluorescence efficiency in the 4 to 14 Å wavelength region is typically 10^{-4} photons/electron/steradian at 7 kV (7). This efficiency increases rapidly with voltage, but so also does the bremsstrahlung background. Also, the deeper penetration of the electrons into the target leads to strong target reabsorption of the soft x-rays. In the case of copper and molybdenum targets the operating voltage must be below the threshold for the excitation of K radiation.

Because of target reabsorption, the soft x-ray flux is most intense normal to the target surface, so that image foreshortening cannot be used to increase the effective intensity, as is done in hard x-ray tubes. In a soft x-ray tube, the filament must be shielded from the target to prevent the deposition of a tungsten layer, which would strongly reduce the output flux.

The above requirements on the x-ray lithography source cannot be met by any commercial x-ray tubes. However, we found a commercial electron beam evaporation gun (8) which did meet all of the critical requirements. The unit has a circular filament about 2 cm in diameter, which is shielded from a stationary water-cooled target. The electrons are electrostatically deflected through a trajectory of about 180° inward and converge to a 1 mm diameter focal spot. A target current density in excess of 20 A/cm^2 is possible. We generally operate the unit at voltages between 5 and 10 kV and currents between 50 and 100 mA. Exposure times less than 10 min. can be obtained at a distance of 1 inch from the target. A factor of 20 further decrease in exposure time could be achieved by using a water-cooled rotating anode, as is available in a number of commercial hard x-ray units.

X-RAY RESIST

When an x-ray is absorbed by an atom in a polymer resist, photoelectrons and Auger electrons are ejected. These randomly directed electrons interact further with the polymer and play the dominant role in altering its chemistry. In negative type resists the dominant reaction is cross-linking and in positive type resists it is chain scission (1). The range of these electrons obviously influences pattern resolution. In Fig. 2, the calculated electron range is shown for electron energies from 0 to 4 keV in a medium with a density of 1 gm/cm^3, a typical value for polymers. In this region the range varies as the 5/3 power of the electron energy and inversely

with the density of the medium (9). The energies of the characteristic copper, aluminum and molybdenum x-rays are indicated for comparison. The corresponding energies of the ejected electrons are, of course, less than these values. Clearly, resolutions better than about 0.2 μm are obtainable with all three sources. With the copper source a resolution of 500 Å is possible (10).

Only about 5% of an incident flux of 8.3 Å x-rays are absorbed in a 5000 Å film, so the exposure is essentially uniform throughout the film thickness. Except for the small fraction absorbed, the soft x-rays pass through the film without deviation. The absorbed x-ray transfers its energy to electrons with very short ranges. This leads to an exposure profile with no variation along the line of incidence, for both positive and negative type resists. In scanning electron beam lithography, on the other hand, high energy electrons are used (5-20 keV). A large percentage of these pass through the polymer film, enter the substrate, and then scatter back through the film. This leads to an undercut profile in the case of positive resists and a long sloping tail in the case of negative resists (2, 11).

Most of our work with positive resists has been confined to polymethyl methacrylate (PMMA) because of its availability and insensitivity to light. Our material was obtained commercially (12), dissolved in methyl ethyl ketone, and spun onto samples in film thicknesses ranging from 1000 Å to 15,000 Å. After irradiation, the exposed PMMA was removed with a mixture of 40% methyl isobutyl ketone and 60% isopropyl alcohol. The utility of a resist/developer system depends not only upon the effect the radiation has on the polymer, but also on the ability of the developer to distinguish between the exposed and unexposed areas. Results of x-ray exposure tests on PMMA show that the dissolution rate in the 40/60 developer varies as the 3rd power of the radiation dose. Because of this images can be produced with exposure masks having relatively low contrast, and the effect of penumbral blurring is considerably reduced. For example, a mask contrast ratio of only 3:1 (i.e. a 5 dB absorber layer) gives a 27:1 differential dissolution rate between the "exposed" and "unexposed" portions of a PMMA film.

The exposure time needed in x-ray lithography is given by

$$T = \frac{R^*}{\Phi' \mu} \quad , \tag{2}$$

where R^* is the required radiation dose, Φ' is the incident x-ray flux corrected for the transmission factor of the mask, and μ is the x-ray absorption coefficient of the polymer film. ($\mu \sim 1000$ cm^{-1} at 8.3 Å for PMMA.) PMMA requires about 500 J/cm^3 for adequate exposure, whereas Kodak Micro-Negative resist (KMNR) (13) is about five times more sensitive.

MASK FABRICATION

The construction of the soft x-ray mask is the key to x-ray lithography. The exposure contrast of an x-ray mask is given by the attenuation in the absorber film which should be greater than about 5 dB. At sub-micron resolutions it appears that this absorber can be no thicker than about the minimum pattern linewidth. As a result, only the most highly absorbing

materials are useful, and the x-ray wavelength must be greater than about 4 Å in order to obtain about 20 dB/μm attenuation. The attenuation coefficients of gold, silicon and beryllium in the 1 to 20 Å region are shown in Fig. 3 (Ref. 14). Note that the attenuation of gold rather conveniently peaks at ~ 5.6 Å to match nicely with the molybdenum L line. Gold is exceeded in absorption coefficient only by uranium, and has the advantage that a well developed technology exists for fabricating thin film patterns with it.

In the wavelength region near 10 Å the absorption coefficients of materials do not exhibit as wide a variation as they do in the more familiar hard x-ray region near 1 Å. This is because the K, L and M absorption edges of the high Z elements occur for $\lambda <$ 10 Å. Near 10 Å the absorption coefficients of beryllium and uranium, for example, differ by only a factor of 100. As a result, the substrate of a soft x-ray mask must be quite thin, on the order of microns; otherwise exposure times become prohibitive. The preparation of this mask membrane is a major challenge since it must be flat and self-supporting over the pattern area. We assume that this membrane should absorb no more than about 3 to 5 dB, and thus even beryllium would have to be less than about 30 μm thick. Silicon is more absorbing than Be, but has a much more highly developed technology. High quality silicon is readily available as well as techniques to selectively etch the material. Silicon's large K absorption edge at 6.8 Å just below the K_α line of aluminum makes it an excellent mask in combination with an aluminum source. The membrane thickness should not exceed 3 μm to 5 μm.

The mask substrate needs to be thin only in the areas of the pattern, leaving the remaining areas to serve as structural support. In the original x-ray masks (3) an electrochemical method was used to etch away an n^+ silicon substrate from beneath an n-type epitaxial surface layer. More recently, we have preferred the chemical etch ethylene diamine, pyrocatechol and water at 115°C (Ref. 15). This solution etches all types of silicon except that very heavily doped with boron. In addition, it does not attack chromium, gold or SiO_2, so that the latter can be used as the mask for etching. Figure 4 is a transmission photograph of a 7 x 7 array of 5 μm thick, boron diffused silicon membranes, 60 mil square, supported by a lattice of 200 μm thick n-type silicon. This was made from a < 100 > boron diffused silicon wafer simply by etching from the back surface through windows in an SiO_2 layer. The above etch has a strong dependence on crystallographic orientation, etching 16 times faster into the < 100 > plane than the < 111 > plane. Thus, in etching the < 100 > silicon through a square opening in a back surface SiO_2 layer, the hole obtained has the shape of a near perfect truncated pyramid with sides of <111> planes, thereby providing good structural support and allowing full use of the membrane area.

The 5 μm thick silicon is optically transparent, showing a red-orange color in transmission with a fluorescent lamp. Silicon 2-1/2 μm thick shows a yellow-green color. Thus, the uniformity and thickness of the membrane can be visually determined. The membranes are generally uniform to better than 0.1 μm, and quite flat due to the fact that boron diffused silicon has a slightly smaller lattice constant than undoped silicon, so that a membrane

is actually under tension. The membranes are surprisingly rugged, and can be handled and cleaned with only minimal precautions to avoid applying too large a force normal to the membranes. Residual liquid films can be blown off the surface with an air brush without damage if done at a glancing angle.

It should be mentioned in passing that the radiation pattern transmitted by an x-ray mask is essentially unaffected by dust and other contamination. This is because such contamination has negligible attenuation relative to the gold absorber pattern. In practice, this could be quite significant and also implies that the x-ray masks, once made, need not be processed or cleaned extensively.

Because they are flat, the silicon membrane masks can be used with a small but finite mask-sample gap or, if intimate contact is desirable the membrane can readily be made to conform to a sample surface by applying a very small pressure differential. Less than 1/10 atmosphere pressure can displace a 60 mil square membrane a few microns. The many attractive features of this boron diffused silicon mask structure and the ease and control with which the etching is done make large area x-ray masks a reality.

In making an x-ray mask, any photolithographic or electron beam technique which produces the desired absorber pattern is acceptable. The etching of the windows is always done after the absorber pattern is defined. For sub-micron resolution patterns, we are forced to use electron beam lithography and PMMA resist films, and have used different procedures depending on whether a "positive" or "negative" pattern is desired. This is because the electron beam cannot with equal ease make patterns of either polarity.

In fabricating a "negative" x-ray masks, the Hatzakis lift-off technique (2) is used. We begin with a < 100 > silicon wafer diffused with boron such that the critical concentration exists at a depth of 5 μm. An oxide layer is put on the back side. The wafer is coated with PMMA, and the desired pattern written with the electron beam. The image is developed and chromium and gold evaporated over the surface. Rinsing with trichloroethylene dissolves the residual PMMA and carries away the metal evaporated onto it, leaving behind a gold pattern corresponding to the areas exposed by the beam. The final step is the chemical etching of the bulk of the silicon beneath the gold pattern, leaving it supported by the thin membrane of boron doped silicon.

Our procedure for making a high resolution positive x-ray mask is outlined in Fig. 5. The same silicon is used but now with a 300 Å layer of chromium for adhesion (not shown) and a 0.4 μm thick layer of gold r.f. sputtered over it. PMMA about 0.3 μm thick is spun over the gold. The desired pattern is then exposed in the electron beam apparatus, after which development yields the type of profile shown in Fig. 5b. The wafer is next placed in a neutralized ion beam sputter etching unit (16) and sputter etched until a relief pattern as shown in Fig. 5c is obtained. We found that gold is sputtered at about six times the rate of PMMA. After removing any residual

PMMA, windows are chemically etched in the silicon behind the pattern areas.

EXPOSURE RESULTS

High frequency interdigital electrode surface acoustic wave transducer patterns (17) have provided an excellent test of the resolution capabilities of x-ray lithography. Figure 6a is a photomicrograph of a portion of an x-ray mask with 0.6 μm wide gold electrodes on 1.3 μm centers. The gold is 0.3 μm thick, and was fabricated by the lift-off technique. The dark spots in the background are due to imperfections in a 2000 Å Al_2O_3 film covering the silicon. Figure 6b shows the relief pattern of PMMA obtained after x-ray exposure and developing. This photomicrograph reveals an edge definition better than 0.2 μm, the limit of detection of the optical microscope. Note the ripple along the edges of the PMMA fingers. This was also present in the x-ray mask, being generated by a small 60 cycle component on the vertical deflection coils of our scanning electron beam apparatus.

Figure 7 is an electron micrograph showing the edge profile of a relief pattern in PMMA produced by x-ray lithography. The pattern was produced in a 1.1 μm thick layer of PMMA and has a 2.5 μm center to center spacing. Note the very steep edges of the resist, at least 85° with respect to the wafer surface. This demonstrates at once the uniformity of exposure with depth. Clearly, penumbral blurring of the x-ray image and the range of the electrons do not present a problem here.

Some exposure tests have been carried out with KMNR. Figure 8 is a photomicrograph of a fully developed 1-1/4 μm line pattern in a 2000 Å KMNR film produced by an 8 minute x-ray exposure. This exposure time is about 1/5 that required for PMMA. We have yet to fully evaluate the capabilities of this resist in conjunction with x-ray lithography, but clearly 0.3 μm resolution is possible with this particular negative resist.

We have used the metal lift-off technique to produce metal structure from the x-ray exposed PMMA patterns. The 0.6 μm line pattern of Fig. 6 has been produced in a 0.1 μm thick layer of chromium and gold, without difficulty. In order for this film lift-off technique to work, the vertical edge of the resist profile must be very steep (18). An operational 690 MHz surface wave transducer fabricated on $LiNbO_3$ using an x-ray mask which was produced by photolithographic means (18) is shown in Fig. 9. The interdigital electrodes consist of 300 Å of chromium and 500 Å of gold and were produced by the lift-off technique. In addition to film lift-off, the x-ray resist patterns could also be used as masks for sputter etching, ion implantation or even chemical etching.

SUMMARY

X-ray lithography is a new technique. The results we have obtained after working on it for only 1-1/2 man years have been extremely promising. X-rays in the 4-14 Å wavelength region must be used to achieve sub-micron resolution

replication. Reasonably short exposure times have been obtained using an inexpensive, modified electron beam evaporation system as the soft x-ray source. The problems involved in the construction of soft x-ray masks have been discussed. A gold absorber layer on silicon appears to be the best choice, as the required thin membranes of silicon are easily fabricated in a rugged, supported structure. Functional x-ray masks with sub-micron linewidth patterns have been fabricated using electron beam lithography. Acoustic surface wave transducer patterns with 1.3 μm electrode spacings have been replicated with soft x-rays, faithfully reproducing imperfections in the SEM generated mask less than 0.2 μm in size. The developed relief structures in polymethyl methacrylate resist show very nearly rectangular cross sections, allowing us to fabricate devices or mask reversals using the film lift-off technique. We have also found negative type resists to be very useful in x-ray lithography, and they appear to be much more sensitive than PMMA. The simplicity of x-ray lithography and its relatively low cost lead us to expect it will give rise to a far wider utilization of the ultra-high resolution fabrication capabilities of scanning electron beam lithography.

References

1. I. Haller, M. Hatzakis and R. Srinivasan, IBM J. Res. Develop. 12, 251 (1968).

2. M. Hatzakis, J. Electrochem. Soc. 116, 1033 (1969).

3. D. L. Spears and Henry I. Smith, Electronics Letters 8, 102 (1972).

4. V. E. Cosslett and W. C. Nixon, X-ray Microscopy (University Press, Cambridge, 1960).

5. B. L. Henke in Advances in X-Ray Analysis, Vol. 5, W. M. Mueller, Ed. (Plenum, New York, 1962), p. 285.

6. D. L. Spears and Henry I. Smith, Solid State Technology (to be published July, 1972).

7. M. Green, X-ray Optics and X-ray Microanalysis, H. H. Pattee, V. E. Cosslett and A. Engstrom, Eds. (Academic Press, New York, 1963), p. 185.

8. Veeco Instruments Inc., Vacuum Generators Limited Model EG-1.

9. C. A. Andersen, in The Electron Microprobe, T. P. McKinley, K. F. J. Heinrich and D. B. Wittry, Eds. (Wiley, New York, 1966), p. 58.

10. S. K. Assunma, Nature 186, 1036 (1960).

11. R. J. Hawryluk and Henry I. Smith, these proceedings.

12. Esschem Corp., Essington, Pa. mol. wt. 950,000.

13. Eastman Kodak Company.

14. K. F. J. Heinrich, in The Electron Microprobe, T. P. McKinley, K. F. J. Heinrich and D. B. Wittry, Eds. (Wiley, New York, 1966), p. 296; B. L. Henke, R. White and B. Lundberg, J. Appl. Phys. 28, 98 (1957).

15. R. M. Finne and D. L. Klein, J. Electrochem. Soc. 114, 965 (1967); J. C. Greenwood, ibid, 116, 1325 (1969); A. Bohg, ibid, 118, 401 (1971).

16. Veeco Instruments Inc. Microetch System.

17. A. N. Broers, E. G. Lean, and M. Hatzakis, Appl. Phys. Letters 15, 98 (1969).

18. Henry I. Smith, Frank J. Bachner, and N. Efremow, J. Electrochem. Soc. 118, 821 (1971).

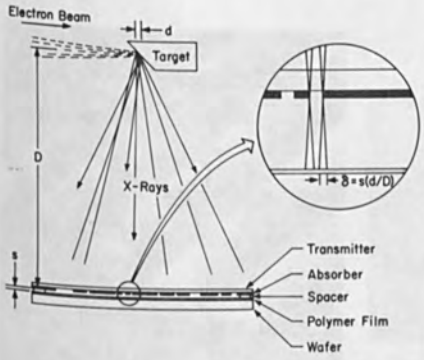

Fig. 1. Schematic diagram of the soft x-ray lithographic system. The inset illustrates the image blurring caused by the finite size of the x-ray source.

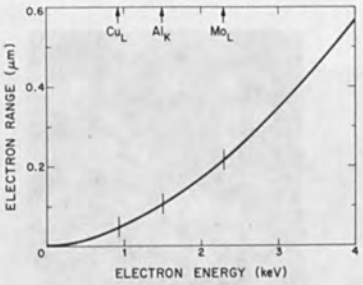

Fig. 2. Characteristic electron range as a function of electron energy for a typical polymer film (ρ = 1 gm/cm^3). The energy of three useful x-rays (Cu_L, Al_K, Mo_L) are indicated.

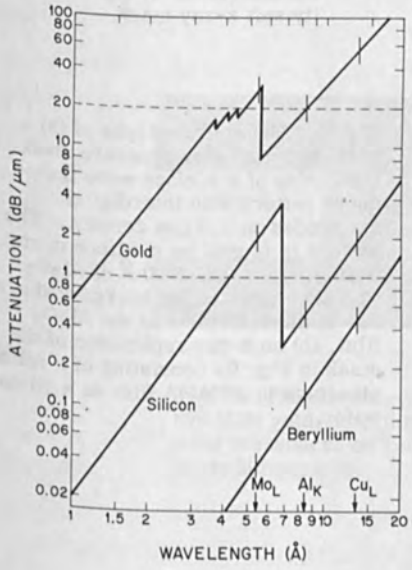

Fig. 3. Attenuation coefficient as a function of x-ray wavelength for gold, silicon and beryllium. The two dashed lines indicate roughly the minimum attenuation coefficient necessary for the absorber film and the maximum attenuation coefficient allowed for the substrate of an x-ray mask. The Mo_L, Al_K and Cu_L wavelengths are also indicated for comparison.

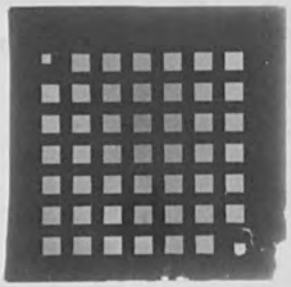

Fig. 4. Photograph of a silicon/silicon x-ray mask substrate with an array of transparent silicon windows, 60 mils square and 5 μm thick.

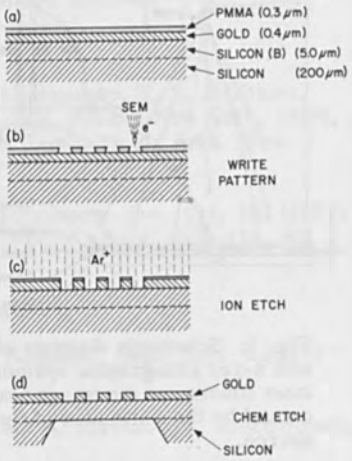

Fig. 5. Schematic representation of the steps involved in the fabrication of a positive polarity soft x-ray mask.

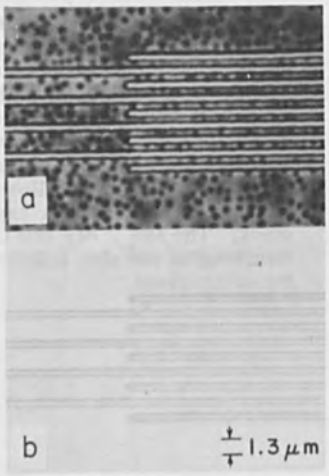

Fig. 6. Photomicrographs of (a) a portion of an x-ray exposure mask consisting of a surface wave transducer pattern with interdigital electrodes on 1.3 μm centers. The pattern is in gold on a silicon membrane coated with 2000 Å of Al_2O_3. The dark spots in the background are due to imperfections in the Al_2O_3 film, (b) an x-ray replication of the mask in Fig. 6a consisting of a relief structure in a PMMA film on a silicon wafer.

Fig. 7. Electronmicrograph showing the end profile of relief pattern in 1.1 μm of PMMA produced by x-ray lithography. The pattern has a 2.5 μm periodicity.

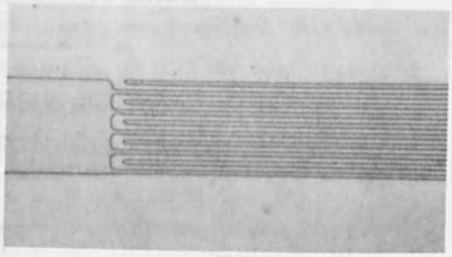

Fig. 8. Photomicrograph of one end of a fully developed interdigital surface acoustic wave transducer pattern in 2000 Å of KMNR produced by x-ray lithography. The center-to-center line spacing is 2.5 μm.

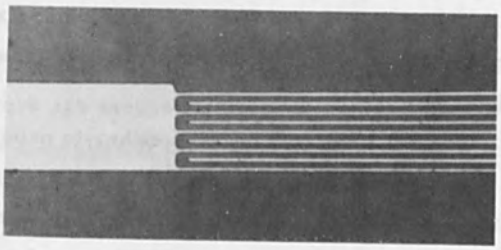

Fig. 9. Photomicrograph of one end of a 690 MHz gold, interdigital surface acoustic wave transducer on $LiNbO_3$ fabricated using x-ray lithography.

AUTOMATIC CONTROL OF AN ELECTRON BEAM PATTERN GENERATOR

O. CAHEN, R. SIGELLE, J. TROTEL
THOMSON-C.S.F., Corbeville, 91 - ORSAY (France)

INTRODUCTION.

It is now well known that the electron beam masking technique can give an order of magnitude improvement over conventional photomasking in the resolution of masks.

Our goal was to keep this accuracy on an industrial machine ; the electron masking machine was designed to produce 2 inch masks with .1 micron accuracy, consistent with the requirements for reliability and cost.

Execution time and human handling are reduced in the fully automatic machine with direct data access from a computer aided design system.

The machine may be used either to produce master masks on photographic or resist-coated chromium plates, or to expose patterns directly on silicon wafers ; the latter process requires a means of superposing successive masks on the same wafer with .1 micron accuracy.

LARGE-AREA MASKING OPERATION.

The electron beam cannot scan a large area with .1

micron resolution, because a large area deflection system is very sensitive to spurious magnetic field variations.

As two or three inch-masks are required, this area must be covered by moving the sample, so that the beam scanning amplitude can be as small as necessary for the required pattern accuracy, for instance half a millimeter. The principle of operation is shown in figure 1.

The table motion is governed by the automatic positioning control according to the movement program specified by the computer.

The table position is measured with a precision of 400 Å by two laser interferometers ; the table is moved by two stepping motors until the difference between the measured position and the position specified by the computer is less than five microns. No attempt is made by mechanical means to further reduce this 5 micron uncertainty ; once the motors are stopped, the beam is tilted by the position correction coils by a quantity equal to the remaining error.

This correction on the beam is maintened during periods when the motors are stopped ; the effects of mechanical vibrations or shocks are cancelled if they do not exceed a few microns in amplitude.

GENERATION OF THE ELEMENTARY SHAPES OF A MOTIF.

When the desired position is obtained, the automatic positioning control gives an order to the scanning generator (S. G.) to scan the beam over a motif specified by the computer.

The motif has been previously decomposed into ele-

mentary shapes : rectangles, parallelograms and triangles. Each shape is characterized by five parameters : local X and Y coordinates (lower left corner), width and height (l and h) of the shape, and a code indicating its nature.

The data is entered into the system by paper or magnetic tape. Tapes are either produced manually for simple motifs or by a C. A. D. system.

The data is stored in the computer memory and is supplied shape by shape to the S. G. on request of the latter.

During the drawing sequence of a motif, the computer transmits to the scanning generator the five parameters of each elementary shape of the motif which are read from the memory. For each shape, the scanning generator supplies convenient Vx and Vy deflection voltages. These voltages drive the deflection amplifiers of the drawing coils. The scanning generator also supplies a beam blanking signal and a "S. G. busy" signal during the scanning of the shape. The end of the "S. G. busy" signal calls for the transmission of the data of the next shape. Vx and Vy are initially set to the coordinate values x and y of the left lower corner. After the arrival of the start signal, the Vx voltage increases from x to (x + 1). Then Vy is increased by one step, and Vx decreases again to its minimum value and Vy is increased again. This process continues until h steps of Vy have been counted. The rectangle drawing is then complete. The beam blanking signal is set back at this time.

Although the drawing of a rectangle is executed by a stepping process, the surface of the shape is quite homogeneously exposed, since the diameter of irradiated resist is larger than the step.

The scanning generator provides also the means to scan 45° parallelograms and triangles. The code is 0 for rectangles, 1 and 2 for left and right for parallelograms, 4 to 7 for the four types of triangles.

When a shape has been scanned, the S. G. asks the computer for new shape data until the motif generation is complete ; the computer then asks the automatic positioning system for a new position.

ALIGNMENT SYSTEM.

In the case of direct masking on a silicon wafer, successive masks need to be aligned : alignment means are provided first to look at two alignment marks made during the previous masking so as to determine the real position of the wafer on the sample holder and second to take into account the variations of this position from one mask to another.

The observation of the marks is made by using the system as a conventional scanning electron microscope. An operator only needs to determine the coordinates of the alignment marks and enter this data into the computer. Recall that this operation is to be done for only two marks to align the entire wafer.

The angular misalignment of the wafer on the sample holder is not corrected mechanically : the computer generates a new set of coordinates for the position control of each mask.

ELECTRON OPTICS.

Electron optics are derived from a commercial CAMECA scanning electron microscope with some improvements in the stability of the magnification electronics and increased shielding against spurious magnetic fields.

The electron source is a tungsten hairpin filament ; three lenses give an ultimate resolution of 100 Å for the microscope, but we use the column with 1 nA of beam current at 20 kV which leads to a 1000 Å diameter spot.

INTERFEROMETRY.

A helium neon laser feeds two Michelson interferometers, in X and Y. One of these interferometers is shown in figure 2.

A $\lambda/8$ birefringent plate makes a $\lambda/4$ optical length difference between two crossed polarization directions in one arm of the interferometer. Hence, two optical detectors, sensitive to these polarization directions, give two interference fringe systems, phase shifted by $\pi/4$, the phase shift sign giving the direction of the motion.

These electrical signals are processed so as to give one pulse for each $\lambda/16$ displacement, i.e. about 400 Å.

PROCESS OPERATING SYSTEM.

The machine is operated with a Varian 620 i (or 620 1) computer with 8 K 16 bit words core memory and a magnetic tape memory.

The mask description comprises the motifs array features, in term of rows and columns, and the elementary shapes data of each motif.

In very large scale integrated circuits, the motifs can be different from one another and the data of all of them can be stored in the magnetic tape memory.

The program described below is simpler. It is now commonly used if the pattern to be drawn contains a regular array of identical motifs and two marks for the alignment.

Figure 3 shows the structure of the operating program.

This program starts after the resist-coated chromium mask or silicon wafer is introduced and locked on the moving table.

The data of the motif are fed in the computer by a punched paper tape.

The operator is asked on the teletype :

- the ordinal number N of the masking operation on the same wafer (if it is a master mask on a chromium plate, he answers 1)

- the number of rows and columns

- the X and Y steps in mils or microns

The table is then moved to the first mark left by the (N-1) th masking operation on the wafer. An area matched to the shape of this mark is then scanned with a fast repetition. The mark is displayed on the control oscilloscope of the machine with a very large magnification. The operator is required to center the mark in the scanned area by means of the X and Y fine beam deflection potentiometers, and to copy the dial numbers on the teletype.

The same operation is repeated on the second mark,

at the other end of the wafer.

The exact position of the wafer is then known, so that the computer can control the complete process without anymore help from the operator.

The new marks are then drawn, so that they will be ready for use at the (N + 1) th masking operation, and the complete array is also drawn. The table is turned back to the starting position, and the wafer can be unlocked and taken away.

The operation of the electron beam pattern generator is very fast : for instance, an array of 100 motifs of a circuit with ten logic gates could be generated in less than one hour. The same time will be required for a standard two inches integrated circuit mask with a line definition of .25 micron and a step accuracy of .1 micron.

CONCLUSION.

The electron beam machine described in this paper has all the features of a complete system for fast production of very accurate patterns over a large area. These patterns can be made on master masks and then reproduced by an electron image projection system. The patterns can also be made directly on silicon wafers, with a production rate suitable for new circuit development or for the fabrication of special high performance circuits, like microwave transistors or monolithic wideband amplifiers.

A computer aided design system can be directly coupled to this electron beam machine, so that the data transfer errors

should be eliminated. With this computer aided design system, the machine is also suitable for programmed interconnection.

This machine will be a new step forward for the new generation of very large scale integrated circuits.

ACKNOWLEDGMENTS.

The work was sponsored by the French Government (D. G. R. S. T.).

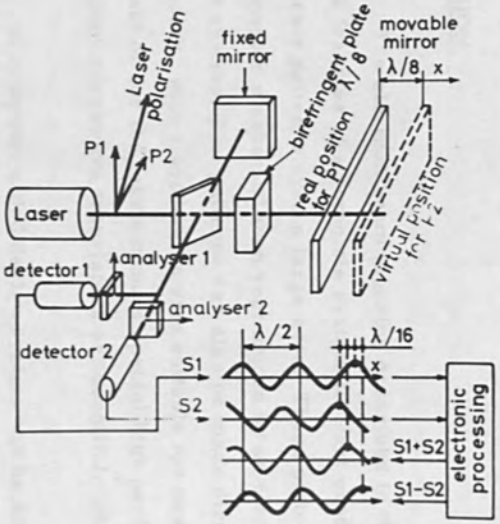

FIGURE: 2 1/16 TH WAVELENGTH INTERFEROMETER

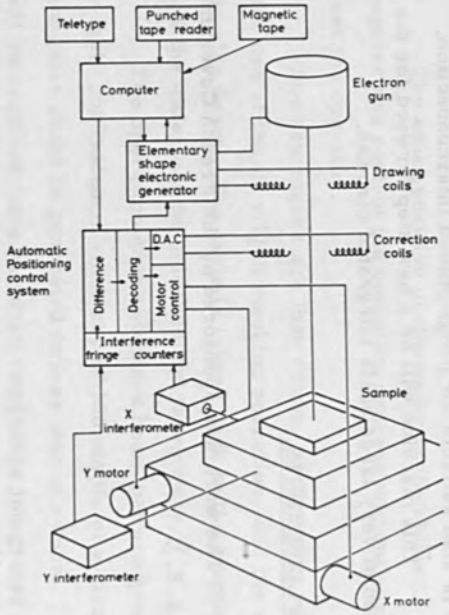

FIGURE: 1 BLOCK DIAGRAM OF THE SYSTEM

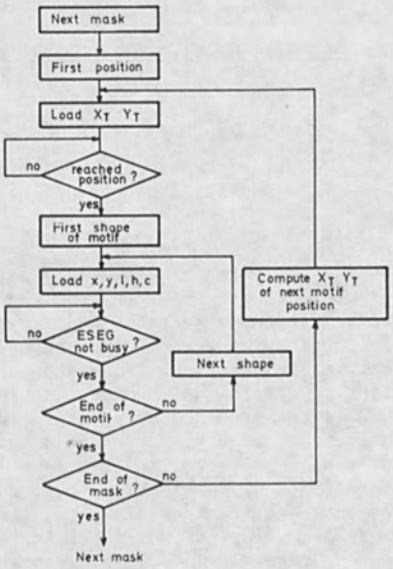

FIGURE: 3 MASKING SEQUENCE PROGRAM

DIRECT FORMATION BY ELECTRON BEAM OF PASSIVATING AND PHOSPHOSILICATE GLASS FILM PATTERNS

E.D. Roberts

Mullard Research Laboratories
Redhill Surrey England

Siliceous film patterns are formed by exposure of a cyclic siloxane polymer to an electron beam and they may be converted to silica by suitable heat treatment. Tests on MOS capacitors having the electron beam defined silica films as dielectric show that the films should serve as satisfactory passivating layers in semiconductor devices. Instability, attributed to the presence of positive ions within the layer, has been overcome by application of a thin layer of a mixture of cyclosiloxane polymer with an organosilylene phosphate in a pattern defined by an electron beam, which may be converted by subsequent heat treatment to phosphosilicate glass. Two systems for producing the phosphosilicate glass are described, requiring exposures of 1000 $\mu C/cm^2$ and 2 - 10 $\mu C/cm^2$, respectively. Capacitance-voltage characteristics of MOS capacitors demonstrate the stabilising effect achieved. Patterns having very fine geometry may be prepared using either of the phosphosilicate glass systems.

INTRODUCTION

In many semiconductor devices, particularly those made on silicon substrates, silicon dioxide (silica) films are used as diffusion barriers and as passivating layers. In conventional processing of silicon substrates, the silica film is commonly formed by heating the substrate in an oxidising atmosphere such as oxygen containing water vapour. Windows for the diffusion of impurities into the substrate to form base and emitter regions, for example, or to allow metal electrical contacts to be made to these regions, are opened at the desired sites by producing the appropriate pattern of apertures in a film of photoresist followed by etching of the exposed silica by hydrofluoric acid and removal of the photoresist.

It is now well-known that if silica film patterns produced in this way are used as passivating layers, the devices formed exhibit instability exemplified by changes in threshold voltage of MOS devices, and reduction of gain and increased leakage currents in bipolar devices.

The instability has been attributed to the presence within the passivating layer of positive charges, possibly sodium ions, which can move under the influence of temperature and an applied electric field, inducing an accumulation or depletion of electrons near the surface of the silicon according to the position of the positive ions. These changes in concentration of electrons near the surface of the silicon result in changes in the characteristics of the device.

Although great care may be taken during fabrication, it is almost impossible to eliminate completely contamination by traces of impurities such as sodium, but methods of reducing their undesirable effects have been devised. One such method is based upon the observation (Ref. 1). that if the silica passivating layer bears an appropriately chosen surface layer of phosphosilicate glass the devices remain relatively stable. In making n-p-n devices the final (emitter) diffusion process is usually a phosphorus diffusion and the phosphosilicate glass is formed incidentally, but in the case of p-n-p devices, it is necessary to perform a special operation to produce the phosphosilicate glass layer. In both cases, care must be taken not to remove the phosphosilicate glass during the final cleaning process for it etches much more rapidly in hydrofluoric acid solutions than silicon dioxide does. The presence of the phosphosilicate glass over the silica passivating layer reduces or prevents the movement of positive charges within the layer when temperature/voltage stresses are applied.

In our method of fabricating semiconductor devices by electron beam techniques, chemical etching steps have been avoided in order that the potentially high resolution which the method offers shall not be reduced. A previous publication (Ref. 2) described the use of a polymethylcyclosiloxane (PMCS) for preparing siliceous films in patterns defined by an electron beam for use as diffusion barriers. Irradiation by electrons produces cross-links in PMCS and renders it insoluble in solvents. An irradiated pattern may be developed by rinsing with a solvent when only the unirradiated portions are removed. An accompanying paper (Ref. 3) described an electron beam machine in which patterns of very fine geometry could be exposed. Patterns defined by exposing PMCS films on silicon to electrons and developing in acetone have been used successfully as barriers against arsenic, phosphorus and boron diffusion, and transistors have been made by this method. In contrast to conventional practice, in our electron beam technology the silica residue on the substrate is completely removed after each diffusion and a fresh film of PMCS is applied and exposed by the electron beam to produce the mask for the next stage. Thus when all the diffusion cycles are complete, the silicon surface is clean and bears no oxide to serve as a passivating layer. It has been found, however, that a film pattern produced by

electron exposure of a PMCS film also makes a very satisfactory passivating layer when subjected to suitable heat treatment.

PASSIVATING LAYERS FROM PMCS BY ELECTRON BEAMS

The capacitance-voltage (C-V) characteristics of MOS capacitors made with electron beam defined films of PMCS on 5Ωcm n-type silicon have been used to determine the effect of various treatments on the suitability of PMCS films as passivating layers using the method developed by Kerr (Ref. 4). The silicon substrate formed one electrode of the capacitor, the other being a film of aluminium evaporated through a contact mask on to the PMCS to give a 1mm. square electrode. The bias voltages quoted throughout this paper refer to the potential of the aluminium electrode relative to the silicon substrate. Fig. 1 shows the C-V characteristics of PMCS films exposed at 250 $\mu C/cm^2$, and developed in acetone, and the effects of heat treatments upon the characteristics, the capacitance being determined at 150 KHz. Although the exposed film, Fig. 1(a), shows considerable hysteresis and other irregularities sometimes appear, a wet oxidation treatment for 15 mins. at 650°C largely eliminates these and the densification treatments in nitrogen at 800°C and 1050°C bring still further improvements as shown in Fig. 1(b). It has also been shown by infra-red spectroscopy that these processes eliminate organic residues (methyl groups, alkylene bridges, etc.) from the film. It seems likely, therefore, that the hysteresis in the curve shown in Fig. 1(a) is due largely to the presence of organic residues though radiation damage may also play some part. Determinations of refractive index and etching rate in hydrofluoric acid of the heat-treated PMCS films result in the same values as are observed for thermally grown silica.

Fig. 2 shows C-V characteristics measured after the capacitors had been heated for 30 mins. at 180°C with ±22.5V/μm applied across the capacitor and cooled with the bias still applied. The shift of the curves along the voltage axis is due to the changing position of mobile positive charges within the silica layer under varying bias conditions. Little difference is seen in these effects when the bias voltage is increased to ±45V/μm, and they are similar to those observed in a thermally grown oxide film tested in the same way, results on which are shown in Fig. 3.

PHOSPHOSILICATE GLASS LAYERS BY ELECTRON BEAMS

It was thought that the application of a phosphosilicate glass layer over the PMCS passivating layer should stabilise the mobile positive ions as happens in conventional processing, but as in our

method there is no phosphorus diffusion following the application of the final PMCS passivating layer pattern, it was necessary to be able to apply the glass or compounds to produce it over the PMCS pattern only, leaving the contact windows clear. Of the known compounds containing both phosphorus and silicon and being likely to form films which could be cross-linked by exposure to an electron beam and developed to produce a pattern, tris-(dimethylsilylene) diphosphate seemed to be suitable. Although the ratio of phosphorus to silicon was higher than seemed desirable, it was thought that this ratio might be adjusted by mixing with the appropriate quantity of PMCS, and as the phosphate was a neutral compound (free from acidic hydrogen atoms) this should be possible without affecting the stability of the PMCS.

The phosphate was prepared by adding phosphoric acid carefully and slowly to dimethyldichlorosilane in stoichiometric quantities according to the following equation (Ref. 5).

$$3\left(CH_3\right)_2 SiCl_2 + 2\,H_3PO_4 \rightarrow \left[\left(CH_3\right)_2 Si\right]_3\left(PO_4\right)_2 + 6HCl.$$

The mixture gradually increased in viscosity as the acid was added and when addition was complete, the mixture was heated for 6 hours at 100°C followed by a further 4 hours at 100°C under vacuum (1-2 mms Hg) to remove any residual hydrogen chloride. The glassy solid product was dissolved in methylated spirit to give a 25% w/w solution. Molecular weight determination indicated that the phosphate was monomeric. A suggested structure is shown in Fig. 4.

Films of the phosphate were spun on silicon slices and exposed to electrons, followed by development in methylated spirit. It was found that an exposure of at least 800 $\mu C/cm^2$ was required to produce a developable image. Experiments with mixtures of PMCS and the phosphate showed that although films could be produced at lower doses, they appeared to consist mainly of cross-linked PMCS and contained insufficient phosphorus to give the desired stabilising effect. The exposure needed to be high enough to produce cross-links in the phosphate itself to avoid its being leached out of the film during development.

MOS capacitors were prepared, as described above, the dielectric now being a double layer. The first layer consisted of a PMCS film about 5000Å thick exposed at 250 $\mu C/cm^2$, developed in acetone and heat treated to convert it to silica, the film being finally about 3500Å thick. A film consisting of a mixture of PMCS and the phosphate in proportions to give an atomic ratio Si:P = 95:5

was then applied to the substrate to give a 1000Å thick film and exposed at 1000 $\mu C/cm^2$, this exposure being coincident in position with the underlying silica film. The exposed pattern was developed in methylated spirit and heated at 650°C in wet oxygen to remove organic matter and in nitrogen at temperatures up to 1050°C to form the phosphosilicate glass.

Fig. 5. shows C-V characteristics of layers produced in this way. Although there is a small movement along the voltage axis after voltage/temperature stress, this is independent of the polarity of the voltage applied during the heat treatment and occurs only during the first stress cycle. Subsequent cycles reproduce the initial bias curves and the unbiassed curve then lies close to them. A possible explanation is that any residual mobile positive charges in the passivating layer are swept into the phosphosilicate glass during the first negative cycle and become trapped there. (cf. Ref. 4).

PHOSPHOSILICATE GLASS PATTERNS DEFINED AT LOW EXPOSURES

The exposure required to produce the film pattern containing phosphorus using the system described above is very high and it seemed desirable to see if a more sensitive material could be prepared. It is usually the case that introduction of a vinyl group into a molecule renders it much more sensitive to the action of electrons, probably because their action is supplemented by a chain reaction involving the vinyl groups and initiated by the ion or free radical produced in the primary act. Chain reactions of this type are not possible when the substituents are saturated as in the system described above, and every cross-link in this case must be produced by a bombarding electron.

Methylvinyldichlorosilane was prepared by reacting vinyltrichlorosilane with methyl magnesium iodide, and was used to prepare tris-(methylvinylsilylene) diphosphate in a manner analogous to that used for the dimethylsilylene diphosphate. Films of this compound were found to require an exposure only 0.5-1 $\mu C/cm^2$ to produce a developable image. The phosphorus-silicon atomic ratio was adjusted in this case by mixing the phosphate with polyvinylcyclo-siloxane, (Ref. 2) the exposure range of which matches more closely that of the tris-(methylvinylsilylene) diphosphate than does that of PMCS.

MOS capacitors were again prepared, using a lower layer of electron beam exposed PMCS. The upper phosphorus containing layer was produced by exposing a film of the mixture of vinyl compounds to the electron beam at 10 $\mu C/cm^2$ to produce a pattern coincident in position with the PMCS pattern. The phosphorus - containing image was again developed in methylated spirit. It was found beneficial in

this case to increase the time of heating in wet oxygen at 650°C from 15 mins. to 30 mins. to ensure the complete removal of the larger amount of organic residues present in the vinyl compounds.

Fig. 6. shows C-V characteristics of the capacitors made with phosphosilicate glass layers containing silicon/phosphorus atomic ratio 95:5. The shift of the curves along the voltage axis under voltage/temperature stress is a little more than occurred when tris-(dimethylsilylene) diphosphate was used, but it is again independent of the polarity of the applied voltage. Fig. 7 shows characteristics of films containing twice as much phosphorus. These appear to be better in that the shift under voltage/temperature stress is smaller, and the change in capacitance occurs at a lower voltage, indicating a lower fixed charge within the passivating layer. An exposure of only 2 $\mu C/cm^2$ is adequate for this system, curves identical to those shown in Fig. 7 being obtained.

FINE GEOMETRY PATTERNS OF PHOSPHORUS GLASS

Fig. 8 shows some patterns made in the high resolution machine (Ref. 3). The patterns in Fig. 8(a) were prepared by exposing PMCS/tris-(dimethylsilylene) diphosphate films at 1000 $\mu C/cm^2$, those in Fig. 8(b) & (c) by exposing polyvinylcyclosiloxane/tris-(methyl-vinylsilylene) diphosphate at 10 $\mu C/cm^2$ and at 2 $\mu C/cm^2$, respectively. The resolution of both types of materials seems to be satisfactory.

CONCLUSION

Films produced by electron beam exposure of polymethylcyclo-siloxane may be used as passivating layers, and tests on MOS capacitors indicate that they should perform in semiconductor devices in a satisfactory manner after heat treatments designed to eliminate organic residues and densify the films. The undesirable effects attributed to mobile positive charges within the layer can be reduced or eliminated by the application of a thin layer of a mixture of a cyclosiloxane polymer with a tris-(dialkylsilylene) diphosphate in a pattern defined by the electron beam, and which after subsequent heat treatments is converted to a pattern of phosphosilicate glass. The introduction of a vinyl group into the compounds used for forming the films resulted in a marked increase in sensitivity to electrons, enabling patterns to be formed at reasonably low exposures.

The next stage of this work involves development of a system in which the passivating layer and the phosphosilicate glass patterns may be applied, and both layers exposed to the beam simultaneously to avoid an extra alignment procedure.

ACKNOWLEDGEMENTS

The author thanks the directors of Mullard Research Laboratories for permission to publish this paper. He expresses appreciation of helpful discussions with Dr. P.J. Daniel, Mr. H.N.G. King, Dr. T.R. Neill and Dr. J.P. Scott, and acknowledges the contributions of Mr. B.F. Martin who prepared and tested most of thefilms, and Mr. R.C. Barclay who prepared the patterns of fine geometry.

REFERENCES

1. D.R. KERR, et al. "Stabilisation of SiO_2 Passivation Layers with P_2O_5" I.B.M. Journ. 8, 376 (1964).

2. E.D. ROBERTS, "Rapid Direct Formation of Siliceous Diffusion Barriers by Electron Beams", Proc. 3rd. Int. Conf. on Electron & Ion Beam Science & Technology, Boston, May 1968, p.571.

3. R.A. FORD, et al. "High Resolution Electron Beam Techniques for Transistor Fabrication", Ibid. p. 561.

4. D.R. KERR, "Effect of Temperature and Bias on Glass-Silicon Interfaces", I.B.M. Journ. 8, 385 (1964).

5. M.G. VORONKOV and V.N. ZGONNIK, "New Methods of Synthesis of Tris-(Trialkylsilyl) Phosphates", C.A. 52, 3669 (1958).

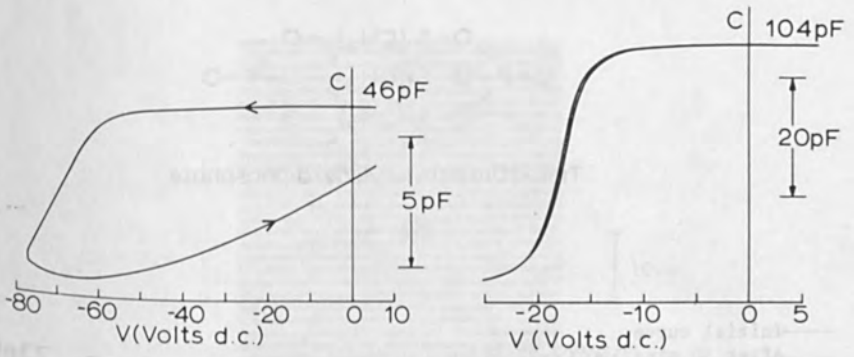

Fig. 1. CV characteristics of PMCS exposed at 250μC/cm^2.

(a) Film thickness ∿ 5000Å

(b) Heated 15 mins/650°C/wet O_2
15 mins/800°C/dry N_2
15 mins/1050°C/dry N_2
Film thickness ∿ 3000Å

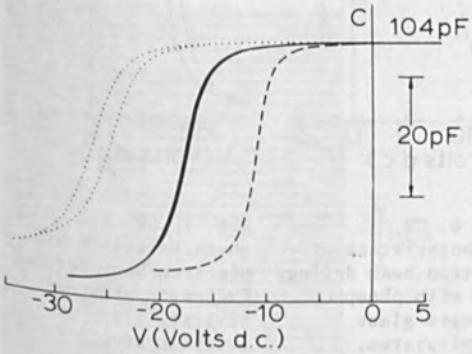

Fig. 2. CV characteristics of PMCS exposed at 250μC/cm^2.
Heated 15 mins/650°C/wet O_2
15 mins/800°C/dry N_2
15 mins/1050°C/dry N_2
Film thickness ∿ 3000Å

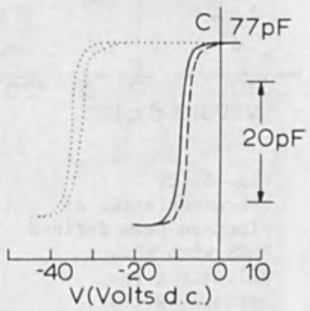

Fig. 3. CV characteristics of thermally grown silica films.
Film thickness ∿ 4500Å

———Initial curve
__ __After 30 mins/180°C/-22.5V/μm
·····After 30 mins/180°C/+22.5V/μm

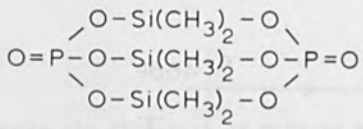

Tris-(Dimethylsilylene) diphosphate

Fig. 4.

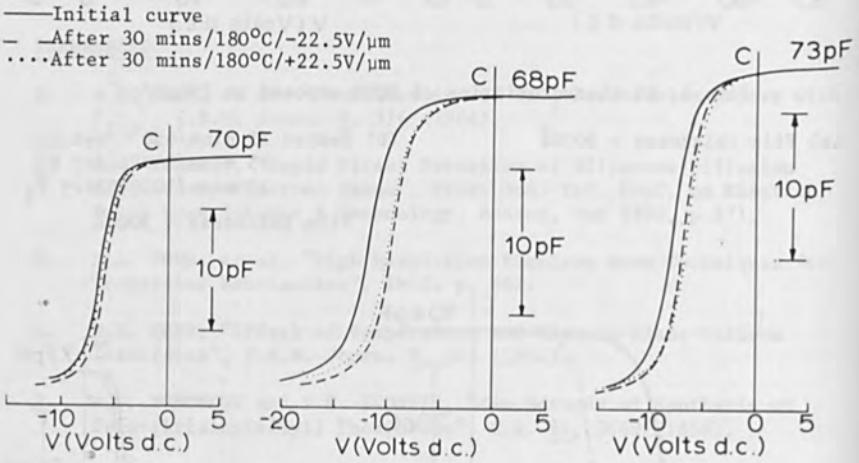

Fig. 5. CV characteristics of electron beam defined PMCS with phospho-silicate glass (methyl system, P:Si = 5:95)

Fig. 6. CV characteristics of electron beam defined PMCS with phospho-silicate glass (vinyl system, P:Si = 5:95)

Fig. 7. CV characteristics of electron beam defined PMCS with phospho-silicate glass (vinyl system, P:Si = 10:90)

Total film thickness ~ 4500Å
PMCS heated for
15 mins/650°C/wet O_2
15 mins/800°C/dry N_2

Glass heated for
15 mins/650°C/wet O_2
15 mins/800°C/dry N_2
15 mins/1050°C/dry N_2

Glass heated for
30 mins/650°C/wet O_2
15 mins/800°C/dry N_2
15 mins/1050°C/dry N_2

Glass heated for
30 mins/650°C/wet O_2
15 mins/800°C/dry N_2
15 mins/1050°C/dry N_2

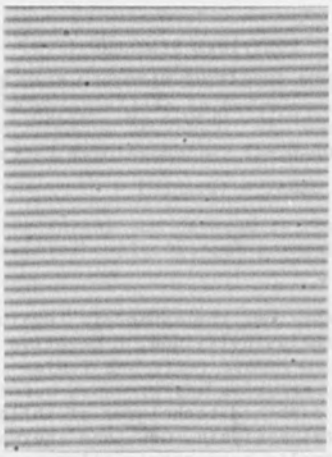

(a) Methyl system exposed at 1000μC/cm^2.

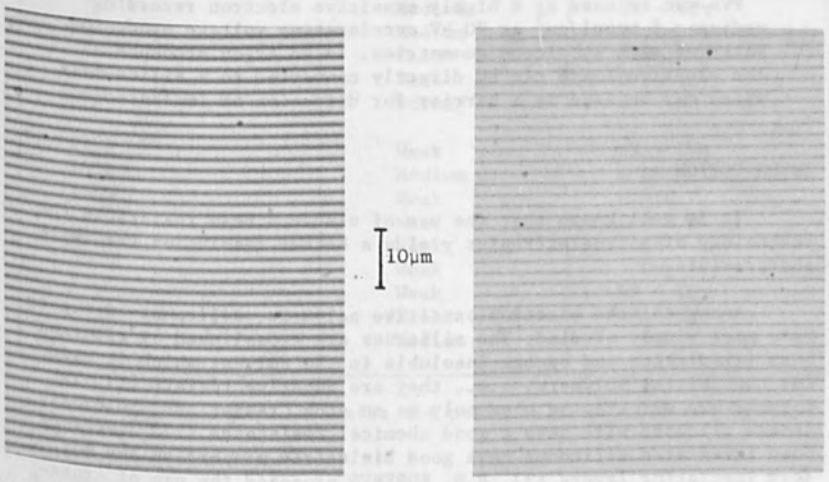

(b) Vinyl system exposed at 10μC/cm^2.

(c) Vinyl system exposed at 2.5μC/cm^2.

Fig. 8. Lines of siloxane/phosphate mixtures exposed in high resolution electron beam machine.

POLYVINYL SILOXANE (PVS)
A HIGHLY SENSITIVE ELECTRON-BEAM RESIST

J.C. DUBOIS, M. GAZARD

THOMSON-C.S.F. - Laboratoire Central de Recherches

91 - ORSAY - (France) -

- - - - - -

ABSTRACT

This article describes the synthesis, evaluation and characterization of polyvinylsilane, a negative electron sensitive resist.

The use of the combined techniques of infrared and NMR spectroscopy, elemental analysis, GPC, and thermal analysis allows one to deduce a cyclic tetrametric siloxane containing vinyl, hydroxyl, and methyl groups attached to silicon atoms in the ratio of 8 : 2 : 2.

PVS can be used as a highly sensitive electron recording medium : 5 $\mu coul/cm^2$ at 20 kV accelerating voltage producing patterns with submicron geometries. In an argon atmosphere the electron image can be directly converted to a silica mask which may be used as a barrier for diffusion or implantation.

INTRODUCTION

It is well known that the use of electron beam resists in the technology of microelectronics yields a better resolution than with photoresists.

Among all the electron-sensitive polymers, silicones have ever been most widely studied. The silicones are crosslinked by electron beam irradiation and become insoluble in the solvent which is used for the initial polymers, i.e., they are negative resists (1). The polymer may directly be used only as an etch resist and the crosslinked silicone will have a good chemical resistance (2). Electron beam irradiated silicones have good dielectric properties and may form insulating layers (3). E.D. ROBERTS proposed the use of crosslinked silicones as diffusion barriers (4).

This paper describes the synthesis, characterization and use of a negative electron beam resist - : - polyvinylsiloxane (P.V.S.). The crosslinked resist is converted to silica after heating at 800°C and is used as a diffusion and implantation barrier.

SYNTHESIS AND CHARACTERIZATION

Polyvinylsiloxane is synthetised from vinyl-trichlorosilane * The chlorosilane is hydrolysed in ethyl ether, then polymerized with ammonium hydroxyde. The white powder obtained after drying is kept in a dry atmosphere; otherwise crosslinking occurs.

The nature of the resist was deduced through the use of infrared, NMR spectroscopy, elemental analysis, gel permeation chromatography (GPC) and osmometry.

Figure 1 shows the infrared spectra of the polyvinylsiloxane as determined with a UNICAM SP 100 . The bands indicate the presence of hydroxyl, methyl and vinyl groups and a cyclic siloxane tetramer. The table below presents the correlation between absorption bands and structures.

Absorption band cm^{-1}	Intensity	Assignment
770	Medium	Si - CH_3
880	Medium	OH in Si-OH
960	Weak	CH = CH_2
1000	Weak	C = CH_2
1080	Strong	Si-O-Si cyclic tetramer
1290	Weak	Si - CH_3
1400	Medium	- CH = CH_2
1600	Weak	C = C
1930	Weak	C = C
2970	Weak	CH
3000	Weak	CH_3
3040	Weak	CH = CH
3060	Weak	CH = CH
3300	Medium	OH

The NMR spectrum indicates the presence of OH, CH3 and CH = CH_2 groups :

* SCHUCHARDT - 8 München 80, Gaisbergstr. 1-3 - Germany

Frequency (Hz)	Relative intensity of protons	Assignment
75	2	2 - OH
132	6	2 - CH_3
364	24	8 - $CH = CH_2$

- CH_3 and - OH groups are on the same silicon atom.

The elemental analysis of the resist give the following results:

% C : 26,8

% H : 4,43

% Si : 34,5 (by neutron activation)

% O : 29,7 (by neutron activation)

All these results suggest the following formula for the synthetised product :

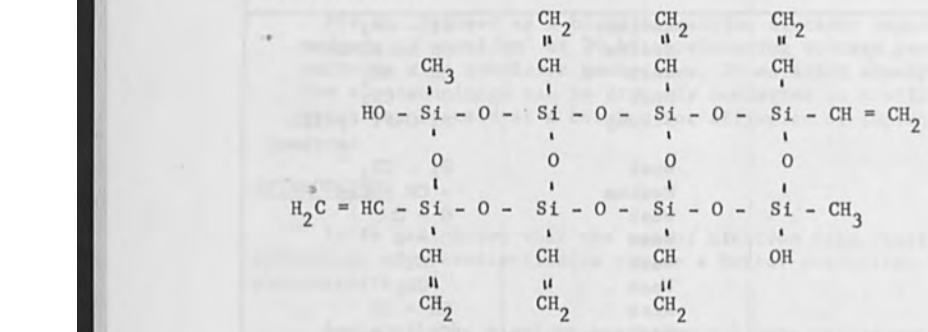

The molecular weight of the polyvinylsiloxane is determined by use of osmometry and GPC. The GPC method gives 660 when a calibration curve is made with polyglycols, which is in agreement with a molecular weight corresponding to the proposed formula (633). With a Hewlett - Packard vapor pressure osmometer a molecular weight of 1345 is found when chloroform is the solvent. This weight of 1345 is twice the weight given by GPC, which means that two molecules can be associated so that they form a dimeric molecule.

ELECTRON BEAM EXPOSURE

Procedure for using PVS

PVS is dissolved in 2 - propanol which was found suitable for PVS storage and coating processes.

Silicon wafers are coated with PVS by spin coating after ultrafiltration of the solution. Thickness of resist layers depends on the concentration of the solution and the spinning speed - Figure 2 presents the relation between thicknesses of the resist film and concentration of PVS in 2 - propanol at 12 000 rpm. The solvent is evaporated at room temperature. The relative humidity of the ambiant atmosphere is a very important parameter; if it is too high the layers will not be homogeneous.

The resist must not be heated above 75°C or crosslinking takes place.

Electron-beam exposure

Exposures of layers are made in a "Cambridge mark II" scanning electron microscope at 10 and 20 kV.

In determining the sensitivity of the resist the electron-beam scans an area of 2 mm x 2 mm. The line frequency is choosen so that the line detail is not resolved. Electron currents vary over the range of 10^{-12} to 10^{-8} amperes. The scanning time of each test area is 40 seconds.

In determining the resolution, two types of exposure are made :

a) Several lines are scanned with a line frequency of 5000 lines/mm,

b) The electron-beam is modulated according to an optical mask scanned by a flying spot tube. The light signal falls on a photomultiplier and the electrical signal modulates the beam.

Under electron-beam irradiation PVS crosslinks. The infrared spectra after crosslinking showsa decrease of the bands which are characteristics of vinyl groups (figure 3) : the crosslinking is accomplished through the vinyl groups. The intensities of the C-H and O-H bands decrease under irradiation .

The thickness of the resist decreases and the ratio of crosslinked thickness to initial thickness depends on the charge dose density, as shown in figure 4. The maximum is reached for a charge density range lying between 5.10^{-6} and 8.10^{-6} Cb/cm^2. Those values are obtained for 10 and 20 kV electron-beam accelerating voltages.

Development

Immediately after exposure, the wafer is developed by soaking in acetone for ten seconds and dried by blowing dust free nitrogen over the surface.

Resolution

Lines 0.4 μ in width were obtained as shown in figure 5 in PVS 0.6 μ thick, with a current of 10^{-10}A at 20 kV and a scanning speed 0.4 s/line, (5 mm/s).

Lines 0.5 μ in width were obtained with the use of an optical mask to modulate the electron-beam.

RESISTANCE OF PVS TO ETCHING SOLUTIONS

The chemical resistance of irradiated polyvinyl-siloxane has been studied in acidic reagents :

Chemical reagent	Resistance
Phosphoric acid	Good
Iodine-Potassium iodide	Good
Hydrofluoric acid	Moderate

Thus, crosslinked polyvinylsiloxane may be used as etch-resists.

SILICA CONVERSION

When heated the crosslinked resist is converted to silica as shown in the infrared spectra represented in figure 6. Only the Si-O band remains after heating. The conversion is done completely at 800°C during two hours in a dry argon atmosphere. At lower temperatures the total conversion needs longer times (for example, 24 hours at 350°C).

The thickness of amorphous silica is about 50 % of the initial thickness of resist.

In order to determine the dielectric properties of silica the following procedure is followed :
PVS is spun onto a polished silicon wafer, irradiated, developped and heated at 1000°C for one hour. Aluminium is then deposited by vacuum evaporation on the silica.

Resistivity is evaluated by measurements of current variation versus voltage variation. The dielectric constant is obtained by measuring the capacitance with an applied voltage of 10 Volts.

The study of the capacitance of the metal-silica-semiconductor structure as a function of the applied voltage allows the evaluation of the surface state charge density.

The results are listed in the following table :

Resistivity	10^{12} Ωcm
Dielectric constant	4 to 6
Dielectric strength	5.10^{5} V/cm
Surface states density	10^{10} cm^{-2}

USE OF SILICA MASKS FROM PVS

The silica mask is used for doping silicon wafers with boron or phosphorus.

For ion implantation the properties of silica are comparable to those of thermal silica : for example 0.1 µm is a good mask thickness for implantation of P of 30Kev energy in p silicon; 0.2 µm is a good mask for implantation of B of 30Kev energy in n silicon. The I-V characteristics of diodes made by this way are shown in figure 7.

Silica is also useful for thermal diffusion of boron and phosphorus.a 0.1 µm thickness of silica from PVS is a good diffusion barrier for P and B. Diodes were made to show this property - - their characteristics are represented in figure 8.

CONCLUSION

Polyvinylsiloxane needs a charge density of 5 $\mu Cb/cm^2$ to become insoluble in the solvent of the resist. This highly sensitive electron beam resist possesses a good resolution capability and permits one to fabricate small geometry circuit elements.

The crosslinked resist is converted to a silica whose dielectric properties are somewhat inferior to those of thermal silica : resistivity and dielectric strength are lower and the dielectric constant is greater than that of thermal silica. However, this silica may be used as an implantation or diffusion mask.

ACKNOWLEDGMENTS

The authors thank the "Direction des Recherches et Moyens d'Essais" and the "Délégation Générale à la Recherche Scientifique et Technique" for partial support of the research described here.

We wish also to thank "General Telephone and Electronics Laboratories" for their aid in determining the structure of polyvinylsiloxane.

REFERENCES

1 - A. CHAPIRO

"Radiation chemistry of polymeric systems"

Interscience - High Polymers - vol. 15

2 - YASUO YATSUI, TOSHITAKE NAKATA, KAZUO UMEHARA

"Electron Beam Exposure of Silicones"

J. Electrochem. Soc. vol. 116 - January 1969 - pp 94-97

3 - HIROYUKI AOE, YASUO YATSUI, TOSHIAKI HAYASHIDA

"Dielectric Properties of Silicone Thin Films Cross-linked by an Electron Beam"

Microelectronics and Reliability (1970) vol. 9 - pp 267-270

4 - E.D. ROBERTS

"Rapid Direct Formation of Siliceous Diffusion Barriers by Electron Beams"

Third Internation Conference, Electron and Ion Beam Science and Technology, Boston 1968

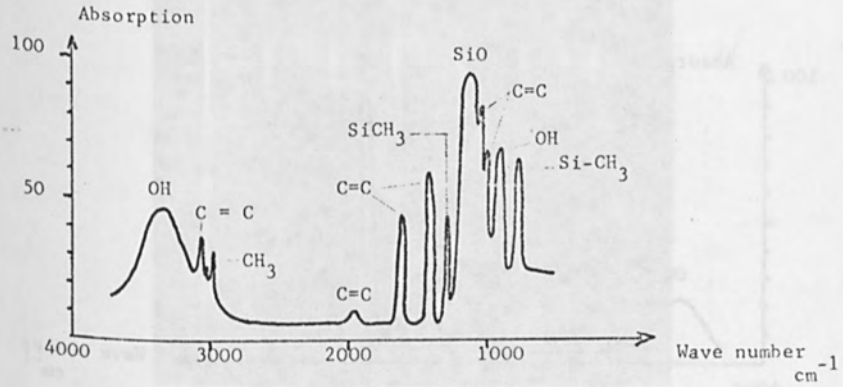

Fig. 1 - Infra-red spectra of PVS

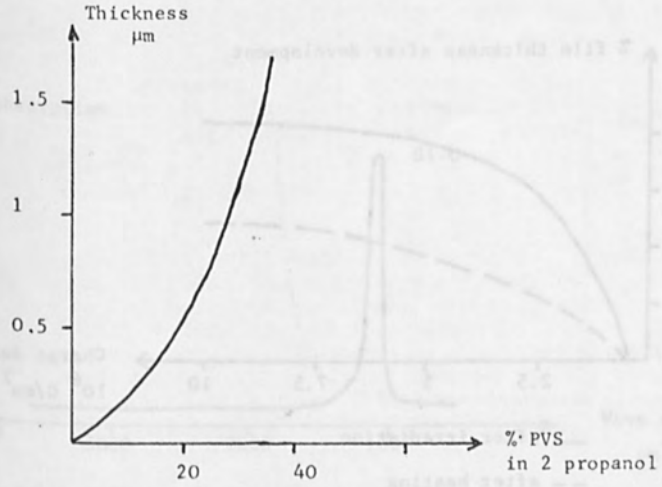

Fig. 2 - Film thickness versus concentration in 2 propanol

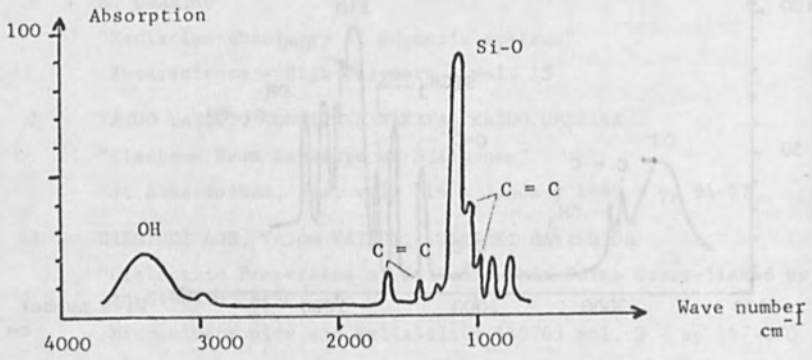

Fig. 3 - Infra-red spectra of irradiated PVS

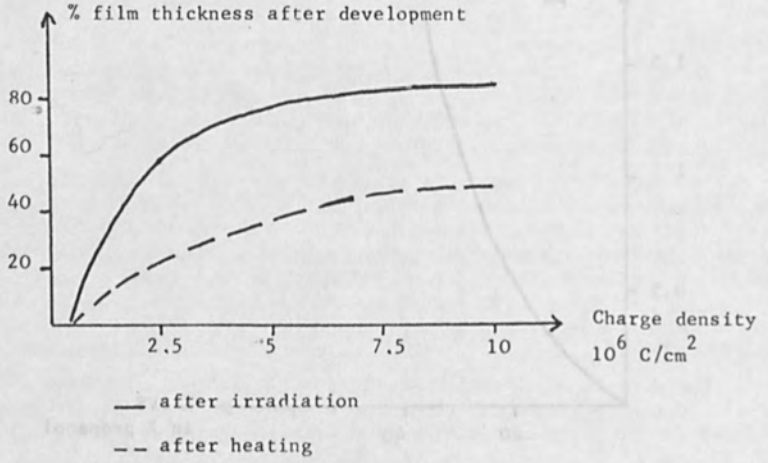

Fig. 4 - Exposure characteristics of PVS

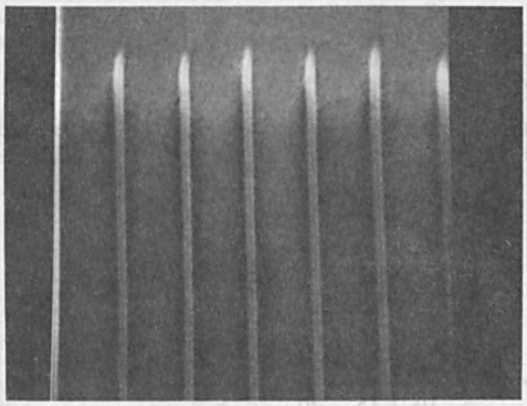

Fig. 5 - Lines of 0.4 μ in width in PVS

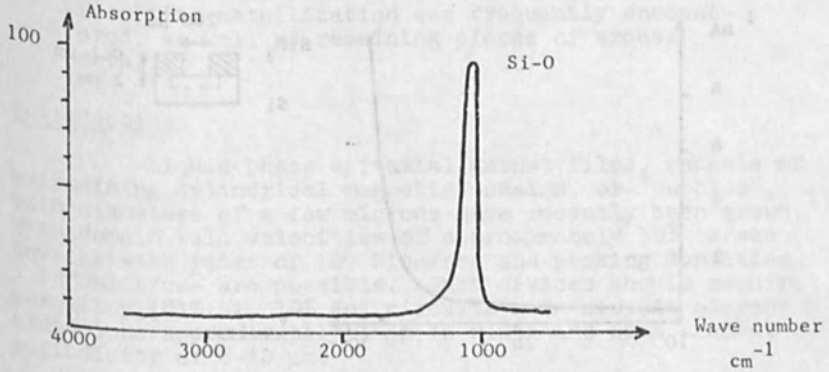

Fig. 6 - Infra-red spectra of irradiated PVS after heating at 800°C during 2 hours

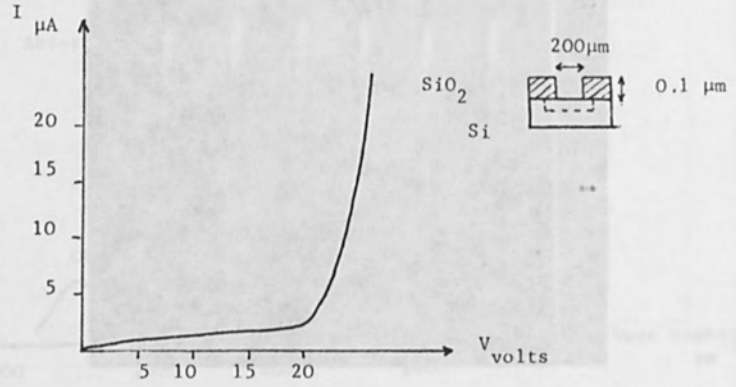

Fig. 7 - Reverse characteristic of implanted diode
Implantation of P (30 kV) in p silicon
(0.1 - 0.5 Ωcm)

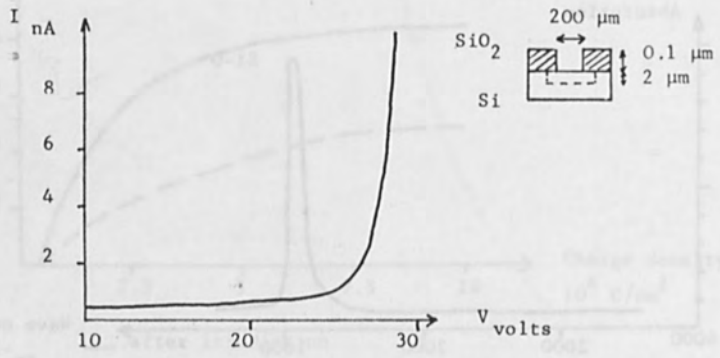

Fig. 8 - Reverse characteristic of diffused diode
Diffusion of P (3.10^{21} at/cm^2) in p
silicon (0.1 - 0.5 Ωcm)

Fabrication of Micron Sized Permalloy Circuit Elements Suitable for Magnetic "Bubble" Propagation Using Electron Beam Lithography

R. C. Henderson, W. B. Suiter and T. A. Weber
Bell Laboratories
Murray Hill, New Jersey 07974

Abstract

The propagation of 2-4 μm cylindrical magnetic domains ("bubbles") in garnet platlets requires correspondly sized permalloy circuit elements such as T-bars or chevrons. An electron beam lithography technique termed "lift-off" has been used to make these circuits with permalloy elements 1-1.2 μm in width, separated by 0.7-1 μm, and with an 8-10 μm periodicity. These structures have shown successful bubble propagation up to 100 kHz at threshold fields of 30 Oe.

While the desired patterns were in fact successfully made, it became clear during the work that the lift-off technique, which has been extensively used in the past, has a number of drawbacks. Poor adherence of the resulting metallization was frequently encountered, as well as remaining pieces of excess metal.

Introduction

Liquid phase epitaxial garnet films, capable of maintaining cylindrical magnetic domains, or "bubbles", with diameters of a few microns have recently been grown.[1] With domain wall velocities of approximately 10^3 cm/sec devices with rates of 10^6 bits/sec and packing densities $> 10^6$ bits/cm^2 are possible. Such devices should require permalloy (81% Ni, 19% Fe) circuits with circuit element dimensions approximately 1 μm in width and with element periodicity of 8-10 μm.

A suitable method for defining such patterns is electron beam lithography, because compared with conventional photolithography one can expect increased resolution and greater depth of field.[2] These advantages have been successfully utilized to make surface wave

transducers,[3] junction field effect transistors,[4] as well as other devices.[5]

In this work electron beam lithography has been used to construct permalloy circuit elements that have successfully propagated 2-3 μm diameter bubbles. The general prescription (known as lift-off[5]) to define the circuit was as follows: A scanning electron microscope (Cambridge Stereoscan Mark II A) was used to generate a fine (< 0.2 μ diameter) electron beam of 10 keV energy. The sample to be metalized was coated with a 4000 Å film of poly methyl-methacrylate (PMM) - a high resolution positive resist that is often utilized for electron beam lithography.[5] After writing and developing the pattern the sample was covered with permalloy by vapor deposition The success of the process depended upon electron scattering causing an undercut to be formed in the developed resist pattern, so that upon the subsequent permalloy evaporation a discontinuity was maintained between the material deposited in the pattern and that on top of the resist layer. Finally, the excess permalloy was removed by dissolving the remaining resist.

In the following section we describe two methods for generating the deflection and blanking signals in order to define the patterns. Further sections describe the most successful deposition parameters for the subsequent metalization and discuss the material problems encountered. Preliminary results of testing the permalloy structures and an evaluation of the metalization are also presented.

Pattern Definition

Two different permalloy patterns have been defined (Fig. 1). Figure 1a shows a pattern consisting of T-bar circuit elements and Fig. 1b circuits consisting of chevrons. Both structures have been used for bubble propagation but interest recently has centered on the chevron configuration due in part to the built-in redundancy of the pattern, i.e., missing a chevron bar does not eliminate bubble propagation.

The T-bar pattern was generated by amplifying the voltages generated by a Graphics 101C facility[6] and using these to drive the scan and blanking coils of the scanning electron microscope. For this procedure an XYMASK deck is fed into the card reader of the Graphics 101C terminal using the stand-alone XYMASK system.[6] The figures comprising the desired metal pattern are displayed in a random access mode using two 10-bit D/A converters

allowing one part in 1024 resolution in each of two dimensions.* The pattern is moved to the desired position by viewing on the storage display unit of the G101C terminal prior to exposure of the pattern in the scanning electron microscope. The stand-alone XYMASK display processor then decomposes each figure into a set of rectangles. The voltages corresponding to the coordinates of a corner of the rectangle are transmitted for 160 μsec (to allow for decay of transients in the deflection coils). The rectangle is then painted in by incrementing the voltages point by point in a boustrophedonic* raster covering the rectangle. The variables with this method are the number of addresses per circuit element dimension and the number of 5 μsec beam pulses per address. Reasonable resolution and uniformity of exposure were achieved using 8 addresses/element when defining elements of 1 μm width. The number of beam pulses was adjusted empirically but worked out to approximate an exposure of 10^{-9} C/cm when calculated by

$$E = \frac{A\left(\frac{\text{addresses}}{\text{element}}\right) \times \left(\frac{\text{pulses}}{\text{address}}\right) \times t\left(\frac{\text{sec}}{\text{pulse}}\right) \times I\left(\frac{\text{C}}{\text{sec}}\right)}{W\left(\frac{\text{cm}}{\text{element}}\right)}$$

Because the stand-alone XYMASK system was limited to rectangular, or "Manhattan," geometry an optical scanner technique was developed to define the chevron circuits. The scan generators of the scanning electron microscope are used to raster a spot over a high resolution phosphor screen. The desired mask is fixed to the screen surface and a photomultiplier (EMI, type 9524 B) tube detects the signal. The amplified voltage then drives the beam blanking circuit. The rise time of the phosphor was determined to be $\sim 10^{-3}$ sec so that a scan rate of 10 cm/sec was used to successfully resolve the 1/2 mm mask elements. Within an eight cm diameter area the response of this system was fairly even. Exposure, in this mode is controlled by adjusting beam current.

Metalization

A number of different substrates have been used. In the early phases the substrates were soda lime glass

---

* In principle 1 part in 4096 is available with the PDP8/L computer but a 12-bit D/A would be required.

* Writing alternate lines in opposite directions.

squares ~ 1 cm^2 and coated with 200 Å of either Cr or permalloy. Later, garnets or garnets with overlayers of 5000 Å SiO_2 were coated with 200 Å of Cr and used as the substrates. The metal layer serves as a conducting path to discharge the sample during electron beam writing. The 200 Å of nonmagnetic Cr does not seriously interfere with optical observation of the bubbles and in any case could be removed by preferential etching. In all cases the Cr was vacuum evaporated at pressures near 10^{-5} Torr onto substrates held at 300°C.

After the pattern had been exposed the resist was developed by immersing the sample for 20 sec in a 1:3 methyl isobutyl ketone/2-propanol solution followed by a 20 sec spray with the same solution. Subsequent metal adherence required additional cleaning. This consisted of 30 sec immersions in 2-propanol, 10% HCl solution, and 2-propanol again. Ultrasonic agitation while in the HCl bath helps wetting but tended to tear narrow lines of resist.

The sample, along with a control substrate of glass covered with 200 Å Cr, was then mounted on a heatable substrate holder and placed in the vacuum system. At a pressure less than 10^{-6} Torr the substrate holder was heated to 75°C for from 5 to 10 minutes. Then in less than 5 minutes both a 500 Å Chromium adhesion layer and a subsequent 1500 Å permalloy layer were vapor deposited.

Both metal vapors were generated by electron beam heating of melts in carbon crucibles using high purity crystalline chromium and vacuum grade permalloy. In order to minimize radiant heating of the PMM resist, the maximum deposition time of each metal layer was less than 20 sec.

Immediately after permalloy deposition the substrate holder was heated to 340°C, typically at 25°/min, and held at this temperature for 40 minutes. This post anneal relieved stress in the metallic films. Measurements of the control substrate showed this anneal also lowered the permalloy coercivity from ≈ 20 Oe to ≈ 2 Oe.

After the 40 min. anneal, the heating power was turned off and the substrates cooled at 4°C/min. Below 200°C, cooling gas was passed through the heater block until the sample reached room temperature. The substrates were then removed from the vacuum station and placed in boiling acetone in order to dissolve the remaining PMM and carry off the excess permalloy. Mild ultrasonic agitation was found necessary to remove final clinging

pieces of excess metal.

Results.

Metal structures produced by the above procedure may be seen in Figs. 1-3. Figures 1a and 1b are the structures produced. Higher magnification micrographs are shown in Figs. 2 and 3. The T-bar structure (Figs. 1a and 2) was deposited upon a Cr covered glass substrate whereas the chevron structure was deposited upon Cr covered garnet. The occasional bright spots are pieces of excess metal. An occasional element can be seen to be lost. In the case of the T-bar pattern in Fig. 2a the elements are 1 μm wide with 8 μm spacings. The chevron elements (Fig. 3a) are 1.2 μm wide with an interelement spacing of 7 μm and with a periodicity of 10 μm. In the chevron pattern of Fig. 3a the individual scans of the beam cause the fine scallop along the edges of the metal. Figures 2b and 3b are micrographs of the respective structures viewed at 74° from the normal. These views show that the metal structures are lying flat. Improperly processed structures often exhibit curling at edges and corners as seen in Fig. 4.

Both structures have been tested by observing in polarized light propagation (of bubble domains) due to a rotating magnetic field. The T-bar structures were tested by laying a suitable garnet over the permalloy structure. In the case of chevron circuits bubble propagation was observed up to 100 kHz at a threshold field of 30 Oe.

Discussion.

The major problem with early permalloy depositions was poor adhesion. Ordinarily, this problem can be circumvented by depositing films at 300°C which presumably volatilizes surface contaminants and anneals stress in the films. However, temperature in excess of 100°C are not possible when depositing upon PMM because the PMM flows and the pattern degrades. Yet when deposits are made at room temperature severe stress is generated in the films and the structures are observed to curl from the substrate.

To alleviate this problem it was thought that an adherence layer of Cr (or Ti) might prevent plastic deformation so that the stress could be annealed after metal deposition. This turned out not to be sufficient. Moreover, scanning electron micrographs of the resulting structures indicated that adhesion failure was occurring at the Cr-Cr interface rather than the Cr-permalloy interface.

A series of etching experiments convinced us

that this failure was due to a residual contaminant film left in the pattern after development with the methyl isobutyl ketone/2-propanol mixture. For example, we tried spray etching of the 200 Å conducting underlayer. The etching time was four times that required to remove a bare 200 Å metal film. Moreover, when etching did start it nucleated at specific points and then metal removal spread in a circular fashion. This behavior is consistent with the view that a thin contaminant film is slowly penetrated by the etchant and then undercut. With patterns given the additional cleaning using 2-propanol and HCl solution, the etching rates of the patterns and bare permalloy films were the same, and the Cr/permalloy deposits were markedly improved.

Nonetheless, even with these procedures curling of edges and corners was often observed (Fig. 4). Thus, the additonal step was taken to warm the substrate to 75°C during the deposition in order to relieve some stress in the films. From the micrographs in Fig. 2b and 3b it is evident that this combination of substrate preparation and deposition parameters successfully eliminated curling.

The in situ 340°C anneal step serves the purpose of relieving stress as soon as possible after deposition. PMM flow at this point is inconsequential. Moreoever, the anneal has the added benefit of reducing the coercivity to the acceptable value of ~2 Oe.

When depositions are carried out as described above there is always an initial mount of excess metal that clings to the pattern. Apparently, with these permalloy depositions the discontinuity is not always as sharp as desired. This does not seem to be too serious a problem as (a) bubble propagation is little affected by the excess metal, (b) excess metal is easily removed by mild ultrasonic agitation. On the other hand this latter step has the effect of occasionally losing one or two elements of the circuit. As mentioned above this need not be a fatal error in the case of the chevron structures.

Thus, although the procedures describes in this report have produced successful small bubble propagating circuits, alternative metallization schemes are being investigated.

Acknowledgements

We would like to acknowledge the help of R. F. W. Pease for his continuous support of this project and R. F. Helm for constructing the optical scanner.

L. R. Thibault designed and constructed the interface used for driving the scanning electron microscope with the Graphics 101 C facility and also helped with the T-bar pattern definitions. J. L. Bartelt provided the PMM and development techniques. The etching experiments were done with the collaboration of J. Reekstin. A. H. Bobeck and E. Walters obtained the bubble propagation results. The efforts and support of W. J. Tabor are also acknowledged.

References

1. H. J. Levinstein, S. Licht, R. W. Landorf, and S. L. Blank, Appl. Phys. Letters 19, 486 (1971).

2. George W. Brewer, IEEE Spectrum 8, 23 (1971).

3. A. N. Broers, E. G. Lean, and M. Hatzakis, Appl. Phys. Letters 15, 98 (1969).

4. E. D. Wolf, W. E. Perkins, and P. J. Coane, Proc. Cambridge Stereoscan Colloquium, 99 (1970).

5. M. Hatzakis, J. Electrochem. Soc. 116, 1033 (1969).

6. The Graphics 101 C facility consists of a PDP8/L computer, 32 K disc, 600 cards per min. card reader and two storage scopes. XYMASK is a Bell Telephone Laboratories graphical language used to define the mask patterns.

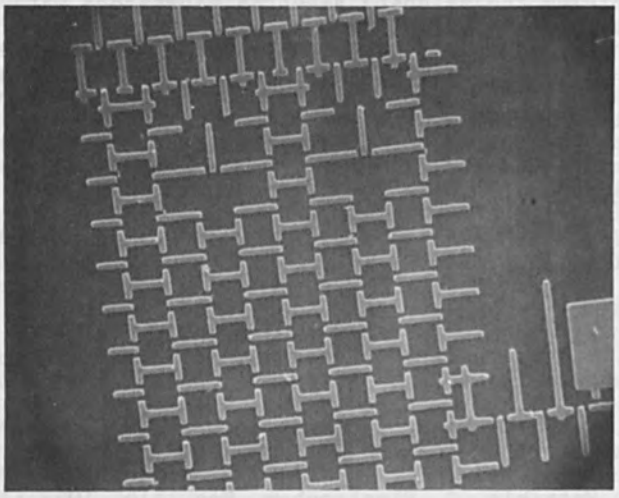

A

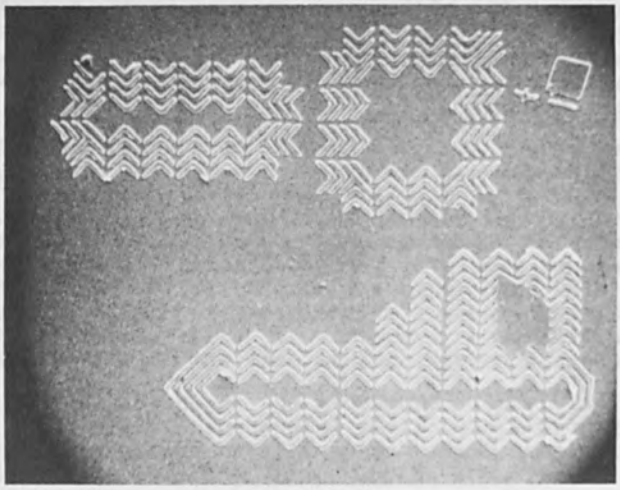

B

Fig. 1a Permalloy T-bar pattern. Field of view 100μm.
1b Permalloy chevron pattern. Field of view 190μm.

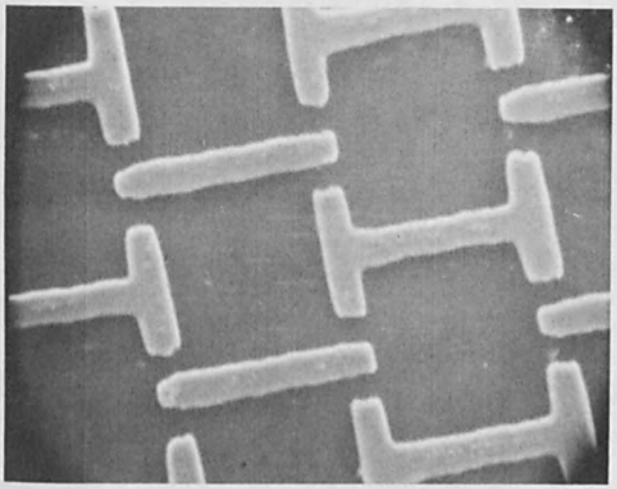

A

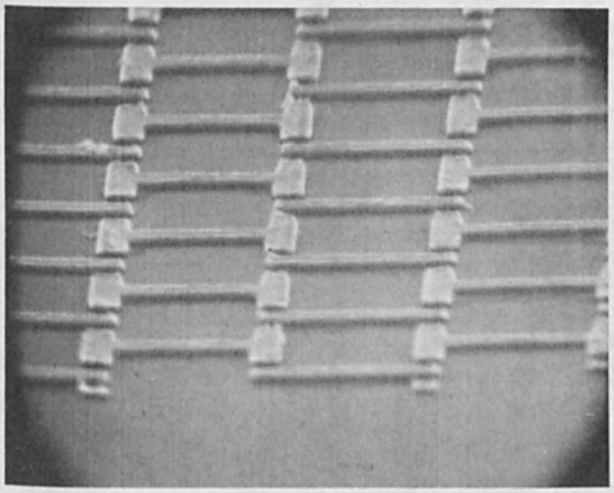

B

Fig. 2a T-bar elements. Field of view 17μm.
2b T-bar pattern viewed at 74° to the normal. Field of view 25μm. Element width 1μm with 8μm periodicity.

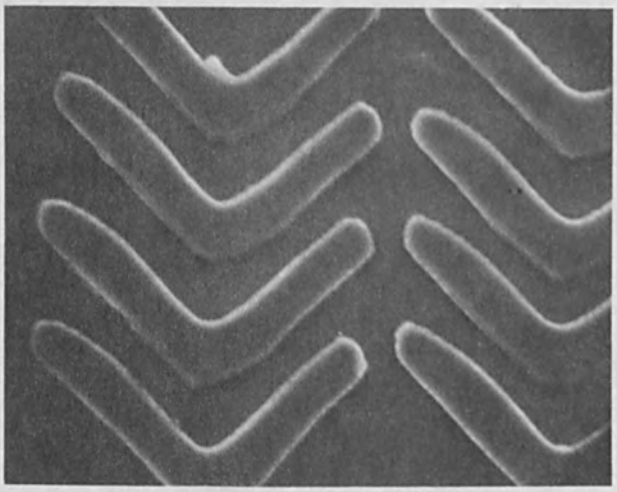

A

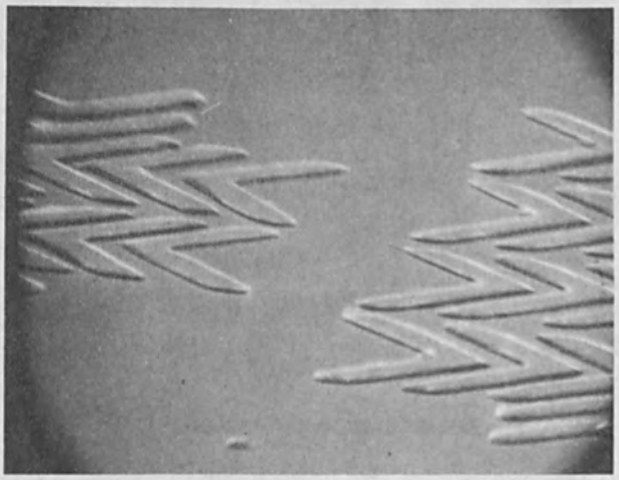

B

Fig. 3a Chevron elements. Field of view 21μm.
3b Chevron pattern viewed at 74° to the normal. Field of view 21μm. Element width 1.2μm with 10μm periodicity.

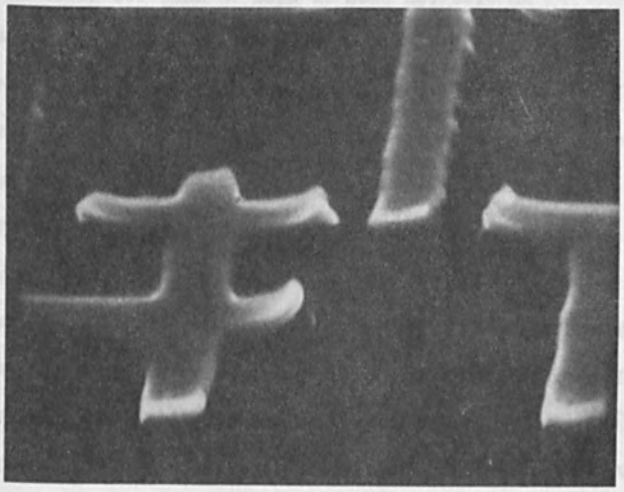

Fig. 4 Earlier metallization effort using T-bar pattern showing edge curling. Field of view 10μm.

4-polybutadiene, of which sensitivity in common use is 5×10^{-8} C/cm^2)[17], is coated on the chromium. After electron irradiation, the unirradiated resist is washed off by the developer (cyclohexanone) and the bare chromium is etched with an alkaline solution of potassium ferricyanide. Then a chromium mask having optical density above 2 is obtained[18].

In Fig. 5, upper left and lower left pictures show the enlarged portions of point chromium matrices. The number of chromium points in the frame is 6×10^6 for the lower left picture. Diffraction patterns are shown on the right side.

Examples of images reconstructed of the holograms are shown in Fig. 6. Measured diffraction efficiencies of (1,0) and (2,0) order for the patterns shown in Fig. 2 are 2.8 % and 1.0 %, respectively.

2.3 PHASE HOLOGRAM

There are many reports[19 ~ 26] concerning photoresist as holographic recording medium, but no report about the direct electron-beam-exposure technique.

Fig. 7 shows the fabrication steps of phase hologram. An electron-resist[17] is coated on the nesa-coated glass plate. The thickness of the resist is about 0.8 μm. After the resist is irradiated with an electron beam and is developed, the relief of the resist is obtained. This relief itself is the phase hologram. The process of chromium etching or bleaching is not necessary.

The reconstructed images of the amplitude and phase holograms are shown in Fig. 8.

3. DIFFRACTION EFFICIENCY OF THIN GRATING

3.1 BINARY AMPLITUDE GRATING

Binary amplitude grating is made of chromium mask with an electron beam as amplitude hologram made (Fig. 4). Diffraction efficiency of a grating is defined[27] as the ratio of the diffraction intensity of required mode number beam to the intensity of the incoming beam.

For one-dimensional grating, diffraction efficiency η_1 of the first order is

$$\eta_1 = B^2 \sin^2 (A\pi)/\pi^2 \ , \tag{1}$$

where A is line-width ratio, and B^2 is transmission power ratio. The measured values of η_1 are shown in Fig. 9.

For two-dimensionally symmetrical grating (opaque square type), diffraction efficiency η_{10} of order (1,0) is

$$\eta_{10} = A^2 B^2 \sin^2 (A\pi)/\pi^2 . \tag{2}$$

The measured values of η_{10} are shown in Fig. 10.

3.2 BINARY PHASE GRATING

Binary phase grating is made of resist-relief with an electron beam as phase hologram made (Fig. 7).

For one-dimensional grating, the diffraction efficiencies η_0 and η_1 are

$$\eta_0 = 1 - 4 A (1 - A) \sin^2 B, \tag{3}$$

$$\eta_1 = 4 \sin^2 B \sin^2 (A\pi)/ \pi^2 \ , \tag{4}$$

where 2B is the optical path difference angle. The measured values of

η_1 are shown in Fig. 11.

For two-dimensionally symmetrical grating, diffraction efficiency η_{10} of order (1,0) is

$$\eta_{10} = 4\ A^2\ \sin^2\ (A\pi)\ \sin^2\ B/\pi^2. \qquad (5)$$

The measured values are shown in Fig. 12.

4. DISCUSSION

Diffraction efficiencies of thin holograms are shown in Table 1. Efficiency of phase grating is four times higher than that of amplitude grating. Moreover, the phase hologram or grating of resist-relief type is useful for vinyl copy. Kinoform[6] is made of resist-relief with an electron beam. Details will be reported in future.

5. CONCLUSION

Computer-generated holograms are drafted using an electron beam with two methods. Binary thin amplitude holograms are made of chromium masks, and binary thin phase holograms are made of resist-relief. Diffraction efficiencies of holograms, one- and two-dimensional gratings are calculated and measured. Efficiency of phase grating is four times higher than that of amplitude grating.

The authors would like to express their thanks to Messrs. Y. Honda, Y. Miura, K. Katou, Drs. S. Nonogaki and T. Munakata.

REFERENCES

1) B. R. Brown and A. W. Lohmann: Appl. Optics 5 (1966) 967.

2) A. W. Lohmann and D. P. Paris: Appl. Optics 6 (1967) 1739.

3) B. R. Brown and A. W. Lohmann: IBM J. Res. Develop. 13 (1969) 160.

4) A. J. Meyer and R. Hickling: J. Opt. Soc. Amer. 57 (1967) 1388.

5) L. B. Lesem et al.: Proc. Symp. modern Optics (Polytechnic Press., N. Y., 1967) p. 681.

6) L. B. Lesem et al.: IBM J. Res. Develop. 13 (1969) 150.

7) Y. Ichioka et al.: Appl. Optics 8 (1969) 2461.

8) M. C. King et al.: Appl. Optics 9 (1970) 471.

9) Wai Hon Lee: Appl. Optics 9 (1970) 639.

10) Y. Ichioka et al.: Appl. Optics 10 (1971) 403.

11) L. F. Shew: Sixth I. Q. E. C. (Kyoto, 1970) p. 34.

12) C. Munakata et al.: Japan. J. appl. Phys. 9 (1970) 1187.

13) N. Saitou et al.: Japan. J. appl. Phys. 10 (1971) 351.

14) S. Yonezawa et al.: Japan. J. appl. Phys. 10 (1971) 1279.

15) A. Maekawa et al.: Japan. J. appl. Phys. 10 (1971) 1658.

16) A. Maekawa et al.: Proc. fourth int. Conf. Electron and Ion Beam Sci. Tech. (Electrochem. Soc., 1970) p. 503.

17) T. Hirai et al.: J. Electrochem. Soc. 118 (1971) 669.

18) A. Maekawa et al.: Japan. J. appl. Phys. 10 (1971) 810.

19) D. W. Maurer and E. E. Francois: IEEE J. QE-3 (1967) 246.

20) N. K. Sheridon: Appl. Phys. Letters 12 (1968) 316.

21) H. J. Gerristein et al.: Appl. Optics 7 (1968) 2301.

22) A. Labeyrie and J. Flamand: Optics Comm. 1 (1969) 5.

23) J. Nakajima et al.: Fujitsu J. 6 (1970) 69.

24) R. Bartolini et al.: Appl. Optics 9 (1970) 2283.

25) M. J. Beesley and J. G. Castledine: Appl. Optics 9 (1970) 2720.

26) R. G. Brandes and R. K. Curran: Appl. Optics 10 (1971) 2101.

27) H. Kogelnik: Proc. Symp. modern Optics (Polytechnic Press, N. Y., 1967) p. 605.

Table 1 Diffraction efficiencies of binary thin gratings and an hologram

TYPE	ORDERING NO.	THEORETICAL	MEASURED
AMPLITUDE	η_1 (ONE-DIM.)	0.1013	0.10
	η_{10} (SYMMETRY)	0.0340	0.030
	η_{11} (SYMMETRY)	0.0103	0.010
	η_{20} (SYMMETRY)	0.0149	-----
	η_{10} (HOLOGRAM)	------	0.028
	η_{20} (HOLOGRAM)	------	0.010
PHASE	η_1 (ONE-DIM.)	0.4035	0.40
	η_2 (ONE-DIM.)	0.1013	0.09
	η_{10} (SYMMETRY)	0.1360	0.12
	η_{11} (SYMMETRY)	0.0411	0.033

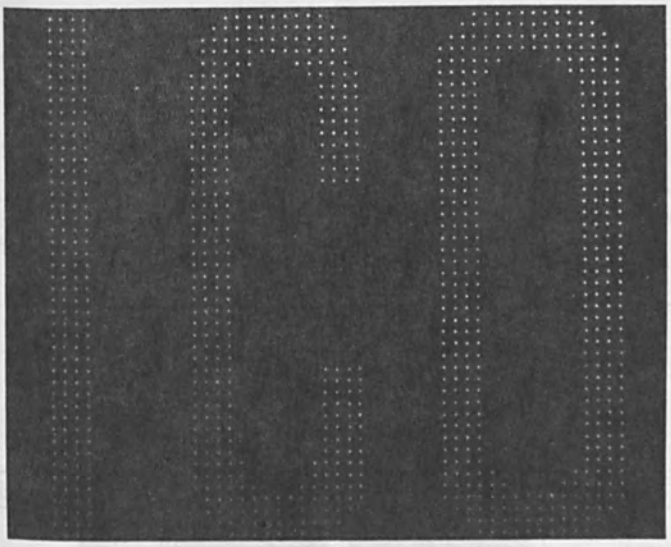

Fig. 1 Original pattern data

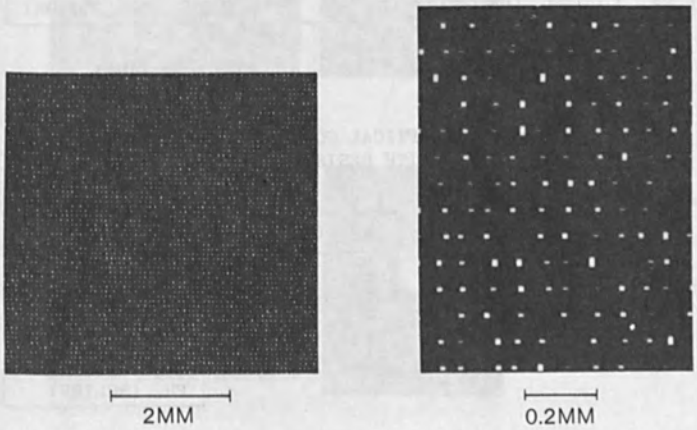

(a) Whole hologram

(b) An enlarged portions of the hologram

Fig. 2 Hologram

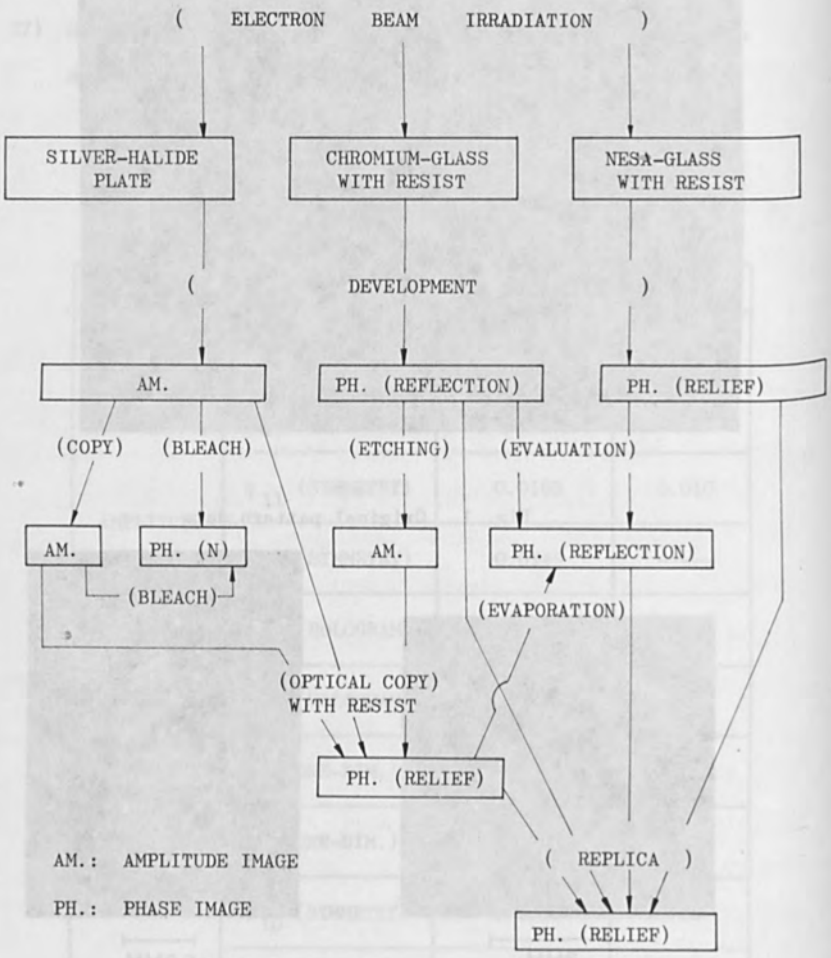

Fig. 3 Image recording methods with electron beam

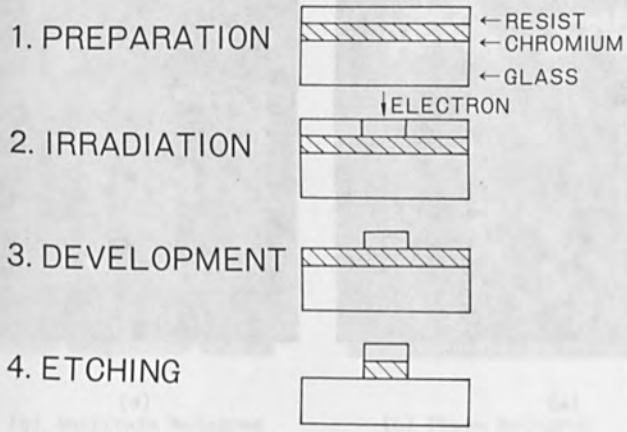

Fig. 4 Fabrication steps of amplitude hologram

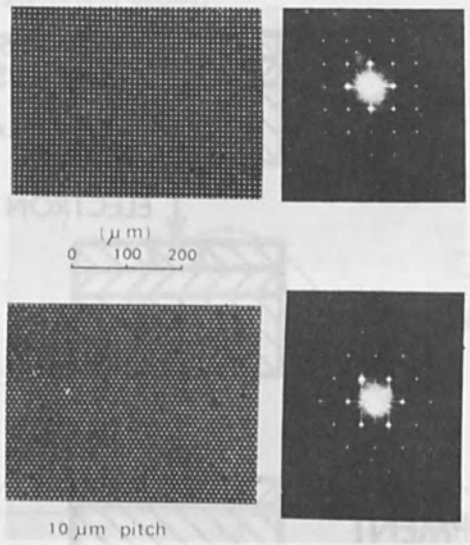

Fig. 5 Enlarged portions of point chromium matrices
(left: etched chromium plates,
right: diffraction patterns)

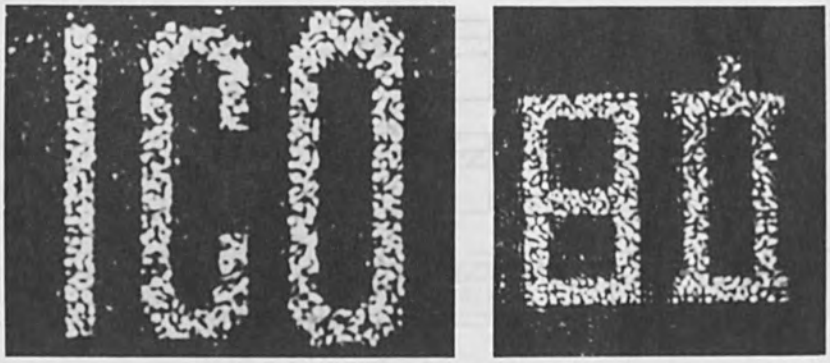

(a) (b)

Fig. 6 Reconstructed images of amplitude hologram

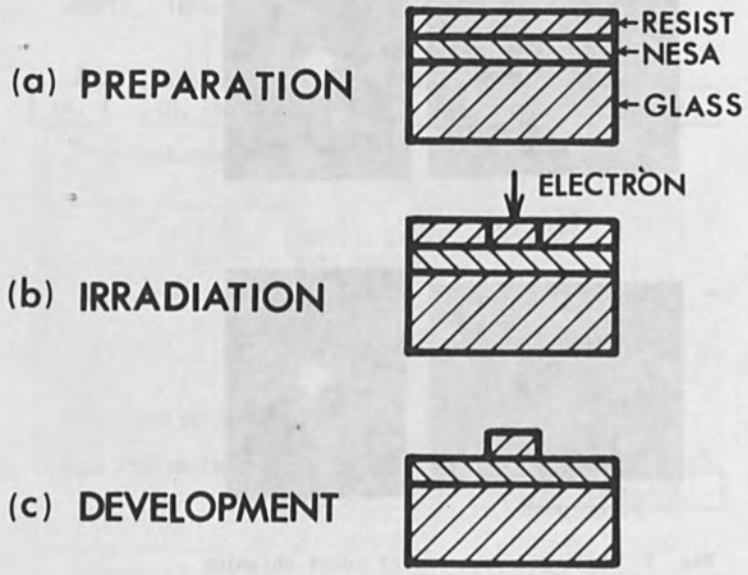

Fig. 7 Fabrication steps of phase hologram

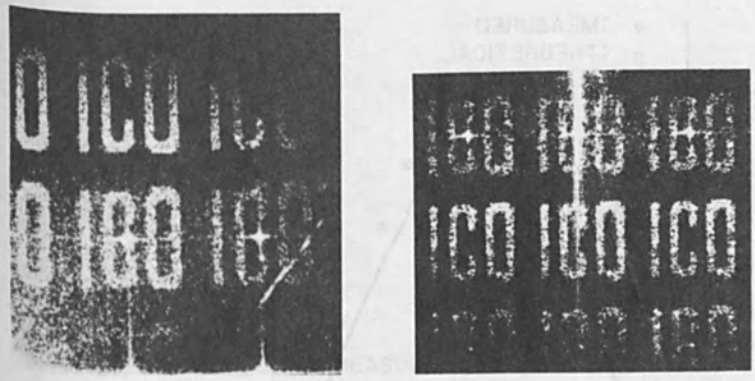

(a) Amplitude hologram (b) Phase hologram

Fig. 8 Reconstructed images of holograms due to different fabrication methods

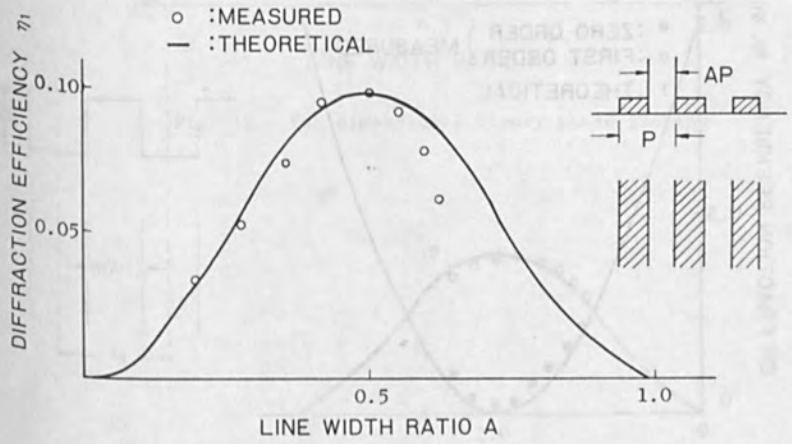

Fig. 9 One-dimensional binary amplitude grating

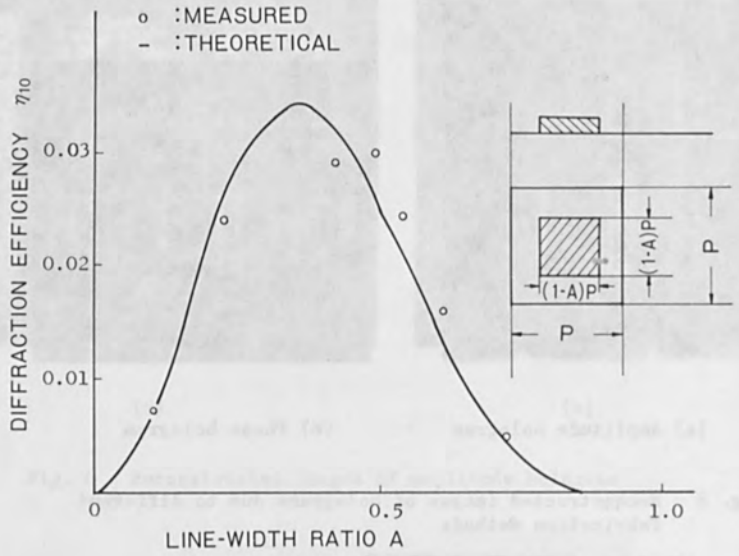

Fig. 10 Two-dimensional symmetry binary amplitude grating (opaque square type)

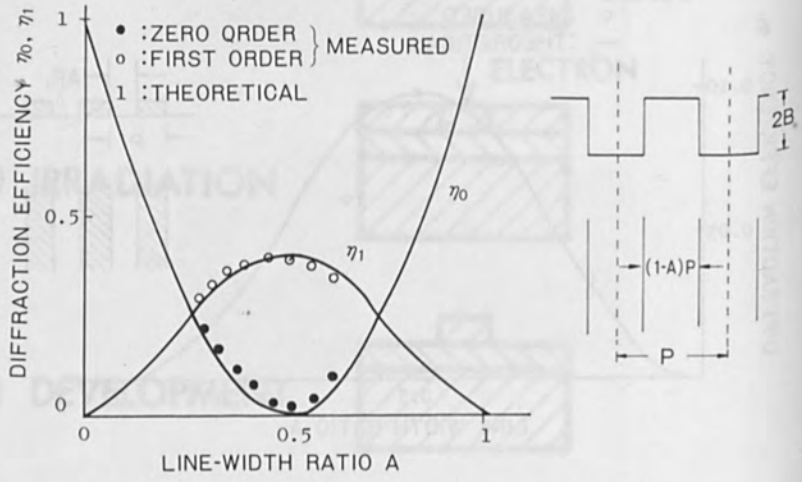

Fig. 11 One-dimensional binary phase grating

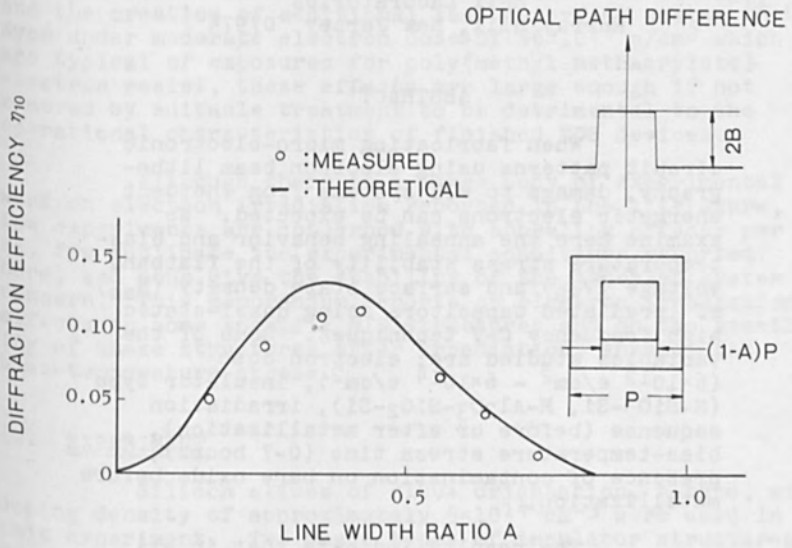

Fig. 12 Two dimensional binary phase grating

ELECTRON IRRADIATION OF MIS CAPACITORS - ANNEALING AND BIAS-TEMPERATURE STRESS STUDIES

L. R. Thibault and K. A. Pickar
Bell Laboratories
Murray Hill, New Jersey 07974

ABSTRACT

When fabricating micro-electronic circuit patterns using electron beam lithography, damage to MIS systems from incident energetic electrons can be expected. We examine here the annealing behavior and bias-temperature stress stability of the flatband voltage (V_{FB}) and surface state density (N_{ss}) of irradiated capacitors using quasi-static high frequency C-V techniques. Some of the variables studied are; electron dose (6×10^{12} e/cm^2 - 6×10^{14} e/cm^2), insulator type (M-SiO_2-Si, M-Al_2O_3-SiO_2-Si), irradiation sequence (before or after metallization), bias-temperature stress time (0-7 hours), presence of contamination on bare oxide before metallization.

The results indicate that in all cases the large increases in N_{ss} seen after irradiation can be annealed with low temperature ($\lesssim$450°C) heat treatments. B-T stressing with negative field-plate bias produced only negligible differences in surface state density between irradiated and unirradiated capacitors. Radiation induced shifts in V_{FB} also anneal at low temperatures to $|V_{FB}| < 1$ Volt. However, under bias-temperature stress, latent damage is revealed by the V_{FB} shift in Al_2O_3-SiO_2 structures. The flatband voltages of single oxide samples are stable under B-T stress.

I. INTRODUCTION

Planar Technology has primarily relied on photoresist techniques to define patterns for integrated circuits. An alternate method using scanning electron beam

techniques to polymerize or de-polymerize selected regions in a resist film is being developed to fabricate more complex and/or smaller integrated circuit geometries.[1-3] However, in the process of fabricating circuit patterns on oxidized silicon substrates using scanning electron beam microscopy, radiation damage to the oxide may be expected. This can result in shifts of the MOS flat-band voltage and the creation of additional fast interface states.[4-6] Even under moderate electron doses of $\sim 6\times10^{14}$ e/cm^2 which are typical of exposures for poly(methyl methacrylate) electron resist, these effects are large enough if not removed by suitable treatment to be detrimental to the operational characteristics of finished MOS devices.

Although there is a large body of experimental work on electron irradiation reported in the literature, few experiments are concerned with annealing effects per se, few duplicate the experimental conditions reported here, and none give the stability of the annealed system of concern. This memorandum reports on electron irradiation effects on some specific MIS structures and on the stability of these structures after irradiation, anneal, and bias-temperature stress.

II. EXPERIMENT

Silicon slices of <100> orientation, n-type, with doping density of approximately 5×10^{14} cm^{-3} were used in this experiment. Two basic types of insulator structures were fabricated.

Type I (single insulator)

1 - Oxidation in wet O_2 at 1100°C to 1000 Å

2 - Evaporation of Al (3000 Å thick) dots and back contacts on some wafers

Type II (double insulator)

1 - Oxidation in wet O_2 at 1100°C to 1000 Å

2 - Anneal at 1100°C in dry N_2

3 - Al_2O_3 deposition (500 Å)

4 - Standard Ti-Pd evaporation followed by Au plating on some wafers until Au is opaque. Some wafers are not metallized.

Several different metallization-irradiation sequences are studied to test the relative effects of resist contamination of a bare oxide and electron irradiation on the MOS parameters of single oxide structures.

1) Al dots are evaporated immediately after oxidation. After the metallization, parts of each sample are exposed to e-beam irradiation with some dots left as unirradiated controls.

2) The bare SiO_2 film is coated with electron resist poly(methyl methacrylate). After exposing to the e-beam and developing the pattern, the bare SiO_2 regions are cleaned in 100:1 HF for thirty seconds. The Al field plates are then defined using "lift-off" techniques.[7]

3) The bare SiO_2 film is deliberately contaminated with photoresist. The resist is removed, the slice is cleaned and an Al film evaporated. Some of these devices are irradiated and some are left as a control.

In addition, for the double insulator capacitors, the sequences are:

4) An evaporated Ti-Pd, Au plated film is deposited on the Al_2O_3-SiO_2 film followed by irradiation.

5) The bare Al_2O_3-SiO_2 film is irradiated and subsequently Al metallized with dots defined using conventional photolithography.

A summary of these experimental conditions imposed on each insulator system is shown schematically in Fig. 1. Electron irradiation at 20 KeV and doses of 10^{-4} to 10^{-6} coul/cm^2 (6×10^{14} - 6×10^{12} e/cm^2) was performed in a scanning electron microscope. For simplicity, most data presented here are generated from specimens exposed to the larger dose of 10^{-4} coul/cm^2, representative of worse case conditions. Only a portion of each slice was irradiated; the remainder of each slice was left as a control. Surface state density, N_{ss}, was measured before and after irradiation using the high frequency and low frequency (quasistatic) method.[8,9] N_{ss} was determined by averaging the values obtained at several random points on the

C-V curves. These points were chosen in the depletion region prior to the onset of inversion. This averaging is permissible if the surface state density does not vary greatly with location in the energy gap. The results indicate this variation is less than a factor of two. To check this further the quasi-static capacitance curve was integrated[10] to give the variation in surface states over the bandgap for a number of representative samples.

The flat-band voltage V_{FB} was measured directly by plotting electronically $(C_{ox}/C)^2$ vs. V where C is the high frequency capacitance (1 MHz) and C_{ox} is the oxide capacitance.[11] This method is valid providing N_{ss} is small enough to not significantly distort the high frequency C-V curve in depletion. By comparing the flat-band voltage results obtained with this method to the flat-band voltage obtained using ideal MOS curves[12] (surface states neglected) agreement to $\lesssim$ 0.05 Volts is obtained when $N_{ss} \lesssim 10^{11}/cm^2$-eV. For $N_{ss} \sim 10^{12}/cm^2$-eV (as occurs after irradiation) the "flat-band voltages" obtained using the two methods differ by $\gtrsim$ 0.5 V and are thus not recorded here.

Thirty minute isochronal anneals are performed in dry N_2 gas with N_{ss} and V_{FB} determined after each anneal.

Bias-temperature stressing was then performed at 300°C in dry N_2 with the metal field plate held at -10 Volts. After various time periods up to 7 hours the MOS characteristics were remeasured at room temperature.

III. RESULTS - SURFACE STATES

The experimental results for the determination of surface state density, before and after irradiation, after anneal and after B.-T. stress are summarized in Table I.

A. Dose

Figure 2 shows the effect of dose on the density of surface states after irradiation. Large damage effects are seen even for the lowest dose used, $\Phi = 10^{-6}$ coul/cm^2. Because electrons backscattered from the sample can be subsequently backscattered from the final microscope lens, increases in surface state density are observed in capacitors not directly scanned by the electron beam. These indirectly exposed capacitors were ~150 mils from the

irradiated area. Capacitors beyond ∿300 mils from the irradiated area were essentially unaffected by the radiation. All control capacitors used in this experiment were protected by an overlaying silicon mask during irradiation as were ares irradiated by different doses.

The single-oxide control sample is not given any high or low temperature anneal before measurement and thus has an initial N_{ss} of $2\times10^{10}/cm^2$-eV. The double insulator sample sees a high temperature anneal after oxidation and thus the unirradiated capacitors show a much lower surface state density, $N_{ss} \sim 7\times10^{9}/cm^2$-eV.

B. Anneal and Bias-Temperature Stress

Typical high and low frequency measurements made before and after irradiation (Fig.'s 3a, b), after anneal (Fig. 3c) and after B-T stress (Fig. 3d) for an SiO_2 system metallized before irradiation to indicate the large changes in surface state density observed in this experiment.

There is a large decrease in N_{ss} after anneal from $\sim4\times10^{12}$ to $\sim5\times10^{9}/cm^2$-eV. The latter value is lower than the N_{ss} of the preirradiated sample. This large change is thus due in small part to the anneal of surface states associated with the oxide growth. The control capacitor for SiO_2 systems anneal to a higher value ($1\text{-}2\times10^{10}/cm^2$-eV) as shown in Table I.

The devices made by lift-off also anneal to a slightly higher value ($\sim4\times10^{10}/cm^2$-eV). However, both the contamination of the bare oxide and the irradiation effects characteristic of the lift-off process are performed separately using the conventional metallization and the resulting capacitors show no increase in surface states over their controls. These anneals were made at 350°C. No further improvement is seen after a 450°C anneal. For the Al_2O_3-SiO_2 capacitors some radiation damage remained after a 350°C anneal (irradiated samples - $N_{ss} \sim 4\text{-}7\times10^{10}/cm^2$-eV; control $N_{ss} \lesssim 6\times10^{9}/cm^2$-eV). After a 450°C anneal all double insulator capacitors had essentially a perfect interface $\gtrsim 6\times10^{9}/cm^2$-eV. Values of $N_{ss} \gtrsim 6\times10^{9}/cm^2$-eV are not accurately measurable.

Referring still to Table I, the surface state density of all single insulator systems is $\sim1\times10^{11}/cm^2$-eV after seven hours B-T stress independent of prior treatment. This is a saturated value reached after only half

an hour. All double insulator systems have surface state densities after stress of $3\sim4\times10^{10}/cm^2$-eV reached after $\sim$6 hours. No effects of prior radiation damage or contamination could be seen from the surface state measurement in either case. To examine this point further, the surface potential was determined to a additive constant using the method of Berglund[10] in order to obtain the surface state density as a function of energy cross the bandgap. The constant term was obtained by setting the experimentally determined flat-band voltage to the fermi-level of the silicon with an n-type doping of 6×10^{14} cm^{-3}. A plot of surface state density as a function of location in the bandgap is shown in Fig. 4. This location is only approximate for the sample just after irradiation because of the indeterminary in measuring V_{FB} for capacitors with $N_{ss} \sim 10^{12}/cm^2$-eV. After B-T stress both the irradiated single oxide (uncontaminated) and the unirradiated control have approximately the same number of surface states. These distributions are flatter than that of the annealed irradiated sample prior to stress.

IV. RESULTS - FLAT-BAND VOLTAGE

Table 2 gives a summary of the results for flat-band voltage. In all cases except for the lift-off metallization the results are expressed in terms of a shift in the flat-band voltage from unirradiated control capacitors on the same slice. For lift-off slices where an unirradiated control is obviously not possible the voltages shown are within 0.3 volts of unirradiated capacitors with KMER contamination made with conventional metallization.

The flat-band voltage data for the SiO_2 system irradiated after metallization is shown in Fig. 5. The flat-band voltage is obtained by extrapolating the straight line portion of the curve to the accumulation base-line where $\left(\frac{C}{C_o}\right)^2 = 1$. It is seen in this case that the shift after anneal, or after B-T stress is negligible and within the experimental accuracy of the technique $\pm.05$ V. For the other SiO_2 systems, there is a shift after irradiation which disappears after 350°C anneal and remains negligible after B-T stress.

However for the Al_2O_3-SiO_2 systems, apparent large negative shifts are seen after irradiation. After a 350°C anneal, there is substantial unannealed damage in

the Al_2O_3-SiO_2 samples giving a flat-band voltage shift ∿-2 volts. However after a 450°C anneal this negative flat-band voltage shift disappears.

When the sample is subsequently subjected to B-T stress, (referring to Table 2) a positive shift appears revealing unannealed latent damage in the irradiated Al_2O_3-SiO_2 capacitors.

It is also of interest to note how the controls behave. For the single oxide systems the flat-band voltage of unirradiated capacitors is ∿-0.6 V before and after anneal and ∿-0.8 V after B-T stress. For the Al_2O_3-SiO_2 systems the flat-band voltage of control capacitors are initially ∿-0.45 volts. After anneal V_{FB} ∿0.0 volts. After B-T stress, however, the controls change to ∿+3 V for the sample metallized before irradiation and -0.6 V for the sample metallized after irradiation. Despite the different behavior of the controls, the shift of the irradiated capacitors from the respective controls in both cases was of the same order and in the same direction.

V. DISCUSSION

The results shown here, that radiation induced changes in N_{ss} and V_{FB} of SiO_2 systems, and of N_{ss} in Al_2O_3-SiO_2 systems are annealable with no latent damage observed, indicates that no permanent damage is done to the Si-SiO_2 interface by 20 keV electrons. The positive shift of the Al_2O_3-SiO_2 systems after B-T stress is thus attributed to effects in the alumina. This shift corresponds either to an increase of negative charge in the Al_2O_3 layer due to electron injection from the metal field plate into trapping states or to a shift in the existing electron charge distribution towards the Al_2O_3-SiO_2 interface aided by an increased bulk trapping density. There is insufficient experimental evidence to choose between the two possibilities. An attempt to remove this latent damage by annealing to 900°C (the Al_2O_3 deposition temperature) was unsuccessful. Although ΔV_{FB} was small after this anneal N_{ss} increased to $\sim 3\times10^{11}/cm^2$-eV. Both N_{ss} and ΔV_{FB} were unstable after a subsequent 350°C anneal, in the absence of an applied bias.

The latent damage effects observed here in SiO_2-Al_2O_3 are consistent with the unpublished work of Labuda et al (13,14) for e-gun evaporated Pt metal contacts. In these experiments the x-rays emitted by the

bombarded source apparently caused a similar shift in V_{FB} which appeared after the B-T stress of the annealed target.

Si-Al_2O_3-Al capacitors[15,16] are sometimes used for radiation resistant MOS capacitors. In these structures the shift of flat-band voltage during irradiation is said to be less than for a comparable SiO_2 structures. This attributed to electron trapping effects preventing the charge separation of e-beam created hole-electron pairs in the insulator with a resulting buildup of a space charge layer. For composite SiO_2-Al_2O_3 structures results similar to SiO_2 were found.[17] The problem is complicated by the absence of applied external bias during irradiation in the present experiment.

VI. CONCLUSIONS

The conclusions derived from this experiment may be summarized as follows:

1. The large increases in N_{ss} of SiO_2 and Al_2O_3-SiO_2 capacitors produced by 20 keV, 10^{14} cm^{-2} electron irradiations may be annealed out at 350°C (SiO_2) to 450°C (Al_2O_3-SiO_2). Bias-Temperature stressing of the annealed structures at -10 V, 350°C for 7 hours produces only negligible differences in surface states between irradiated and unirradiated capacitors.

2. Large increases in N_{ss} are seen for even the lowest dose used (6×10^{12} e/cm^2).

3. Radiation induced shifts on the flat-band voltage also anneal at the above temperatures. However, latent damage is revealed in the Al_2O_3-SiO_2 structure under B-T stress. The SiO_2 flat-band voltage is stable under B-T stress.

4. From 1. and 3. above, electron radiation effects in SiO_2-Si interfaces are annealable. The positive shift seen in the Al_2O_3-SiO_2 system suggests a shift of negative charge in the alumina towards the Al_2O_3-SiO_2 interface arising from charge separation effects in the Al_2O_3 or injection of additional electrons from the metal into the alumina. There is insufficient experimental information to choose a correct model.

5. These experimental results are in accord with previous observations by Labuda et. al. who found that e-gun evaporation of metal contacts on SiO_2-Al_2O_3 insulators (which subjects the alumina to soft x-ray bombardment) gives capacitors which are bias-temperature unstable. This effect was not observed in SiO_2 capacitors.

6. Capacitors stable under B-T stress can be made on SiO_2 insulators using e-beam exposure of resist deposited either before metallization on the bare oxide (lift-off) or after metallization.

This work will be continued in a subsequent memorandum to give results for positive bias-temperature stressing, different metallizations and higher temperature anneals.

ACKNOWLEDGMENTS

The authors would like to thank E. G. Parks, Jr. for sample preparation and A. D. Lopez for advice on quasi-static - high frequency C-V measurement techniques. We acknowledge useful discussions with R. F. W. Pease, E. F. Labuda, E. H. Nicollian, C. N. Berglund and R. H. Walden.

References

1. George R. Brewer, IEEE Spectrum 8, 23 (1971).

2. M. W. Larkin and R. K. Matta, Solid State Electronics 10, 491 (1967).

3. S. Magdo, M. Hatzakis, and C. H. Ting, IBM Journal of Res. and Dev. 15, 446 (1971).

4. J. P. Mitchell, D. K. Wilson, B.S.T.J. 46, 1 (1967).

5. E. H. Snow, A. S. Grove and D. J. Fitzgerald, Proc. IEEE 56, 1168 (1967).

6. K. H. Zaininger, A. G. Holmes-Siedle, RCA Review, 208, (1967).

7. M. Hatzakis, J. Electrochem. Soc. 116, 1033 (1969) The "lift-off" sequence for metallization includes the exposure and development of a resist pattern on the substrate, evaporation of the desired metal, dissolution of the resist pattern in an appropriate solvent which "lifts-off" those metal regions coating the resist.

8. M. Kuhn, Solid State Electronics 873, (1970).

9. A. D. Lopez, (private conversation).

10. C. N. Berglund, IEEE Trans. Electron. Devices, ED-13, 701 (1966).

11. A. S. Grove, "Physics and Technology of Semiconductor Devices", John Wiley and Sons, Inc., New York (1967).

12. A. Goetzberger, B.S.T.J., 45, 1097 (1966).

13. R. H. Dudley, E. F. Labuda, IEDM Washington (1969).

14. E. F. Labuda (private conversation).

15. A. S. Waxman, K. H. Zaininger Appl. Phys. Lett. 12, 109 (1968).

16. K. H. Zaininger, C. C. Wang, Proc. IEEE 57, 1564 (1969).

17. Radiation Effects in Majority Carrier Devices 11, K. G. Kerris et al Report No. FR 68-10-518 AD 838923 (1968).

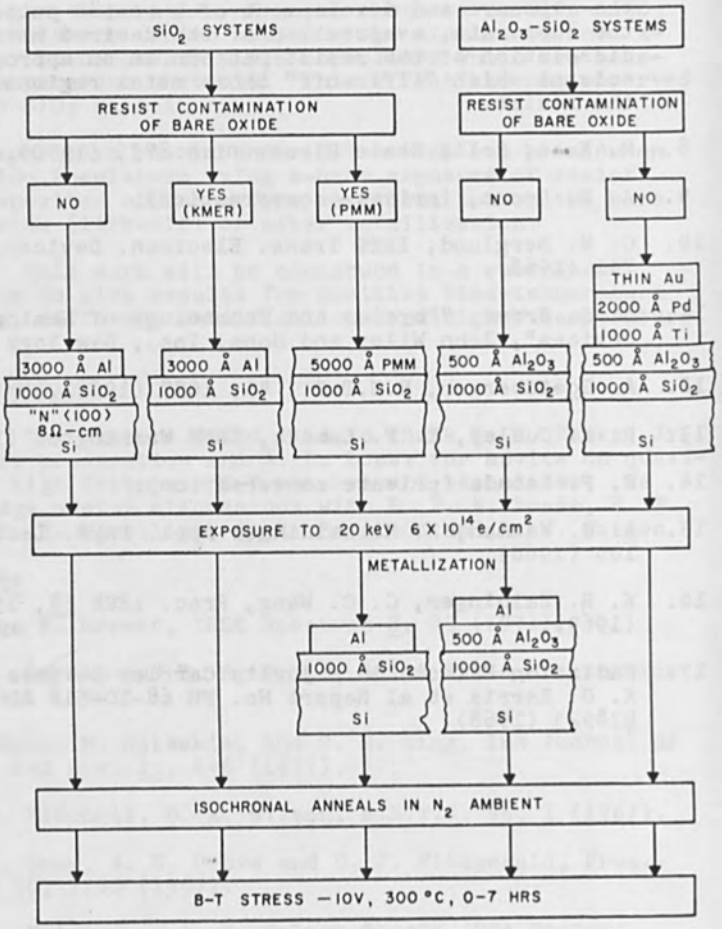

Fig. 1 Flow diagram of experimental procedure.

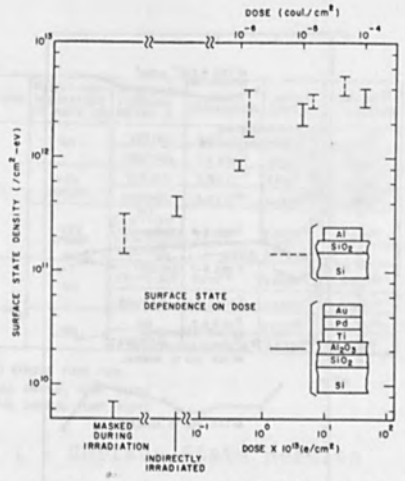

Fig. 2 Average Surface State Density vs Dose for Single and Double Insulator structures. Also shown are the results for unirradiated controls masked during irradiation and capacitors indirectly irradiated.

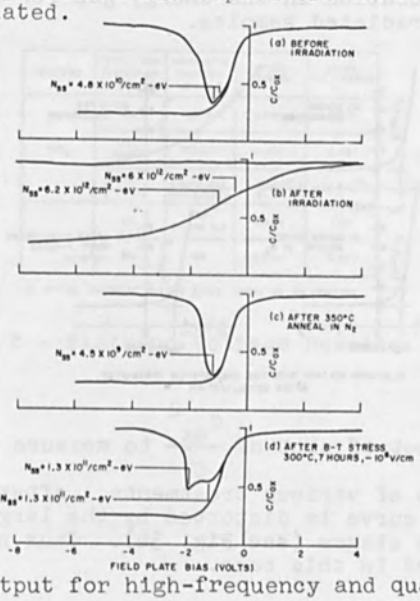

Fig. 3 C-V output for high-frequency and quasi-static curves.

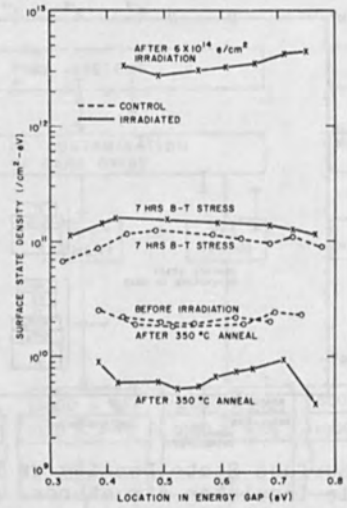

Fig. 4 Variation in Surface State Density as a function of location in the energy gap for irradiated and unirradiated samples.

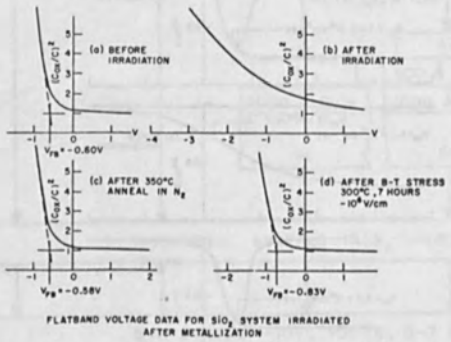

Fig. 5 Output of plot of $\frac{C_{ox}^2}{C^2}$ to measure V_{FB} as a function of various treatments. After irradiation the curve is distorted by the large number of surface stages (see Fig. 3b). Thus no V_{FB} is determined in this case.

SYSTEMS	RESIST CONTAMINATION OF BARE OX.	IRRADIATED THROUGH METAL ?	AFTER IRRADIATION	AFTER ANNEAL	AFTER ① B-T STRESS
SiO_2	NO	YES (Al)	3.5×10^{12}	$\leq 6 \times 10^{9}$ ②	1.2×10^{11}
		CONTROL	2.2×10^{10}	2×10^{10} ②	1.0×10^{11}
	YES (KMER)	YES (Al)	2.6×10^{12}	8×10^{9} ②	7.6×10^{10}
		CONTROL	3.0×10^{10}	1.3×10^{10} ②	9.8×10^{10}
	YES (PMM)	NO (LIFT-OFF TECHNIQUE)	4.5×10^{12}	3.8×10^{10} ②	1.3×10^{11}
		CONTROL	NOT APPLICABLE		
Al_2O_3-SiO_2	NO	YES (Ti-Pd-Au)	4×10^{12}	$\leq 6 \times 10^{9}$ ③	3.5×10^{10}
		CONTROL	$\leq 6.5 \times 10^{9}$	$\leq 6 \times 10^{9}$ ③	3.8×10^{10}
	NO	NO	3.3×10^{12}	$\leq 6 \times 10^{9}$ ③	3.9×10^{10}
		CONTROL	1.2×10^{10}	8.6×10^{9} ③	3.1×10^{10}

① B-T STRESS TIME 7 hrs
② FINAL ANNEAL TEMP. 350°C
③ FINAL ANNEAL TEMP. 450°C

Table 1 - Surface State Results

SYSTEMS	RESIST CONTAMINATION OF BARE OX	IRRADIATED THROUGH METAL ?	AFTER ANNEAL	AFTER B-T STRESS
SiO_2	NO	YES (Al)	0.08V	-0.01V
	YES (KMER)	YES (Al)	0.09V	-0.08V
	YES (PMM)	NO (LIFT-OFF TECHNIQUE)	-0.66V*	-0.61V*
Al_2O_3-SiO_2	NO	YES (Ti-Pd-Au)	-0.15V	1.5V
	NO	NO	-0.08V	0.62V

* ACTUAL VOLTAGES QUOTED SINCE THERE IS NO CONTROL.

Table 2 - Flatband Voltage Results

PROFILING A HIGH POWER DENSITY ELECTRON BEAM FOR PRECISION THERMAL MACHINING

Walter W. Koste and Walter Bojman

IBM Components Division
East Fishkill Facility
Hopewell Junction, New York 12533

A mechanical beam attenuator is used to reduce beam current density temporarily for analysis without altering any beam-generating parameters. This attenuated, non-destructive EB is then analyzed in the target plane using a pinhole beam analyzer with a CRT display. Precise adjustment and measurement of the beam's shape, focus, diameter, current density distribution, and position are possible.

Examples of beam profiling are shown; this beam-profiling method is essential for making thermal machining a predictable, reliable, and precise process.

INTRODUCTION

Numerous thermal EB machining applications have been demonstrated. The quality of the machining depends mainly on beam-current density distribution in the target plane (1,2,3,4). In an electron-optical system, however, some beam defects cannot be avoided. The positional instability of the electron emitter at high operating temperatures is a major contributor to random defects. It is doubtful that a thermal EB machine can be designed, operated, and maintained with long-term stable beam characteristics.

If this process is to find production applications demanding predictable, consistent results and high pattern accuracies, a method is needed for characterizing and adjusting the beam cross-section in the target plane prior to its application on the target. The precise beam position must also be measured periodically for accurate target registration. The destructive nature of the high-power beam precludes convenient analysis and subsequent correction of the beam defects. Previously reported work employs a flyby knife edge, slit, wire, or hole and is mainly useful for beam focusing (4, 5, 6).

A new method for characterizing the beam conveniently in the target plane is described. A mechanical beam intensity attenuator is inserted in the beam path for characterization. The attenuator greatly reduces the beam current density and renders it non-destructive to the analyzing element in the target plane.

To characterize the attenuated beam, a pinhole detector is mounted in the target plane. The electron beam raster scans the area surrounding the pinhole in synchronism with a raster scan on a CRT. The instantaneous beam current detected under the pinhole modulates the intensity of the CRT spot. In this way, a magnified image of the beam cross-section at the pinhole (target plane) is displayed on the CRT for convenient analysis. The pinhole signal is further processed; isograph lines representing loci of constant beam current densities are superposed on the image. The result is a set of curves forming a three-dimensional graph of the beam cross-section. This display permits accurate measurement of the size, circular symmetry, current density distribution, and peak current density of the beam. The experimental work was carried out with a modified Zeiss EB cutting machine Model BFM-100.

The following topics will be discussed:

1. Experimental setup
2. Thermal considerations.
3. Beam analysis.
4. Melt marks versus beam cross-sections.

EXPERIMENTAL SETUP

A schematic of the electron beam apparatus is shown in Fig. 1. The main components in the electron optical column are a tungsten hairpin filament, beam centering coil, stigmator, blanking plates, aperture, focusing lens and deflection coil.

The beam attentuator (a key element for beam analysis) is located under the deflection coil and can be manipulated from the outside of the work chamber. The attenuator element is a 100μm thick Mo sheet with an array of small holes. This element is clamped in the massive attenuator arm which serves as a heat sink. The beam attenuation factor (α) is defined as the ratio of total beam current (I_b) to attenuated beam current ($I_{\alpha b}$). α can either be measured with a Faraday cage or calculated. For example, an attenuator having 25μm dia. holes on 125μm centers has an attenuation factor

$$\alpha = \frac{(125\,\mu\text{m})^2}{\pi/4\ (25\mu\text{m})^2} = 32.$$

On the X-Y stage a reference plate is fixed at a convenient height. The bottom surface of the reference plate is defined as the target plane. A target and a pinhole element are mounted against the bottom of the plate to assure precise coplanar location of both. The pinhole element is a 50μm

thick Mo sheet with a single 10μm dia. hole in it. Acceptable resolution for beam analysis is achieved when the beam diameter is more than 3X the pinhole diameter. An electron collector plate under the pinhole monitors the transmitted beam current (i_a). As the relatively large beam cross-section sweeps over the small pinhole, the instantaneous beam curent density is

$$j = \alpha \frac{i_a}{(\pi/4)\, d_p^{\,2}} \quad (A/cm^2),$$

where i_a is the transmitted fraction of the attenuated beam current (in amps); d_p is the pinhole diameter in cm. Since α and d_p are fixed quantities of the apparatus, j is determined simply by measuring i_a.

The beam analyzer consists of an X-Y deflection system and isograph generator (Fig. 2). The deflection system is an asynchronous raster pattern circuit; the horizontal line rates can be varied from 40 to 300 lines/sec and the vertical sweeps from 2 to 6 per second. This produces a raster of 20 to 50 lines. Experience shows this to be adequate for the application, while minimizing circuit complexity. Each horizontal sweep line is accompanied by a beam ON signal; during the intervals between sweeps the beam is disabled. Thus, a low duty cycle is maintained, keeping the average beam power input to the pinhole element low.

The deflection signals are applied simultaneously to the deflection coil of the beam and to the X and Y inputs of the CRT display unit. The instantaneous beam current through the pinhole is amplified and applied to the Z-input of the CRT with suitable signal levels. Thus, the CRT screen displays an image of the beam's current distribution in the target plane. The polarity is chosen so the brightest point on the screen corresponds to the highest intensity point of the beam.

This is one of several recognized methods for displaying the shape of an electron beam. While it permits a qualitative evaluation of intensity distribution, resolution suffers, and the skirt zone of the beam, i.e., the steepness of the edges, cannot be adequately characterized quantitatively.

By further processing the display, quantitative, three-dimensional information is obtained through the isograph generator which displays on the CRT screen a family of curves representing loci of constant beam current density. For convenience four curves were chosen; the current density corresponding to each curve is known. The visibility of the curves is much better than that of the beam itself because the curves are produced at CRT saturation level.

The isograph circuit consists of a bank of high-speed voltage comparators. The current detected through the aperture of the analyzer is amplified and applied to the comparators. As each comparator detects the signal crossing, a short pulse is generated. All the pulses are OR-connected and mixed with the pinhole signal before applying the combined signals to the CRT display unit. The pinhole current amplification factor and the CRT display magnification factor are variable and are calibrated for convenient measurement of beam current density and diameter.

THERMAL CONSIDERATIONS

During beam analysis the attenuated beam raster scans a small area surrounding the pinhole (~4x4 beam diameters). Since the beam is focused on the pinhole element its intensity must be sufficiently attenuated to prevent destruction of the pinhole element. The tolerable peak beam power density (P_o) can be calculated using an expression for EB heating a thin foil with conduction losses (7). Modified for convenience,

$$P_o = \frac{52.5\ R\ kT}{\ln\left(\frac{16Kt}{d^2} + 1\right)} \quad \text{in W/cm}^2,$$

where
- R = Electron penetration range (cm).
- k = Thermal conductivity [cal/(cm sec ^oK)].
- T = Temperature rise above ambient (^oC).
- K = Thermal diffusivity (cm^2/sec).
- t = Beam on-time (sec).
- d = Beam diameter (cm).

For this analysis R = 15μm in Mo at 100kV, T = 2590^{o}C to reach the melting point of Mo, d = 30μm, and t = 60μsec beam dwell time at the practical sweep speed of 100μm/200μsec. With the above values,

$$P_o = 2.5 \times 10^6\ \text{W/cm}^2$$

and the current density (J_o) at the center of the beam spot is:

$$J_o = \frac{2.5 \times 10^6\ \text{W/cm}^2}{10^5\ \text{V}} = 25\ \text{A/cm}^2.$$

This is a worst-case analysis because some of the beam energy is reflected and the pinhole element is thicker than R. Therefore, a well heat-sinked Mo pinhole element can be raster scanned safely at $J_o < 25A/cm^2$.

A typical cutting beam may have $J_o = 250A/cm^2$. If an attenuator with $\alpha = 20$ is inserted in the beam path, the intensity at the pinhole element is reduced to a harmless $J_{o\alpha} = 12.5A/cm^2$. Although the attenuator usually absorbs more than 90% of the beam's power, excessive heating can be prevented easily if the attenuator is well heat-sinked and located where the beam cross-section is relatively large.

BEAM ANALYSIS

For the following beam analysis beam conditions were: accelerating potential $E_a = 10^5V$; beam current $I_t = 1.0mA$ (measured at the target in a Faraday cage); focal length f = 12.5 cm, pinhole diameter $d_p = 10^{-3}cm$, and the attenuation factor $\alpha = 17$. The attenuator was located 3.3cm above the target plane.

Figures 3(a) and (b) are a profile and an isograph of a beam's cross-section. Pinhole current amplifier gain is adjusted until the inner circle is reduced to a point. This permits instant reading of J_o from the calibrated gain potentiometer. The four loci of constant current densities (toward the beam center) correspond to $0.25J_o$, $0.5J_o$, $0.75J_o$, and J_o. Depending upon the application, beam diameter may be defined, for example, at $0.25J_o$. Line broadening is a measure of beam jitter -- the sum effect of electric noise and stray magnetic fields. Finally, the oval beam shape is immediately apparent on the isograph, but not on the profile display. Therefore, the isograph is the preferred display of all pertinent beam characteristics.

The effect of beam focusing is demonstrated in Fig. 3(c). A reduction of only 0.3% in the lens excitation current resulted in the shift from 3(b) to 3(c). $J_o = 190\ A/cm^2$ for both focus conditions. Adding the stigmator, the beam in Fig. 3(d) was obtained with beam current density increased to $J_o = 220\ A/cm^2$.

This analysis reveals the profound effect of focusing and astigmatism adjustment on the beam's shape and current density distribution; it also demonstrates that a beam of $P_o = 2.2 \times 10^7\ W/cm^2$ can be analyzed conveniently.

MELT MARKS VERSUS BEAM CROSS-SECTIONS

The following experiment tested whether the cross-section of the attenuated beam remains unchanged when the attenuator is withdrawn. First, the isograph of a particular beam cross-section was obtained and then a Mo target was positioned under the beam. The target was mounted coplanar with the pinhole element. With the attenuator withdrawn, one 6-μsec beam pulse

was released to form a melt mark on the target. Four beam isographs with lens excitation increased in 0.3% steps and the corresponding melt marks are shown in Fig. 4.

The results demonstrate that the cross-sections of the attenuated and corresponding full beam are not identical in shape. However, each isograph does match the melt mark at 0.3% higher lens excitation; for example, isograph (a) matches mark (b), etc. This means the anomaly between the attenuated and the full beam can be compensated for simply by increasing the lens excitation by a predetermined amount or by mounting the pinhole element slightly above the target plane.

The observed focusing shift may be attributed to electron-electron interactions. With the attenuator in place, the smallest beam cross-section is in the target plane; beam current is reduced by a factor of 20 between the attenuator and the target plane. As the attenuator is withdrawn the electron-electron interactions in the full beam produce a divergent effect on the beam, shifting the smallest beam cross-section below the target plane. To counteract this effect more lens excitation is required. This condition is in agreement with the experimental results.

During the thermal machining process the plasma generated may have a focusing effect on the beam. This and any other machining effects are not the subject of this paper. Whatever influences the beam during application on the target (for example, plasma generation), presetting the beam characteristics is essential for achieving predictable and consistent results. Therefore, the usefulness of the beam analyzer is not impaired.

CONCLUSIONS

Leaving all beam-generating parameters fixed, a beam of $J_o = 220 A/cm^2$ was reduced in intensity to $J_{o\alpha} = 13 A/cm^2$ by inserting a mechanical attenuator in the beam's path. With a pinhole beam analyzer the attenuated beam cross-section in the target plane was displayed as a magnified isograph on a CRT. The beam's shape, diameter, current-density distribution, and peak current density were obtained conveniently from the isograph. The effects of focusing and of astigmatism correction on the current density distribution were demonstrated. The effect of electron-electron interactions in the high current density beam was compensated by a slight increase in lens excitation.

This work is limited to demonstrating the capability of characterizing an otherwise destructive high power density electron beam. The advantages of this method are:

1. The high power density can be reduced without altering the beam generating parameters;
2. The reduced-intensity beam can be analyzed conveniently.

This method is valuable for presetting beam characteristics to achieve predictable thermal effects repeatedly as well as target registration with a high power density beam. It is also a useful tool for basic studies of thermal machining as a function of beam characteristics.

ACKNOWLEDGMENTS

The authors wish to thank A. J. Juras, Jr. and P. Reichert for their assistance, and H. Pfeiffer for his valuable comments on the electron optical effects.

REFERENCES

1. S. Schiller, et al., "On the Behavior of Electron Beams in Weak Vacuum," Fourth Int'l. Conf. on Electron and Ion Beam Science and Technology, R. Bakish (Ed.), Electrochem. Soc. Inc., N.Y., 1970.
2. K. H. Steigerwald, "New Developments in EB-Drilling and Perforating Processes," 10th Symposium on Electron, Ion and Laser Beam Technology, L. Marton (Ed.), San Francisco Press, Inc., Calif., 1969.
3. M. Boncoeur, et al., "The Influence of Electron Beam Focusing on the Shape and Dimensions of Welds in the EB Welding Process," Third International Conference on Electron and Ion Beam Science and Technology, R. Bakish (Ed.), Electrochem. Soc., Inc., N.Y., 1968.
4. A. Matting, G. Sepold, "Basic Research on Welding with Electron Beams of High Intensity," Third International Conf. on Electron and Ion Beam Science and Technology, ref. cit.
5. E. B. Bas, G. Cremosnik, "Experimental Investigations of the Structure of High Power Density Electron Beams," First International Conference on Electron and Ion Beam Science and Technology, R. Bakish (Ed.), J. Wiley, N.Y., 1965.
6. D. J. Sandstorm, "The Relationship of Beam Parameters to Weld Geometry in Electron Beam Welds," Fourth International Conference on Electron and Ion Beam Science and Technology, ref. cit.
7. Tung-Po Lin, "Estimation of Temperature Rise in Electron Beam Heating of Thin Films," IBM J. Res. Dev., Sept. 1967, pp. 527-536.

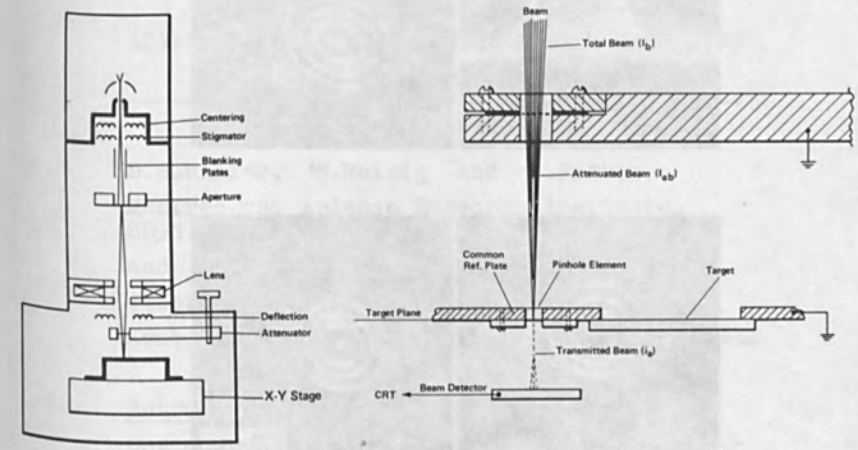

Fig. 1. EB apparatus:
(a) Over-all diagram
(b) Relative positions of attenuator, pinhole, target and beam detector.

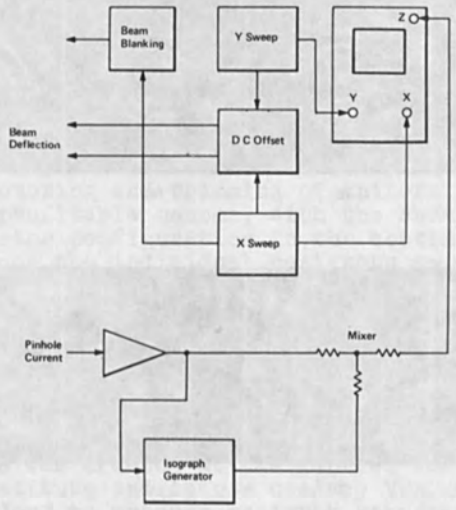

Fig. 2. Beam analyzer schematic.

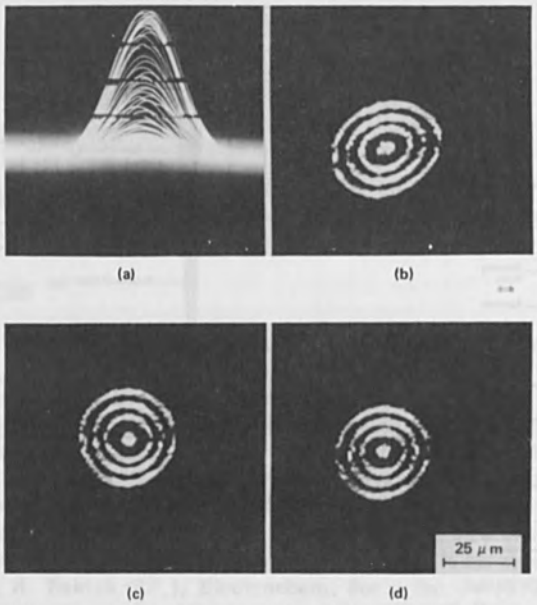

Fig. 3. Beam cross-section CRT displays:
(a), (b) 190A/cm^2; (c) 190A/cm^2; (d) 220A/cm^2.

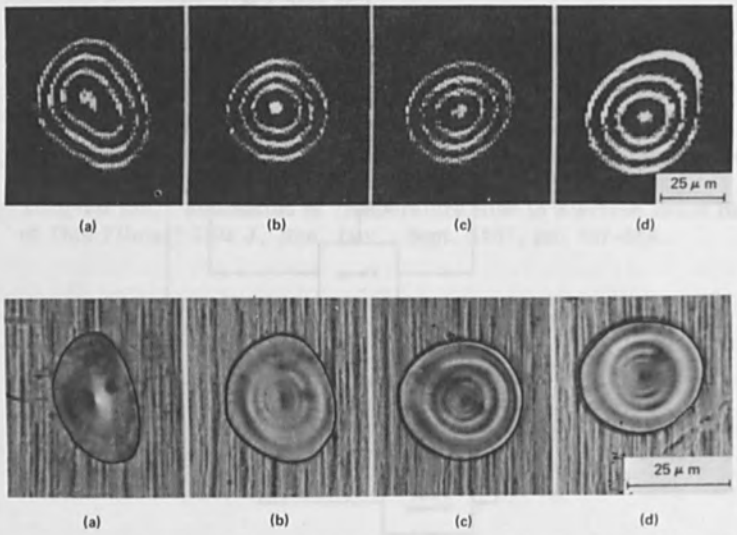

Fig. 4. Beam cross-section isographs and associated melt marks. Lens excitation increased in 0.3% steps. Current densities (A/cm^2):
(a) 140, (b) 190, (c) 180, (d) 130.

ADVANCES OF THERMAL ELECTRON BEAM MACHINING OF THIN-FILMS

S.Schiller, U.Heisig and S.Panzer -
Manfred von Ardenne Research Institute,
8051 Dresden, GDR
and
J.Henneberger -
Kombinat VEB Keramische Werke Hermsdorf, GDR

1. Introduction

One conventional method to produce resistor networks for thin-film hybrid circuits is the directed coating through masks. Wherever the usual tolerances of resistance values inherent to this process (about 5 per cent) are still insufficient, coating is followed by trimming through fine sand-blasting, sparking as well as laser and thermal electron beam processing. Principally, however, working speed of the first three processes is restricted to less than 1 cm/sec., and trimming can be used only in conjunction with the structured coating of resistive films. Hence, resistor configuration has to be shaped already prior to trimming; e.g., by coating via masks.

Therefore, only thermal electron beam processing will permit structuring and trimming of uniformly deposited films in a profitable manner; with the beam used to scribe the resistor configuration in the continuous film, and to balance the individual resistors to desired values.

All advantages emerging from this concept brought about advanced thermal electron beam processing of thin-films for resistor networks [1, 2, 3, 4]. One essential step with regard to the introduction of this process in modern technology is the development of automated 'air--to-air' electron beam processing plants [5]. Equipment of this type was created at the Manfred von Ardenne Research Institute and is now used by VEB Keramische Werke Hermsdorf to produce resistor networks for thin--film hybrid circuits.

Characteristic of the state of art hitherto found in practice are the following parameters: beam deflection velocity $\leq$ 1 m/sec., max. deflection $\lessapprox$ 25 mm, accuracy of alignment $\lessapprox$ 0,3 mm, trimming accuracy 1 to 2 %, range of resistance values 100 ohms to 1 kohm.

Experience with actual processing plants has shown that advanced thermal electron beam technology is likely to increase the technical and economical parameters of this process still further. Moreover, it was felt desirable to investigate the various possibilities of using the electron beam also with respect to other tasks in the manufacture of resistor networks. In the course of development, thermal electron beam processing of thin-films reached a new stage, the results of which shall be described in the following chapters.

2. Progress in Thermal Electron Beam Machining

2.1. The new Stage of Electron Beam Equipment

Essentially, a plant of this type comprises the electron gun for creating a precise electron probe as well as the associated power supply and vacuum equipment. Starting from a **Model** ESB 80/200 Electron Beam Processing Plant of VEB **Elektromat**, further development took place in close cooperation with the manufacturer; aiming at larger maximum deflection, increased working speed, improved long-term stability and perfected reproducibility of the electron probe.

2.1.1. Electron Gun and Beam Deflection

Extending the image width of the projecting lens to 250 mm was the precondition for employing a new deflecting system with an increased max. deflection. An 8-coil singlelayer Schlesinger System has been used as deflecting unit which - due to the selected winding mode - enables both simple and efficient compensation of deflection distortion and astigmatism. Moreover, the set-up permits precise directional allocation of deflections both mutually as well as relative to the working plane.

This simple yet precise directional deflection control is achieved electrically by superimposing components of the deflection current of the individual coil pairs.

In one direction, this will yield a maximum deflection of 60 mm. After distortion correction, the still remaining deflection linearity error can be further re-

duced with the aid of electronic deflection current correction. Referred to maximum deflection, this will result in a relative residual error of $\leq 2 \cdot 10^{-4}$.

Another advantage of this specially designed deflection system is the high cut-off frequency which - in spite of the mentioned high maximum deflections and only minor deflection errors - enables a working speed of $\leqq$ 2 m/sec. with freely programmable processing structures.

2.1.2. Long-Term Adjustment Stability

The special design of the electron source brought about high long-term stability of electron gun adjustment. To approach this goal, direct mechanical connection had to be established between anode, control electrode and cathode, using suitable insulators for this purpose. This further results in superior stability of the electron current which passes the aperture diaphragm. Altogether, positioning adjustment features such a stability that corrections will be needed only after more than 4 hours. Within this period, drift of the working current will remain well below 2,5 per cent.

2.2. Extended Electron Beam Utilization in Thin-Film Processing

Workpiece-adapted loading and transfer facilities, pressure drop systems and digital process control systems for programmed electron probe control with respect to timing and location - as well as for additional operations - have been incorporated in electron beam processing plants to create modern production tools of extended applicability in the fabrication of resistor networks. Further efforts were concentrated on improved process parameters to open up new opportunities in the field of thin-film processing.

2.2.1. Range of Resistance Values and Trimming Accuracy

Possible spans of resistance values and attainable trimming accuracy are among the most essential process parameters. Here the use of programmable, selective measuring assemblies for high and low resistance levels now enables to cover a balancing range of $\leq$ 1 ohm to $\leqq$ 1 Mohm. Improved high-speed measuring equipment further contributes to take full advantage of the high trimming accuracy even at increased deflection velocities. Belancing is also improved by means of special

two-stage coarse and fine trimming. Coarse trimming, on the one hand, takes place at a high rate of resistive changes needed for structuring. Fine trimming, on the other hand, is made close to the earthed contact of the resistor to be balanced, and performed practically without any change in resistivity; i.w., generally at a rate of rise which has been reduced by about 10 to 100 times. Coarse and fine trimming, however, will be performed at the same deflection velocity.

Fig.1 serves to illustrate 2-stage coarse and fine trimming by way of an example regarding the fabrication of resistors by meandering between two contact fields.

After machining the marginal lines, which determine the resistor area, structuring is effected by scribing a meander geometry in the resistive film. Within the prospective range of coarse trimming, machining takes place with the measuring equipment turned on until the resistance level closely approaches the desired value. This is followed by scribing fine trimming lines which will narrow down the nonstructurized residual resistor area. In this way it is solely the arrangement of processed lines which reduces the rate of rise in resistance as required.

Typical process-inherent tolerances in the aforementioned span of resistance values are ± 0,5 per cent for coarse trimming and less than ± 0,1 per cent for fine balancing.

2.2.2. Alignment Accuracy

Another decisive parameter - which determines both surface utilization and possible degree of network integration - is the alignment accuracy of processing structures. Here this accuracy means the precision with which the structure can be processed relative to structures already contained on the substrate or workpiece. The given alignment accuracy depends on the tolerances used in fixing the substrate with respect to a given working location. Moreover positioning accuracy of the conductive tracks and contact structures relative to the target edges as well as the drift of deflection currents definite had a bearing on alignment accuracy. Without resorting to special means, the latter amounted to 0,3 mm.

Application of the electron beam as working tool may still be expanded by using it to check workpiece positioning prior to machining. Secondary effects will occur as soon as the beam impinges on the target.

Because the emission of secondary electrons from a tin track differs from that of a thin NiCr film on glass by a factor of about 4, it will be possible to distinguish between thin track structures and NiCr films simply by scanning the target with the electron beam. Naturally, any change in the flow of secondary electrons will also have a certain bearing on the current drain at the substrate to be processed. This alteration has been used to carry out comparisons between the desired and actual characteristic coordinates of track structures on the target, and to obtain a dead match between the coordinate system of the programmed structure and the actual position of the conductive track. This is accomplished electronically, eliminating the difference between desired and actual electron beam position on the workpiece by resetting the deflection currents accordingly. Special compensation of this type needs no computing operations to determine correction values and automatic positioning (cp. Fig. 2) permits to perform the following corrections: -

X - zero position
Y - zero position
X - amplitude
Y - amplitude
φ - shifting of deflection directions.

Execution of a complete positioning programme for one resistor network will take about 50 milliseconds.

This mode of automatic positioning resulted in an alignment accuracy within the entire working area which is equal to the focal spot diameter (e.g., 30 µm) when producing resistor networks with the aid of thermal electron beam processing.

It is a special advantage of the described positioning mode that the actual conductive track and contact structures are used to determine the correction values. Hence, there is no need to apply additional positioning marks to preselected locations of the workpiece.

Apart from improved surface utilization of the resistive film and the increase in the possible degree of network integration obtained as a direct consequence of automatic positioning, there are still two more advantages which shall be cited here.

With a given tolerance gap between conductive track and processed structures, rejects due to faulty positioning of the processed structure are reduced to a minimum.

Including the drift of the deflection in the correction process not only reduces the requirements with respect to longterm deflection stability but also eliminates the rather complex layout needed to control the deflection currents electronically and temperature compensation of the power supply as well.

2.2.3. Integrated Machining

A decisive increase in productivity was obtained through integrated processing of large, divisible substrates by introducing electron-mechanical step-and--repeat techniques where the beam processes about 10 to 100 resistor networks on one and the same substrate.

Controlled by an electronic step of the processing programme, and without mechanical repositioning of the target, the resistor networks covered by a maximum deflection of 60 mm are processed one after the other. When one network is processed, the d.c. level is used for repositioning the deflection and to repeat the run of the processing programms for the following network.

After all networks within reach of the maximum deflection are processed, a mechanical step rectangular to the said electronic step will index the hitherto untreated sub-areas in the coverage of the beam. Then the electric step-and-repeat system takes over again to handle these sub-areas in a similar manner. Shifting speed of the mechanical step is as high as 100 mm/sec. because the mechanical limit positions have to be approached with tolerances of only about 0,1 mm. The latter are then eliminated in the course of automatic positioning.

3. A New Generation of Automatic Electron Beam Processing Plants for Thermal Thin-Film Machining

The described developments in equipment and the extended technological opportunities of electron beam application in the field of thin-film processing have been incorporated in an advanced automatic electron beam processing plant.

Fig.3 gives the overall view of the new unit. Shown on the left is the electron beam processing device with workpiece-adapted magazine and transfer system. On the right is the process control unit with cycle controlling monitor.

In the fabrication of resistor networks, the automatic electron beam processing plant will handle the following tasks:

- Automatic positioning
- Dividing the resistor surface in sub-areas
- Generating the resistor structures
- Resistor trimming
- Tolerance checking of resistors
- Insulation testing of mutually separated resistors
- Labelling with respect to quality and type.

From these seven processes, five may be handled by the beam directly. Referred to a typical 10-resistor--network of about 2 cm^2 surface it takes only about 0,6 sec. to handle all these processes.

Fig.4 shows an electron-beam-processed substrate of 60 mm x 100 mm prior to subdivision in a total of 30 single circuits. Here the cycle time inclusive of transfer, loading and other non-machining times only amounts to about 30 sec.

With its technical and economical parameters, this recent development represents a new generation of electron beam systems for processing thin-film components.

Practical application raised the fabrication of resistor networks to a higher and more favourable technological level and opens up new opportunities for components of this type.

References

[1] H. Kimura, H. Tamura, K. Ikegami and K. Sakashita
"Fabrication of Microelement Resistors by Electron Beam, Their Characteristics" in R. Bakish "Electron- and Ion-Beam-Science and Technology", John Wiley and Sons, Inc., New York 1965, p. 283

[2] D.J. Garibotti, L.R. Ullery
"Production-line packaging of solid state circuits"
Electronics, Sept. 7, 1964, p. 73

[3] M. von Ardenne, U. Heisig, S. Panzer, O Thieme, J. Henneberger
"Automatisiertes Elektronenstrahl-Abgleichen von Dünnschichtwiderständen mit kontinuierlichem Durchlauf der Bauelemente durch die Bearbeitungskammer"
in J. Berghammer, Microminiaturization, JFAC/JFJP, Symposium, Okt. 1965, München, Oldenbourg Verl. 1966, p. 533

[4] M. von Ardenne, U. Heisig, S. Panzer, K. Jessat, G. Bahr and H. Döhler
"Continuous Electron Beam Processing Plant for Plane Thin-film Resistors"
Microel. and Reliab. 5 (1966), p. 255 - 263

[5] M. von Ardenne, S. Schiller, U. Heisig
"Automated electron beams process thin-film components"
Electronics/March 7, 1966, p. 110 - 115

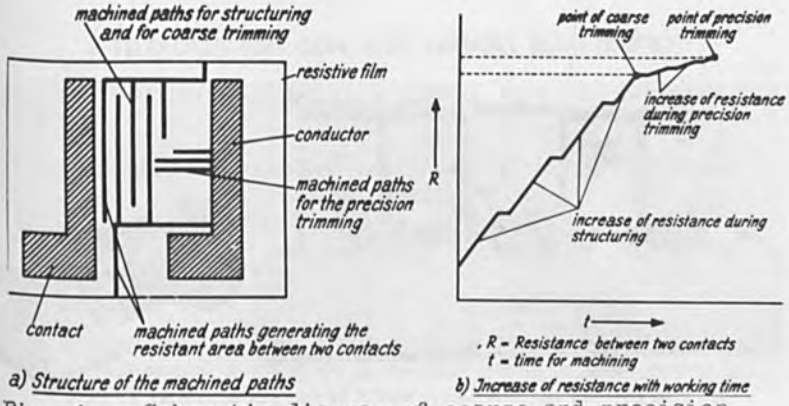

Fig. 1 : Schematic diagram of coarse and precision trimming

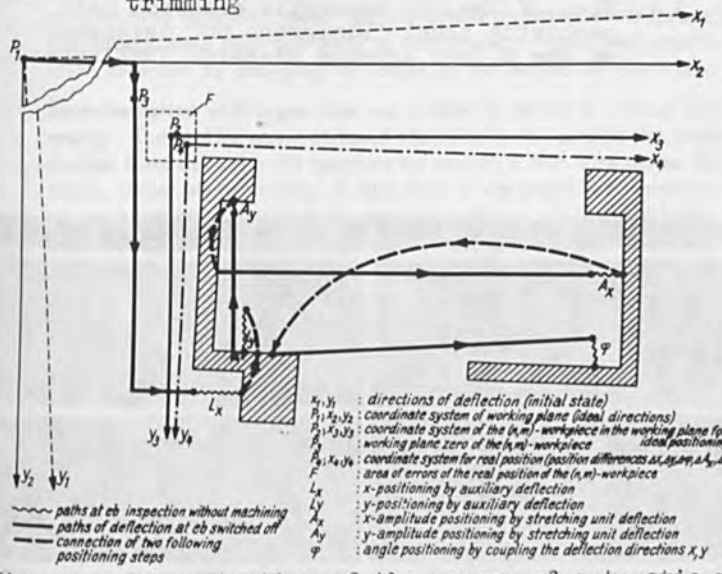

Fig. 2 : Demonstration of the course of automatic positioning for a real structure with position difference. The real structure in a partial area of the total working plane is machined by an electrical step- and repeat-technique with (n, m) workpieces. Shown is the course of deflection (-line) and the correction (~~ -line) during the positioning program.

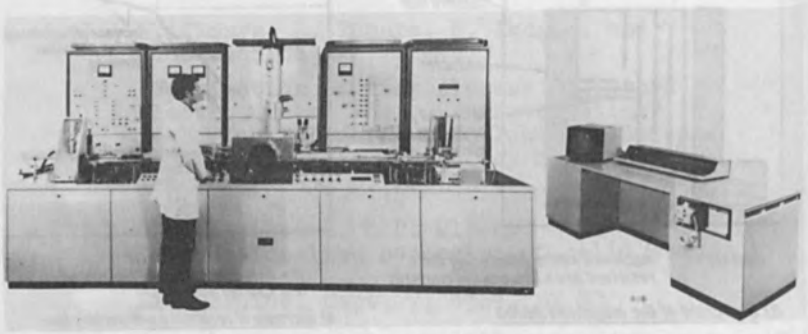

Fig. 3 : View of the new automatic electron beam machining plant "Elmigraph 60" developed of the M. von Ardenne Research Institute

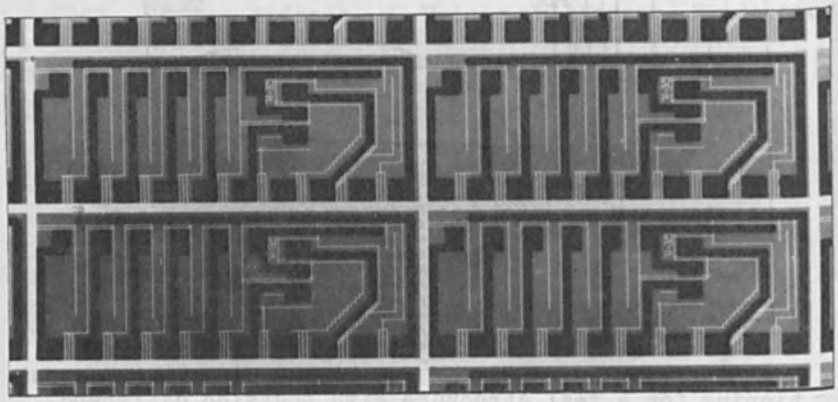

Fig. 4 : Part of an extended electron-beam-processed substrate of 60 x 100 mm^2 area with 24 single thin film circuits

A TELEFOCUS ION GUN WITH VARIABLE BEAM PROFILE

K. Wittmaack and F.Schulz

Gesellschaft für Strahlen- und Umweltforschung mbH München
Physikalisch-Technische Abteilung
8042 Neuherberg, Germany

ABSTRACT

The influence of extraction gap distance, extraction potential, and current density on the shape of the beam profile has been studied in a 50 kV telefocus ion gun of triode type. The gun consists of a hot cathode PIG source, a movable extraction cup electrode, and an acceleration tube electrode. The extraction potential could be varied through more than one order of magnitude at fixed final acceleration potential by changing the length of the extraction electrode.

Beam formation with argon ions was studied in detail at a fixed final energy. The profile was monitored electrically far outside the acceleration field behind a slit aperture by moving a thin wire across the beam. Under all conditions of operation it was possible to produce an ion beam and focus it at the monitor position. At low and high beam currents, however, distortions usually occurred on the profile which could only be removed in the low current case by increasing the extraction gap distance. Under well-defined conditions it was possible to produce ion beams with constant current density over about 60% of the beam diameter. This operation mode has been used successfully for large area of ion implantation and sputtering.

Work supported by grant of the German Federal Ministry of Education and Science within the frame of the Technology Program.

1. INTRODUCTION

The wide spread interest in ion implantation which rose remarkably during the last decade has again focused the attention of scientists at a detailed study of the properties of ion accelerators in the 100 kV range /1,2/. Although there is a general agreement as to the principles of accelerator design the details of construction differ markedly. The reason for the difference in construction is that most of the components which are combined to produce a current of some sort of ions of a certain energy at a given target position can in principle be arranged in a more or less arbitrary way.

There is only one detail that is found to be uniform in nearly all machines: the arrangement of electrodes for ion extraction and first focusing. This primary step of beam formation is usually achieved by an extraction electrode at a potential of about 50 kV with respect to the ion source followed by an einzel lens which serves to focus the beam diverging after extraction (fig. 1a). The extraction gap distance is of the order of 50 mm in that case.

Ion guns of this type have been studied thoroughly in isotope separators /3,4/. They have probably been used so far with only very few exceptions /5,6/ because a high extraction potential at a first glance seems to favour the production of high current density beams. This is, however, not supported by the space charge law /7/. On the contrary, as Chavet and Bernas /8/ have already pointed out the opposite might be true. If one combines the space charge law and the experimentally determined voltage dependence of the critical distance for electrical breakdown /9/ to estimate the maximum ion current I_m obtainable at a given extraction gap distance d one finds that I_m is proportional to 1/d. Hence it should be advantageous for high current density beams to use a seperate extraction electrode at a low potential V_1 close to the ion source exit followed by an acceleration electrode at a high potential V_2 (fig. 1b).

Before such a system can be realized experimentally some general considerations seem to be necessary. Beam formation in an ion gun of this type takes place in two steps which depend upon each other because the extraction potential determines both the conditions for ion emission from the source and the ion optics of the immersion lens constituted by the acceleration stage.

The lens parameters are well-known in case of long coaxial double cylinders of equal diameter D /10/. These data can be applied in the present study to calculate approximately the potential ratio V_2/V_1 necessary for focusing at different extractor length L (fig. 2). In the range of interest, i.e. for $V_2/V_1 > 10$, this does not seem to be difficult since the lens data change only slightly with increasing V_2/V_1 /10/. If one assumes that for proper focusing of the beam the focal point F_1 on the low potential side should lie within the extractor than the lower limit of extractor lenght is estimated to range from L/D = 1.0 to 1.6 for V_2/V_1 between 50 and 10. In view of the uncertainties as to the true ion optics in the acceler-

ation space it seems to be reasonable, however, to allow the extractor length to be varied in a larger range, i.e. between about L/D = 0.8 and 1.8.

A somewhat more complicated situation exists in the extraction region if the ions are supplied by a plasma in a gas-discharge source which is usually the case. Position and shape of the ion emitting plasma surface are not fixed but depend upon all the parameters of the discharge, the extraction potential, and the shape of the surrounding metal electrodes /3,8,11/. The shape of the plasma boundary has a strong influence on the trajectory of the ions since they leave normal to the surface.

As the current from the plasma is diffusion-limited and hence only depends upon plasma density and temperature, position and shape of the plasma boundary at a given extraction geometry may roughly be estimated from the space charge law. If one assumes that beams of a certain quality can only be achieved at some optimum plasma surface shape, one consequently has to adjust the extraction potential in each case according to the plasma density. The acceleration potential adequate for beam focusing is thus likely to be predetermined in ion guns with low potential extraction electrodes of constant length.

Such a limitation in ion energy or current density also exists in ion guns with an einzel lens. To change the current people normally give up severe requirements as to the shape of the beam profile. Only in very few accelerators current density and extraction gap can be matched at a fixed extraction potential by use of a movable extraction electrode /12/. This flexibility was thought to be necessary also in an ion gun with a low potential extraction electrode because it might allow an adjustment of operating parameters in such a way that an optimum plasma boundary is obtained in a wide range of current density.

The aim of the present investigation was twofold. First a general knowledge of the characteristics of an ion gun with a low potential extraction electrode was tried to be obtained. This included an evaluation of the conditions for the production of beams with distortion-free profiles. Second the capability of such a gun for special purposes was studied. This mainly concerned the possibility to obtain beams with constant current density over a large part of the beam diameter. Such beam profiles are necessary for homogeneous large area sputtering and ion implantation.

2. EXPERIMENTAL

2.1. Construction of the ion source

The ion gun is shown in fig.3. Although the construction is quite simple the apparatus has a high degree of flexibility.

The ion source is a simplified version of the magnetically confined, oscillating electron bombardmet type with hot cathode and extraction of ions parallel to the magnetic field /13,14/. According to Carlston and Magnuson /14/ such a source delivers ions with a low energy spread of only 2 eV. This is of considerable im-

portance in the present case because strong distortions might occur on ion beams with higher energy spread since extraction potentials as low as some hundred volts can be applied. The operating conditions of the ion source were studied thoroughly. Details will be reported elsewhere /15/. For this investigation it is sufficient to note that the source works very stable and allows the plasma density to be changed quite easily by varying the heating current of the filament (0.5 mm diam tantalum wire). The anode voltage was kept low (30 to 40 V in case of Argon) so as at avoid formation of double ionized particles and sputtering of the filament. The magnetic field was usually set at 300 Oe. In this range high gas efficiency can be achieved at a low power consumption. Only 30 W were needed for ion currents of about 100 μA through an ion source opening of 1.5 mm diam.

The length of the extraction electrode could be varied by inserting intermediate rings of different thickness. The 3 mm diam extractor opening was kept fixed during this study. Extractor movement during gun operation was achieved from the ground potential side via insulating shafts. The extraction gap distance could be changed between zero and about 7 mm. The position of the acceleration electrode entrance was changed according to the respective extractor length by withdrawing or inserting the rings used for extractor length variation. The acceleration gap distance g was thus always in the range 3 to 10 mm depending only upon the setting of the extraction gap. All the modifications in connection with extractor length variation could easily be achieved after dismounting the ion source.

The complete ion gun as shown in fig.3 was mounted to a conventional vacuum system pumped by an oil diffusion pump with a baffle-reduced pumping speed of about 200 liters/sec. The background pressure in the system was usually 2×10^{-6} Torr. This increased by only 1 to 2×10^{-6} Torr during source operation with argon.

2.2. Description of the beam monitor

The beam monitor is shown schematically in fig.4. It mainly consists of a beam defining slit aperture (0.4 mm wide) made from 5 mm stainless steel plates and a tantalum wire (0.4 mm diam) each clamped to a slide. The two slides are mobile perpendicular to one another and normal to the beam direction and can be removed sufficiently far off axis so that the beam can pass through without touching them. In that case either position and shape of the beam can be monitored optically on a polished aluminum plate or the beam current can be measured with a Faraday cage. The optical detection was taken as simple means to determine and correct any misalignment of the extraction electrode with respect to the gun axis. Adjustment was necessary after each repeated variation in extractor length because such a change required dismounting of the ion source and the extractor, as already mentioned above.

To measure the profile the slit aperture was placed at the axis of the beam and the wire was moved across that small cut-out. Simultaneously the ion current to

the wire was detected thus producing a mapping of the current density profile. The circular cross section of the beam was checked at a fixed wire position by moving the slit across the beam.

It was tried to measure the ion current to the wire accurately by suppressing the secondary electrons. In that case, however, there was always a small negative background current which probably consisted of secondary electrons produced at the slit aperture. Some of these electrons are likely to be attracted by the space charge of the beam. They will subsequently accompany the ions and may in part be extracted by the positive potential applied to the wire for suppression of the secondary electrons ejected from the wire.

As the background current could not be eliminated without a sophisticated construction it was decided to measure the ion current to the wire without secondary electron suppression. This had the advantage that the measured current increased by a factor of up to about 7 for energies of up to 50 keV thus allowing profile recording without current amplification. The correction factor was determined by comparison with profiles measured at low current density with secondary electron suppression. This factor was checked by a comparison of the integrated current density profile with the total beam current measured with the Faraday cage. Thus it was possible to evaluate true current density profiles.

3. RESULTS

3.1. General behaviour of the beam profile

All experiments reported were done with argon ions. The beam profiles were usually measured in the focused state. With this we mean a setting of the gun parameters at which the current density reaches a maximum on axis at the monitor position. Focusing was achieved at constant ion energy eV_2 by adjusting the extraction voltage V_1. This corresponds to the normal situation in irradiation experiments where the beam current is usually optimized at a certain ion energy. Moreover V_2 was kept fixed rather than V_1 because of the difficulties that might arise from the energy dependence of secondary electron production. In the vast majority of investigations V_2 was set at 40 kV. This energy allowed beam production at ion currents well above 100 μA and at the same time gave proper light intensity for optical beam monitoring.

It was checked that the constancy of V_2 did not influence the principle behaviour of the beam upon a variation of the voltage ratio V_2/V_1. As we shall see below V_1 normally has to be changed much less upon a variation of the plasma density than to be expected from the space charge law. This means that the respective magnitude of V_1 is determined by a complex interplay between ion extraction from the plasma and subsequent beam focusing by the immersion lens.

During some early investigations of beam formation at distances Q = 0.25 to 0.40 m behind the acceleration gap it was found that a focus of less than 1 mm in diameter may be produced at ion currents as high as 100 μA. This focusing property of the system caused the designation "telefocus" ion gun. With respect to future experiments such as large area sputtering or ion implantation a beam diameter of about 5 mm was thought to be necessary. It was found that a distance Q between 0.5 and 1.0 m from the acceleration gap would be adequate as a target position. The actual distance to measure the beam profile electrically was taken to be Q = 0.7 m (Q/D = 15).

An example for the changes observed in the shape of the beam profile upon variation of the extraction voltage V_1 is shown in fig. 5. One can see that focusing is achieved in that special case at V_1 = 0.93 keV. Increasing V_1 to 1.00 kV reduces the maximum current density and broadens the profile. Such a reduction in the voltage ratio V_2/V_1 was usually found to shift the position of the focus further away from the ion source, i.e. in the direction of beam propagation. The shape of the beam profile at 1.00 kV is similar to that in the case of focusing. The opposite is true if one reduces V_1 to 0.85 kV. In that case a dip in current density is observed on axis of the beam. Such a behaviour is, however, not generally typical for defocusing of the beam. In many cases a reduction of V_1 gives the same shape of the beam profile as an increase of V_1 does and sometimes dips are produced in either case. The details of beam profile change were found to depend upon all parameters of gun operation.

It should be mentioned that the profiles in fig.5 were measured at constant plasma density in the ion source. As expected there is no dependence of the total current on V_1. This is due to the fact that the current from the plasma is diffusion-limited and position and shape of the plasma boundary do not change very much upon such small variations of V_1. Moreover the divergence of the beam in the extraction region is so small that all ions pass through the 3 mm diam extractor opening.

One can try to get an idea as to position and shape of the plasma boundary by a comparison of the respective operating parameters with the space charge limited current between plane electrodes. The relation between sheath thickness and extraction voltage as shown in fig.6 was calculated for different argon ion currents between two circular electrodes of diameter b_s, i.e. equal to that of the ion source opening. V_1 rather than $V_1 - V_p$ was taken as the potential difference between extractor and plasma because the plasma potential V_p is usually less than 10 V below the anode potential /14/. Therefore V_p is small compared to V_1. But even without neglecting V_p it is very difficult to apply the calculated data to the experimental situation because the field penetration through extractor and ion source opening will be strong at small extractor separations. Hence one can only use the data of fig.6 to identify extreme positions of the plasma boundary as seen from large differences between extraction gap distance and calculated sheath thickness. Accidentily these two quantities roughly coincide for the measurements shown in fig.5.

One can thus assume that the plasma boundary lies close to the ion source exit and is only slightly curved.

3.2. Beam profiles at different plasma densities

The conditions for beam formation can be expected to very strongly upon a change in plasma density. Fig.7 shows that this is reflected in the beam profile by the occurance of a variety of profile shapes. Similar observations have been reported by Rautenbach /11/ who studied the effect of the total ion current on the beam form in a system with high extraction voltage (20 to 60 kV) and large extractor separation (60 to 110 mm) without subsequent focusing. In that case one can use the beam width as a measure of beam divergence. Here we are facing a more complicated situation due to the fact that ions are not only postaccelerated immediately after extraction but also propagate a long way through a field free space. As there was no possibility so far to measure the beam profile simultaneously at different positions no decision can be made as to the question whether the profile measured under focusing conditions is a true image of some object in the vicinity of the ion source outlet or a waist as determined by the emittance of the beam.

Beam current and extraction voltage belonging to the profiles of fig.7 are shown in fig.8. In the high current range the beam current is found to be proportional to the emission current. Such a linear dependence was found at all extraction gap distances if the plasma boundary was only slightly curved and the extractor opening did not define the maximum beam divergence. The emission current was thus assumed to be proportional to the plasma density at the ion source exit. The extraction voltage varies only slowly with the emission current. Therefore position and shape of the plasma boundary are likely to change with increasing beam current in such a way that the boundary moves towards the extraction electrode and the curvature becomes more and more convex. As a result the beam divergence will increase. This might produce aberrations if the beam diameter becomes too large upon entering the immersion lens stage. The distortions on profile (e) may thus be explained in terms of spherical aberration of the immersion lens. A more thorough study will be given below.

Another irregularity that has to be discussed appears at low currents. A comparison of figs.7 and 8 shows that the distortions occurring on profile (b) coincide with an irregularity in extraction voltage and beam current. One might argue that this kind of distortion arises from the small extraction gap distance $d = 1$ mm. As we shall see this is not the case. The only thing special is that the transition between the broad gaussian-like profile shape as found in case (c) and (d) and the strongly peaked distribution (a) is more clearly evident than at larger gap distances (see below).

The increase of the extraction voltage V_1 in cases (a) and (b) is astonishing. According to the continuous run of the V_1-curve in the normal current range one would

expect that V_1 should be lowered upon a further reduction of the plasma density. If one sets V_1 at the extrapolated value the profile shows the usual shape but the beam current is much less than to be calculated from the emission current. This reduction results from a strong broadening of the beam which leads to bombardment of beam defining apertures or even of the acceleration tube. The secondary electrons thereby produced cause the reduction of the measured beam current.

This deviation from the normal behaviour can be avoided by increasing the extraction voltage. In that case not only the beam current approches the expected value but also a strong increase in maximum current density is observed. True focusing can thus only be obtained by increasing the extraction voltage. It is obvious that such a change of V_1 will shift the position of the plasma boundary into the ion source and produce a concave curvature. On comparison with fig.6 an even more detailed statement can be made. One finds that $I = 30\ \mu A$ and $V_1 = 1.7\ kV$ (case (b)) correspond to a sheath thickness $t = 6\ mm$. This is so much greater than the gap distance $d = 1\ mm$ that neither a strong curvature of the plasma boundary nor field penetration through the openings can account for the difference. Obviously one can no longer assume that the plasma boundary is anchored to the metallic rim of the ion source exit as usually. It is not surprising that in some sort of transition state between anchored and non-anchored boundary beams are produced with a central core and an external "halo" (profile (b)). This "halo" disappears upon a further reduction of the plasma density because the ion emitting surface is shifted so far into the source that only the central part contributes to the beam current (profile (a)).

If this description of "halo" formation were true one would expect a drastic change upon an increase in extraction gap distance. This assumption is confirmed by figs. 9 and 10 which show results for $d = 5\ mm$. The emission current below which the extraction voltage has to be raised for beam focusing is shifted from $i = 18\ mA$ at $d = 1mm$ to 5 mA, in agreement with the space charge law according to which a larger sheath thickness corresponds to a smaller beam current. A "halo" is, however, not observed. This might result from the fact that the 3mm diam extractor opening works as a beam defining aperture. Since the "halo" is formed by ions strongly diverging upon extraction these are likely to strike the electrode at large extractor separation and thus do not appear in the beam.

This shutter effect is obvious also at high emission currents where a strong deviation from linearity is observed for the beam current. In spite of the fact that the beam divergence is aperture-limited distortions occur on profiles at currents above about 120 μA. An order of magnitude comparison with the space charge law shows that this again is an extreme case because now the sheath thickness is smaller than the gap distance. For $I = 150\ \mu A$ and $V_1 = 2\ kV$ one finds $t = 3\ mm$ compared to $d = 5\ mm$. This deviation can be accounted for if one assumes a plasma boundary of hemispherical shape close to the exit of the ion source. A too strongly convex boundary has thus to be avoided because it leads to a primary beam divergence that cannot be accepted by the immersion lens.

To support this interpretation of beam formation and occurance of distortions figs. 11 and 12 show results of measurements which were done at the same extractor separation and the same extraction voltage as in figs. 9 and 10 but at an acceleration voltage reduced from 40 to 20 kV. This lowering of V_2 was achieved by an increase of the extractor lenght from L/D = 1.22 to 1.65. The irregularity in extraction voltage appears at the same emission current in either case (note the change in scaling factor of the abscissa in fig. 12). Thus the strongly peaked profiles at low currents are due to ion extraction from a highly concave plasma boundary which lies well inside the ion source.

Opposite to the low current case the profile distortions occuring at a convex boundary are observed at different emission currents for L/D = 1.65 (i = 35 mA) and 1.22 (75 mA). The primary divergence can be assumed to be smaller at 35 mA than at 75 mA but the extracted ions have to travel a longer way to reach the acceleration gap because of a larger extractor lenght (L/D = 1.65). They will therefore enter the main part of the acceleration field with about the same maximum transverse displacement as for L/D = 1.22 and will also suffer about the same spherical aberration. The profile distortions at high emission current can thus also be thought to be well understood.

3.3. Trapezodial beam profiles

In course of a detailed study of the influence of extractor separation on the shape of the beam profile it was found that at well-defined extraction gap distances trapezoidal beam profiles can be produced. An example is shown in fig. 13. The current density is constant over a large central part of the beam. This property of the beam, however, is only found within certain range of beam currents, in case of V_2 = 40 kV between I = 30 μA and 120 μA. Below 30 μA the profile becomes gaussian-like and above 120 μA the well-known distortions occur.

These trapezoidal beam profiles could be obtained with identical shape at different extractor lengths. Fig. 14 shows that the 90% width does not depend on L/D. The extraction gap at which such profiles can be obtained depends strongly upon the extractor length (fig. 15). At each extractor length one has to adjust the extraction gap to within about 0.5 mm to get the desired profile shape. The extraction voltage increases rapidly with increasing extractor length (fig. 16). In this special case the variation of V_1 covers a range within only a factor of three. If one observes beam formation without restrictions as to the production of a special profile shape than V_1 can easily be changed over more than one order of magnitude. In the present study V_1 was found to range from about 0.2 kV to 3.5 kV for L/D between 0.78 and 1.78.

In a first application of the ion gun beams with trapezoidal profile were used as a means for large area sputtering in secondary ion mass spectrometry (SIMS) /16/. Homogeneous sputtering is necessary in SIMS if this method is applied to a deter-

mination of concentration profiles as introduced e.g. by ion implantation.

4. SUMMARY

It has been shown that the operating parameters of the telefocus ion gun and the shape of the beam profiles can be explained by combined effects introduced by ion extraction from the plasma boundary and beam focusing by the immersion lens. All kinds of distortion that might occur on the profile can thus be explained. Beam profiles with a special shape such as trapezoidal can be produced. The conditions for their occurence, however, can only be given phenomenologically.

Acknowledgement

We thank Mr. K. Eicher and Mr. R. Dörfler for carefully machining the ion gun and the beam monitor.

REFERENCES

/1/ Int.Conf.on Applications of Ion Beams to Semiconductor Technology, Ed. by P.Glotin, Editions Ophrys, Grenoble 1967

/2/ J.G.Bannenberg and A.J.H.Boerboom, Nucl.Instr.Meth. 91 (1971) 269

/3/ O. Almen and K.O.Nielsen, Nucl.Instr. 1 (1957) 302

/4/ W.E.Frahn, W.L. Rautenbach and L.E.Wåhlin, Nucl.Instr.Meth. 7 (1960) 253

/5/ F.Schmitthenner, Ann.Phys. /5/ 42 (1942) 273

/6/ K.Wittmaack, phys.stat.sol. 37 (1970) 633

/7/ I. Langmuir, Phys.Rev. 33 (1929) 954

/8/ I. Chavet and R.Bernas, Nucl.Instr.Meth. 47 (1967) 77

/9/ M.Rabinovitz and E.E.Donaldson, J.Appl.Phys. 36 (1965) 1314

/10/ F.H.Read, A.Adams and J.R.Soto Montiel, J.Phys.E: Sci.Instr. 4 (1971) 625

/11/ W.L.Rautenbach, Nucl.Instr.Meth. 12 (1961) 169

/12/ K.O.Nielsen in /1/, p.27

/13/ K.O.Nielsen, Nucl.Instr. 1 (1957) 289

/14/ C.E.Carlston and G.D.Magnuson, Rev.Sci.Instr. 33 (1962) 905

/15/ K.Wittmaack, to be published

/16/ J.Maul, F.Schulz and K.Wittmaack, Frühjahrstagung der Deutschen Physikalischen Gesellschaft, Regensburg 1972, Verhandl. DPG (VI) 7 (1972) 444

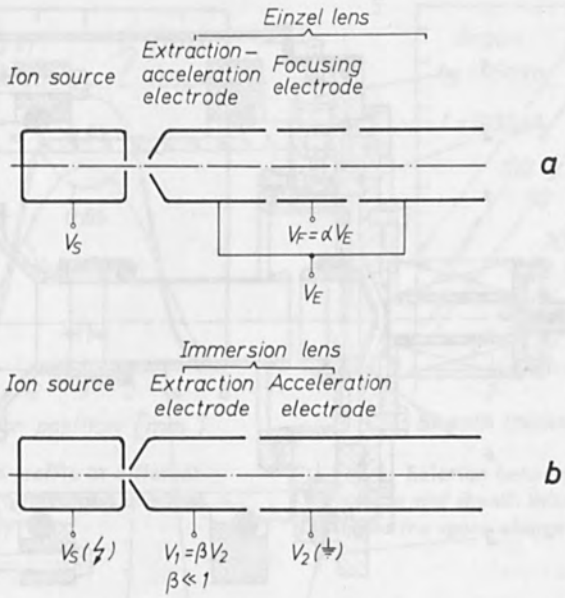

Fig. 1. Principal arrangement of extraction and acceleration electrodes in ion guns:
(a) usual system with einzel lens
(b) system with low potential extraction electrode and immersion lens

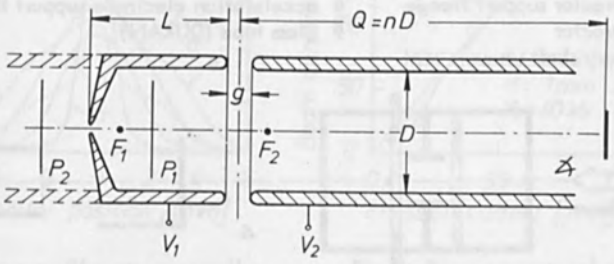

Fig. 2. Details of the immersion lens. Position of focal points F_1 and F_2 and principal planes P_1 and P_2 shown for long cylinders and $V_2/V_1 = 50\ /10/$.

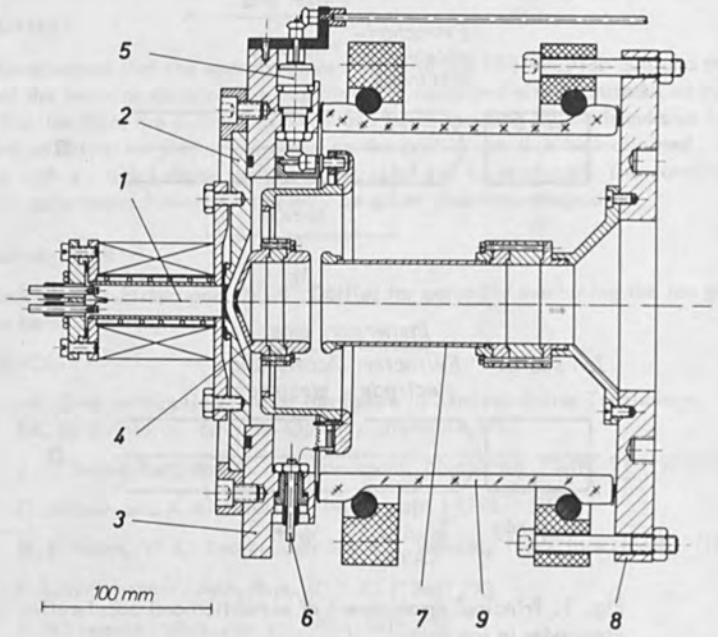

Fig.3. Construction of the ion gun

1 ion source
2 ion source support flange
3 extractor support flange
4 extractor
5 rotary shaft vacuum seal
6 extraction voltage lead-through insulator
7 acceleration electrode
8 acceleration electrode support flange
9 glass tube (DURAN)

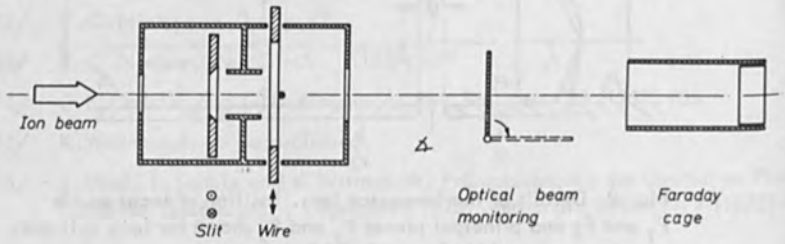

Fig.4. Schematic drawing of the beam monitor

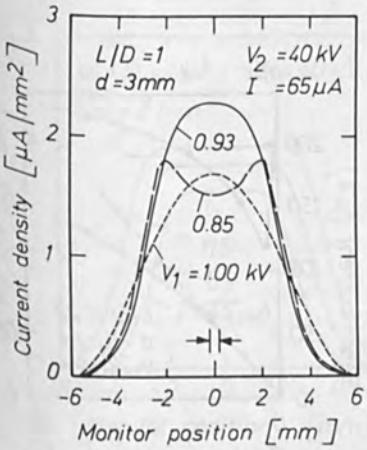

Fig.5. Beam profile at different extraction voltages and constant plasma desity

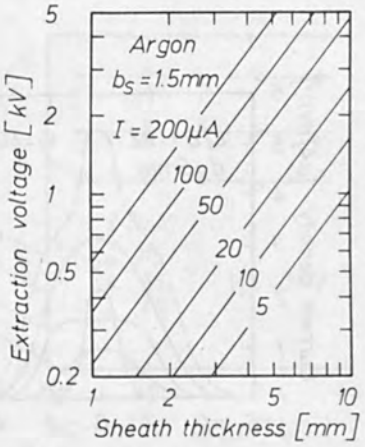

Fig.6. Relation between extraction voltage and sheath thickness according to the space charge law

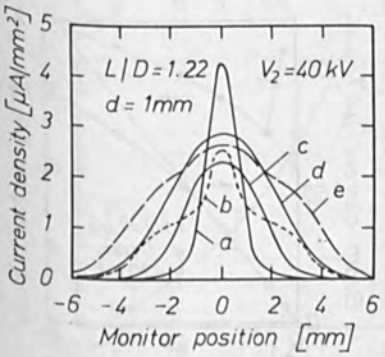

Fig.7. Beam profiles at very small extraction gap distance and different beam currents

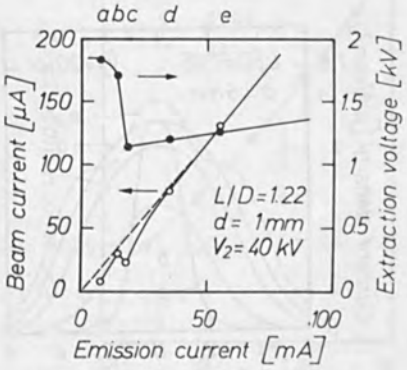

Fig.8. Beam current and extraction voltage for profiles of fig.7. Profile designation on top

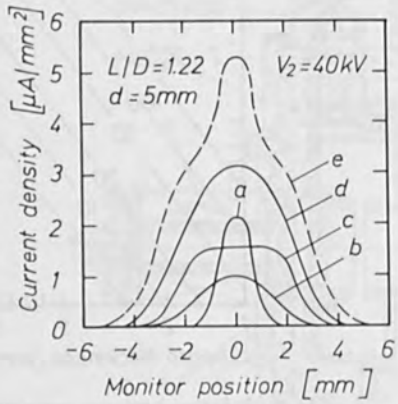

Fig.9. Beam profiles at medium extraction gap distance and different beam currents

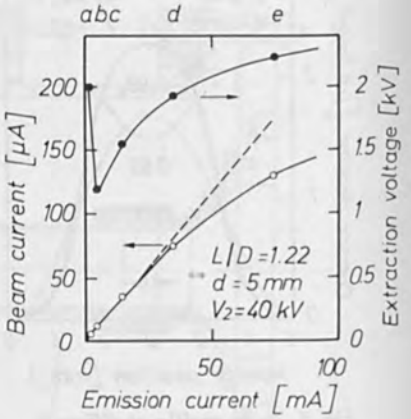

Fig.10. Beam current and extraction voltage for profiles of fig.9. Profile designation on top

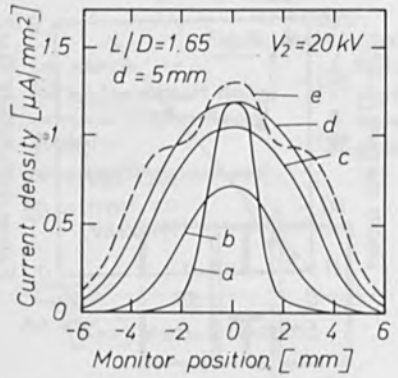

Fig.11. Beam profiles at medium extraction gap distance and different beam currents

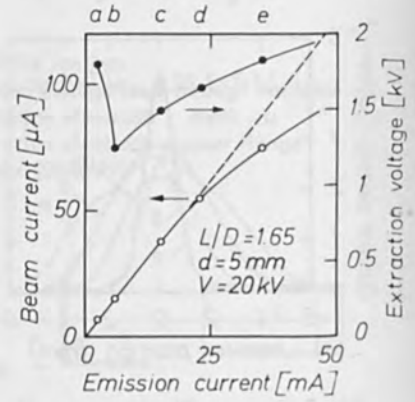

Fig.12. Beam current and extraction voltage for profiles of fig.11. Profile designation on top

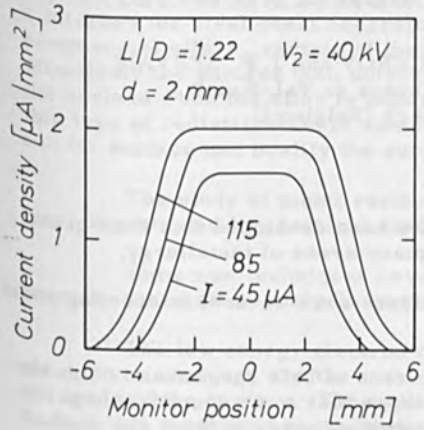

Fig. 13. Trapezoidal beam profiles at well-defined extraction gap distance and different beam currents

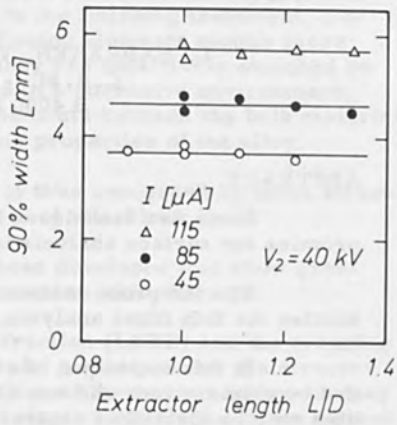

Fig. 14. 90% width of trapezoidal beam profiles versus extractor length. Parameter: Beam current

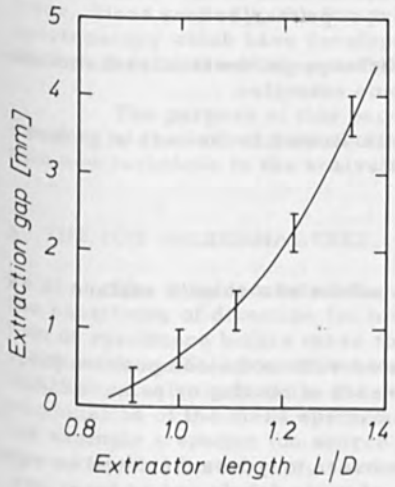

Fig. 15. Extraction gap distance versus extractor length for production of trapezoidal beam profiles

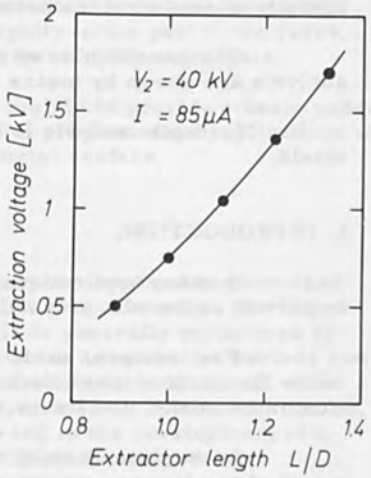

Fig. 16. Extraction voltage versus extractor length for production of trapezoidal beam profiles

POSSIBILITIES OF THE ION MICROPROBE IN SURFACE ANALYSIS.

L. HABRAKEN, V. LEROY and J. P. SERVAIS
C. R. M. - Abbaye du Val-Benoît
B 4000 Liège (Belgium).

ABSTRACT.

Some new techniques have been developed that show great promise for surface analysis in many areas of metallurgy.

The ion probe microanalyser show several interesting possibilities for thin films analysis.

In this technique, the surface of bulk specimens is bombarded by primary ions and one observes that some secondaries particles may be ejected as neutral atoms but many of them are ejected as positives or negatives ions; these secondaries ions may be used in order to analyze the surface of the bulk material.

The authors analyze, in polycristalline specimens some problems related to the shape and the flatness of the crater due to primary beam and to the nature of the primaries ions.

The possibilities of this technique in the field of the microanalysis are shown by means of some examples.

In-depth analysis is also illustrated in the case of coated steels.

I. INTRODUCTION.

In many applications, the nature of a sheet's surface is as important as its bulk properties.

For instance, oxide films as well as the composition just below the surface may affect adherence of coating or paint, oxidation or corrosion resistance, ...

In the case of steel, the surface may be considered as composed of two layers - an outer one of oxide debris and an inner one that is part of the substrate but differs in chemical composition from the bulk steel, as suggested by D. L. Blickwede (1).

The thickness of these two layers varies from 0 up to about 2 microns for steel sheet according to the finishing treatment. For commercial alloys, certain of the alloying elements modify more effectively the surface than others; they are selectively enriched on the surface when the alloy is exposed to a corrosive environment; this type of redistribution of some elements between the bulk material and its surface can modify the surface properties of the alloy.

The study of metal surface is thus concerned by some structural aspects and by chemical analysis of thin films.

Some new techniques have been developed that show great promise for surface analysis in many areas of metallurgy.

The low energy electron diffraction (LEED) and the scanning electron microscopy are the most useful techniques for the structural study of the surface. The application of the former technique may be however restricted to the study of single crystal; the latter method is a very useful technique for the study of pores, voids and grains size in fractured scale, due to its great depth of focus.

For chemical analysis of surface layer, the most important progress has been due to the application of electron probe microanalyser. More recently, the ion probe microanalysis and the AUGER spectroscopy which have developed rapidly in the past three years, show several interesting possibilities for thin films analysis.

The purpose of this paper is mainly to provide a basic understanding of the ion microanalyser and to present some applications of this new technique to the analysis of metal surface.

2. THE ION MICROANALYSER.

The development of the mass spectrometer has increased the sensitivity of detection for most elements. However, the ionisation of specimens before mass analysis is generally performed by spark source. This ionisation source is not adequate for surface and thin films analysis because the depth of analysis is too great. The combination of the mass spectrometer with a controlable ion source, for example a sputter ion source, has led to the development of a new analytical instrument, the ion probe microanalyser.

There are several types of ion microprobes now in use (2, 3, 4); the ion source and the performances of the mass separation technique are different from one to another.

In our paper, we restrict ourselves to the ion microprobe developed by Slodzian and Castaing (5, 6) and improved by Rouberol and al (7). This ion microprobe combines a mass spectrometer with an ion emission microscope as suggested in fig. 1. The instrument had a radio-frequency sputter ion source which permits to product a plasma of monoatomic inert gas, or reactive gas (oxygen, nitrogen, ...). A beam of primary ions is then extracted through a pinhole and bombards the specimen on an area of a few mm^2. The primary beam intensity varies up to 30.10^{-6} Amp and the accelerating voltage is equal to 5.5 kV.

The primary ions may be also formed by means of a duoplasmatron; the primary beam may be focused to obtain a spot of 30 microns in diameter. The beam may be rastered along the surface of the specimen in order to scan a large area.

The secondary ions are extracted through a diaphragm by means of an electrostatic immersion lens and directed into the mass spectrometer.

The mass spectrometer selects the ions so that a given m/e ion beam is extracted. A filtration in energy is operated by means of an electrostatic mirror which reflects the ion beam back through the second magnet.

The mass spectrometer has both radial and transverse focusing properties so that the analysed ion beam is preserved as an ion image. This ion image is projected on an image converter which gives an electron image.

This new electron image may be displayed on a fluorescent screen or recorded by means of a camera. The image observed on the 25 mm diameter screen corresponds to an area of 150 microns in diameter; the magnification of the instrument is about 150 x. The lateral resolution of this image is about 1 micron; the resolution in depth is much more higher and is mainly a function of the sputtering rate and of the crater flatness.

This electron image may be also integrated and recorded by using a scintillator and a photomultiplier. In this manner, the total ion current corresponding to an isotope is converted in electron current and recorded versus the time, thus as a function of the penetration in the specimen.

3. THE CATHODIC SPUTTERING.

If the surface of bulk specimen is bombarded by primary ions having an energy of a few-kiloelectron volts, one observes the erosion of the surface. The ions of the primary beam have much higher energy than the bonding energies of atoms in the solid sample and thus are able to eject atoms from the target. These particles may be ejected as neutral atoms but many of them are ejected as positives or negatives ions. These ions form the "secondary ion emission" and can be analysed separately by adjusting the polarisation of the immersion lens.

Thus, we have to distinguish between the sputtered atoms and the sputtered ions emissions due to the bombardment by a primary ion beam.

As suggested by Silsbee (8), sputtered atoms are ejected as a result of multiple focused collision process along crystallographic directions of high atomic density. The sputtered atom yield is thus anisotropic.

The sputtered atom yield varies also with the angle of incidence of primary beam with the surface. The ion bombardment shows the grain boundaries of polycrystal specimens since the sputtering of each crystal depends of its orientation with respect to the primary beam.

Fig. 2 shows an interferogram of a crater produced by a focused argon beam bombarding a steel target. At the same figure we have also reported an electron micrograph given by the scanning electron microscope in the same area.

This picture and the profile obtained by means of a Talysurf microrugosimeter along a line crossing the crater, shows the difference of the sputtering rate for adjacents grains. Finally it is also necessary to take account that the yield of sputtered atoms and thus the sputtering rate increase with the mass of the bombarding primary ion and with its energy.

By using a duoplasmatron ion source with a scanning system it is possible to obtain a more flat crater as shown by the interferogram in fig. 3 in the case of a Fe 3% Si steel bombardment at different sputtering rates.

From pulverisation tests of Ta coating on glass, by measuring the intensity of the primary beam, the profile of the crater and the thickness of the coating, it is possible to estimate the sputtered atom yield of tantalum. This yield is about equal to 5 ejected atoms for 1 incident argon ion with an energy of 5. 5kV. This value is in good agreement with experimental data given by Almen and Bruce (9) for several elements bombarded by argon ions, as reported in fig. 4.

The ions emitted by a metal M bombarded by an ion beam of a few keV are mainly ions M^+ with a single charge; in the case of a metal with several isotopes the isotopic ratios are preserved for the secondary ions. It is also possible to observe some polyatomic ions of the type Mn^+ for which several atoms transport a single charge and some polycharged ions which are monoatomic ions with two or several charges. The mass spectrum of a LD steel bombarded by argon ions of 5. 5 kV is given in figure 5. One observes single and polycharged ions for iron and polyatomic argon ions which are reflected or reemitted by the surface. The reemitted ion may be a primary ion which is trapped in the solid due to the collisions with atoms of the solid and is ejected du to the sputtering by the primary beam.

In some case, molecular ions such as AlO^+, $AlOH^+$, ... may be observed; such ions are still characteristics of the surface but may be due to the residual gas in the vacuum chamber. The formation of positive molecular ions may be increased by bombarding the surface with a reactive ion beam as shown in figure 6 for LD steel bombarded by oxygen ion with an energy of 5. 5 kV.

In addition to the formation of molecular ions, it appears that the use of oxygen primary beam increases the intensity of secondary emitted ions as shown for the carbon and nitrogen elements in figures 5 and 6. The use of an oxygen primary beam instead of an argon beam increases the sensitivity of the carbon and nitrogen analysis in steel by a factor 4 for the same primary intensity and accelerating voltage. However, the sputtering rate of an oxygen beam is lower as compared with the sputtering rate of an argon beam. In the case of complex molecular negative ions, sputtered by bombarding ionic compounds, experimental data show that the ion yield is the most higher for the negative ion (MO_{n-1}) where n is equal to the chemical valence of the element M.

Secondary ions intensities obtained by bombarding a natural hematite crystal are reported in Table I. These results show clearly that the more intense secondary ions are $(FeO_2)^-$, $(AlO_2)^-$, for trivalent metallic element, and $(TiO_3)^-$ for tetravalent element.

Table I - Negative secondary ion intensities of natural hematite bombarded by A^+ (in Amps)

FeO^-	$2.2\ 10^{-13}$	AlO^-	$13\ 10^{-16}$	TiO	$2.1\ 10^{-15}$	VO^-	$3.2\ 10^{-16}$
FeO_2^-	$16.0\ 10^{-13}$	AlO_2^-	$56\ 10^{-16}$	TiO_2^-	$12.8\ 10^{-15}$	VO_2^-	65.10^{-16}
FeO_3^-	$1.6\ 10^{-13}$	AlO_3^-	$3.3\ 10^{-16}$	TiO_3^-	$25.0\ 10^{-15}$	VO_3^-	380.10^{-16}
						VO_4^-	

It may be concluded that specific ion yields are affected by the type of gas used.

The secondary ion output is directly related to the bombarding intensity as shown in figure 7 in the case of a cobalt single crystal bombarded by argon ions. In the same conditions, one observes more dispersed data in the case of steel (Fig. 8); this is probably due to the polycristalline nature of the specimen.

The secondary ion emission depends also on the nature of the chemical binding of this element in the target as reported by Slodzian and Hennequin (10); more precisely, the ionic compounds give a more intense secondary ion emission.

In this manner, iron oxide gives a more intense emission for iron ion than pure iron as suggested by distribution maps in fig. 9. This figure gives the distribution of iron and oxygen in oxide layer formed on steel by oxidation at 600° C during 60 seconds in air. The distribution of iron and oxygen are given after a time of sputtering equal to 100 seconds; at this moment, oxide layer is removed by sputtering in some places and the steel is apparent; at these places the iron ion emission is less effective than in the oxide layer.

The "chemical flash" or the reinforcement of the secondary ion emission observed in the case of a metal at the beginning of one in depth analysis, may be due to the chemical binding with the adsorbed oxygen on the surface.

4. QUANTITATIVE ANALYSIS SENSITIVITY.

For the present, quantitative work in the dilute solid solution range can be made by using the familar working curve approach.

The analysis of magnesium and iron in aluminum solid solution is reported by Andersen (11) in the range from 0.01% to 0.1% for Mg and from 0.1 to 1% for Fe.

Quantitative analysis of boron in silicon by means of standardization curve have been performed by Blanchard-Hilleret and Quoirin (12).

Figure 10 shows the calibration curve obtained for the analysis of oxygen in tantalum; in this figure, the concentration of oxygen is given versus the ratio of secondaries ionic intensities from oxygen and tantalum. The intensity of the argon ions primary beam is equal to $5\ 10^{-6}$ A and the accelerating voltage for argon ions is equal to 5.5 kV.

The analysis were performed at a residual pressure equal to 10^{-7} torr after a pumping down of the vacuum chamber to 10^{-8} torr For carbon analysis in steel, the calibration curve is given at figure 11; the standards for ion microanalysis are heat treated at high temperature under argon and water quenched in order to preserve an homogeneous structure ; the specimens for chemical analysis are machined after a recovery at 500° C under argon.

The ion microanalysis needed for these calibration curves are obtained in 10 seconds with a sputtering rate approximately equal to 20 A/sec which is adequate for thin films analysis; in these conditions, the ion microanalysis are representative of a layer 200 Å in thickness. From the calibration curves, it appears that in our experimental conditions, the sensitivity of the equipment is, at this moment, equal to 100 ppm for oxygen analysis in tantalum and 250 ppm for carbon analysis in steel.

The sensitivity is an increasing function of the sputtering rate and a decreasing function of the thickness of the layer to be analysed.

Owing to the possibilities of the mass spectrometers, the ion microanalyser has high sensititivy for most elements. In practice, the sensitivity for a given element in a particular matrix has not yet been measured in many cases.

The sensitivity is affected by the matrix, the nature of the bombarding gas, the sputtering rate, the chemical bonding of the element. Up to now, the best analytical procedure is to use an homogénéous standard of the same matrix which has been analysed by some other techniques.

5. SPATIAL IMAGING IN ION MICROANALYSIS.

Owing to the radial and transverse focusing properties of the mass spectrometer, the instrument can perform an actual ion image of a particular isotope, corresponding to an area of 150 microns in diameter.

Fig. 12 shows an internal oxidation phenomena in a 3% Cu-3%Ni steel heat-treated at 1200° C during 3 hours in air. The micrography represents an area located just below the oxide layer.

The distribution maps of the elements Fe, Mn, Cu, Ni, Si, Al and O_2 are given in figure 13. These ion images show that the elements Fe, Si and Al are presents as oxides in the grains boundary; on each side of these oxides, one observes an enrichment of the elements copper and nickel which diffuse from the grain boundary to the grain during the internal oxidation. The manganese is present mainly as small oxides particles in the metallic matrix. Some experiment are now in progress in order to study the spatial imaging of the technique in the field of the light elements analysis.

In the case of a niobium carbide coating of about 100 microns in thickness, optical microscopy reveals the presence of several differents layers in the coating as shown in figure 14. Ion images for carbon and niobium are given at the same figure. The carbon image shows clearly that the carbon segregation corresponds to some layers appearing in the optical micrography.

6. IN DEPTH ANALYSIS.

A three-dimensional analysis of a bulk material may be performed by sputtering successive layers of a specimen. Owing to the sputtering rate ranging from a few Å per second to one thousand A per second as a function of nature of primary ions, intensity of the primary beam, it is possible to perform good in depth analysis of thin films.

6.1. Analysis of coating on steel.

Fig. 15 is an electron scanning micrography of a Ni-Cr coating formed by metallisation under vacuum on a LD steel. The thickness of the coating is about equal to 1 micron.

Fig. 16 gives the concentration profiles determined by means of the ion microprobe as a function of the penetration in the specimen.

For the oxygen curve, we observe a peak located at the interface between the coating and the steel as shown by referring to the iron profile.

At the same interface, the silicon profile shows also an important peak that it is not easy to explain by a migration of silicon diffusing form the bulk material. The presence of these elements is due to the pickling bath used for the preparation of the substrate. In the present case, silicate solution was used.

At the present time, it is not easy to decide if the enhancement phenomena observed in the distribution profiles of Mn, Cr, Ni elements at the coating-substrate interface, are due to a concentration effect or to a chemical effect due to the presence of oxygen, which increases the secondary ion emission.

From distribution curves for these different elements, it appears that the interface between coating and substrate is located between 8000 and 12.000 Å. The resolution may be hampered by the addition of ions ejected from the sides of the crater to the ions coming from the center of the same crater.

It is also necessary to take accound of the polycristalline nature of the specimen and of the poor flatness of the steel sheet as shown by the scanning electron micrography (fig. 16).

6.2. Analysis of oxidation layers.

Very thin oxide layers on steel have been made by heating steel under vacuum and oxidizing the specimen during 1 minute at 500°, 600°, 700° or 800° C. The specimens were cooled to room temperature in air. The distribution curves of Fe, O and C after oxidation at 500° or 600° C during 60 seconds are reported in fig. 17.

In order to compare these oxide layers, we normalize the two sets of curves by adjusting the secondary emission for iron in the oxide layers. In both cases, we observe a very low carbon content in the oxide layers and the same peak in the carbon profiles appearing at the oxide-steel interface.

These carbon peaks may be interpreted in terms of a concentration effect due to the diffusion of carbon or in terms of a chemical emission due to the simultaneous presence of oxygen and carbon at the interface. Oxidation of stainless steel AISI 430 at 800° C during 60 seconds in air gives an oxide layer 4500 Å in thickness. The distribution curves for positive metallic ions M^+ and positive molecular ions MO^+ are given in figure 18.

We observe that the oxide layer is enriched mainly in chromium and depleted in iron; this enrichment of chromium in the oxide layer corresponds to the passivation phenomena. At the interface between the oxide layer and the stainless steel, some peaks in manganese, aluminum, carbon are present which may be due to a concentration effect or to a chemical effect.

7. CONCLUSIONS.

The ion probe is able to perform microanalysis with a good lateral resolution and also to produce in-depth analysis of both bulk material and thin films and in this manner to provide a three-dimensional analysis of a specimen. With usual primary ion source, it is possible to achieve sputtering rate ranging from a few up to 1000A/sec.

Many problems still remain in understanding namely the model in which the positive or negative ions are formed from the sputtered surface; calibration curves of the output of the ion probe permit already some quantitative work but preparation of homogeneous standards is certainly a considerable work.

Owing to its possibilities, the ion microanalyser is a powerful tool in solid materials science and more especially in the field of surface analysis.

BIBLIOGRAPHY.

1. Blickwede
Metal Progress, November 1969, 77.

2. A. E. Barrington, R. K. Herzog
Progress in Nuclear Energy, Serie IX, Anal. Chem. Pergamon Press, Oxford 1966.

3. H. Liebl
J. Appl. Phys. 16, 1965, 5277.

4. A. J. Socha
Surface Science, 25, March 1971, 147.

5. R. Castaing, G. Slodzian
J. Microscopie 1, 1962, 395.

6. G. Slodzian
Anal. Phys. 9, 1964, 591.

7. J. M. Rouberol, J. Guerme, P. Descamps, J. P. Dagnot, J. M. Guyon
Proc. 16th Annual ASTM Conf. Mass. Spect. Pittsburgh, 1968, 216.

8. R. H. Silsbee
J. Appl. Phys. 28, 1957, 1246.

9. O. Almen, G. Bruce
Nuclear Instruments and Methods, 2, 1961, 257?

10. G. Slodzian, J. F. Hennequin
C. R. Acad. Sc. Paris, 263, 1966, 1246.

11. C. A. Andersen
J. Mass. Spect. and Ion Physics, 1, 1969, 61.

12. B. Blanchard, N. Hilleret, J. B. Quoirin
International Meeting on Chemical Analysis by Charged Particle Bombardment, Namur, septembre 1971.

13. M. Kaminsky
Atomic and Ionic Impact Phenomena or Metals Surface
Springer Verlag, Berlin 1965.

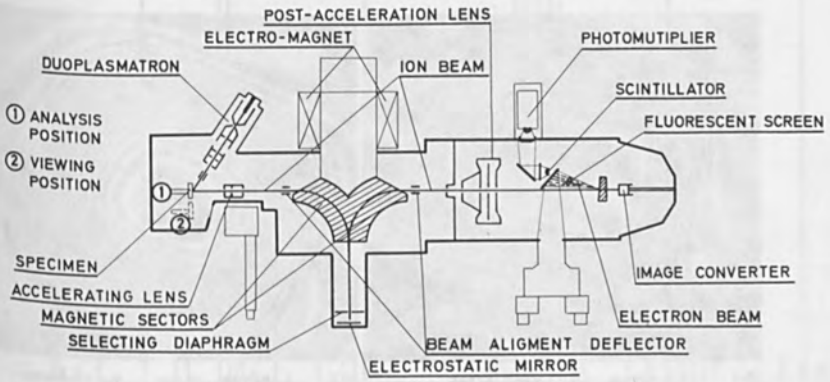

Fig. 1. Schematic diagram of the ion probe microanalyser.

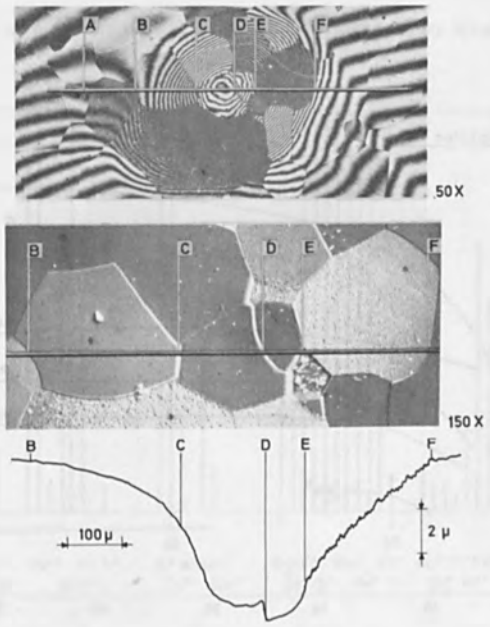

Fig. 2. Crater produced in steel (RF ion gun).

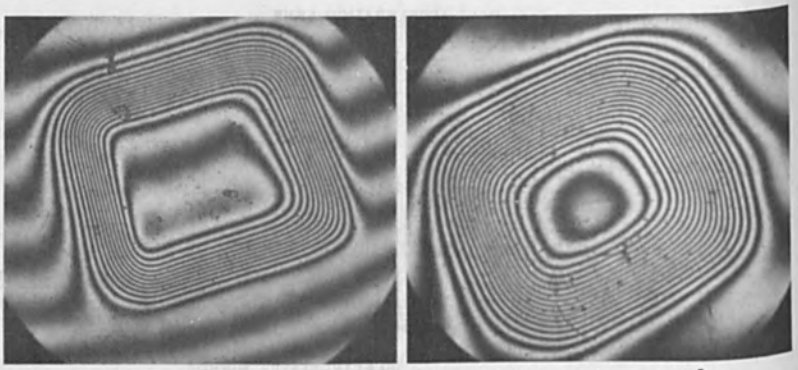

Fig. 3. Crater produced in Fe - 3% Si steel (duoplasmatron gun)

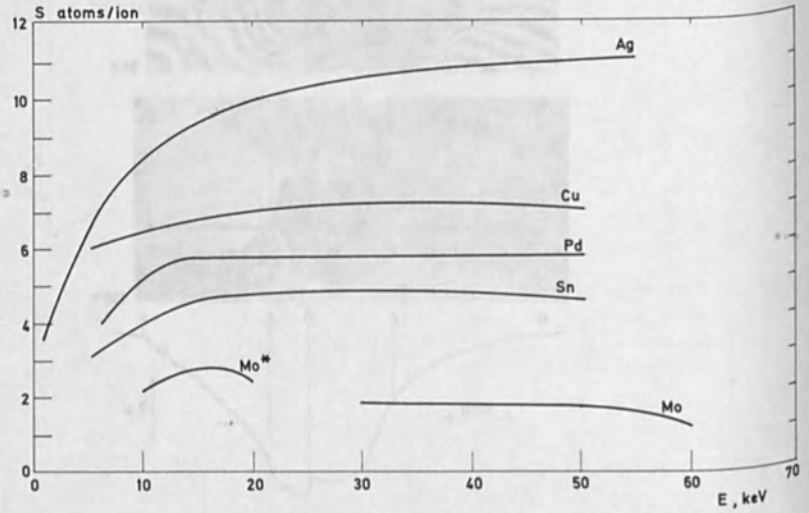

Fig. 4. Sputtered atom yield versus the primary ion energy.

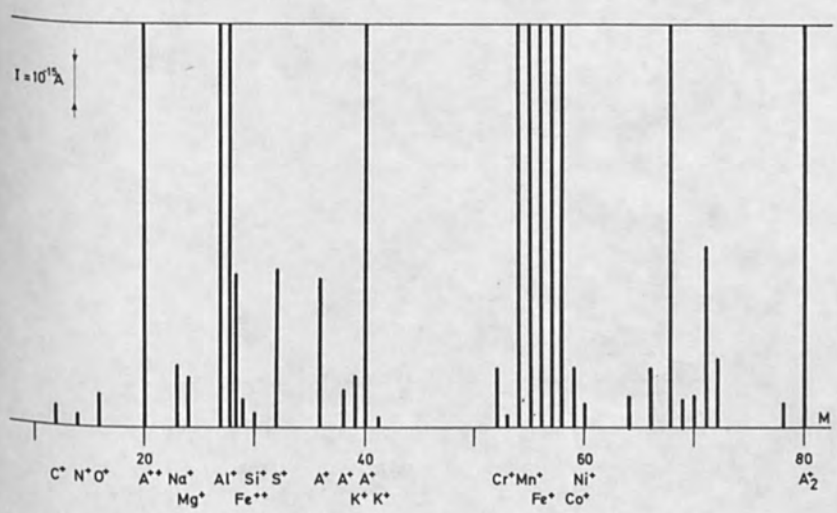

Fig. 5. Mass spectrum of a LD steel bombarded by argon ions.

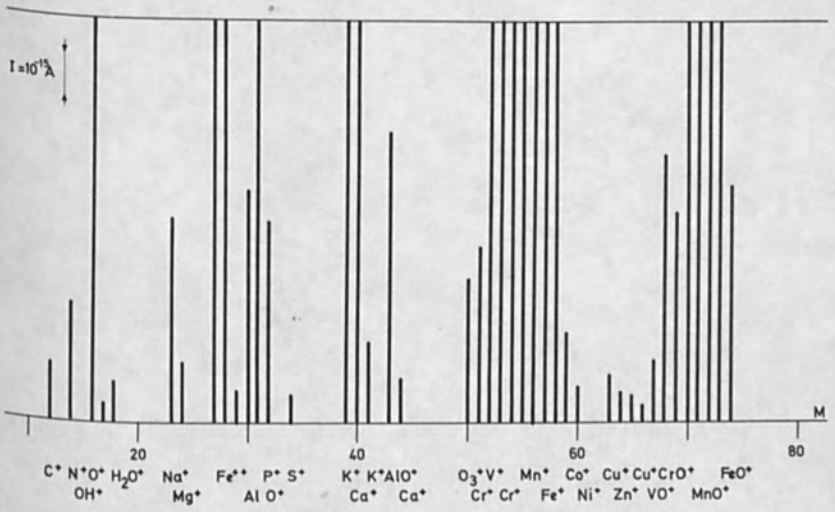

Fig. 6. Mass spectrum of a LD steel bombarded by oxygen ions.

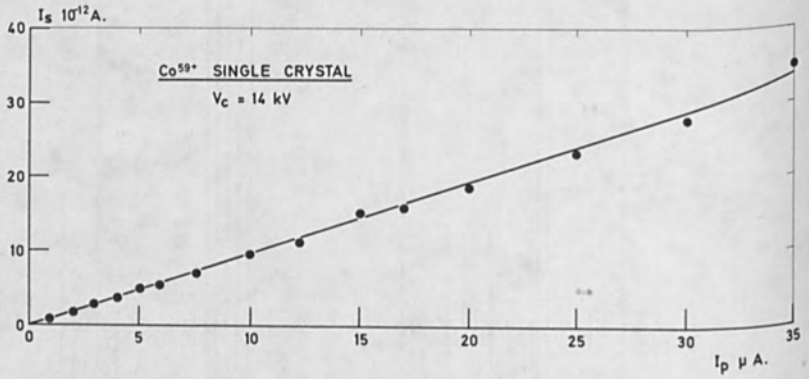

Fig. 7. Secondary ion intensity versus the primary intensity.

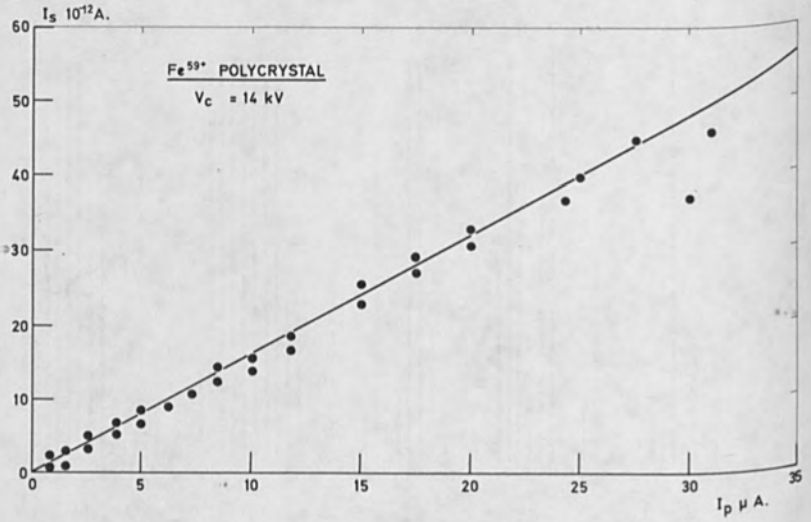

Fig. 8. Secondary ion intensity versus the primary intensity.

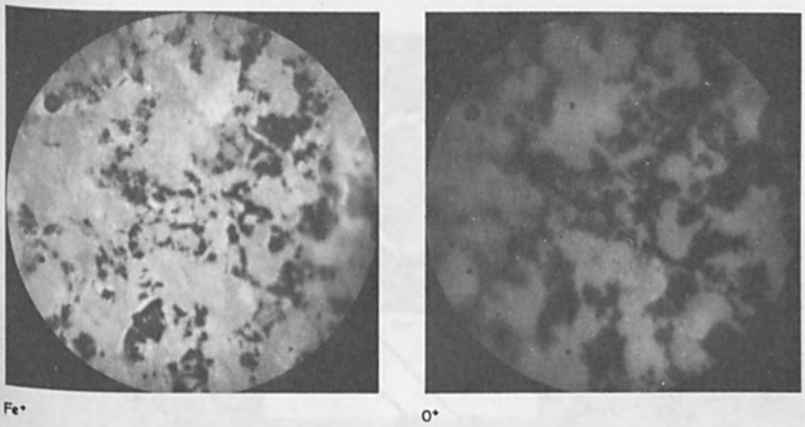

Fig. 9. Distribution maps in oxide layer on steel.

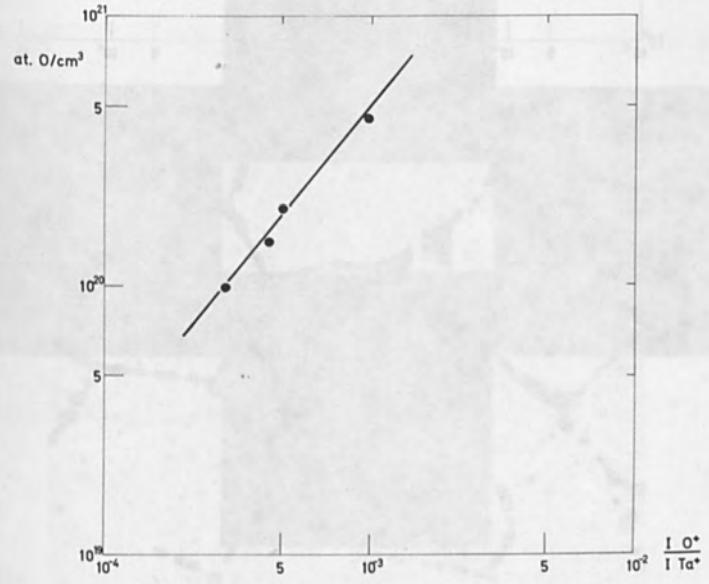

Fig. 10. Calibration curve for oxygen analysis in tantalum.

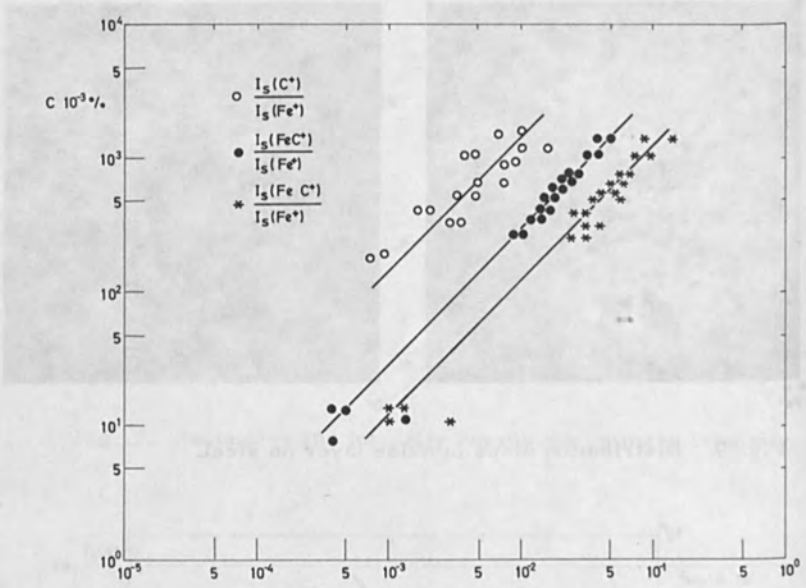

Fig. 11. Calibration curve for carbon analysis in steel.

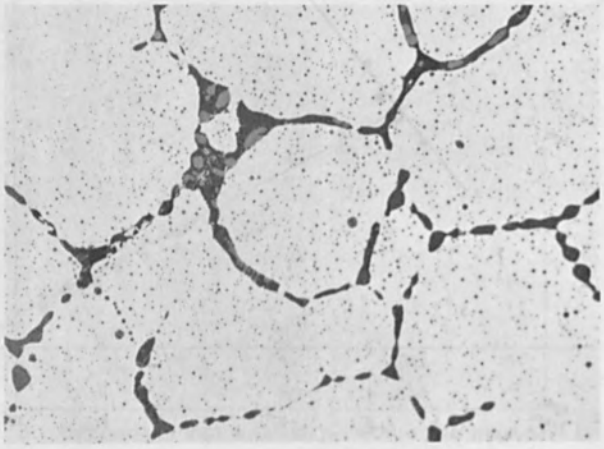

300 X

Fig. 12. Internal oxydation in 3 Cr - 3 Ni steel.

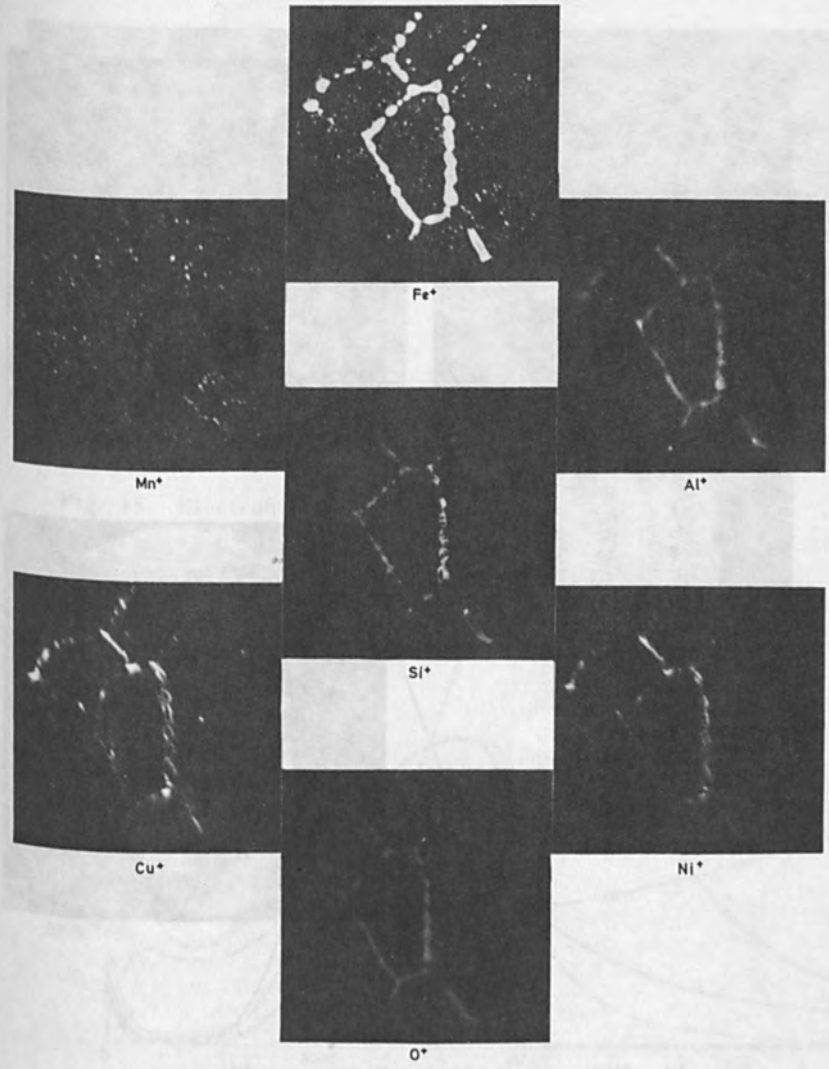

Fig. 13. Distribution maps.

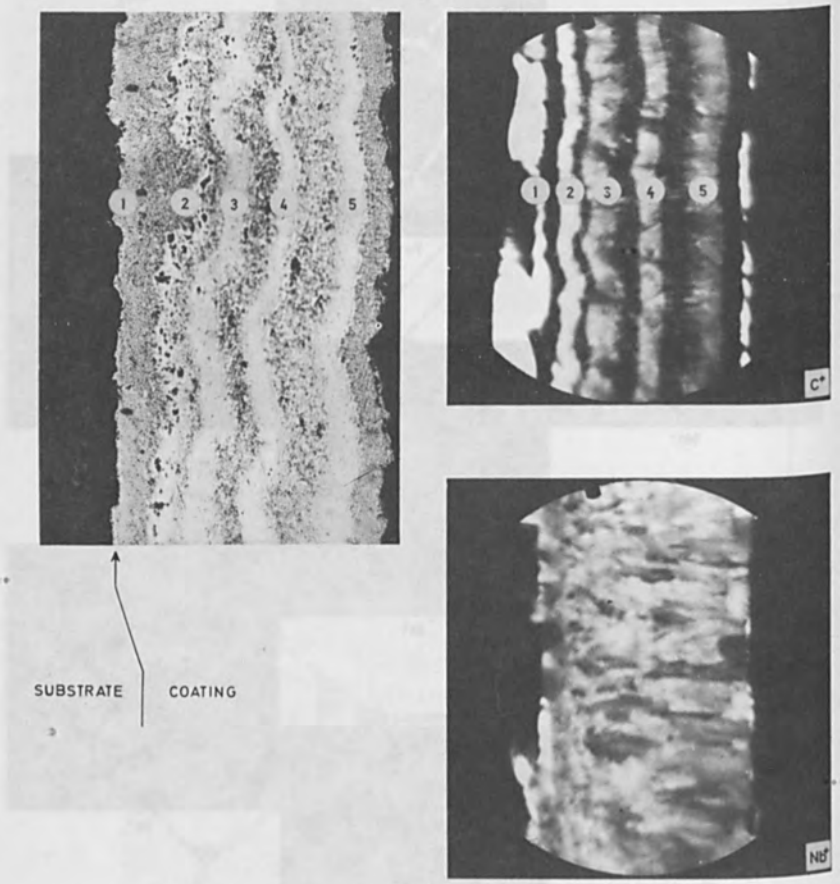

Fig. 14. Niobium carbide coating on graphite.

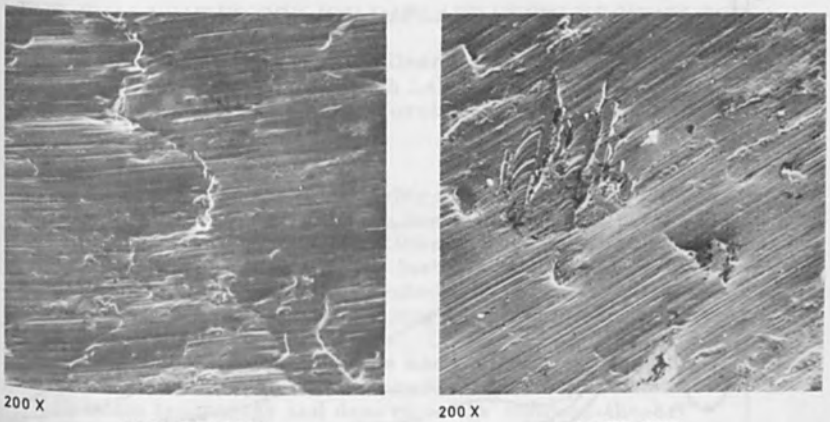

Fig. 15. Electron scanning microanalysis.

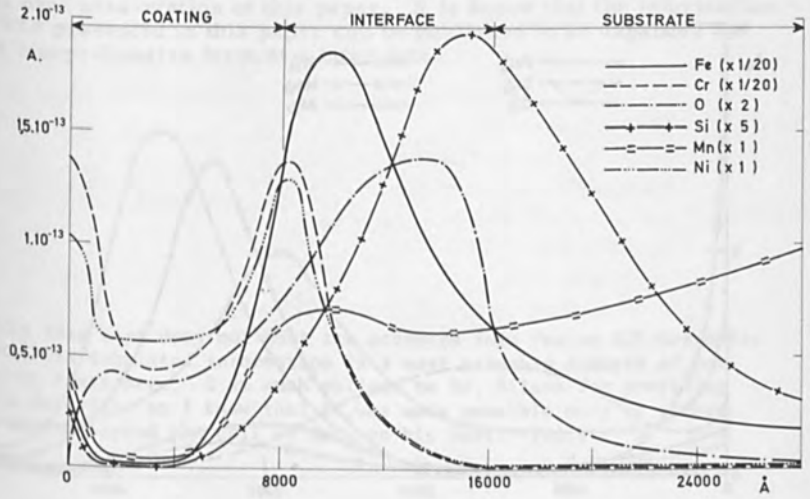

Fig. 16. In-depth analysis of a coated steel.

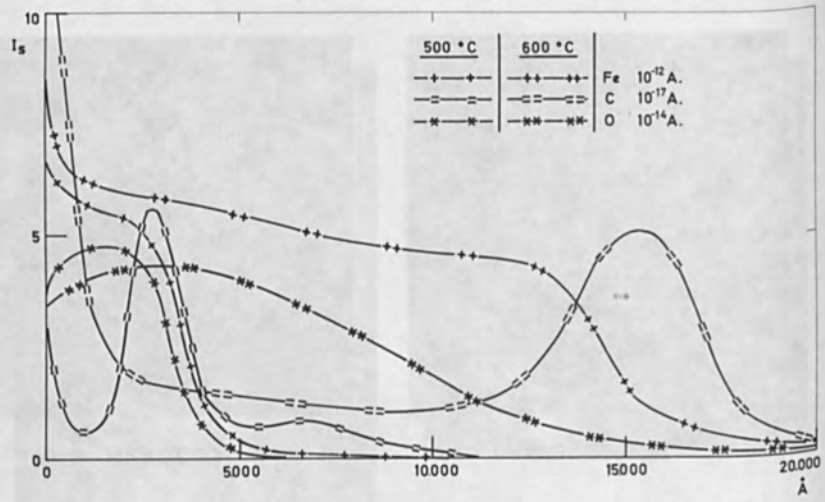

Fig. 17. In-depth analysis of an oxide layer on LD steel.

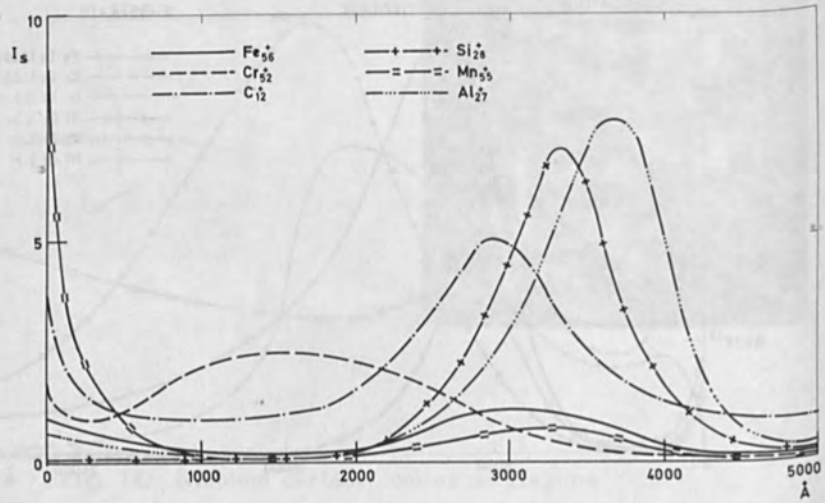

Fig. 18. In-depth analysis of an oxide layer on AISI 430 steel.

THE CHALLENGES FOR ION IMPLANTATION TECHNOLOGY

R. G. Wilson
Hughes Research Laboratories
Malibu, California 90265

Ion implantation technology has faced the healthy problem of keeping up with the demands imposed by an expanding diversity of applications and organizations utilizing the process. During the last year we have seen implantation more widely accepted into production as a complementary step in processing of discrete semiconductor devices and integrated circuits. Other papers in this session describe these devices and circuit processes and applications; this paper stresses the various aspects of this beam technology and describes the state-of-the-art and the major problem areas for each.

Following are copies of some of the viewgraphs given as part of the oral presentation of this paper. It is hoped that the information that was presented in this paper can be published in an expanded and more comprehensive form at a later date.

While this text does not meet the accepted form for an ECS presentation, its tabulated information is a most valuable summary of pertinent facts here. I am much obliged to Dr. Wilson for providing this material, as I know that it was made possible only by effort above and beyond the call of duty on his part. (Ed.)

PURPOSE/GOALS

- Present State-of-the-Art in Ion Implantation Technology (Techniques and Systems)
- Where the Technology is Headed to Meet Future Needs (In My Opinion)
- Some of the Challenges I See in Getting There

AREAS TO BE DISCUSSED

Challenges to ion implantation technology for device/circuit production
Total systems
Variable ranges and accuracies
Ion sources and feed systems
Extraction and interfacing optics
Accelerators
Mass separators
Beam handling, focusing, and monitoring
Beam scanning
Target chambers
Vacuum systems
Terminal control systems
Specialized systems (tiny beams, channeling)

CHALLENGES TO IMPLANTATION TECHNOLOGY FOR DEVICE/CIRCUIT PRODUCTION

- Low-temperature implantation of multiple targets - for producing electrical activation at lower annealing temperatures
  * Even cooler surroundings may be required to prevent target contamination
- Pre-or post-implantation bombardment - to produce electrical activity at lower annealing temperature. This adds a processing step and increases the time.
  * To provide a well-designed system that furnishes e.g., Si^+ in addition to B^+ efficiently (economically in cost and time) (SiF_4 and BF_3 are compatible - N_2 vs Si is a problem)
- Learning optimum annealing conditions for more than B in Si (900°C for 15 min.) for large electrical activation - or what lower temperature during implantation or what pre-or post-implantation bombardment treatment is required (e.g., $Si^+ \rightarrow Si$, $Ge^+ \rightarrow Ge$)
- Learn better how to control profiles (tails) to relax the oxide thickness requirements to control accurately ρ_s, e.g., 1000 Å of SiO_2 to keep ρ_s to 2% for 60 keV $B^+ \rightarrow Si$.
- Learning better how to calculate and measure profiles beyond B and P in Si, etc.
- Learning how to make pinhole-free oxide implantation masks

REPRESENTATIVE SYSTEM INFORMATION

Voltage (kV)	Cost (K$)	$/$V_{max}$	Number Suppliers (of 9*) (readily available)
PRODUCTION(OR PROTOTYPE)			
(5) 60 (75)	50-70	1.0±	4 (2)
(5-30) 150	70-80 (130)	0.5± (0.8)	8 (5)
[(30) 300	80	0.27	1]NS/O
RESEARCH AND DEVELOPMENT			
2-60	50-70	1	2 (1)
2, 20-150	75	0.5	2 (1)
2, 30-300	90 (145)	0.3	3 (2)
5, 20-400	100	0.25	2 (1)
30-600	200	0.33	1

CHALLENGE AREAS: Production systems of V > 150 kV

R and D Systems: more compact, more versatile, more routinely operable, less costly at V - 150, 300 kV.

*Note: Since this information was collected two of the US suppliers have withdrawn from the field, a third has sold little equipment, and of those remaining, three are European.

VARIABLE RANGES AND ACCURACIES

VARIABLE	STATE OF THE ART		FUTURE NEEDS	
	RANGE	ACCURACY	RANGE	ACCURACY
Voltage (kV)	5 to 450	~ 3%	2-600 (or 300 & good ++)	0.5 to 1%
Dose (ions/cm^2)	10^{12} to 10^{16}	±15% to ± 2%	10^{10} to 2 x 10^{17}	± 2%
Area Uniformity	± 1 to 3%		± 1 to 3 %	
Ions	B, P, As, H		Be, Zn, Cd, Al, Si, Sb, S, Te	
Target Temperature (°C)	Ambient to 700	± 50	LN_2 to 1000	± 5
Target Alignment	7° ± 1° tilt & 17° ± 1° rot. from (111) or (110)		Three dimensional variation	± 0.05
Mass (amu)	1-31 (75)	± 1	1-130	± 1
TC Pressure	$5x10^{-7}$ to 10^{-6}		10^{-7} (oil free)	
Power Supply Stability		3 to 5%		1%
Dose Rate		Problems noted, e.g., >~ 10^{15}/cm^2-sec in Si		
Number of Samples	10 to ~200		10 to ~200	

ION SOURCES: FUTURE NEEDS

- Longer lifetime with low maintenance but not higher currents than S.O.A (B^+, Al^+, P^+, As^+)

  Low dose applications 5-10 μA for 10,000 hours
  Moderate dose applications 50-100 μA for 1000 hours

- More B^{++}, P^{++}, etc Need say 10% (~1% now quoted)
  To extend ion energy with low voltage systems for economy (Need clean P^{++})
  Need say 1-5 μA of X^{++} for 1000 hour (to 30% $^{++}$ of heavier elements)

- More B_2^+ (P_2^+ now sufficient at 200 to 300 μA but B_2^+ is negligible)
  To increase currents (dose) at low energy

- Multiplicity of ions in production systems - for smaller manufacturer who can't afford many systems
  Source fuel feed systems for several ions, easily switchable, with long life (poisonous-corrosive) R&D systems exist but need engineered production

- Provide new ions for new materials beyond Si in future, viz:
  SiO_2 radiation hardening Al^+ 20 μA for 1000 hours
  GaAs possibly Be^+, Si^+, Te^+, (Al^+) 10-50 μA for 1000 hours

- Consider LN_2 cooling at source for commercial use for long life
  Consider improved alignment techniques and easier cleaning capability, interchangeable sources

- Higher brightness, moderate current, low energy spread for tiny, focused, deflection programmed beams

Technique	Mode		Intensity	Diameter	Total Beam Cross Section
	Interrupting	Continuous			
Scanning wire profiler (with slotted plate)		X	Semiq.	Semiq. Quant.	
Quartz plate	X		Qual.	Semiq.	X
Sensitive paper	X		Semiq.	Quant.	X
Faraday cup shutter	X		Qual.	Semiq.	
Gas pressure luminescence		(X)	Qual.	Semiq.	(X)
Quadrutured aperture elements coupled to deflection plates		X	Semiq.	Qual.	
Off-axis image converter		X	Qual.	Qual.	X
"Pepperpot"	X		(Quant.)	Qual.	

APPLICATION: LARGELY R&D, PRODUCTION NEEDS STABILIZATION

CHALLENGES: ADEQUATE - MOST ANY NEED CAN BE MET FROM THESE TECHNIQUES (SOME ENGINEERING MAY BE NEEDED FOR SOME)

ION SOURCES: STATE OF THE ART (From 9 Commercial Suppliers* and Hughes)

Type of Source	Companies Selling (of 9)	Companies Using In II Systems (of 10)	Ion	Fuel	Current (μA)	~ Lifetime, (hr)	ΔE (eV)	~Temp. for II (°C)	Power (W)	~Cost (K$)	Comments
• Radio frequency	5	4(~0)	B	BF_3	15-20	20-30	50-100	300-600	350	0.2	1000 μA too much (doping rate)
			P	PCl_3, PF_3	20-25	40-100(B, P)					100 μA OK
			As/	AsF_3	40	25-30(As)					$\geq 10^3$ hr desirable
• Duoplasmatron (tri)	3	2(1)	B	Elem.	50-80	1	15-25	1-2000	>500	11	$\leq 10^2$ too short for production
			B	BCl_3	15	50-100					OK R&D
			P	Elem.	25	14(+)					>~2K$ too much
○ Hot Filament Electron Impact (OED)	6	7(5)	HAC B	BF_3	30	100	1-2	200-700 (500-1000)	80-120	1	30 min. change to another 100 hr.
			HAC Al	$AlCl_3$	40	>10					
			HAC P/P_2	Several/P	60/200	100					
			HAC As/As_2	AsF_3/As	65/200	100					
• Cold Cathode	4	5(4)	HAC B^+	BCl_3	20-30	≥1000	$10-10^3$	100-300	100	1	30 min. change to another 1000 hr.
			HAC P^+	PCl_3	30	≥1000					
			B^+	BF_3	75	>100					
			P^+	PF_3	150	>100					
			As^+	AsH_3	100	>100					
			B^+	BF_3	50	100					
			P^+	PCl_3PF_3	50	100					
			As^+	AsF_3	40	100					
○ Hollow Cathode	1	1(1)	B	Elem.	50^+	10(B) 30-50(source)	≥2000			(10)	thermomech. support difficult, high maintenance
			B	Gas	100^+	30-50					

• Others not commonly used: Spark ioniz., surface ioniz., beam-plasma interaction

*Note: Since this information was collected two of the US suppliers have withdrawn from the field, a third has sold little equipment, and of those remaining, three are European.

MASS SPECTRA AND SEPARATION

WHY NEED 1) TO IDENTIFY ION SPECIES IN BEAM AND TO LOCATE DESIRED ION SPECIES

2) TO DETERMINE ADJACENT ION IMPURITY INTENSITIES AND WHETHER THEY WILL STRIKE TARGET DURING SCANNING

APPLICATION: LARGELY R & D (PRODUCTION DEVELOPMENT)

CHALLENGES: DIFFICULT AT LOW ENERGY (2-20 keV) - Pre-acceleration separation largely solves this and is efficient.

TARGET CHAMBERS

No. 2-in Wafers	No. Suppliers	No. 3-in Wafers	No. Suppliers	Types
24-30	4	18-40	3	Carrousel
35-60	2	~200	1	Cassette
≥200	2			Trays

CHALLENGES: Adequate, tho' more and better in 100's range

COOLED (LN_2)	HEATED (~600°C)	GONIOMETER (< 0.1°)
Number of Suppliers With Options		
6	5	4

CHALLENGES: Great here, State of the Art inadequate (if needed). Better multiple wafer schemes needed.

SCANNING

	2-D Electrostatic	2-D Mechanical	Hybrid
No. Suppliers	9	1	1

CHALLENGES: More good purely mechanical scan schemes

Advantages of mechanical scan: No variation of angle of incidence - better depth control
Shorter system - Cheaper? /no scanner and less line but TC more expensive

MASS SEPARATION

	Bending Magnet		ExB
	Pre	Post	
No. Suppliers	4	4	3

TERMINAL POWER SCHEMES

Alternator in terminal driven by motor at ground. Power supplies in terminal. (400 Hz 115 V)

Rack of laboratory power supplies, isolated through isolation transformer and varied by insulated shafts.

Teminal of power supplies driven by variacs varied by insulated shafts; single, isolated 115 VAC, 60Hz power source.

Power supplies in oil (or gas) at ground potential with individual isolation transformers and leads to source; programmed controls at ground, e.g. potentiometers and SCR's.

Warning: protective circuitry required for solid state circuitry at high voltage to prevent damage resulting from arcs.

SPECIALIZED TECHNIQUES

CHANNELING — For doping profile control

Requirements: Beam collimated or parallel to ~ 0.1 or 0.01°
Goniometer to manipulate sample
Very accurately cut wafers or auxiliary Rutherford backscattering equipment
Mechanical scan technique or double deflection electronic scanning to less than 1° or 0.1°

State-of-the-art/Challenges: Adequate in R&D for one sample.
Great challenge for development if deemed desirable.

TINY BEAM — For computer-programmed, maskless fabrication of specialized devices/circuits. For device concepts requiring dimensions below limits of photolithography. Not likely for mass production or conventional devices. Ultimate goal $< 1\mu m$ beam.

State-of-the-art: a few μm beam deflection progmammed over $\sim$ 1mm

Challenges: Technology in development. Many technical challenges before commercial exploitation.

SEMICONDUCTOR DEVICE PRODUCTION
A CHALLENGE TO ION IMPLANTATION

C. M. Pleass
Bell Telephone Laboratories, Incorporated
Reading, Pennsylvania 19604

To fulfill the commercial promise of implantation one must use it to gain precise control of dopant in the sensitive regions of silicon devices, regardless of dopant concentration, and at overall costs competitive with diffusion. Trade-off's against equipment cost include tighter distributions, improved device characteristics, and reduction or elimination of process steps such as in-process testing, spiking, glass removal, etc. This second generation of implanted devices should include bipolar transistors and silicon integrated circuits.

Specific device applications are described including boron and As SIC implants, in which implant must compete with diffusion, to illustrate the machine requirements. Particular attention is paid to the case of ion predeposition, where equipment is in its simplest, most compact form, and acceptance on the factory floor the most plausible.

THE DEPENDENT DEVICES

The ease with which Ion Implantation is accepted into semiconductor device production will depend on the commercial value of the improvements it offers. Its advantages can be broadly categorized as:

1. New product, dependent on implant.
2. Better product: improved characteristics meet more customer requirements.
3. The same product, cheaper.

The term "dependent" is used to describe devices which cannot be made in adequate yield without implant. They include hyperabrupt diodes, JFETS, high value resistors, and some IGFETS. If one examines their characteristics it is clear that the critical requirement which demands ion implantation is, in the

majority of cases, that of dose control at low dose levels. Figure 1 blocks out the various devices which fall in each decade of ion dose. Thus typical implant doses on hyperabrupt diodes are 9×10^{11} ions/cm^2, resistors fall in the range 10^{12} -10^{14} ions/cm^2, JFETS are commonly made at 10^{13} ions/cm^2, and IGFETS vary with the purpose of the implant, threshold voltage control demanding a dose of $1\text{-}5 \times 10^{11}$ ions/cm^2, and p-well doping for C-MOS circuits, approximately 10^{13} ions/cm^2.

To get these low dopant levels into perspective it is appropriate to recognize that a monolayer of Si contains $\sim 7 \times 10^{14}$ atoms/cm^2. At typical diffusion furnace temperatures of 1100°C and a hypothetical sticking coefficient of unity, monolayer coverage of a (silicon wafer) surface with ambient gas molecules will occur in approximately 10 nanoseconds. If the carrier gas contains one part per billion of a relevant impurity (one capable of disturbing the silicon doping) > 10^{17} of these impurity atoms will collide with each square centimeter of surface in the course of a relatively short 30 min. furnace treatment. Sticking coefficients for relevant impurities at high temperature are unknown, but even if they were as low as 0.1% one would lose long-term control of doping levels < 10^{14}/cm^2. The basic problem is that we have no practical way of controlling or even monitoring gas purity in a furnace at the part per billion level. Process control becomes a game of chance.

Ion implant represents a finite source of dopant which, ironically, can be controlled far better than it can be monitored in silicon. The measurable properties of "dependent" devices are usually dominated by other variables such as silicon quality or oxide charge. The remaining challenge within this area is therefore the elimination of other process variables. Figure 2, taken from a recent paper by Dill, et al., [1] illustrates this clearly: the actual threshold voltage of a device that has been adjusted by boron implantation shows a larger scatter than the increment due to the implant. In this case ordinary process variations such as SiO_2 thickness and surface states, Q_{ss}, contribute larger variations than the actual implantation. In the case of IC compatible JFET's, variations in resistivity within the epitaxial layer which receives the implant are dominant. Oxide quality runs a close second: $Q_{ss} > 5 \times 10^{11}$ could invert a p-channel device.

Let us regard the dependent devices as representative of a foothold in ion implantation. Figure 3 shows that all these low dose implants can be carried out at an economical rate on currently available equipment. Beam currents of < 10μa are entirely adequate to give throughputs of fractions of a minute per 2" wafer, and there are many machines with this capability on the market.

COMPETITIVE AREAS

Looking ahead to examples of devices where total dopant requirements are higher, and control easier, we find a strikingly different set of conditions limiting the introduction of implant to the production floor. The most fundamental is that there is no longer a choice of equipment which can perform the implants in times < 1 min. per 2" wafer. The other is that the situation is competitive: one can do a relatively good job with conventional diffusion technology. Thus boron doping from a BN predeposit in an open tube furnace can be held to ρ_S = 200Ω/□ , 3σ ∿ 20% over periods of many months, and doped oxide or sealed ampoule diffusions can do even better. Before one can move toward changing a production line from furnaces to implanters, the cost balance must be studied in detail. The final cost per wafer of the implantation, including the amortization of the equipment and realistic estimates of the value of improved device characteristics, must be no greater than that of the diffusion it replaces.

It is informative to calculate back from the cost/wafer in a conventional furnace diffusion to find out what production people would be willing to pay for implant equipment as a direct substitute for furnace capability. Assume that a modern BN furnace can accommodate 100 2" wafers per hour, including loading and unloading time. The cost of a facility capable of this would be approximately $10,000. Implant equipment is available which can match this throughput at the required base dose of 7×10^{14} ions/cm^2, and it can be used to improve both the uniformity and the reproducibility of the boron predeposition. However its cost is more than an order of magnitude greater. Thus for boron base predeposition it is obvious that the technical advantages which implant offers must be substantial if changeover is to be contemplated seriously.

If laboratory data are admitted in evidence, established advantages include tighter distributions, reduction in active areas, cost reduction through process simplification, and, ultimately, the opportunity for process automation. Tight distributions lead directly to better device yields and new freedom in design. Figure 4 shows typical data from Van der Pauw control wafers implanted at 50 kV with B^+ to a dose of 10^{14} ions/cm^2. The data covers an eight-month period, and it is clear that a 600Ω/□ B^+ implant can be controlled to $3\sigma < 9\%$. This is much better than the control available from boron nitride, which runs at 200Ω/□ $3\sigma \sim 20\%$ over long periods. Increased control leads directly to more uniform transistor characteristics. It may also encourage designers to move toward lighter base and resistor doping, even though the area saving must be compromised by a contact diffusion.

Cost reduction through process simplification can come from the elimination of steps such as glass removal, resistivity testing, and spiking. Since the error inherent in implant is substantially less than the error in a typical 4 point probe ρ_S measurement, the only reason for continued in-process testing would be to evaluate the effect of drive-in or annealing furnace control, and test frequency could drop drastically. Figure 5 shows an example of a state-of-the-art glass problem. In this case glass formation occurred during doped oxide diffusion, and "standard" procedures for removing the residues proved ineffective. This can be insiduous, since a wafer can often pass casual inspection while carrying traces of glass. The alternative, overetching, usually increases leakage in devices with fine geometries. The advantages of doping techniques that do not generate glass are substantial, and can be reflected in real dollar savings.

With all these lab data to refer to, the case for the introduction of implant seems likely to be a strong one. However, it is not sufficient to demonstrate a process improvement in the R and D lab, and expect instant response from the production floor. The normal prerequisite to introducing a more expensive new process to production is a statistically significant demonstration of superiority in the production line environment. This can be problematical, and needs illustrating with a specific example. Figure 6 gives laboratory ρ_S data from boron base-resistor implants, carried out on seven different occasions. The objective value was 200Ω/□, and it is clear that this was met to very close limits.

Figure 7 represents a "split lot" on a production line, with the implant performed under nominally identical conditions to those of Figure 6, and the control diffused. The median value came out at 245Ω/□, and there was no distinguishable difference between the implanted wafers and the diffused controls. Fortunately, these data were generated by someone who wanted to believe in the advantages of ion implantation and an alternative analysis as $\Delta\rho_S$ (Figure 8) showed that both the implant and the control had broken distributions, suggesting that something else in the process was out of control. This justified running another split lot, and for the first time, some sign of the ρ_S control that had been seen in the laboratory implant data began to emerge, (Figure 9).

This example should make it clear that the future of implant as a production technique for semiconductor doping is tied to the quality of the other process steps which come between the act of implantation and the next significant electrical test. The engineer interested in promoting implant in high volume, economically significant processes, must be prepared to become involved in many other aspects of Si device processing, and improve these to the point where the advantages of implant are demonstrable.

There is one exception to this which is particularly interesting in that it provides a painless route to the justification of high beam current implant equipment. That is the implantation of arsenic, to form transistor emitters or buried collectors. Since arsenic is a metalloid with a high vapor pressure, it is relatively easy to make ion sources which use the elemental form, and which are consequently quite efficient. An ion implanter which normally gives ten microamps of B^+ from BCl_3 and an RF source would be expected to produce approximately 30μa of As^+. Similarly, isotope separator sources should be capable of producing several milliamps of As^+.

Conventional diffusion sources for As leave much to be desired. This is partly due to the inherent hazard: high temperature diffusions using As_2O_3 or elemental As have to be regarded as dangerous when used in a production environment, even if they are carried out in closed vessels. Some commercial thin film sources have been developed but in general these either limit the maximum attainable surface concentration or give rise to glass removal problems. The best of them appears to be Ge/As doped SiO_2, but commercial equipment which can

deposit doped oxide on 50 2" wafers an hour will cost approximately $50,000. This makes a high current ion implanter a cost-competitive source of As. Indeed it is possible that dedicated As implant machines can be constructed at substantially lower cost.

There are also substantial technical advantages to this kind of As source. It is easily controlled over a wide range of required concentrations, and does not give rise to glass formation. Attainable surface concentrations are limited only by the solubility of As in Si, and both emitters and buried collectors may be prepared with resistivity < 10Ω/□ .

CONCLUSION

Each specific device application must be examined in terms of the economic balance between demonstrable process control, change in process complexity, throughput, and facility cost. When applied to modern high volume transistor and SIC technology, such an analysis leads to the conclusion that a prerequisite to large-scale industrial use of ion implantation is the introduction of high current, high throughput equipment.

Various applications of ion implantation to Si device production have been examined. The example of As implant was discussed at some length because it represents one of the few shortcuts to the justification of high current ion implant equipment. Analysis of the utility of implant in the preparation of boron doped bases and resistors leads to the more general conclusion that the future of implant in semiconductor device production will be profoundly influenced by the rate at which other steps in the semiconductor device manufacturing process are brought under control. Processing steps such as oxide growth or drive-in diffusion can swamp the control intrinsic to implant and foster a negative attitude. Individuals interested in promoting implant as a commercially viable technique cannot remain aloof from the other processing problems which currently limit yield and device cost.

ACKNOWLEDGEMENTS

The author is indebted to R. J. Duchynski for helpful discussions and technical data, and to C. W. Brownmiller and R. A. Clapper for the characterization of machine performance.

REFERENCE

1. Dill, H. G., Toombs, T. N., and Bauer, L. O., Proceedings of the 2nd International Conference on Ion Implantation in Semiconductors, p. 315, 1971.

SEMICONDUCTOR DEVICE DOPING LEVELS

DEVICE TYPE	>10K Ω/□ Resistors	2 10K Ω/□ Resistors	0.5 2K Ω/□ Resistors	Bipolar Transistor Bases	Transistors Emitters
	Hyperabrupt Diode	p Channel JFET	n Channel JFET	SIC Base and Resistor	SIC Buried Collectors
	IGFET Threshold		IGFET p well	IGFET Self Aligned Gate and Contact	SIC Isolation
ION DOSE/cm²	10^{11}	10^{12}	10^{13}	10^{14}	10^{15} 10^{16}

FIGURE 1

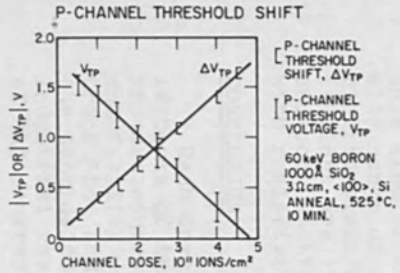

FIGURE 2

BEAM CURRENT REQUIREMENTS AND AVAILABLE EQUIPMENT

ION CURRENT FOR ONE 2" WAFER MIN		1ua	10ua	100ua	1ma
DEVICE TYPE	>10K Ω/□ Resistors	2 10K Ω/□ Resistors	0.5 2K Ω/□ Resistors	Bipolar Transistor Bases	Transistors Emitters
	Hyperabrupt Diode	p Channel JFET	n Channel JFET	SIC Base and Resistor	SIC Buried Collectors
	IGFET Threshold		IGFET p well	IGFET Self Aligned Gate and Contact	SIC Isolation
ION DOSE/cm²	10^{11}	10^{12}	10^{13}	10^{14}	10^{15} 10^{16}
COMMERCIAL MACHINE DESIGNS ADVERTISED AS CAPABLE		6	6	2	1

FIGURE 3

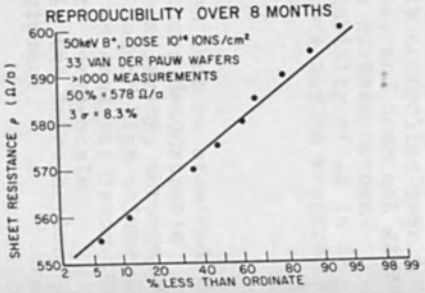

FIGURE 4

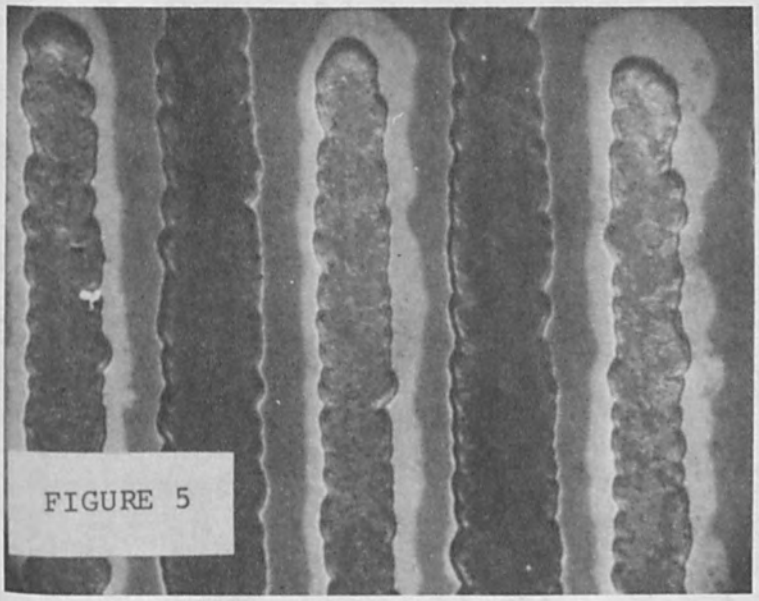

RESIDUAL As GLASS IN MICROWAVE
EMITTER WINDOWS

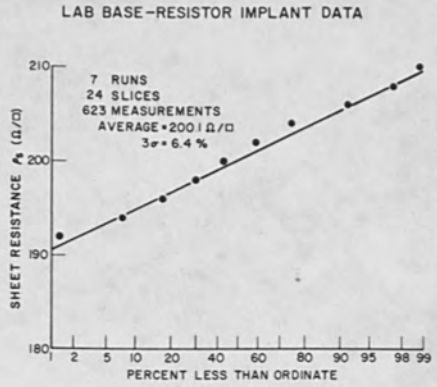

FIGURE 6

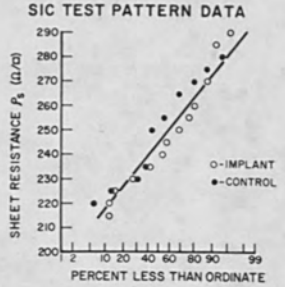

FIGURE 7

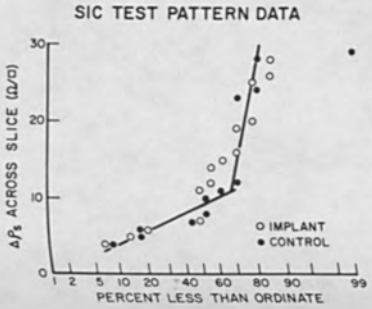

FIGURE 8

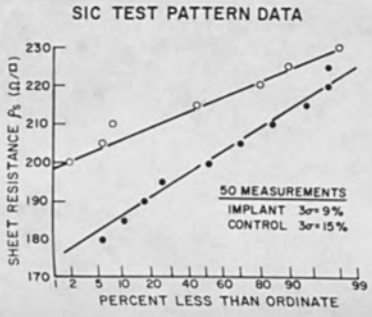

FIGURE 9

PRODUCTION MACHINE REQUIREMENTS FOR ION IMPLANTATION PROCESSING IN THE SEMICONDUCTOR INDUSTRY

M. R. MacPherson

National Semiconductor Corporation
2900 Semiconductor Drive
Santa Clara, California 95051

ABSTRACT

Production machine characteristics are dictated by the manufacturing processes needed. The three major requirements for MOS circuits are: 1) Threshold shifting for low threshold enhancement mode devices or for depletion mode load transistors; 2) Precise predep charge for CMOS p wells; and 3) small accurate resistors. It is clear that ion implantation must not introduce significant deviations from present MOS process tolerances. To that end, dose and energy repeatability must be greater than ±2% throughout their respective ranges. A dose range of 10^{11} to 10^{14} ions/cm^2 (within certain time limitations) at energies from 10 to 150 keV should be available. Overall wafer uniformity should be within ±5%. Finally, a production ion implantation machine must be capable of processing several thousand wafers per week.

INTRODUCTION

Ion implantation, in order to be viable, must perform a function that is not possible with existing techniques, or do the same job better or cheaper. The process does offer several unique advantages:

1. Wide variety of impurities.
2. Low temperature processing.
3. Control of profile.
   a. Shallow distribution
   b. Dose control
   c. Low lateral spread as compared to diffusion

Of these, the most important is control through precise doping in a concentration region which is very difficult to obtain with standard diffusion techniques. Ion implantation has now become sufficiently practical to move from the R&D stage into production.

The applications of ion implantation to discrete devices are by no means small, however, I believe that the most rapid development in the near future will be in integrated circuits. Bipolar circuits

use ion implantation principally for resistors. High volume production of the bipolar devices themselves appears to be still in the future. By far the widest variety of uses are found in MOS circuits. Some of the most important are resistors, threshold shifted enhancement mode devices, depletion mode loads, and predeposit for field doping or CMOS p wells. The following discussion will be limited to MOS IC applications.

THE PRODUCTION ION IMPLANTATION MACHINE

Characteristics for an implant machine are determined by the present requirements of the IC process. Considering first the source, we must specify what dopant species and what doping concentrations are needed. Boron and phosphorous, with the possible addition of arsenic, provide all of the necessary dopants for existing production needs. The current output of the source will determine maximum doping concentrations for the process, due to time limitations. Currently available sources yield 10 to 20 μA of boron on target. We might arbitrarily divide the doping spectrum into segments for analysis:

1. Threshold Shift - 10^{11} to 5×10^{12} ions/cm^2
   Suitable through depletion mode devices.
   Source current $\leq 1\mu$A for a 30 second implant.
2. Resistors and Pre-dep - 5×10^{12} to 10^{14} ions/cm^2
   Source current $\leq 20\mu$A for 30 second implant.
3. p^+ and n^+ pre-dep and low value resistors $> 10^{14}$ ions/cm^2
   Beyond present source capability for B^{11}.

Leaving number 3 to diffusion which for the present does the job better, there remains a large segment of doping applications for ion implant with currently available sources.

The next consideration is how uniformly can the dopant be distributed across a wafer. Threshold shifting for enhancement mode devices uses the smallest doping concentration. Further, dopant implantation is usually done through a gate oxide of low energy. Both tend to degrade uniformity. Existing production techniques yield very uniform gate threshold voltages. In order to be useful, implanted devices must exhibit essentially the same uniformity. We might examine what an existing production implant machine will yield along these lines. Figure 1. displays uniformity of enhancement mode devices after a 0.8 volt threshold shift by boron. The standard device and shifted device Gaussian distributions are shown in addition to the uniformity plot. Figure 2. displays depletion mode p channel threshold voltage uniformity. Similarly, one can say the same for resistors and pre-dep applications. Figure 3. and 4. show uniformity plots for low and high temperature annealed resistors, respectively. Low temperature devices were implanted after metal etch and annealed

at 545°C. High temperature devices were implanted after gate oxidation and annealed at 1000°C. Two sheet resistivities are shown for each; variations are probably due to processing. Figure 5. shows equivalent pre-dep uniformity. These results are entirely useful for a production process.

Dose accuracy should be good, but need not be spectacular. As with most such processes repeatability is the key. Integrator accuracy must be around ±1% or less so that high repeatability may be achieved. Energy requirements for production processes may range from 10 to 150 keV. Higher voltages for boron will cause penetration of field oxide. Of course, higher voltages for phosphorous or arsenic could be used, but with appreciably amounts of P^{++}, depths compariable to boron may be achieved. Higher energy machines increase cost, complication, and X-ray output. However, if deep penetration of a heavy ion such as arsenic is needed for special pre-dep requirements, higher energy may be mandatory. Again, repeatability is far more important than absolute accuracy. Shallow implantation through gate oxide will tax repeatability most.

A good sized semiconductor house may process in excess of 10,000 silicon wafers a week. If ion implantation is to be used on a significant portion of these, a wafer processing problem will soon have to be faced. For sake of illustration assume 2 shifts use a single machine yielding 14 usable hours of operation. Take a 4 day week (allowing 16 hours down time) and one comes up with a capacity need of 90 wafers per hour. If the average implant time is 30 seconds we have only 15 minutes per hour for shuttling wafers in and out of the machine. Obviously, pumpdown and shuttling time must be held to a minimum.

INTEGRATION INTO A PRODUCTION LINE

Finally, an implant machine must be integrated into an existing production facility. Ideally, it should be within the process flow. Large producers would require many machines; one or more per product line. Although there are obvious advantages to such a system, most companies at present would find it more economical to have a single centralized facility. There must be as smooth a flow as possible to and from implant and within the implant processing area. To that end, we have constructed a room with dustfree laminar flow hoods over the machine end station and over the wafer loading area. Further, dry nitrogen storage boxes will be available for trays awaiting implant and returning to the parent product line. A wet hood provides a cleaning facility for both wafers and wafer holders. Figure 6. shows a top view drawing of such a layout. Final integration into a product line will be necessary when the output level for a single process rises sufficiently. For such cases a "dedicated" machine (one that does a specific job such as threshold shifting) is to be favored.

SUMMARY

The following list provides a framework of characteristics for a production ion implantation machine used in current MOS IC manufacturing.

1. Species: B^{11} and P^{31}
2. Dose Range: 10^{11} to 10^{14} ions/cm^2 in less than 30 seconds per wafer.
3. Energy range: should be perhaps 10 to 150 keV for most applications.
4. Dose/energy accuracy and repeatability: should be ±5% and ±2% respectively.
5. Implant uniformity must be within ± 5%.
6. Wafer throughput should be around 5,000 per week.
7. Cost must be competative with other production machines with similar complication and throughput (approximately $50,000 to $70,000).

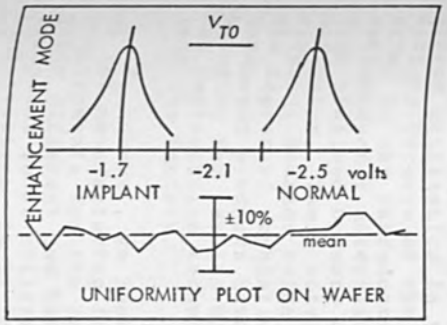

FIG. 1: UNIFORMITY OF ION IMPLANTED ENHANCEMENT MODE MOS TRANSISTORS

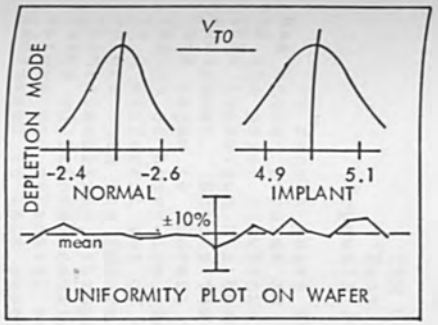

FIG. 2: UNIFORMITY OF ION IMPLANTED DEPLETION MODE MOS TRANSISTORS

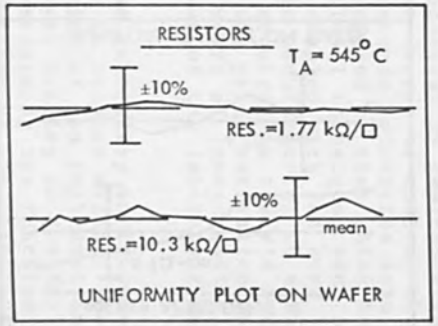

FIG. 3: UNIFORMITY OF ION IMPLANTED RESISTORS - LOW TEMPERATURE ANNEAL

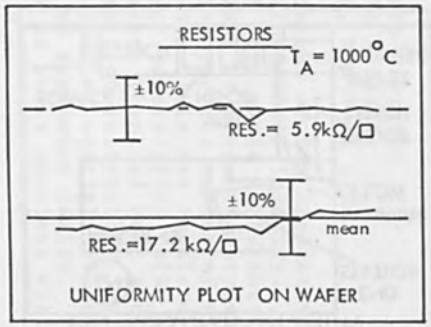

FIG. 4: UNIFORMITY OF ION IMPLANTED RESISTORS - HIGH TEMPERATURE ANNEAL

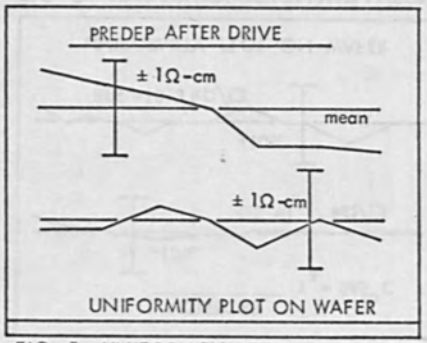

FIG. 5: UNIFORMITY OF ION IMPLANTED C-MOS P-WELL PREDEPOSIT

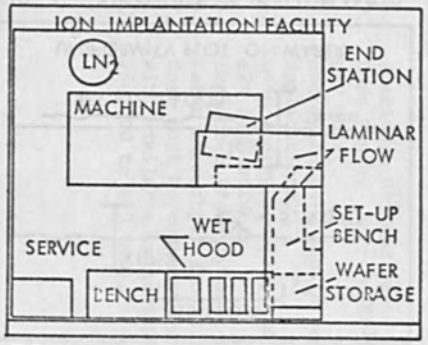

FIG. 6: ION IMPLANTATION MOS IC PRODUCTION FACILITY

ION IMPLANTATION EQUIPMENT FOR SEMICONDUCTOR MANUFACTURING

W. J. Kleinfelder

IBM Components Division
East Fishkill Facility
Hopewell Junction, New York 12533

In recent years the technique of ion implantation has become popular in the semiconductor industry. One of the major drawbacks to the more rapid acceptance of this technique has been the lack of production-type equipment. During the last few years a number of firms have begun to address this need. This has required the design of heavy-ion, low-energy accelerators (<150 Kev) to a different set of constraints than had been addressed before. In the future, emphasis on reliability, safety, maintainability, thruput and further specialization will force additional constraints on equipment design. The nature and potential solution to these problems will be addressed in this paper.

INTRODUCTION

Ion Implantation techniques are rapidly approaching widespread utilization in the production of semiconductor devices because of the greater degree of control they offer in the introduction of atomic impurities into semiconductor materials as compared to that which has been obtained by more conventional techniques such as diffusion. These attributes coupled with the ever increasing demands being made in manufacturing to achieve the degree of sophistication required in today's semiconductor products have been the prime motivation in bringing the results of many years of investigation of ion implantation techniques out of the laboratory and into the factory.

If, however, we look at the laboratory environment vs the manufacturing facility it becomes evident that the requirements for the utilization of ion implantation are quite different and have a great bearing on the design of equipment to be utilized in performing the function of ion implantation. It is the discussion of the significance of this change on the design philosophy of low-energy heavy-ion accelerators that will be discussed in this paper.

LABORATORY VS FACTORY REQUIREMENTS ON ION BEAM EQUIPMENT

Table I contrasts the nature of these two environments in which the ion equipment is used. The general nature of the use of ion equipment in the laboratory environment is the generation of data and gathering of facts with skilled personnel. The primary use of the equipment is experimental and highly flexible. The factory on the other hand is generally a fixed-use environment, highly cost conscious and relatively unskilled. The decision to use ion beam equipment is motivated by reduced manufacturing cost or to achieve added product value by tighter tolerance, improved performance, etc. The design of ion equipment for these needs may be significantly different.

TABLE I. The Environment

	Development	Manufacturing
1. Major Motivation for Use	Investigation of New Techniques	Financial Gain
2. Output	Experimental Results and Hardware	Product
3. Installation Constraints:		
Cost	Not of Major Significance	Important
Reliability		
Safety	Important	Major Problem
4. Thruput Requirements	Very Minor (Not Important)	High (Very Important
5. Equipment Utilization	Highly Flexible	Fixed Process
6. Technical Competence of Personnel	High	Low

Technical Requirements

The first use of ion beam equipment in the factory will be to replace or augment the current use of thermal diffusion as a method to introduce impurities into semiconductors. It is therefore worthwhile to spend some time discussing the implementation of diffusion-type processes in the factory environment and thereby develop some limits on the design objectives for ion implantation equipment.

Table II lists some of the advantages of ion implantation over thermal diffusion. These are the prime motivations for the interest in ion implantation processes and their combined exploitation may permit the design and manufacture of inherently superior and cheaper semiconductor products. Let us now explore the cost of operating a typical conventional diffusion facility in the manufacturing environment.

TABLE II. Advantages of Ion Implantation Processes for the Manufacture of Semiconductor Products.

	Ion Implantation	Diffusion
Process Control		
Dopant Uniformity and Reproducibility	±1% Overall	±5% On Wafer* ±15% Overall
Contamination Danger	Inherently Low	High
Delineation Techniques	Refractory and Non-Refractory Materials: Insulators, Metals, Polymers (Beam Writing)	Refractory Ins. Refractory Metals Poly Silicon
Product Environment	Vacuum (Benign)	High Temp. (Hostile)

* Depends on diffusion parameters and materials as well as doping level.

Figure 1 shows a typical, modern installation of diffusion equipment in a semiconductor process facility. The exact value of the cost of operation is subject to some variability depending on the nature of the facility, the product manufactured, etc.; however, the basic elements of cost remain the same. Table III gives values for some of the relatively fixed elements of cost for a typical installation.

TABLE III. Elements of Diffusion Operations Cost.*

Total Capital Cost of Installation	<$15K
Space Requirements	~75 Sq. Ft.
% Availability	~95%
Operating Personnel	~1/3

While diffusion furnaces and ion implantation equipment resemble each other in function, vacuum evaporation and sputtering equipment are more closely related to ion implantation equipment in configuration. Therefore, as a first order indication of the fixed costs to be expected for ion implantation equipment, we can use figures based upon experience with vacuum evaporators. These are given in Table IV, which shows that all fixed elements of cost are higher for vacuum equipment than those for diffusion equipment. Clearly, if the only element of cost were these, ion implantation would be at a distinct disadvantage relative to diffusion. However, in addition to the fixed elements of cost there are two other major cost determining factors: 1) the amount of product processed per unit time (thruput), and 2) the amount of product scrapped due to failure of the process in question (yield).

TABLE IV. Elements of Vacuum Evaporation Operations Cost.**

Total Capital Cost of Installation	~$30K
Space Requirements	~150 Sq.Ft.
% Availability	~95%
Operating Personnel	~1/2-1

---

* On a per tube basis in a large installation.

** On a per evaporator basis in a large installation.

Figure 2 compares the thruput of 2" wafers through a typical diffusion process to that which may be achieved in an ion implant facility. The thruput in sec per wafer is plotted versus sheet resistivity ρ_s. The curve for ρ_s as a function of implant time is theoretically derived by integrating the differential sheet conductivity over the LSS theoretical profile obtained from the indicated parameters. It has been assumed that the energy is sufficient to achieve the desired junction property without further diffusion of the implanted atoms. The time per wafer does not include the annealing cycle which can often be accomplished in conjunction with other required processing and solid solubility is assumed to be the dopant limit. It is observed that thruput is more dependent upon the variable ρ_s than is the case in diffusion technology. Thus, in cases in which it is necessary to achieve the same thruput as diffusion with high doping levels, beam currents as high as ~1ma may be required. However, a significant portion of processes do not require such heavy doping and therefore may be met with beam currents of about a factor of 10 less.

Because of the tighter control over process variables that has been obtained by ion implantation, the product yield which may be expected with ion implantation processes may be significantly higher than that of an equivalent diffusion process. This means that even in cases in which ion implantation results in lower thruput it may be economically superior.

Beyond the simple considerations of minimizing processing costs ion implantation can offer economic advantages by its ability to achieve significantly more aggressive products. Therefore, profits may be realized by the added value to the product due to increased performance, etc.

Safety and Installation Limitations

Ion equipment in many aspects is potentially more dangerous to operate than equivalent diffusion equipment. Potential safety hazards in diffusion installations include high temperatures, highly toxic substances and high electrical power requirements. Ion beam equipment has the same problems as diffusion equipment with the exception of high temperatures, but has additional serious problems with high voltage, vacuum and radiation. Extensive safety protection may be expected to be required in installations destined to be operated by people who are generally unfamiliar with these potential hazards.

There are specific guidelines established by the Federal government for the installation of manufacturing equipment including ion accelerators. Where Federal laws do not apply, individual states have taken the Federal established guidelines and made them law. Some states have added additional controls to the Federal guidelines.

The Federal "Occupational Safety and Health Act of 1970" (PL-91-596) is designed to give standards for safe working conditions and provides authority to the Department of Labor and to the Department of Health, Education and Welfare in such matters. Table V lists some requirements applicable to the use of ion equipment for factory installation. Designing for these constraints may significantly alter the options available in the construction of ion implantation equipment.

In addition to these safety requirements, general practice also requires extensive automatic features to protect the equipment from damage due to accidental loss of power or other required facilities. The extensive cleanliness associated with typical semiconductor fabrication facilities also may place requirements on the design and installation of ion implantation equipment. This might include such items as separate access to the equipment for maintenance and repair which does not affect the general cleanliness of the part of the facility where the product is handled. The cleanliness of semiconductor facilities, which is necessary to ensure high production yields, will also dictate design constraints on the handling of wafers in the ion implantation equipment itself.

ION BEAM EQUIPMENT DESIGN

The general requirements of the components of a production ion implantation facility revolve around simplicity, safety, maintainability and cost effectiveness. The functional components of a small heavy-ion accelerator are given in Fig. 3. Three basic parts may be distinguished: 1) the ion source, 2) the mass analysis section, and 3) the target chamber. It is important to investigate the nature of various possible configurations of these components in light of the previous requirements and restrictions. It is worthwhile first of all to consider which components will be placed at high voltage.

TABLE V. Safety Requirements*

Toxic Substances

- Separate exhaust to atmosphere for all toxic gases.
- Automatic Fail Safe closure on valves for hazardous materials.

Radiation

- Operator exposure limited to <.2mr/hr. during operation.

High Voltage

- All potentially hazardous volts fully protected from accidental contact.
- All high voltage supplies must self bleed with power off.

General

- Legal restrictions on flammable materials when within 50' of electrical apparatus. (Article 500 National Electrical Code of 1972).
- Primary power emergency disconnect provision required.

---

* Occupational Health and Safety Act of 1970 and revisions.

In the most general accelerator any of the three major sections can be held at high potential and any two sections which are at widely differing potentials will have a buffer region between them, commonly known as an accelerator tube. An accelerator tube is basically nothing more than a vacuum section containing a series of electrodes; the purpose of it is to accelerate the ion beam without changing its focal properties. Along the beam line, there may be any number of pieces of peripheral equipment such as beam deflection plates, electrostatic or electromagnetic quadrapole focussing sections and beam detection equipment. These additional items are not of major importance here. However, it must be kept in mind that in any basic configuration some of this equipment may have to be powered controlled or monitored remotely from a point of differing potential.

Most accelerator installations presently used for ion implantation use DC potentials to accelerate singly ionized atoms to their final energy. This implies that the potential difference from one end of the accelerator to the other is what determines the energy of the ion. This also implies that part of the machine must be at high voltage. In a typical ion implantation installation the source section II (Fig. 3) is isolated at high potential, and the remainder of the accelerator is at ground. These systems employ pre-acceleration through an acceleration column connected between the source and the mass analysis section. The post acceleration section is missing in this case.

Due to safety requirements mentioned earlier, high voltage parts of the equipment must be isolated from any possible contact from the operator. The target area is the point where the product is handled and therefore subjected to severe environmental constraints as well as being exposed to factory personnel. This suggests a strong motivation for having the target end of the accelerator at ground potential. Any other configuration subjects the operator to possible contact with high potentials and creates problems with operator interlock requirements, accessibility and a large utilization of floor space for voltage and environmental isolation. It is also envisioned that the requirements for clean environments in the area where the product is handled through the ion implant equipment makes the problems of having the target at high voltage even more difficult.

The stringent requirements on radiation levels, as indicated earlier, will undoubtedly lead to a strong

motivation to perform mass analysis before the beam undergoes its major acceleration. Because in general the analyzed beam current is much smaller than the source current, this minimizes the radiation generated due to secondary emission and acceleration of electrons, especially at high-beam currents and high-acceleration potentials.

Acceleration after mass analysis also minimizes the problems associated with the design and physical size of the mass separator section of the equipment.

Because the requirements of mass separation in ion implantation equipment are less critical than in other uses such as analytical mass spectrometry, the mass analyzer section will approach the simplest design possible. A permanent magnet will probably prove desirable for all requirements. In all manufacturing installations simplicity is a great asset both in cost, reliability and maintenance aspects.

As an additional note, post-acceleration inflicts far less stringent requirements on the regulation of the high-voltage power supply. Normally, fluctuations in ion energy of a few percent do not affect an implantation process materially, however, fluctuations in pre-acceleration voltage affect the mass resolution of the mass analysis section strongly. With a post acceleration system, good regulation is required only of the lower voltage pre-acceleration supply.

It is important to note that in most manufacturing applications flexibility in utilization is rarely required. That is to say one piece of equipment is rarely used to perform more than one function. A furnace does not perform diffusion of two separate atomic species nor will any one piece of ion implantation equipment installed in a semiconductor factory of any size be required to implant ions of different species at the same time. This is not to say that the basic accelerator design should not be flexible enough to be reconfigured for many jobs. A furnace can be configured to do more than one type of diffusion or an evaporator can be set up to evaporate many types of materials, but not without modifying the equipment in some permanent manner. Ion implantation equipment will take on this same nature; that is constraints on cost, reliability, maintainability and installation space will be met at the expense of flexibility. As an example sources will be customized for a single function, to achieve higher output and longer life. Sources, however, will probably be

interchangeable within a particular accelerator.

Due to the requirements of achieving low radiation levels and reducing the constraints associated with high-voltage insulation, sources producing multiple ionized species will be desirable. A good example is arsenic which is heavy enough to require considerably high potentials for a given penetration into the substrate and has reasonable second and third ionization potentials. This projected range can be approximated by:

$$Rp = 1.08 \times 10^{15} \cdot \frac{E}{N} \cdot \frac{(M_1+M_2)}{(3M_1+M_2)} \cdot \left(\frac{Z_1^{2/3} + Z_2^{2/3}}{Z_1 Z_2}\right)^{1/2} cm$$

where, E = ion energy in volts, N = atomic density of target in atoms/cm^3 and M_1,M_2, Z_1 and Z_2 are the ion and target atomic mass and ion and target atomic number respectively. Therefore, for the same Rp Arsenic requires 2 times the energy of phosphorus for equivalent junction depths. Source materials will also be chosen to be least toxic and to have minimum influence on the system degradation.

CONCLUSION

The following basic design for an ion implantation machine suits the constraints that have been discussed here.

Ion Source

The source will be specifically designed for the ion required. A simple geometry such as a cold-cathode plasma source having a nominal lifetime of ~100-500 hrs. is an example. It will be able to be replaced in <1 hr. and have a repair cost of <$50. The power consumed is not critical but the source will be simple in design and inherently stable.

Mass Analysis

A simple permanent magnet will be located in the high voltage terminal. Control over mass analysis will be obtained by variation of the extraction energy. This is a suitable design since approximately constant beam

current of phosphorus and boron is acceptable. In practice it is observed that for constant extraction potential beam currents of phosphorus exceed that of boron by about a factor of 2.

Beam currents vary approximately as the square of the extraction energy while with a constant magnet flux the radius of curvature varies as the square root of the energy. Therefore, it appears that approximately equal beam currents of phosphorus and boron can be obtained in the manner proposed.

Acceleration

A simple accelerator with few sections and a narrow permissible energy range without mechanical adjustment will be used. Constant-field multiple-stage accelerators are too complicated.

Target Assembly

The design of the target area will be primarily dictated by standard semiconductor processing practice. Future demands will include extreme cleanliness and achievement of high process uniformity including control of incident angle of the ion beam and precision scanning. Beam writing and the utilization of channeling as a manufacturing process are not in the near future and will not be available as options for factory utilization over the next few years.

Overall Considerations

The general complexity of the equipment will be minimized. External controls will also be minimum, and all adjustments to the equipment necessary to hold the process parameters will be done automatically. Fail safe and safety will also motivate overall design consideration. The equipment must take up considerably less space than the typical installation at present (i.e., <300 sq. ft.) and should be less expensive (i.e., <$50 K).

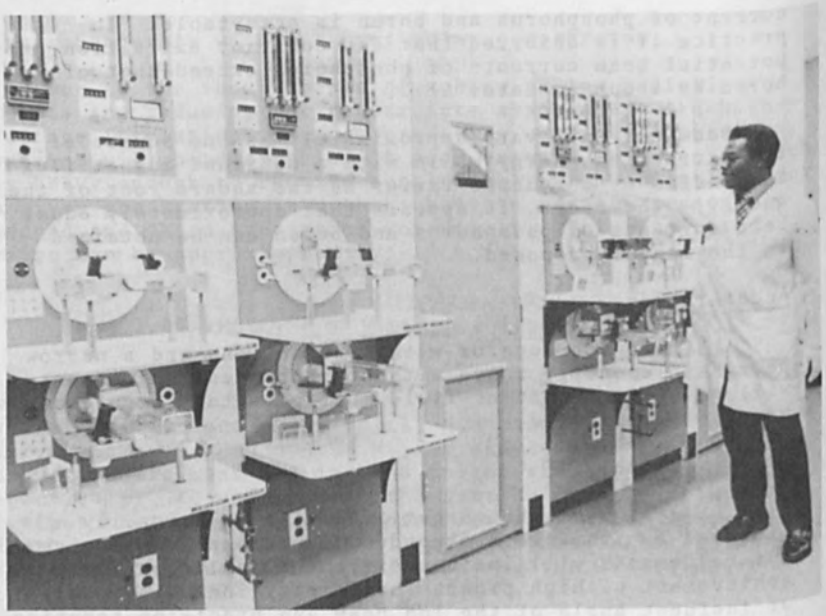

Fig. 1. Typical diffusion furnace installation.

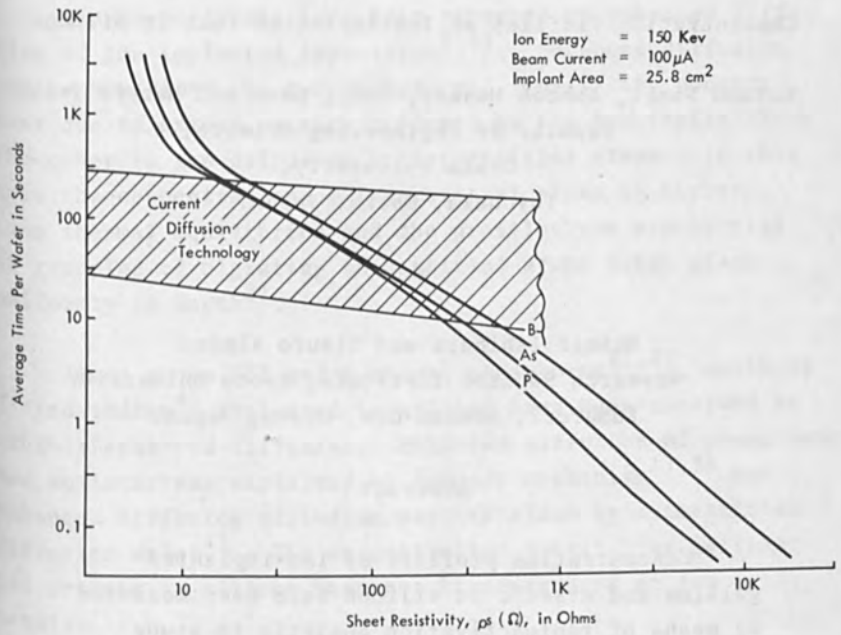

Fig. 2. Average process time per wafer as a function of resulting sheet resistivity ρ_s.

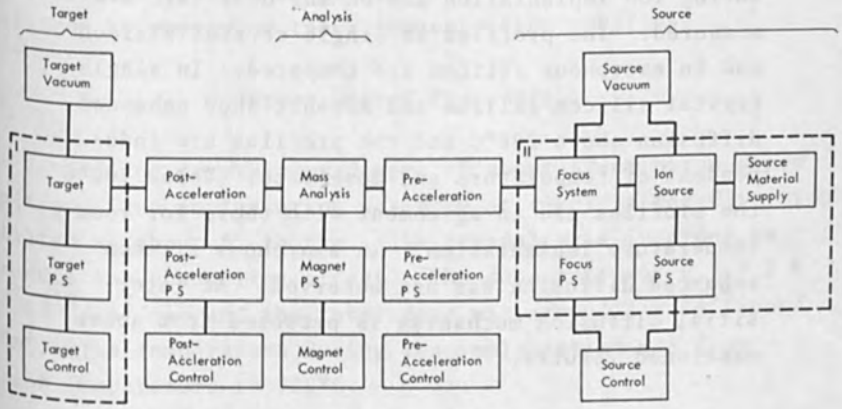

Fig. 3. Block diagram of a general ion accelerator.

Concentration Profiles of Ion-Implanted Ions in Silicon

Susumu Namba, Kohzoh Masuda, Kenji Gamo and Masaya Iwaki
Faculty of Engineering Science,
Osaka University,
Toyonaka, Osaka, Japan.

and

Shinji Ishihara and Itsuro Kimura
Research Reactor Institute, Kyoto University
Kumarori, Sennan-Gun, Osaka, Japan.

Abstract

Concentration profiles of ion-implanted gallium and arsenic in silicon have been measured by means of radioactivation analysis to study enhanced diffusion of ion-implanted impurities. The dependence of the profiles on temperature during ion implantation and on the dose rate are measured. The profiles in single crystal silicon and in amorphous silicon are compared. In single crystal silicon gallium and arsenic show enhanced diffusion above 200°C and the profiles are independent of temperature and dose rate. Below 100°C the profiles are in agreement with those for room temperature implantation. In amorphous silicon enhanced diffusion was not observed. An intersitial diffusion mechanism is proposed from above mentioned results.

Many experiments have been reported on enhanced diffusion of ion-implanted impurities[1-4]. Enhanced diffusion can be explained by two mechanisms. One is the enhancement due to excess vacancy produced by the ion implantation. The other is the diffusion by interstitial atoms. In this case the concentration of interstitial atoms is higher than thermal equilibrium and the profiles are exponential if trapping of migrating interstitial atoms takes place uniformly in depth[5].

Among group III and V atoms, phosphorus[1),2)], antimony[3)] and indium[4)] implanted in silicon have been observed to exhibit enhanced diffusion. Enhanced diffusion of phosphorus and antimony was explained by vacancy mechanism[1),3)] but enhanced diffusion of indium was explained by interstitial diffusion model[4)]. The concentration profiles of gallium and arsenic in silicon have not been measured so far in detail.

The aim of the present report is to investigate the diffusion mechanism of gallium and arsenic implanted in silicon by measuring their concentration profiles.

Experimental Procedure

Silicon crystals used were of about 5Ω-cm boron doped p-type. Ion implantation was made at 45keV in the direction tilted at about 8° to the <111> crystal axis in order to reduce the channeling effect. The dose rate was 0.3~7.2 x 10^{12}/cm^2/sec and the total dose was around 1 x 10^{15}ions/cm^2. The temperature during ion implantation was from room temperature to 700°C.

The neutron activation was carried out after ion

implantation by exposing to a neutron flux of about 2.8 x 10^{13}neutrons/cm^2/sec for 60 or 600 minutes. The sample was sectioned by the successive layer removal technique by anodizing and HF stripping to measure the concentration profiles. NaI scintilation counter and 100 channel pulse hight analyser were used to measure γ rays spectrum. Half-life determinations and γ rays spectral analysis were used for positive identification of the istopes.

Results and Discussion

Figure 1 compares the concentration profiles of room temperature ion-implanted arsenic in crystalline silicon oriented 8° off to the <111> crystal axis and in amorphous silicon. Amorphous silicon was produced by prebombardment with nitrogen molecular ion beam at an energy of 45keV at room temperature with the dose of 5 x 10^{15}ions/cm^2. The profile observed for room temperature ion implantation in amorphous silicon was approximately gaussian. Solid line indicates the theoretical prediction given by LSS theory[6]. Experimental values of the average projected range and the standard deviation were about 290±20Å and 130±15Å respectively and the theoretical values are 287Å and 103Å. The profile for crystalline silicon agreed with that for amorphous silicon except the tail region. This tail may be caused by channeling effect or interstitial diffusion before the damage density becomes sufficiently high.

Moline[7] measured the concentration profiles of room temperature implanted phosphorus in silicon by C-V measurements and concluded that the tail probably results from an anomalous diffusion mechanism such as interstitial diffusion, because the slope of the exponential tail was independent

of the energy of the ions.

The concentration profiles of ion-implanted gallium and arsenic in silicon at various temperature are shown Figs.2 and 3, respectively. The energy of the ions was 45keV. The dose rate of the ions was about 3×10^{11} ions/cm^2/sec and ion implantation was done for 1 hour. The total dose was 1×10^{15} ions/cm^2. As can be seen from Figs.2 and 3, a critical temperature exists for deep penetration to occur. It is between 100 and 150°C for gallium and between 100 and 200°C for arsenic above these temperatures gallium and arsenic penetrate deeper than at room temperature and the concentration profiles were almost independent of temperature and exhibited exponential tail. Below the critical temperature the profiles agree with those observed for room temperature implantation. Channeling[8] and enhanced diffusion are the possible mechanism for the deep penetration. To determine which mechanism takes place it is necessary to measure crystal orientation dependence of the profiles. In Fig.4, the profiles of gallium implanted in the two directions tilted at ~8° and ~50° to the <111> crystal axis are compared. The slope of the exponential tail is almost the same with each other between two directions. From this result, the deep penetration of gallium can be considered to be caused by enhanced diffusion.

The dose rate dependence of the profiles for gallium and arsenic are shown in Figs.5 and 6, respectively. The dose rate was about 3×10^{11} ions/cm^2/sec (low dose rate) and 1.2×10^{12} ions/cm^2/sec (high dose rate) for gallium, and about 6×10^{10} ions/cm^2/sec (low dose rate) and 3×10^{11} ions/cm^2/sec (high dose rate) for arsenic. Ion implantation of gallium was made at 500°C and 700°C for 1 hour

with the low dose rate and 15 minutes with the high dose rate. Ion Implantation of arsenic was made at 700°C for 1 hour with the low and high dose rate. The result shown in Figs.5 and 6. indicates that the profiles for gallium and arsenic are almost independent of the dose rate and that the short period implantation for 15 minutes gives the same result with the implantation for 1 hour. Davies et al[5]. observed the interstitial diffusion of xenon ion-implanted into tungsten crystals. The concentration profiles for xenon exhibit exponential tail. They explanined that the implanted xenon diffuse rapidly through interstitial site until it is trapped at some lattice defects.

As shown in Figs.7and 8 enhanced diffusion of gallium and arsenic was not observed in heavily damaged silicon made by prebombardment with nitrogen molecular ion beam at an energy of 45keV at room temperature. The implantation of gallium and arsenic were made at 300°C and 400°C, respectively. This result suggests that the migration of gallium and arsenic is terminated by trapping at defects.

The migration behavior of gallium and arsenic was almost the same with that of indium[4].

The critical temperature for the onset of enhanced diffusion is determined by the temperature at which the impurities become mobile through probably interstitial site or the temperature at which the concentration of defect produced during implantation becomes insufficient for trapping the implanted ion due to annealing during implantation. It can not be determined at present whether the observed critical temperature corresponds to the temperature for the onset of migration of gallium and

arsenic or to that of effective annealing of defects. Watkins[9] observed that the interstitial aluminum in electron irradiated silicon migrates above 200°C. This temperature is the same at which the enhanced diffusion of gallium and arsenic occur. On the other hand Dearnaly et al.[2] and Moline[7] observed the migration of phosphorus implanted in silicon at or below room temperature for the low dose (5×10^{12} ions/cm^2) implantation.

Conclusion

The followings can be concluded from the present experiment.

1) The migration of ion-implanted gallium and arsenic in crystalline silicon occur at relatively low temperature i,e. 200°C for dose of 1×10^{15}/cm^2.
2) The enhanced diffusion of gallium and arsenic in silicon is independent of temperature and the profiles exhibit the exponential tail.
3) The migration of gallium and arsenic do not occur in amorphous silicon and is terminated by trapping at defects. The migration behavior is almost the same with that of indium except the critical temperature for the onset of enhanced diffusion.

Refrence

1] P.M. Glotin: Can. J. Phys. 46 705 (1968)
2] G. Dearnaley, M.A. Wilkins, P.D. Goode, J.H. Freeman, and G.A. Gard: in Atomic collision Phenomena in Solids, edited by D.W. Palmer, M.W. Thompson, and P.D. Townsend (American Elsevier, New York, 1970), p.633
3] K. Gamo, K. Masuda, S. Namba, S. Ishihara, and I. Kimura: Appl. Phys. Letters 17 391 (1970)

4] K. Gamo, M. Iwaki, K. Masuda, S. Namba, S. Ishihara, and I. Kimura: Proceedings of the 2nd International Conference on Ion Implantation in Semiconductors, May 24-28, 1971, Garmisch-Partenkirchen, Germany.

5] J.A. Davies and P. Jespergard: Can. J. Phys. 44 1631 (1966)

6] D.K. Brice: Rad. Effects 6 77 (1970) and private communication.

7] R.A. Moline: J. Appl. Phys. 42 3553 (1971)

8] J.M. Fairfield and B.L. Crowder: Trans. Met. Soc. AIME 245 469 (1969)

9] G.D. Warkins: IEEE Trans. on Nucl. Sci. 16 13 (1969)

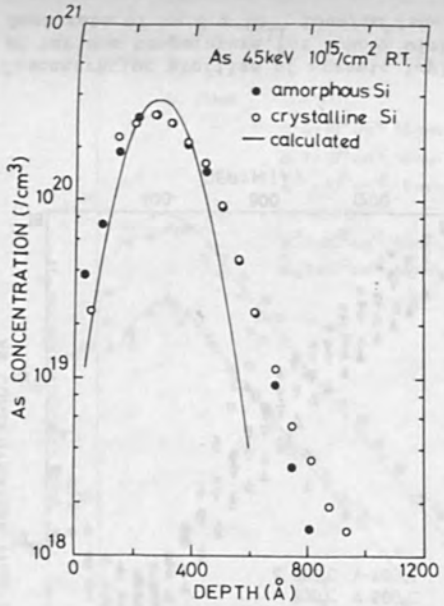

Fig. 1. Concentration profiles of room temperature ion implanted arsenic in amorphous silicon and in crystalline silicon. The solid line indicates the calculated value given by D.K. Brice.[6]

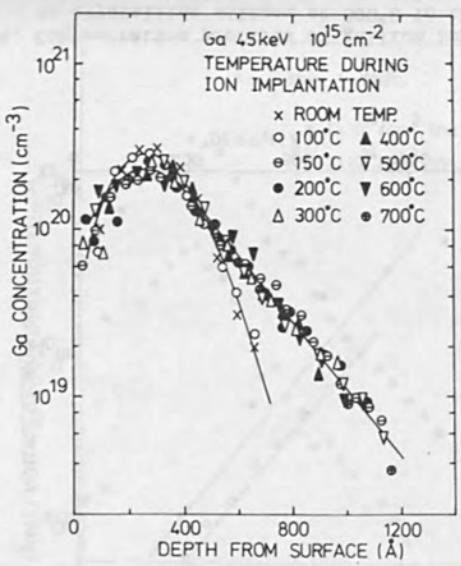

Fig. 2. Concentration profiles of gallium implanted at various temperature for 1 hour with the dose rate of ~ 3 x 10^{11} ions/cm^2/sec.

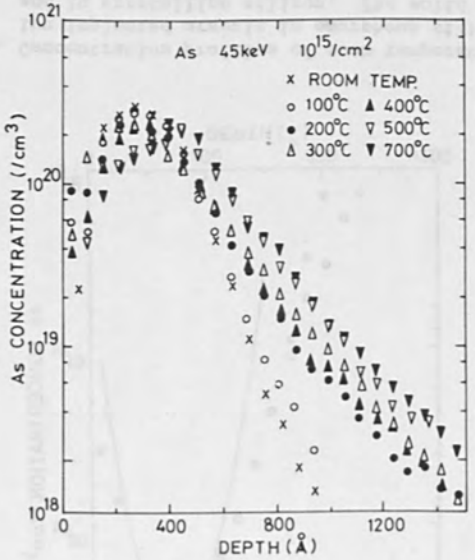

Fig. 3. Concentration profiles of arsenic implanted at various temperature for 1 hour with the dose rate of $\sim 3 \times 10^{11}$ ions/cm^2/sec.

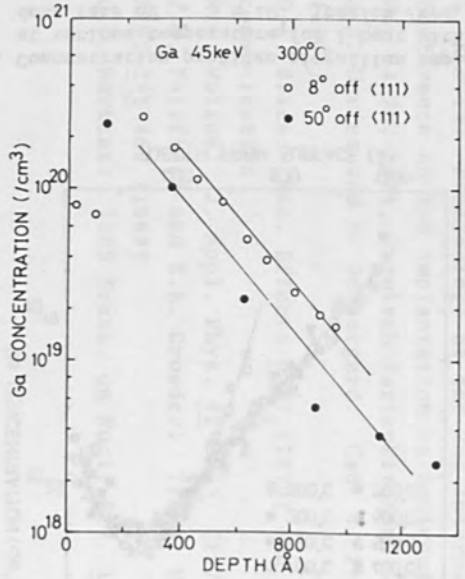

Fig. 4. Concentration profiles of gallium implanted in crystalline silicon at 300°C in the two directions tilted at ~8° and ~50° to the ⟨111⟩ crystal axis.

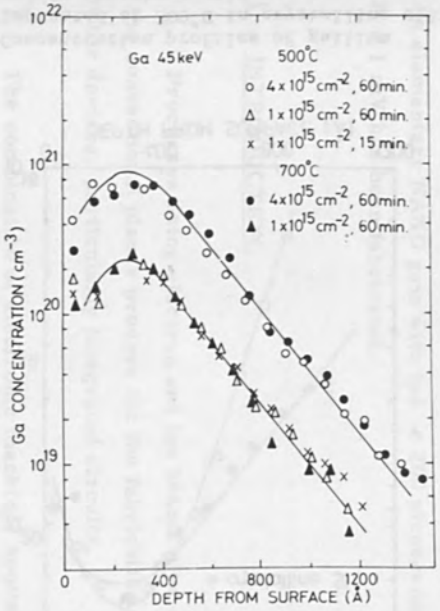

Fig. 5. Dose rate dependence of concentration profiles of high temperature implanted gallium.

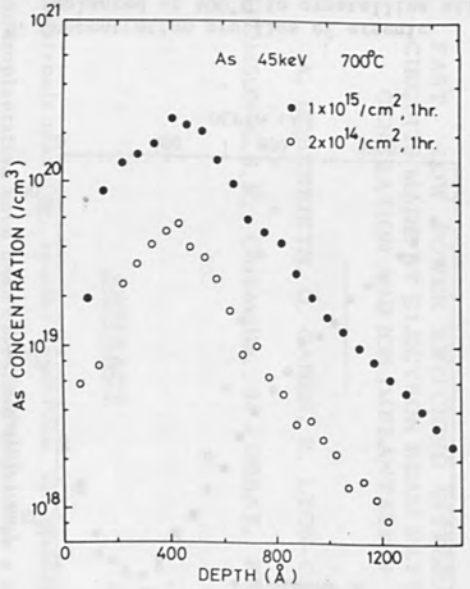

Fig. 6. Dose rate dependence of concentration profiles of high temperature implanted arsenic.

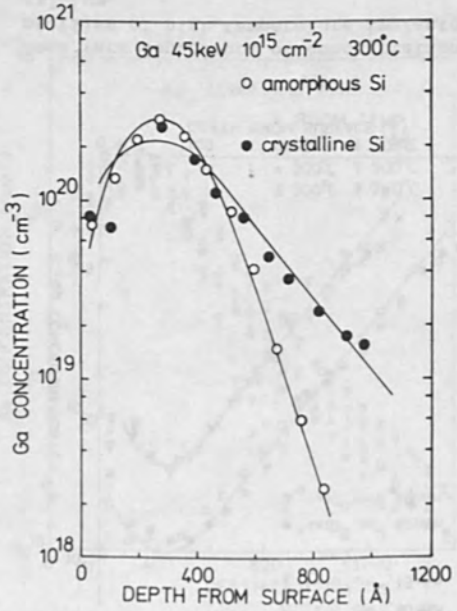

Fig. 7. Concentration profiles of gallium implanted at 300°C in crystalline silicon and in amorphous silicon

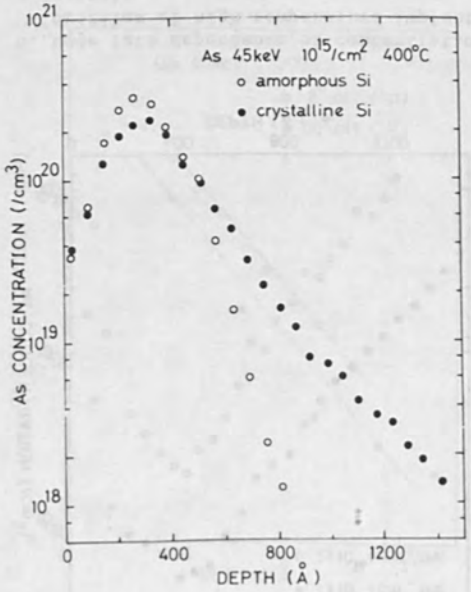

Fig. 8. Concentration profiles of arsenic implanted at 400°C in crystalline silicon and in amorphous silicon

FAST, LOW POWER SWITCHING INTEGRATED CIRCUITS MADE BY ELECTRON BEAM PATTERN GENERATION AND ION IMPLANTATION

A. BOBENRIETH, O. CAHEN, R. LYON-CAEN

THOMSON-C.S.F., Corbeville, 91 - ORSAY, FRANCE

ABSTRACT

Electronic masking, sputter deposition, ion etching and ion implantation have been combined to produce a new integrated JFET structure on a silicon semi-isolating substrate. The complete procedure is less complex than the conventional one and the circuit performance is better. An elementary NAND gate with tpd $<$ 200 picoseconds for P $<$ 1 mV has been fabricated.

1. - INTRODUCTION.

Processes using electron and ion beams give advantages over the conventional planar process for the fabrication of semiconductor devices, particularly integrated circuits.

The combination of electronic masking, sputter deposition, ion etching and ion implantation in our laboratory has led to the design and the realization of a new I.C$_s$ structure with simple

processing, small areas, low consumption and high speed (1, 2, 3, 4, 5).

2. - ADVANTAGES OF NEW PROCESSES.

It is possible to use these new processes to make I. C. s with all 3 transistor types : bipolar, MOSFET and JFET (or MESFET). (For simplicity in this paper we use the symbole JFET for both diffused junction and Schottky barrier FET's).

However a special JFET structure was chosen as a design vehicle due to processing simplicity and because the procedures outlined above permit to overcome the drawbacks of the classical JFET and to emphasize its advantages. Nevertheless, fast lateral bipolar transistor and MOSFET designs are under consideration.

The table below shows the advantages given by the new processes over the corresponding classical ones (in general and in particular for JFET's) which explain the performance improvements claimed above for the new I. C. s.

ELECTRONIC MASKING

ADVANTAGES OVER PHOTOMASKING	I. C. s IMPROVEMENTS
0. 1 μm accuracy : line width ⩽ 1 μm	reduced area : small { capacitance, current; power, transition; energy }
direct masking on wafer	reduced delay between design and manufacture
sequential digital process	quick modifications of components, circuits, LSI

SPUTTER DEPOSITION

ADVANTAGES OVER VACUUM VAPORISATION	I. C. s IMPROVEMENTS
preliminary cleaning by ion etching	reproducibility, reliability } good contacts
higher energy for impinging atoms	adherence of layers } good contacts
deposition from all directions	same thickness on sides : no open connections

ION ETCHING

ADVANTAGES OVER CHEMICAL ETCHING	I. C. s IMPROVEMENTS
etched sides very straight	preservation of small lateral dimensions
etched sides almost normal to surface	small lateral spread of ion implanted layers
no chemical contamination	better yield and reliability

ION IMPLANTATION

ADVANTAGES OVER DIFFUSION	I. C. s IMPROVEMENTS
dose accuracy	reproductibility, low dispersion
accurate thin layers (0. 3 to 0. 1 μm)	JFET with Vp $\leq$ 1 volt ; normally off JFET
short time low temperature anneal	high resistivity substrate : small parasitic capacitance

3. - COMPARISON BETWEEN BIPOLAR, MOST AND JFET.

JFET's present advantages over both bipolars and MOST's :

- the source-drain current is a majority carrier current, so there is no storage time, whereas even for gold doped bipolar transistors, the storage time in saturation is $\simeq$ 3 nanoseconds.

- normal overvoltages on the gate do not destroy JFET's, whereas MOST's are destroyed.

- JFET's support a higher dose of nuclear radiation than bipolars and particularly MOST's.

- the carrier mobility is normal in a JFET channel whereas it is reduced in an enhancement MOST plane channel.

- breakdown occurs at a lower voltage in a MOST.

- a multigate JFET gives a simple "AND" logic function.

However JFET's made by conventional processes present disadvantages (due principally to a large value of channel thickness) which limit their use in logic circuits :

- they need a high gate bias voltage for cut-off : $Vc \simeq -5$ V.

- they have a high pinch-off voltage $Vp = |Vc| = 5$ V, thus they need a high supply voltage $Vs \geqslant 10$ V.

- consequently the voltage shift between the drain of a JFET and the gate of the following one is high (5 to 10 volts) and a level shifter (a zener diode for example) is necessary.

- the range of transition between logic levels "0" and "1" is high, since it is approximately equal to the absolute value of cut-

off voltage Vc or pinch-off voltage Vp.

- finally the lateral dimensions are large, particularly the channel length ; parasitic capacitances are important and the switching time is not small.

The new processes reduce these disadvantages :

- ion implantation permits one to make a very thin channel giving $|Vc| \simeq |Vp| \leq 1$ volt, so the gate bias voltage can be obtained by a diode threshold for a logic circuit group, and the voltage level shift by one or two forward diode thresholds. Moreover, it is possible with ion implantation to make a channel thickness a equal to or smaller than the depletion layer thickness Xm (due to the potential diffusion barrier Vd at the gate-channel junction). For example, with a Molybdenum Schottky diode on $n \simeq 6 \times 10^{16}$ cm^{-3} channel concentration, we have $a \simeq Xm \simeq 0.1$ μm.

We propose to call this "normally off" JFET a forward junction field effect transistor (FJFET) and to call the conventional "normally on" JFET a reverse junction field effect transistor (RJFET).

A FJFET does not need gate bias voltage and a voltage level shifter can be obtained by just one forward diode ; it is not necessary for small supply voltages ($\simeq 0.6$ volts) giving small logic swings ($\simeq 0.2$ volts).

- the combination of the new processes allows one to obtain very small lateral dimensions (for example 1 μm gate and 1 μm space between gate-source and gate-drain) and to use semi-

isolating substrates. The result is a very high frequency limit ($\geq$ 10 GHz) for linear circuits and very low tpd ($<$ 1 nanosecond) for logic circuits. Moreover it is possible to reduce the source - drain current ($I_{DS} \simeq 10\ \mu A$) by decreasing the channel width ($\simeq 5\ \mu m$). So the logic circuits P x tpd is very small ($< 10^{-12}$ joule).

4. - PROCESSING DETAILS OF NEW I. C. STRUCTURE.

For a better understanding we just shall describe the realization of a new RJFET. The other components of an I. C. (FJFET's, linear resistors, saturated resistors, diodes) are obtained simultaneously from RJFET design modifications.

Fig. 1 represents the structure of our RJFET and Fig. 2 is a scanning electron microscope photograph of a real RJFET : gate width is $\simeq 2\ \mu m$ and SG and GD distances are $\simeq 1\ \mu m$.

Fig. 3 shows the different stages of the process with a p^- substrate ($\rho \simeq 10^3\ \Omega$ cm). The process is complementary for n^- substrates.

1 - sputter deposition of $\simeq 0.6\ \mu m$ of silica. It is also possible to use a thermal oxidation in H_2O at 950° C, because this short thermal treatment does not reverse the conductivity type.

2- electronic masking and silica chemical etching of the entire area of the RJFET.

3 - 600 Å silica layer by sputtering or thermal oxidation. The goal is to implant through the $Si\,O_2$ for protection interface, decreasing channeling and maximum concentration at interface for contacts.

4 - sputter deposition of Mo-Au layer ($\simeq$ 3000 Å) for implantation masking.

5 - electronic masking and Au-Mo ion etching for source and drain contact definition.

6 - source and drain contacts ion implantation : P^+ ions, 3×10^{15} cm^{-2}, 50 keV.

7 - chemical removal of Au-Mo mask.

8 - channel ion implantation : P^+ ions, 2×10^{12} cm^{-2}, 70 keV.

9 - electronic masking and ion etching of opening for source-drain contacts and Schottky diode gate, in 600 Å silica layer.

10 - sputter deposition of Mo-Au layer ($\simeq$ 5000 Å).

11 - electronic masking and ion etching of source-drain contacts (and connections for I. C.) and Schottky gate.

This simple process needs only 4 masking steps (3 registrations).

We are trying variations of this process :

- FJFET by channel implantation dose and energy reduction.

- other metals for S-D contacts and Schottky diode : SiPt, SiPd.

- pn gate diode (which needs one more masking and one more implantation, but gives lower reverse gate current for a RJFET and higher threshold for a FJFET).

- complementary process of above (n^- substrate) for making a complementary JFET. It is more difficult to obtain a good Schottky diode on p type channel than on n type channel.

5. - CIRCUIT RESULTS.

For testing the possibilities of this new IC structure we have designed and studied a few integrated nanocircuits described below :

5.1. - Fig. 4 represents a NAND function made by a trigate RJFET with a passive RJFET load (S and G shorted) and a source follower (made by a RJFET and a linear resistor load). For measuring the dynamic response, two input gates are grounded and the third gate is driven by negative pulses (- 1 V) with a risetimes $\simeq$ 300 picoseconds. The output signal is measured on a 50 Ω resistor in series with the source-follower. The input and output signals are compared on a dual-beam sampling scope.

Fig. 5 shows the result : tpd is less than 200 picoseconds. The consumption of the NAND circuit is P = 0.4 mA x 2 V = 0.8 mW. Fig. 6 is a scanning electron microscope photograph of the trigate JFET : each gate is 1 μm width and the space between gate is also 1 μm.

5.2. - Fig. 7 represents the schematic of a ring made with 3 NOR gates and an output source follower for measuring the switching limit speed of the nanocircuits. Fig. 8 shows a SEM photograph of this ring : the total dimensions are about 30 μm by 30 μm. Up to now we have not seen any oscillations with a spectrum analyser. An improved version is being fabricated.

5.3. - Nanoelectronics seems particularly interesting for future large memories with a great number of bits. Fig. 9 shows the design of two memory cells the dimensions of which are only $\simeq$ 30 μm x 30 μm.

6. - CONCLUSION.

We think these results prove the applicability of the combination of the electronic and ion processes we use, that is to say "nanoelectronics", to make a new nanocircuits generation with low power consumption and low propagation delay time or high frequency performances. Further improvements on the P and tpd values obtained up to now seem possible, particularly by decreasing the dimensions and by the use of complementary FJFET structures.

7. - ACKNOWLEDGEMENTS.

We would like to acknowledge all the people who participate in this research and the French Administrations (DGRST, DRME, DI, STTA, SEFT) which support it.

REFERENCES.

- French Patent n° 70. 35702 - 2nd October 1970
- French Patent n° 71. 24683 - 6th July 1971
- A. Bobenrieth, Pham Ngu Tung, C. Arnodo - II International Conference on Ion Implantation in Semiconductors - May 1971 - Garmisch (Germany).
- C. Arnodo, P. Martin - AVISEM 71 - September 71 - Versailles (France).
- A. Bobenrieth - AVISEM 71 - September 71 - Versailles (France).

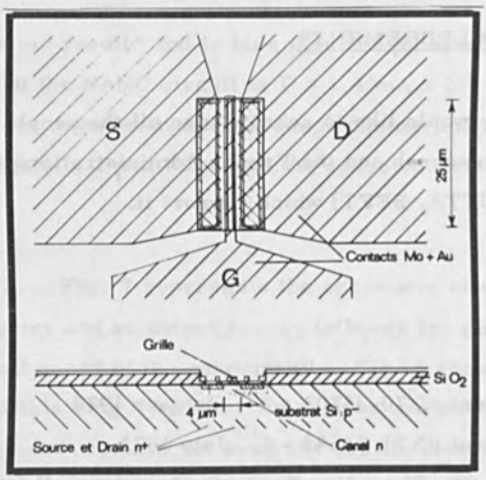

FIG. 1 - NEW JFET STRUCTURE.

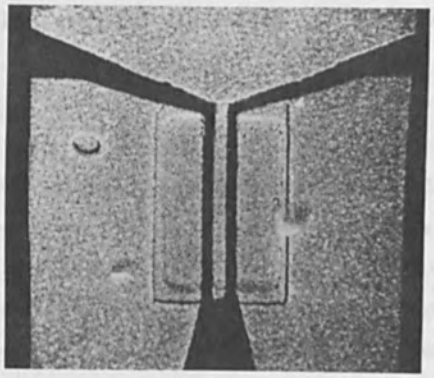

FIG. 2 - NEW JFET (SEM PHOTOGRAPH).

p⁻ Si Substrate ($\rho = 10^3\ \Omega$ cm)

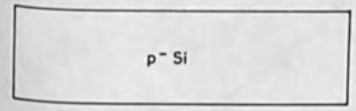

1- 0.6 µm Silica (sputtered or thermal)

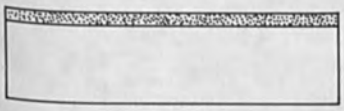

2 - Electronic masking and chemical etching

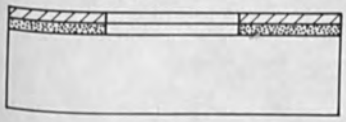

3- 0.1 µm Silica (Sputtered orthermal)

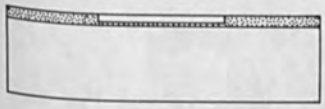

4- 0.3 µm Mo-Au (Sputtered)

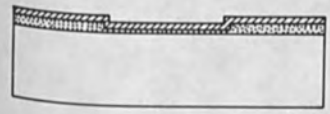

5 - Electr. masking and Au-Mo ion etching for S and D

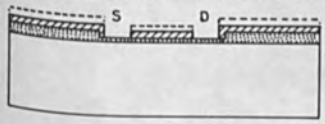

6- S and D contacts ion implantation
(P^+, $3 \times 10^{15}\ cm^{-2}$, 50 keV)

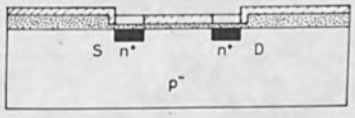

7- Chemical etching of Au-Mo mask

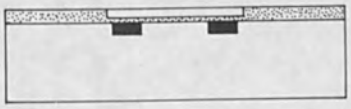

8 - Ion implantation of chanel
(P^+, $2 \times 10^{12}\ cm^{-2}$, 70 kV)

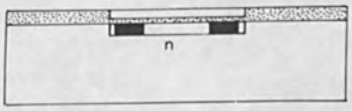

9 - Electr masking and ion etching of S G and D openings

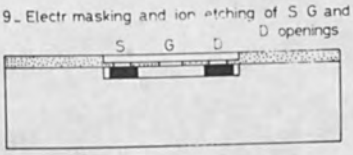

10 - 0.5 µm Mo-Au (Sputtered)

11 - E.M and I.E of S.D contacts and schottky G

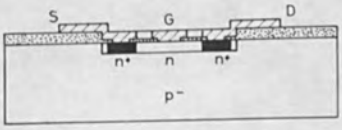

FIG. 3 - NEW PROCESSING

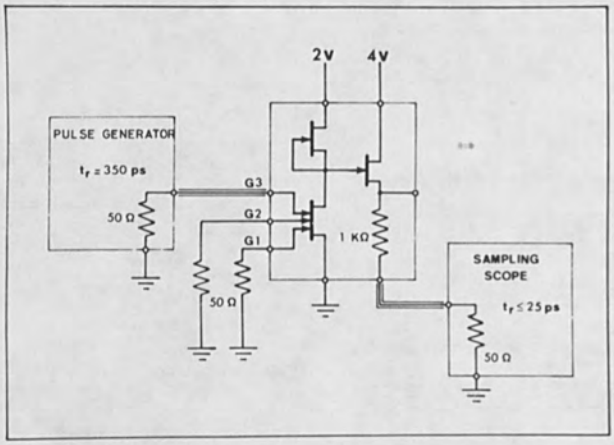

FIG. 4 - NAND CIRCUIT AND TEST NETWORK.

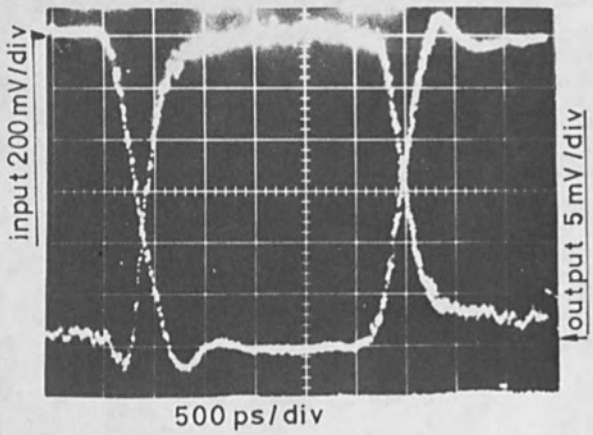

FIG. 5 - INPUT AND OUTPUT SIGNALS OF NAND CIRCUIT.

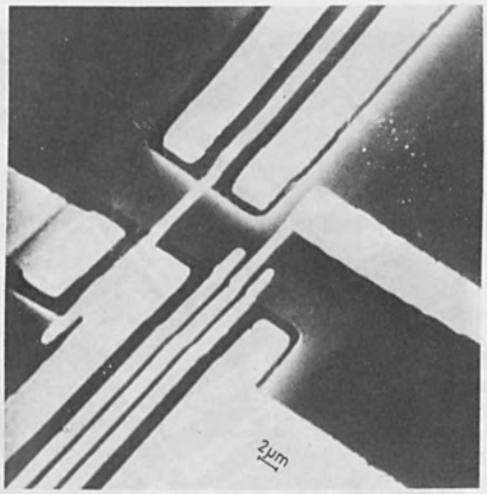

FIG. 6 - NAND CIRCUIT (SEM PHOTOGRAPH X≃2000)

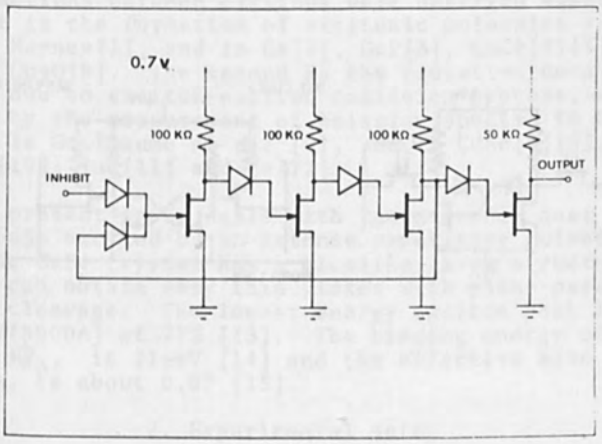

FIG. 7 - THREE NOR GATE RING (SCHEMATIC).

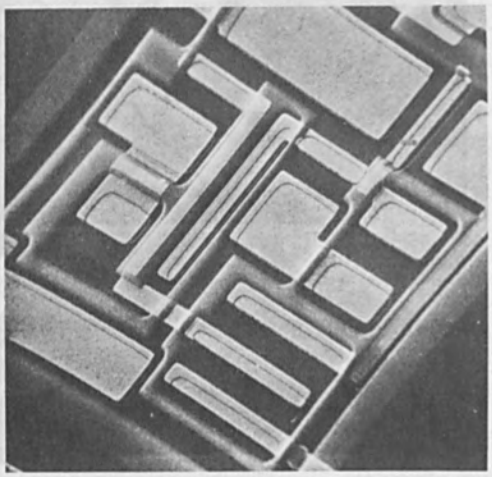

FIG. 8 - THREE NOR GATE RING (SEM PHOTOGRAPH X ≃ 2000)

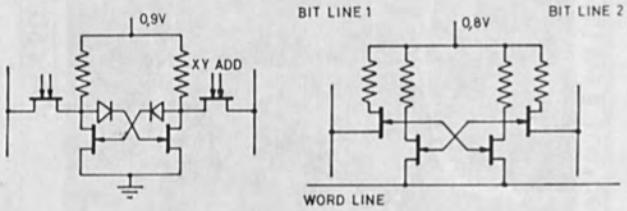

FIG. 9 - MEMORY POINT PROJECT.

Luminescence of GaSe under Intense Excitation by an Electron Beam

T.UGUMORI, K.MASUDA and S.NAMBA
Faculty of Engineering Science, Osaka University,
Toyonaka, Osaka, Japan

Luminescence of GaSe near the band edge region excited by a pulsed electron beam is measured. In the case of intense excitation, one broad emission band called the P band appears at a position shifted by the amount of the binding energy of the exciton from the exciton band. The emission intensity of the P band shows super-linear dependence upon the emission intensity of the exciton band. The recombination mechanism of this emission band is explained by exciton-exciton collision process.

1. Introduction

Recently some behaviors of high density excitons due to interactions between excitons were observed experimentally. The first is the formation of excitonic molecules as observed in Si by Haynes[1], and in Ge[2], GaP[3], CuCl[4][5], CuBr [5] and Cu_2O[6]. The second is the radiative decay of excitons due to exciton-exciton collision process, which was observed by the measurement of emission spectra in CdS by Benoit à la Guillaume et al. [7], and in CdSe[8][9], ZnO[8], Cd(S,Se)[10], InP[11] and Ge[12].

The present paper deals with luminescence near the band edge of GaSe excited by an intense repetitive pulsed electron beam. The GaSe crystal has a micalike layer structure, so that one can obtain very thin flakes with plane-parallel faces by cleavage. The lowest energy exciton peak is located at 2.10eV(5900A) at 77K [13]. The binding energy of the exciton, E_{ex}^b, is 21meV [14] and the effective mass ratio, $\sigma = m_e/m_h$, is about 0.07 [15].

2. Experimental setup

The GaSe crystals were prepared by the Bridgman method. The samples were cleaved from thick crystals perpendicularly to the c axis, and the thickness of platelets was about 10μ.

A sample was stuck with silicone grease to a copper heat sink which was attached to the cold finger of a cryostat. The temperature of the sample was measured by a thermocouple fixed to the surface of the heat sink.

A diagram of the experimental setup is shown in Fig.1. The electron beam energy was usually 25keV, and the maximum current densities were about 4A/cm^2 with a beam diameter of about 1 mm. The beam was pulsed at a rate of 100Hz with the pulse width of 80nsec. The light emitted was detected by an RCA 1P28 photomultiplier through a monochromator in the direction normal to the bombarded surface in order to minimize the reabsorption of the emission. The output signal of the photomultiplier was processed by a boxcar integrator. The averaged output signal was fed into a recorder.

3. Experimental results

Fig.2 shows the temperature dependence of the spectra emitted by GaSe at weak excitation (about 0.1A/cm^2). The emission intensity is plotted on a logarithmic scale. At 15K two emission bands with peaks at 5890 and 5980A are observed. The peak at 5890A corresponds to the exciton absorption line. Therefore this emission band is due to the annihilation of an exciton. The emission intensity of the broad band with the peak at 5980A increases sublinearly with increasing of excitation, while the exciton band increases linearly. So that, the broad band is attributed to the transition between the conduction band and localized levels. The exciton band shifts to the low energy side with increasing temperature. The intensity of the broad band decreases, and at 86K only the exciton band at 5910A is observed. At 300K general features are similar to that at 86K except for the following points: The width of the exciton band is almost three times as large as that of the 86K spectrum, and the emission intensity is reduced by about one order of magnitude.

As shown in Fig.2, near liquid nitrogen temperature only the exciton band predominates and the recombination radiation of conduction band electrons with holes at local levels is negligible. Therefore the measurement of the emission spectra at 86K is suitable to observe the interactions between excitons.

Fig. 3 shows emission spectra at 86K for various excitation intensities. In the case of weak excitation, the exciton emission band called A is prominent. Under intense excitation levels there appears a new emission band called P with a peak at 5990A, that is, at a position about 26meV shifted to the low energy side from the exciton band.

The P band tails towards the low energy side.

The dependences of the A and P emission intensities upon the excitation intensity are shown in Fig.4(A). The emission intensity of the A band, I_A, increases linearly at weak excitation(below $0.5A/cm^2$) and sublinearly at intense excitation (above $0.5A/cm^2$) . The emission intensity of the P band, I_P, increases superlinearly at weak excitation and linearly at intense excitation. The dependence of the P band emission intensity upon the A band emission intensity is shown in Fig. 4 (B). The P band intensity is proportional to $I_A^{1.6}$. The power 1.6 is close to 2.

4. Discussion

The dependence of the P band emission intensity upon the A band emission intensity can be simply explained by assuming recombination mechanisms involving the interaction of two excitons: excitonic molecule [1] or exciton-exciton collision process [7].

We first consider a radiative decay of excitonic molecules. By the electron beam excitation free electrons and holes are generated. Free carriers combine to form excitons, which are then encounter each other forming excitonic molecules. By assuming that the exciton is generated proportionally to the excitation,J, the following results are obtained[16].

$n_{ex} \propto J$ and $n_m \propto J^2$

for weak excitation case

$n_{ex} \propto J^{1/2}$ and $n_m \propto J$

for intense excitation case,

where n_{ex} and n_m are the concentrations of the single exciton and excitonic molecule respectively. For both cases we obtain $n_m \propto n_{ex}^2$. As the A and P bands emission intensities are porportional to n_{ex} and n_m respectively, we obtain $I_P \propto I_A$. The measured dependence of the P band intensity upon the A band intensity is nearly in agreement with these results.

Another process is the exciton-exciton collision process [7]. Namely, two excitons collide with each other and one exciton decays radiatively. In this process the dependence of the P band emission intensity upon the A band emission intensity is same as that of the excitonic molecule[7]. In order to determine the mechanism of the P band,the value

of the binding energy of the excitonic molecule, E_m^b, is estimated from the calculations [17] [18]. This value is calculated to be between 3~7meV. As the thermal energy 7meV at 86K is comparable to or larger than E_m^b, the concentration of the excitonic molecule is considered to be small owing to thermal dissociation effects. So that, the exciton-exciton sollision process rather than the decay of excitonic molecule is reasonable in this case.

The exciton-exciton collision process can be described as follows [7]:

$$\text{Exciton K + Exciton K'} \longrightarrow \text{Exciton O + electron-hole pair}$$
$$\longrightarrow \text{photon } h\nu \text{ + electron-hole pair,}$$

where K, K' and O are the wave vectors of the excitons and $h\nu$ is the energy of emitted photon. From the energy conservation

$$h\nu = E_o - E_{ex}^b - \hbar^2 k_i^2/2\mu + E_K + E_{K'},$$

where E_K, $E_{K'}$ and $\hbar^2 k_i^2/2\mu$ are the kinetic energies of the excitons and electron-hole pair respectively and E_o is the exciton energy. If we consider that the momentum of the excitons are almost equal to zero, $h\nu$ would be about $E_o - E_{ex}^b$ (i.e., 21meV below the exciton line). This position corresponds roughly to the P band (26meV below the exciton band). The shape of this band at OK was calculated by Benoit à la Guillaume et al. [19]. The theoretical shape is asymmetric and tails towards the low energy side. They say that the low energy tail is unaffected and the position of the maximum is only slightly affected by the temperature. The comparison between the shape of the theoretical band calculated at OK and the shape of the experimental band is shown in Fig.5. The width of the latter is almost factor of three as large as that of the former. The difference between the theoretical and experimental results is considered to be due to the effect of the kinetic energies of the excitons and electron-hole pairs. The low energy tail and the peak positon of the P band are well described by this process. From the facts described above the recombination mechanism of the P band is explained by exciton-exciton collision process.

5. Summary

A new emission band at 5990A in GaSe named the P band was observed under the intense excitation by an electron beam at 86K. From the superlinear dependence of the P band emission intensity upon the exciton band emission intensity,

it is suggested that the P band originates the radiative decay of free excitons after scattering with free excitons.

Acknowledgmant

The authors are greatful to Mr. Y.Suzuki for his kindness of supplying GaSe crystals, and Dr. H.Aritome and Mr. S.Iwai for helpful discussions.

References

[1] J. R. Haynes: Phys. Rev. Letters 17 (1966) 860.
[2] C. Benoit à la Guillaume, F. Salvan and M. Voos: J. Luminescence 1,2 (1970) 315.
[3] J.L.Merz, R.A.Falkner and P.J.Dean: Phys. Rev. 188 (1969) 1228.
[4] A.Mysyrowicz, J.B.Grun, R.Levy,A.Bivas and S.Nikitine: Phys. Letters 26A (1968) 615.
[5] T.Goto, H.Souma and M.Ueta: J.Luminescence 1,2 (1970) 231.
[6] E.F.Gross and F.I.Kreingold: JETP Letters 12 (1970) 68.
[7] C.Benoit à la Guillaume, J.M.Debever and F.Salvan: Phys. Rev. 177 (1969) 567.
[8] D.Magde and H.Mahr: Phys. Rev. Letters 24 (1970) 890.
[9] I.Filinski, B.Wojtowincz-Natanson and I.M.Hvam: J. Phys. Chem.Solids 32 (1971) 2193.
[10] H.Kukimoto, S.Shionoya and T.Kamejima: J. Phys. Soc. Japan 30 (1971) 1662.
[11] E.Gobel, H.J.Queisser and M.H.Pilkuhn: Solid State Commum. 9 (1971) 429.
[12] E.F.Gross, A.V. Il'inskii, B.V.Novikov and N.S.Sokolov: Soviet Physics-Solid State 11 (1970) 2437.
[13] F.Bassani, D.L.Greenaway and G.Fischer: Proc.Intern. Conf. on Physics of Semiconductors, Paris (1964) p.51.
[14] J.Halpern: Proc. Intern. Conf. on Physics of Semiconductors, Kyoto (1966), J.Phys. Soc. Japan 21 (1966) Suppl. p.180.
[15] H.Kaminura and K.Nakao: J. Phys. Soc. Japan 24 (1968) 1313.
[16] H.Souma, T.Goto, T.Ohta and M.Ueta: J.Phys. Soc. Japan. 29 (1970) 697.
[17] J.Adamowski, S.Bednarek and M.Suffczynski: Solid State Commun. 9 (1971) 2037.
[18] O.Akimoto and E.Hanamura: Solid State Commun. 10 (1972) 253.
[19] C.Benoit à la Guillaume, J.M.Debever and F.Salvan: Proc.Intern. Conf. on Physics of Semiconductors, Moscow (1968) P.581.

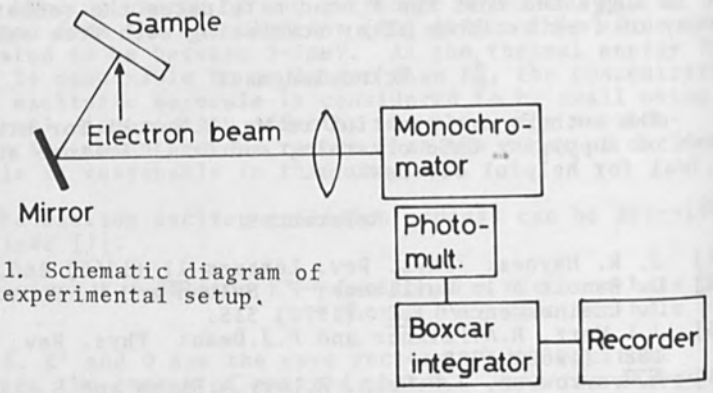

Fig.1. Schematic diagram of the experimental setup.

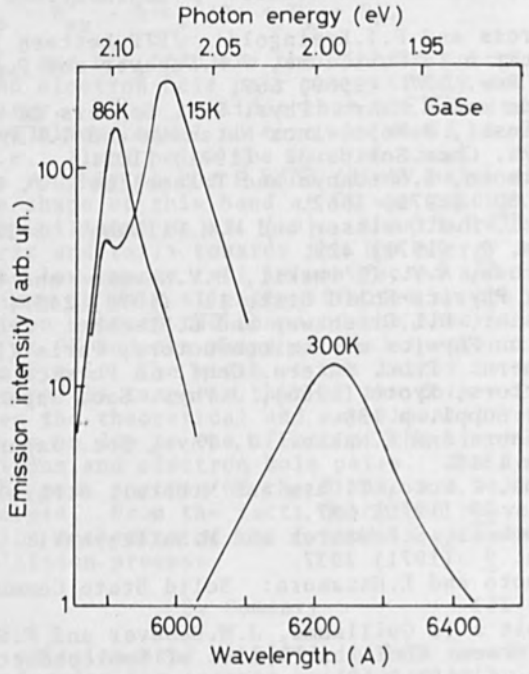

Fig.2. Emission spectra of GaSe under weak excitation for different temperatures.

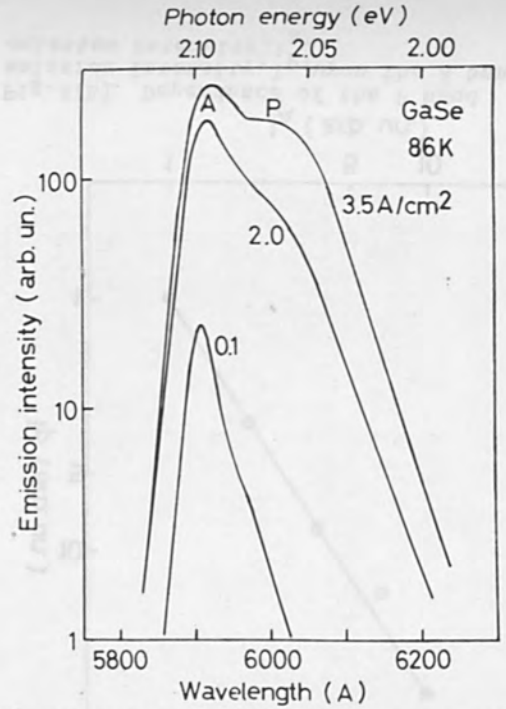

Fig.3. Emission spectra of GaSe at 86K for various excitation levels.

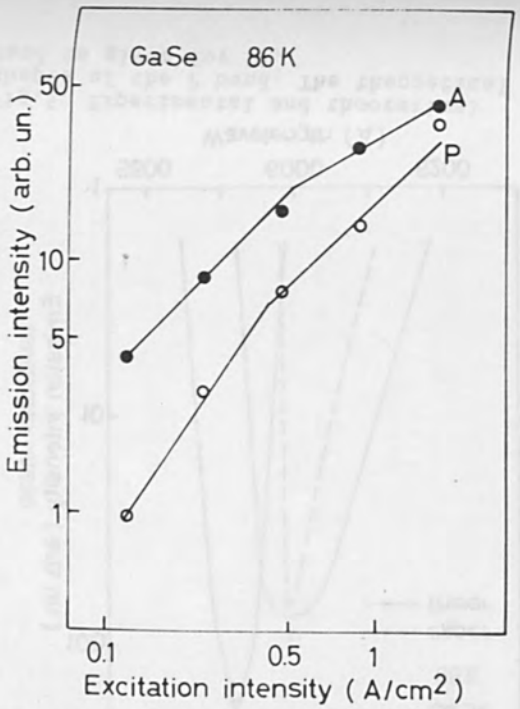

Fig.4(A). Dependences of the A and P emission intensities upon the excitation intensity, measured at 86K.

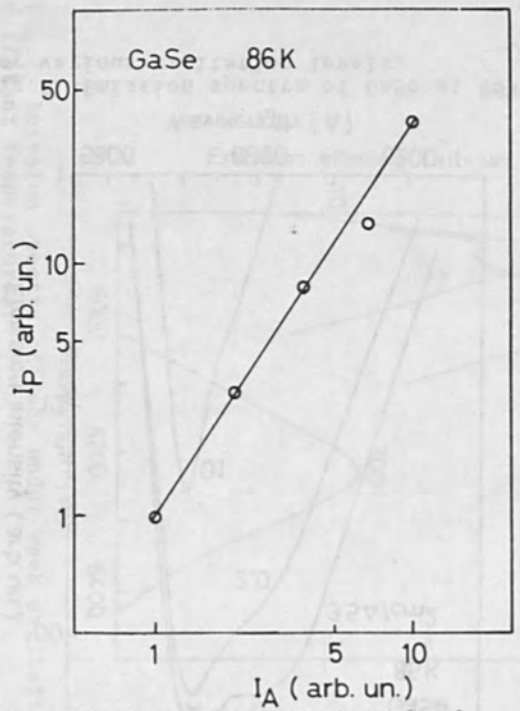

Fig.4(B). Dependence of the P band emission intensity, I_P, upon the A band emission intensity, I_A.

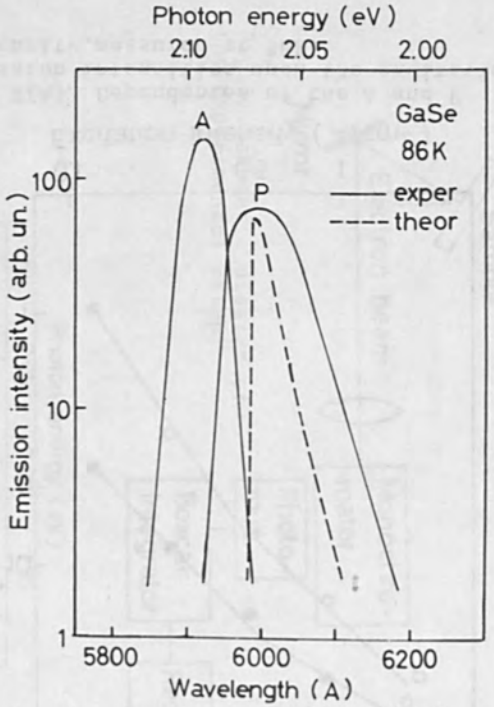

Fig.5. Experimental and theoretical shapes of the P band. The theoretical band is given for 0K.

PRESENTED PAPERS

GROUP II

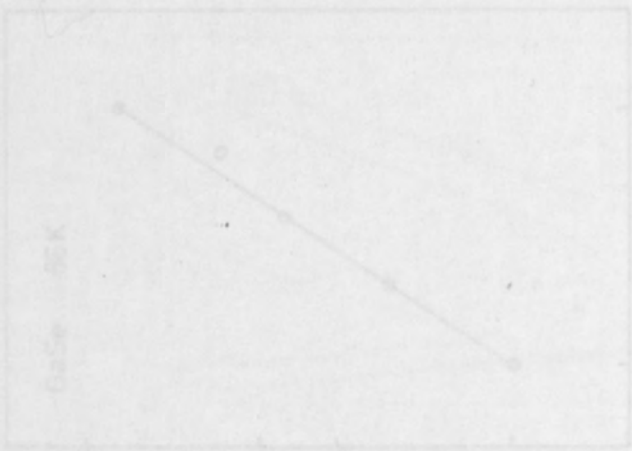

AN EXPERIMENTAL ANALYSIS OF PENETRATION MECHANISM OF HIGH POWER DENSITY ELECTRON BEAM

Toshiyuki MIYAZAKI

Norio TANIGUCHI

The Institute of Physical
and Chemical Research

WAKO-SHI SAITAMA, 351. JAPAN

Abstract

Experiments dealing with the deep penetration mechanism of high power density electron beams are discussed. X-rays generated as a consequence of moving and stationary electron beam bombardment of metal targets are measured. The X-rays generated fluctuate. From this fact and the balance of forces a model for the penetration path of the electron beam is proposed. This model deals with linear cavity configuration. The cavities are unstable and collapse and reform as consequence of thermal fluctuations. The movement of molten zone is also discussed. The collapse and reformation of the cavities and the movement of the molten zone are related to differences in the shapes of the fusion zone in different metals.

1. Introduction

The most unique characteristic of heating by high power density electron beams is the production of the high depth to width ratio fusion zones Such fusion zone is shown in Fig. 1. The mechanism of this phenomenon is not as yet explained to the satisfaction of all.

By Whiddington's Law[1] the penetration depth D is approximately expressed by the following equation (1).

$$D = 2.1 \times 10^{-12} \frac{V_\alpha^2}{\rho} \quad (\mathrm{cm}), \qquad (1)$$

in which V_α is the acceleration voltage of electron and ρ the mass density of material (g/cm^3).

For example with a V_α of 150 KV the D values are 60 μm and 180 μm for iron and aluminum respectively, making it unlikely that the electron beam penetrates directly so deep into metal in the solid state and causing deep melting. One certainly could not rely on ordinary conduction heating due to a surface heat source to explain the narrow and deep fusion zone.

The phenomenon must be explained by the assumption that electron beam brings directly its kinetic energy deeply into metal. An explanation[2] based on this point of view has been proposed:

The electron beam at first melts the projected local portion of the target metal and next produces a kind of channel of very small diameter filled with metal vapor. The vapor in the channel is considered to be reduced to plasma. As a consequence, the electron beam can now go through the channel without any loss of its energy, reaching to the bottom portion of the channel and producing there a new channel. Consequently, the channel extends itself deeply into the target metal, explaining high depth to width ratio fusion zone.

However, it is not likely that a channel of which the diameter is comparable to the size of the electron beam diameter and a length of centimeters could hold its form dynamically stable during processing. Furthermore the etched section of a welded zone is not uniform as would be expected from that channel form. One must therefore assume that the diameter and the length of the channel must change with time and position.

It is the object of this paper to analyse the deep penetration mechanism of high power density beams by using an experimental approach. The discussions concerning the behavior of the moving and stationary electron beam in metal and the model of the deep penetration mechanism are based on X-rays generated by the beam electrons collisions with metal target.

2. Experimental Method

When a high kinetic energy electron collides with a material, the majority of its energy changes into heat and a small part into X-ray. As to the X-rays generated, it can be said that when the electron beam collides with high mass density material, large quantities of X-ray are emitted and when they collide with low mass density material such as gas, small quantities are emitted. Therefore, when electron beam goes through the channel of vapor or plasma, mentioned earlier, the quantity of generated X-ray is small, but if a part of the channel is filled with molten metal, high intensity of X-rays are generated, or in other words, the fluctuations in the state of the channel can be detected by the

measurement of the fluctuation of the emitted X-rays.

To detect X-rays in a specific and small site, the collimator of lead plates is located besides the target metal and perpendicular to the longitudinal path of the electron beam as shown in Fig. 2. A NaI scintillation counter equipped with high speed rate meter[3] and an industrial X-ray film were utilized as X-ray detectors.

Furthermore, in order to measure the secondary electron current simultaneously, a collector was also set over the target metal as shown in Fig. 2. Hence, this made possible to estimate the change of the electron collision point with target.

The experimental conditions are shown in Tab.1. The electron beam diameter is determined by the vaporized width caused in a moving aluminum foil by the electron beam.

3. Experimental results

The targets of mild steel and aluminum were bombarded by moving and stationary electron beams as shown in Tab. 1. Sections of the solidified fusion zones are shown in Fig. 3. There is a difference of shape between the two metal targets, i.e., the shape of mild steel is like a "well" and that of aluminum is like a "wedge". The relations between fusion zone depth and bombardment duration time of electron beam are shown in Fig. 4 for the two targets. The fusion zone depth is established virtually as soon as the electron beam starts bombarding the target, with little and rapid saturation with time. To explain this phenomenon, the X-rays generated were analyzed. The results are shown in Fig. 5. The quantity of generated X-rays is considered to be proportional to the quantity of the absorption energy of electron beam. In the figure, the quantity is shown in arbitrary units. Note, the values are relative to the value at the depth of 0.4 cm. Therefore, from the data, it becomes clear that the quantity of the absorbed electrons varies with respect to the depth from the surface of the target, becoming very small at some depth. Namely, the phenomenon shown in Fig. 4, indicated that the saturation effect with depth of the fusion is caused by the fact that the electron beam virtually can not reach the bottom of the fusion zone, i.e., the electron beam power is absorbed before it reaches the bottom.

Moreover, from the data, it is confirmed that a large quantity of electrons can penetrate as far as 3 cm for mild steel target and 1 cm for aluminum target. The X-ray data obtained from X-ray film shown in Fig. 5 are integrated with respect to time. It must then be considered that the opportunity of the electron beam to reach to the depth of 3 cm for mild steel and 1 cm for aluminum is very frequent. If the electron beam reaches to these depths

into molten metals, the channel, above mentioned, must exist in fully gaseous state through these lengths, because the net penetration depth of electron beam into metal is only 60 μm or 180 μm as shown in equation (1). However, as mentioned formerly, from the point of view of the balance of forces it must be considered very difficult that the channel filled with rarefied plasma gas of which diameter and length are beam diameter and 3 cm or 1 cm respectively can exist so stably.

Therefore, next the fluctuations of the generations of X-rays at several different positions, that is, the fluctuations of the absorption of electron beam power at several different positions were measured under the conditions in Tab. 1. The results are shown in Fig. 6-1, 6-2, 6-3 for mild steel target and Fig. 7-1, 7-2, 7-3 for aluminum target. The figures show the generations of X-rays at the depths of 0.4, 2.4, 4.4 cm for mild steel target and 0.4, 1.4, 2.4 cm for aluminum target and also the secondary electron current at the same time collected over the target. The horizontal line shows the bombardment duration time of the electron beam. The quantities of X-rays and secondary electron current are shown in arbitrary units.

From the figures, it becomes clear that both the generation of X-rays and secondary electrons show violent variation with time, especially, the generation of X-ray fluctuates highly. From these data, it can be concluded that the portion of time at which electron beam power is absorbed always changes. Namely, at the time when the quantity of generated X-rays is large, the stock of molten metal exists at the measured point in the way of channelled penetration path of the electron beam and the electron beam power is absorbed there. Besides, at the time when the secondary electron current is large, the electron beam power is absorbed at the shallower portion. From these data of fluctuations, definite periodicity can not be estimated. The data of the longer bombardment duration times of the electron beam indicates stronger periodicity. This is particularly true near the bottom of the fusion zone where the fluctuation of the X-rays generated appear to have some periodicity.

4. Discussions

4.1. A model of the penetration path of the electron beam

From the data shown in Fig. 6 and Fig. 7, it can be said that a portion of the channelled penetration path of the electron beam is intermittently filled with molten metal and with large part of the beam power is absorbed there with strong generation of X-rays. Therefore, by considering the known electron penetration range into the solid metal and the narrow and long channel mentioned, the following mechanism of penetration is proposed.

The penetration path of the high power density electron beam proceeds by the formation of many in line cavities filled with ionized metal vapor. For example, there is the penetration path as shown in Fig. 8(1). The thickness d_i of thin layer of molten metal between cavities must agree with the following expression (2)

$$\sum_i d_i \ll D \ , \qquad (2)$$

in which the value of D is 60 μm for mild steel or 180 μm for aluminum obtained as electron range from equation (1).

In the model shown in Fig. 8(1), electrons can go through the cavities without any loss of their kinetic energy, but their energy is absorbed in the thin layers between cavities and at the bottom of the molten zone. The absorption rate of electron beam power however is not uniform[4], and becomes very large near the bottom of the cavity. The layers near the entrance of the electron beam scarcely absorb any electron beam power, with the cavities near the entrance being cooled by heat conduction. As a consequence, the state shown in Fig.8(1) is not stable, and the penetration path always changes. Therefore, another model as shown in Fig.8(2) is proposed. It can be used to explain the fluctuation of the X-rays generated.

4.2. Fluctuation of penetration path of electron beam

When the balance of forces in a cavity is considered, there exist vapor pressure p_c inside the cavity, hydraulic pressure p_h caused by molten zone and shrinking pressure p_s caused by surface tension. If the cavity is assumed to be a perfect sphere, from static balance of forces and neglecting the force of inertia,

the cavity expands when $p_c > p_s + p_h$, and

the cavity shrinks when $p_c < p_s + p_h$.

The pressures are given by the following equation (3).

$$p_c = p_c(v) \ ,$$
$$p_s = \frac{2\sigma}{R_o} \ , \qquad (3)$$
$$p_h = \rho_o g h \ ,$$

in which v is the temperature of the cavity, σ the surface tension of the molten metal, R_o the radius of the cavity, ρ_o the mass density of molten metal, g the acceleration of

gravity, and h the depth at which the cavity exists.

The vapor pressure changes greatly with temperature. However, the dependence of surface tension on temperature is small, for example, the equation (4) holds to first approximation.

$$\sigma = \sigma_o - \phi (v_1 - v_2) , \qquad (4)$$

in which σ is the surface tension at temperature v_2, ϕ the coefficient of σ, and as to iron σ = 1535 dyn/cm at 1808°K and ϕ = - 0.03~-0.1 dyn/cm°K.[5]

Considering the dependence of vapor pressure on temperature, the temperature in the penetration path of the electron beam must be estimated. It can be estimated from the experimental rate of evaporation, the gas kinetic theory and vapor pressure data.[6] In the case of mild steel and under the experimental conditions given in Tab.1, i.e., by bombarding the target for 20 seconds, v_o is estimated as:

$$v_o = 2700°K . \qquad (5)$$

This value nearly agrees with the data under nearly the same conditions.[2] In the model of penetration path shown in Fig.8(1), the temperature of all cavities can be assumed to be the same. Assuming that R_o is the electron beam radius (0.025 cm), the values of pressure caused by surface tension and other pressures are given as follows:

$$P_c = 10^5 \text{ dyn/cm}^2,$$

$$P_s = 1.2 \times 10^5 \text{ dyn/cm}^2,$$

in which ϕ = -0.1 dyn/cm°K, (6)

$$P_h = 1.7 \times 10^4 \text{ dyn/cm}^2,$$

in which h ≒ 2.4 cm.

Therefore, p_s is sufficiently larger than p_h , and p_c is nearly equal to p_s, i.e., the cavity is in the stable force-balance. This stable balance of forces holds on the average through all cavities under this experimental condition.

In the case of aluminum, the assumption is made that the cavity is stable on the average when it is of use to the radius of the beam (0.017cm).

Consequently, by the vapor pressure which is assumed to be equal to the pressure caused by surface tension, the temperature in the penetration path of the aluminum target can be estimated to be about 2350°K.

At the thin layers near the entrance of electrons into metal, the electron beam power is scarcely absorbed, therefore the cooling effect due to heat conduction is large. To estimate this numerically, the following assumptions are introduced. The cavitites in a line are considered to form a cylinder which is a perfect conductor surrounded by the material of which mass density, heat capacity, thermal conductivity and thermal diffusivity are ρ_0 g/cm^3. c cal/g·°K, cal/cm·sec°K and κ cm^2/sec respectively. Then the temperature v°K of the cylinder is expressed by equation[7] (7).

$$\frac{v - V_0}{v_0 - V_0} = \frac{4\alpha}{\pi^2}\int_0^\infty \frac{\exp(-\kappa t x^2/R_0^2)}{x\cdot\Delta(x)}dx$$

$$\Delta(x) = \left[xJ_0(x) - \alpha J_1(x)\right]^2 + \left[xY_0(x) - \alpha Y_1(x)\right]^2 \quad , (7)$$

in which J_0, J_1, Y_0, Y_1 are Bessel functions, the region outside the cylinder initially at V_0°K, the region inside the cylinder of which heat capacity per unit length S cal/cm°K initially at v_0°K and $\alpha = 2\pi R_0^2 \rho_0 c/S$.

Furthermore if the heat capacity of the cylinder is equal to that of the surrounding material, then $\alpha = 2$. The values of ρ_0, c, κ of mild steel are about 7.8 g/cm^3, 0.16 cal/g°K and 0.037 cal/cm·sec°K respectively near melting point, and those of aluminum 2.7 g/cm^3, 0.3 cal/g°K and 0.43 cal/cm·sec·°K respectively near melting point. Therefore, the values of κ are about 0.03 cm^2/sec for mild steel and about 0.5 cm^2/sec for aluminum.

If cooling continues for 2 msec,

$$\frac{v - V_0}{v_0 - V_0} = 0.55 \text{ for mild steel, and}$$

$$0.1 \text{ for aluminum,}$$

then,

$$v = 2300 \text{ °K for mild steel, and}$$

$$1100 \text{ °K for aluminum,} \qquad (8)$$

in which v_0 is the experimental temperature in penetration path 2700°K for mild steel and 2350°K for aluminum, V_0 is assumed to be 1800°K for mild steel melting point and 932°K for aluminum melting point.

Namely, if the electron beam is not absorbed for 2 msec, then the cavity cools to 2300°K for mild steel and 1100°K for aluminum. At these temperatures, the vapor pressures are as follows:

$$P_c = 6.7 \times 10^3 \text{ dyn/cm}^2 \text{ for mild steel, and}$$
$$2 \times 10^{-3} \text{ dyn/cm}^2 \text{ for aluminum,} \qquad (9)$$

then,

$$P_c \ll P_s + P_h. \qquad (10)$$

Therefore, the cavity begins shrinking. Considering the very small heat capacity of the cylinder, i.e., the cavity, the value of α is very large and cooling becomes very steep. Moreover, due to the large value of κ, the coooling effect of the aluminum target is much larger than that of the mild steel target. Consequently, the cavity in aluminum target begins shrinking more rapidly than in the mild steel target. One must consider that the shrinking of cavity starts as soon as the cavity stops absorbing the electron beam power.

As to the shrinking itself, the following equation holds.[8]

$$\rho_0 \left[R\cdot\ddot{R} + \frac{3}{2}\dot{R}^2\right] = \Delta p = \frac{2\sigma}{R}, \qquad (11)$$

in which R is the radius of the cavity, $\dot{R}$ denotes dR/dt, Δp the difference of pressures between inside the cavity and at great distance apart from the cavity.

By the cooling, $|\Delta p|$ becomes sufficiently smaller than $2\sigma/R$, and equation (11) is reduced to equation (12).

$$\rho_0\left[R\cdot\ddot{R} + \frac{3}{2}\dot{R}^2\right] = -\frac{2\sigma}{R}. \qquad (12)$$

From equation (12), the necessary time for the cavity to collapse perfectly (R = 0) is given by equation (13).

$$t = \sqrt{\frac{\rho_0}{2\sigma}}\int_{R_0}^{0} \frac{R^{3/2}}{\sqrt{R_0^2 - R^2}}\, dR$$
$$= 0.92\, R_0^{3/2}\sqrt{\frac{\rho_0}{2\sigma}} \text{ , (sec)} \qquad (13)$$

in which R_0 is the initial radius of the cavity, and R_0 is assumed to be 0.

In the case of mild steel the cavity with radius equal to that of

the beam collapses perfectly in about 0.2 msec, while in aluminum, in 0.08 msec..

As a whole, the cavity collapses perfectly in about 2 msec after it stops absorbing the electron beam power, but if the small heat capacity of the cavity is considered, the collapse time becomes smaller. In the case of the aluminum target, because of the steeper cooling and the shorter collapsing time relative to the mild steel target, the collapsing of the cavity in the aluminum target occurs more frequently.

When a cavity cools and collapses, the electron beam is absorbed there again and a new cavity is reformed. This phenomenon occurs in sequence in the penetration path of the electron beam as shown in Fig. 8(2), and in such manner the beam reaches deep into the metal target, but in fact it is only a small portion of it as shown in Fig. 5.

4.3. Flow of molten zone

The discussions mentioned above neglect the flow of the fusion zone, but it must be stated that the fusion zone always moves, and this motion does not invalidate the above mentioned discussions.

In the models in Fig.8(1) and Fig.8(2), there exists also the upward movement of the cavities caused by buoyancy. This movement can be assumed to be in the stable state due to viscous resistance, in which case equation (14) holds.

$$\pi R'^2 (\rho_0 gh - \rho' gh) = \mu \frac{du}{dr} 2\pi R'h \,, \qquad (14)$$

Here R' is the apparent radius of moving molten zone which moves upwards with cavities, ρ_0 the mass density of molten zone, ρ' the apparent mass density of moving molten zone which contains the cavities, h the length of penetration path formed by cavities in a line, μ the coefficient of viscosity, u the upward speed, r the distance from penetration path.

As to ρ', the following equation holds to first approximation.

$$\pi R'^2 h \rho' = (\pi R'^2 h - \pi R_0^2 h)\rho_0 \,, \qquad (15)$$

in which R_0 is the radius of cavities.

Then, the speed u of cavities is obtained by substituting u/R' for du/dr and R_0 for R' in equation (14).

$$u = \frac{1}{2} R_o^2 \frac{g}{\mu/\rho_o} \quad . \tag{16}$$

When R_o is equal to electron beam radius, substituting the value at melting points for μ, that is, 6.7 centipoise for mild steel and 4.5 centipoise for aluminum,

$$u = 30 \text{ cm/sec for mild steel target, and} \tag{17}$$
$$10 \text{ cm/sec for aluminum target.}$$

There being the upward speeds of the cavities in these 2 cases, actually the values of μ change greatly with temperature and as a consequence, the calculated values are very rough. The value of μ of aluminum changing more steeply than that of mild steel. Consequently, from the fact that the temperature in penetration path of aluminum target is sufficiently higher than the melting point, the value of μ is much smaller than 4.5 centipoise, and thus the value of u is considerably larger than the calculated value, that is, it must be considered that the value of u for aluminum target is much larger than that for mild steel target.

One must also consider that the collapse and reformation of cavities must lead to violent movement around the penetration path of electron beam.

These movements in the molten zone and the different absorption rates of the electron beam at the different depth discussed formerly, lead to the shapes of the solidified fusion zones shown in Fig. 3, in the case of an aluminum target being like a wedge while in mild steel target being like a well.

5. Conclusions

The experimental results and the discussions which followed lead to these conclusions.

1. The absorption of electron beam power in the penetration path is not uniform in relation to the fusion zone depth from the target surface in molten zone. Relatively small amounts of beam power reach the bottom of fusion zone.

2. The absorption of electron beam power changes with time, i.e., it occurs as an oscillating phenomenon.

3. From the above conclusions and the range of electron penetration solids, a model for the penetration of the electron beam is proposed, i.e., the penetration path is formed by many in line cavities.

4. These cavities are unstable. The breakdown of the balance of forces in the cavities causes their collapse, and then the absorption of electron beam power in the path forms new cavities.

5. The movement of molten zone is caused by buoyancy, collapse and reformation of the cavities. This movement is more violent in the aluminum target than in mild steel target, and the different shapes of the fusion zones can be explained by the differences in the frequency of collapse of cavity and the movement of the fusion zone.

6. Acknowledgement

The authors thanks to Mr. H. Hase and Mr. K. Shirai of Nippon Electric Company for their co-operation of the experiment, and also to Mr. K. Itoh and Mr. T. Matayoshi of Chiba Engineering College for assistance in collecting data.

References

(1) R. Whiddington: Proc.Roy.Soc. (London) A89,554(1914)
(2) H. Schwarz: J.Appl.Phys. 35,2020(1964)
(3) K. Shimizu, T. Miyazaki, N. Taniguchi: Reports.I.P.C.R., (in Japanese) 48,39(1972)
(4) K.H.Steigerwald: Proc.3rd Symposium on E.B. Tech., 1961
(5) S.Namba, T. Isobe: Proc. 4th Symposium on E.B. Tech., 1962
(6) R.E.Honig: RCA Rev. 23,567(1962)
(7) H.S.Carslaw, J.C.Jaeger: Conduction of Heat in Solids 2nd ed. (Oxford,1959), p.342
(8) H.K.Foster, N.Zuber: J.Appl.Phys. 25,474(1954)

stainless steel (AISA 304)
150 kV, 40 mA, 3×10^6 W/cm²
welding speed : 13 cm/min

1 cm

Fig.1 Example of molten zone by electron beam welding.

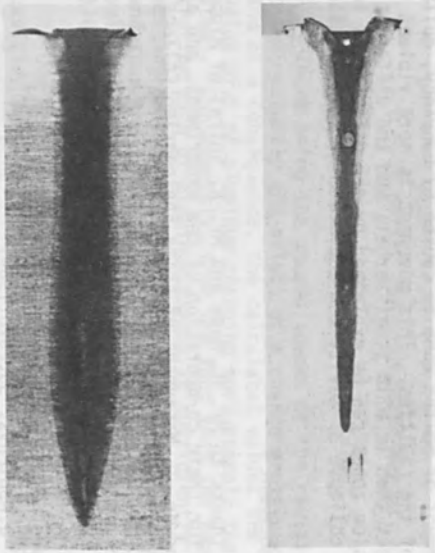

(1) mild steel (2) aluminum

bombardment duration times of electron beam of 2 sec for mild steel (1) and 20 sec for aluminum (2)

1 cm

Fig.3 Examples of molten zones by the continuous and stationary electron beam.

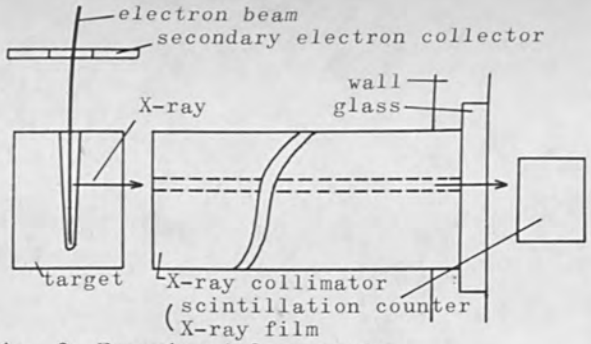

Fig. 2 Experimental apparatus.

target	mild steel	aluminum
acceleration voltage	150 kV	150 kV
beam current	40 mA	20 mA
beam diameter	0.05 cm	0.035 cm
power density	3×10^6 W/cm^2	3×10^6 W/cm^2

Tab. 1 Experimental conditions.

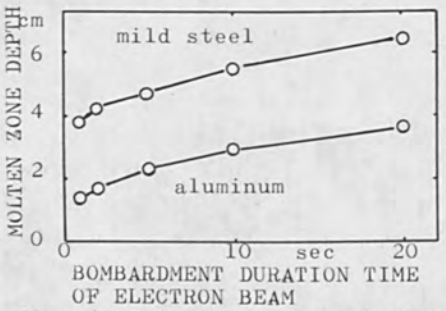

Fig. 4 Relation between bombardment duration time and molten zone depth.

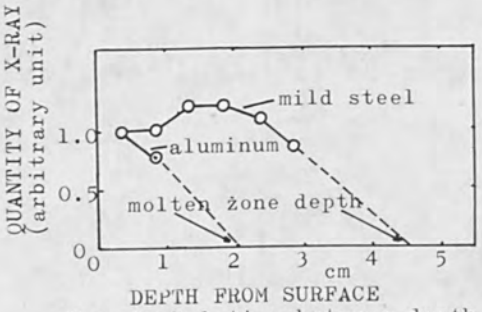

Fig. 5 Relation between depth from surface and quantity of X-ray. (bombardment duration time of 5 sec)

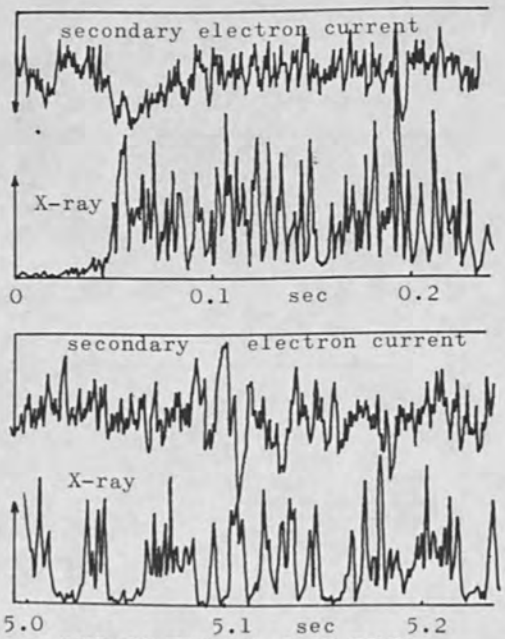

BOMBARDMENT DURATION TIME
scintillation counter fixed at the depth of 0.4 cm

Fig. 6-1 Fluctuations of the generation of X-ray and secondary electron current of mild steel target.

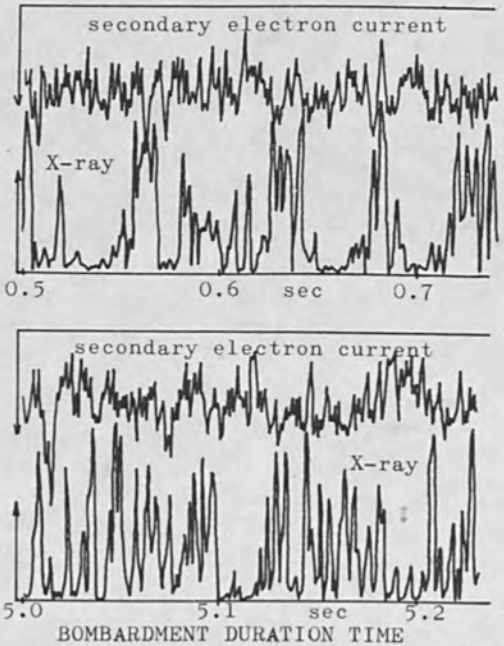

BOMBARDMENT DURATION TIME
scintillation counter fixed at the depth of 2.4 cm

Fig. 6-2 Fluctuations of the generation of X-ray and secondary electron current of mild steel target.

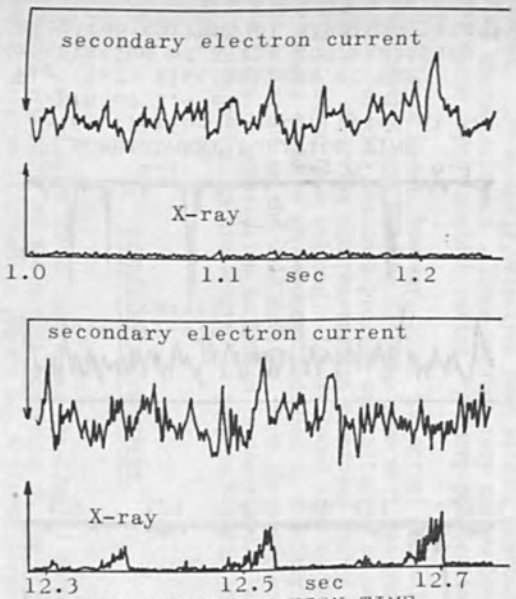

scintillation counter fixed at the depth of 4.4 cm

Fig. 6-3 Fluctuations of the generation of X-ray and secondary electron current of mild steel target.

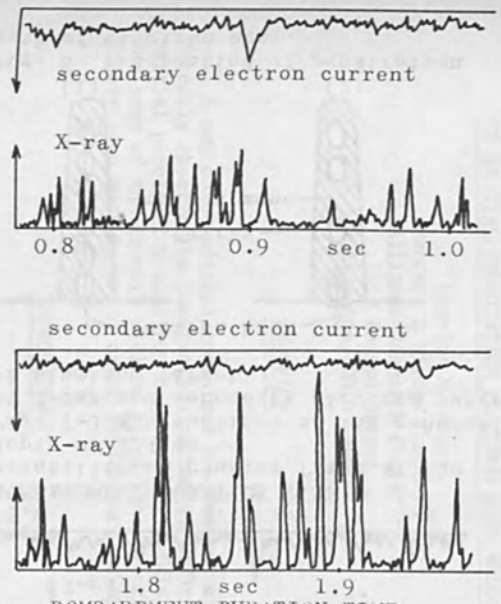

scintillation counter fixed at the depth of 0.4 cm

Fig. 7-1 Fluctuations of the generation of X-ray and secondary electron current of aluminum target.

of the source of the X-radiation. This technique reveals the location in the weld cavity where electrons from the electron beam are colliding with metal atoms in the weld cavity since X-rays are emitted from such collisions.

The pinhole used with this camera is cone shaped and made in one-eighth inch thick lead. A cone shaped pinhole is necessary since the length of the pinhole (1/8 inch) is large compared with the other dimensions. This construction allows for the passage of X-rays that are not aligned with the axis of the pinhole. For example, a cylindrically shaped pinhole would attenuate those X-rays that are not aligned with the axis of the pinhole. This pinhole is mounted to the base plate of the camera which is also of 1/8 inch thick lead. Figure 2 is a picture of the pinhole camera used for this experiment. It contains, in addition to the spools for the X-ray movie film and the driving mechanism, a timing device. This device consists of a small neon bulb wrapped in electrical tape with a hypodermic needle directing the light to the film. With an audio oscillator and an amplifier timing dots are placed on the film to record the film speed.

The film used during this experiment is 35 mm x 25 feet Kodak "No Screen". This is a high speed X-ray movie film not requiring intensifying screens. The electron beam welding machine used during this program was a Hamilton Standard Model No. W1-0 rated at 3 kilowatts.

To compare the X-ray exposures with the penetration pattern, the resulting welds were sectioned longitudinally. Because of the spike like nature of the EB fusion zone extreme care must be exercised to assure that the longitudinal section is at the point of maximum penetration (weld centerline). Butt joints were also used since they can be broken open along the joint to reveal the penetration pattern.

The accelerating voltage was varied between 120 and 150 KV while the beam current was varied between 5 and 10 MA. These two parameters were not varied widely since a large number of energetic X-rays is desired to assure an exposure on the X-ray film in the pinhole camera. The focal area was intended to remain constant at the surface while the welding speed varied between zero and 24 inches per minute. The materials used were 1100 aluminum, 2024 aluminum, 6061 aluminum, 7075 alunimum, 1020 steel, 410 stainless steel, and ETP copper.

RESULTS

To assure that the X-ray exposures of the welds are directly related to the actual penetration, a comparison is made between the penetration determined from the film and the actual penetration. Table 1 gives this information for welds that were made on butt joints

that were broken open to reveal the maximum penetration. The initial penetration was chosen as the point for comparison.

TABLE 1. COMPARISON OF PENETRATIONS OBTAINED FROM X-RAY EXPOSURES WITH OPENED BUTT JOINTS

Weld[a]	Material	Maximum initial penetration from opened butt joint[b]	Maximum initial penetration from X-ray exposure	Percent Difference
39	1020 steel	0.786 cm	0.770 cm	2.0%
40	6061 aluminum	0.834	0.852	2.1
41	410 stainless	0.950	0.912	4.0

[a] All welds made at 150 KV, 10 MA, and 0.93 cm/sec

[b] Maximum initial penetration (occurring within 0.1 sec. of start) was arbitrarily choosen as the point for comparison

Aside from relating to the penetration, the primary value of the X-ray exposures is the illustration of the penetration mechanism. Typical examples of these exposures are given in Figures 3 through 7. Figure 7 is a correlation between the X-ray exposure and a macrograph of a broken open butt joint.

DISCUSSION

The location of the exposures on the X-ray film in the pinhole camera can be directly related to the location of the EB electron collisions in the weld cavity. Magnification of the image is known from the geometry of the set-up. From the films one can determine the location in the cavity where the material intercepts the electron beam.

To determine whether or not the X-ray camera is "seeing" correctly, the initial penetration determined from the exposures is compared to that determined from broken open joints (Table 1). Excellent agreement is obtained. Thus as theoretically expected, the film is accurately recording information.

Also from this data one can get an appreciation of the dimension of the liquid layer surrounding the cavity at its base. The electron beam will impinge on the liquid surface at the base of the cavity. This is the penetration recorded by the film. By cracking open the butt joint and measuring the penetration one is actually measuring

the height of the cavity plus the thickness of the liquid layer at the cavity base plus the thickness of a region that is later melted by thermal conduction as the beam moves on. Comparison of these two measurements will give some idea as to the thickness of this liquid layer. It is seen that the thickness of this layer at the cavity base is approximately two to four percent of the total penetration for those cases considered.

While in some cases this technique could be used to monitor the penetration, the major value of this technique is the portrayal of the penetration mechanism. As the weld is initiated the beam vaporizes the material in its path and thus begins the formation of a cavity. This boring action continues until an equilibrium is established. Once this equilibrium is established, a constant cavity height or penetration is produced (see Figure 3). Regardless of the welding speed, once the equilibrium cavity height is established it remains at that height during the duration of the weld. One might expect that at zero welding speed the beam would just continue its boring action. This has not been observed for welding time of up to 6 seconds.

The time required to reach maximum penetration is less than 50 milliseconds for all cases observed. The actual time depends on the welding conditions and the material, but in all cases it was less than 50 milliseconds.

Once the beam has reached full penetration one might expect a rather static situation. If this were true the X-ray exposures might show just the cavity base where the electrons are hitting. Observation of the exposures show that this is not the case. What is seen on the exposures are spots or regions along the cavity where the EB electrons are colliding with the material (see Figures 3 through 7). These regions may change location with time. At one time the beam may be striking on the cavity base. A few milliseconds later the beam may be striking half way up the cavity or near the surface or at several locations. Since the beam is seen to strike material at various locations, material has been inserted into the path of the beam. This material must be liquid metal falling into the cavity from the surrounding cavity walls. Termed "closures", they can be seen from the X-ray exposures.

Figure 8 provides additional evidence of the closures since this macrograph of a weld cross section shows several closures in the cavity. The material used for this weld is 6061 aluminum. Because of the high thermal conductivity of this material, rapid freezing can be expected when the beam is abruptly stopped. Here the beam has been terminated with the closures present. Rapid cooling of the material preserved this instant, resulting in the capture of closures.

Apparently as the beam strikes the cavity base, it rapidly heats the liquid at the base and pushes it up the cavity walls most likely

in a whirling, dynamic fashion. This liquid metal is in dynamic motion and may become unstable, tending to fall back into the cavity. As it begins to fall into the cavity a closure is being formed. As this closure forms, it intersects the beam. As it intersects the beam, X-rays are produced which show its presence. Also, since this small volume is exposed to the beam it will quickly vaporize and the cavity will again be clear.

This closure-explosion (the small closures as they are quickly vaporized may represent a miniature explosion) mechanism is illustrated in the X-ray exposures (see Figures 3 through 7). While the closure-explosion mechanism is in operation a dynamic equilibrium exists resulting in uniform penetration. Examination of the films show that this cyclic event may proceed from 50 to 200 cycles per second in a uniform way. However, there appears to be an occasional interruption of the closure-explosion mechanism in which the cavity is cleared of metal and the beam dwells on the base of the cavity for an extended period of time, producing a penetration spike. For some reason the closure-explosion mechanism has been inoperative and no closures have formed. With no closures present the extended dwell time will produce a spike. The large spike seen in Figure 7 can be correlated with the absence of closures seen on the X-ray exposure.

Figure 9 is an illustration of the closure-explosion mechanism. More than one closure may also form at a given time. Since this mechanism was observed for all welding speeds considered, including zero speed, it is assumed that this mechanism is the normal mode of operation. Breakdown in the mechanism results in spiking.

Although this mechanism can account for spiking, other defects might find their cause with this mechanism. For example, porosity in the fusion zone could result when a closure forms but does not vaporize completely but freezes off. A portion of the cavity would be trapped, resulting in porosity. Or two closures may form simultaneously. If the beam only vaporizes the upper closure, the lower closure could freeze and yield porosity.

It is well known that the fusion zone of an EB weld is very homogeneous due to excellent metal mixing. These films show the turbulence in the weld cavity. The pumping action of the beam and the formation and vaporization of closures at various locations in the cavity would mix the liquid quite thoroughly.

CONCLUSIONS

From the evidence collected for partial penetration electron beam welding, the following conclusions are possible:

1. The pinhole camera technique can be used to observe the process or mechanism of electron beam penetration.

2. The approximate thickness of the liquid layer at the cavity base is about two to four percent of the total penetration.

3. From the X-ray exposure the penetration mechanism of partial penetration electron beam welding is clarified. With the initiation of the beam, the beam vaporizes the material as it bores its way into the material. Full penetration is reached within 50 milliseconds with the establishment of an equilibrium cavity. The beam impinging on the cavity base pumps heated liquid metal up the cavity walls most likely in a whirling fashion. Closures are produced as liquid from the walls tend to fall back into the cavity. As a closure forms it intersects the beam. This small amount of material inserted into the path of the beam is quickly vaporized. The cavity is again free until another closure or closures form. This closure-explosion mechanism takes place regularly (at a typical rate of 150 cycles per second).

4. Spiking results when there is a failure or breakdown of this cyclic closure-explosion mechanism. When a closure fails to materialize the electron beam is free to dwell on a cavity base for an extended time producing a penetration spike.

ACKNOWLEDGEMENTS

This work was conducted from funding provided by the Atomic Energy Commission from Union Carbide Corporation, Oak Ridge, Tennessee, under Contract W-7405-3NG-25, Subcontract 3347. In particular, Paul Turner is recognized for his support and interest in this work. Appreciation is extended to the Department of Welding Engineering at the Ohio State University for the support and equipment made available. Also, Glenn Mara is thanked for his continuation of this work and the excellent photographs made available.

REFERENCES

1. Matsuda, Fukuhisa, and Hashimoto, Tatsuya, "Compilation of the Reports Published on 'Studies on Electron Beam Welding'" (a

compilation of nine articles appearing in Transactions of National Research Institute for Metals), April 1970.

2. Tong, Henry, "Heat Transfer and Cavity Penetration During Electron Beam Welding," Report No. 69-14 for work sponsored by Lawrence Radiation Laboratory, Livermore, California, June 1, 1969.

3. Weber, C. M., "Penetration Mechanism of Partial Penetration Electron Beam Welding," a thesis, Ohio State University, 1970.

4. Mara, Glenn L., "A Study of the Penetration Mechanism of Electron Beam Welding and the Spiking Phenomena," a thesis, Ohio State University, 1971.

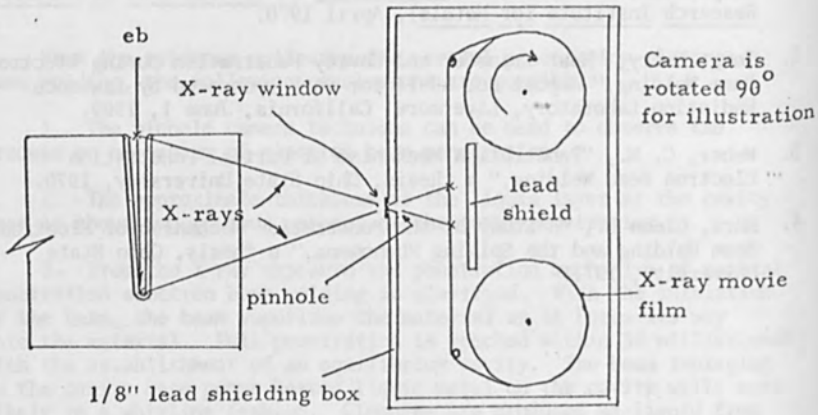

Figure 1 Sketch of Pinhole Camera Technique

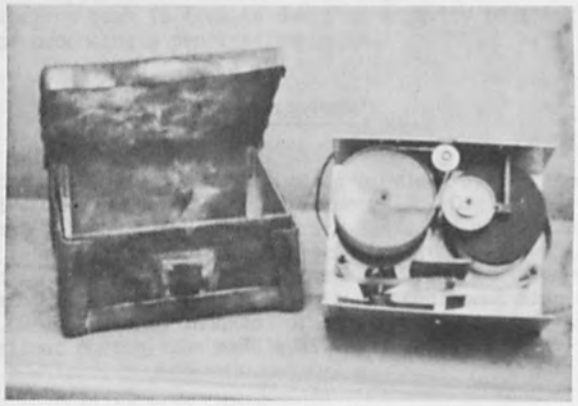

Figure 2 Photograph of pinhole camera revealing working mechanism and lead shielding box with pinhole[3]

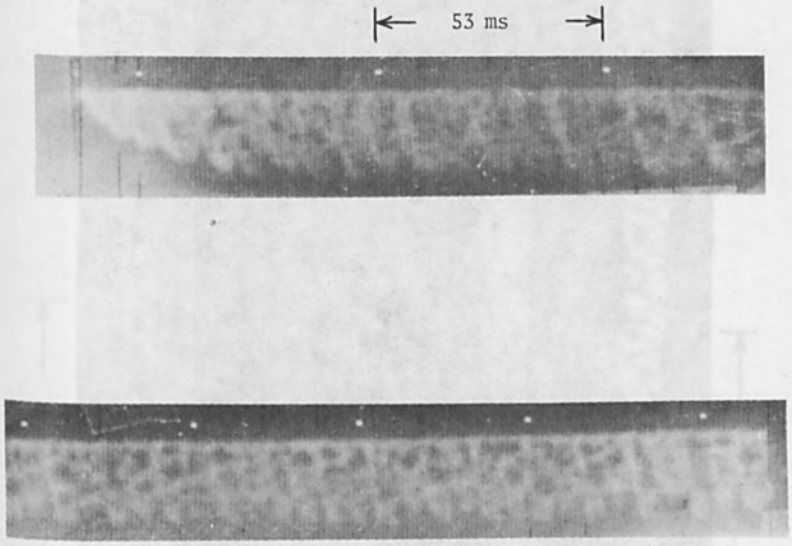

Figure 3 X-ray exposures showing start (top) and end (bottom) of a weld (150 kv, 10 ma, 22 ipm) on 410 stainless steel.[3]

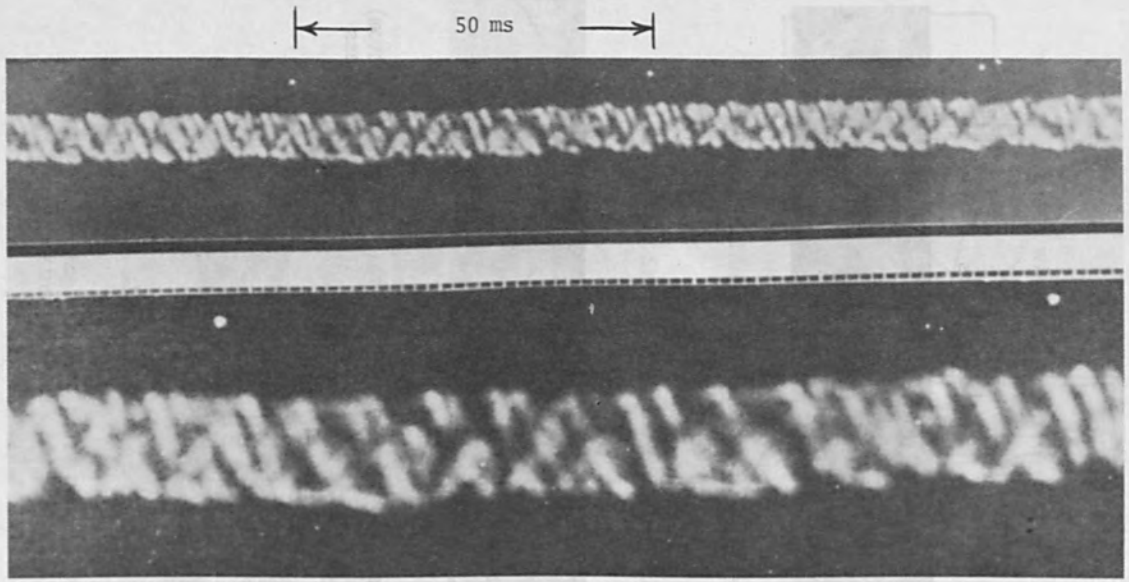

Figure 4 X-ray exposure and enlargement of a weld (122 kv, 10 ma, 21 ipm) on 7075 aluminum showing typical closure activity in the cavity.[4]

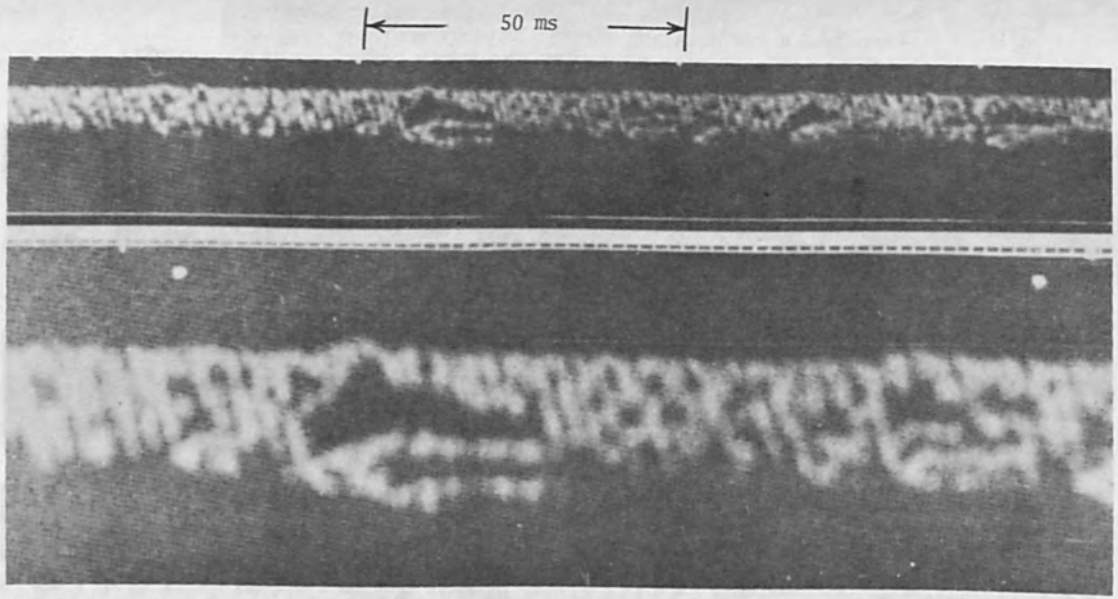

Figure 5 X-ray exposure and enlargement of a weld (122 kv, 10 ma, 21 ipm) on 2024 aluminum showing a breakdown in the closure mechanism producing a spike.[4]

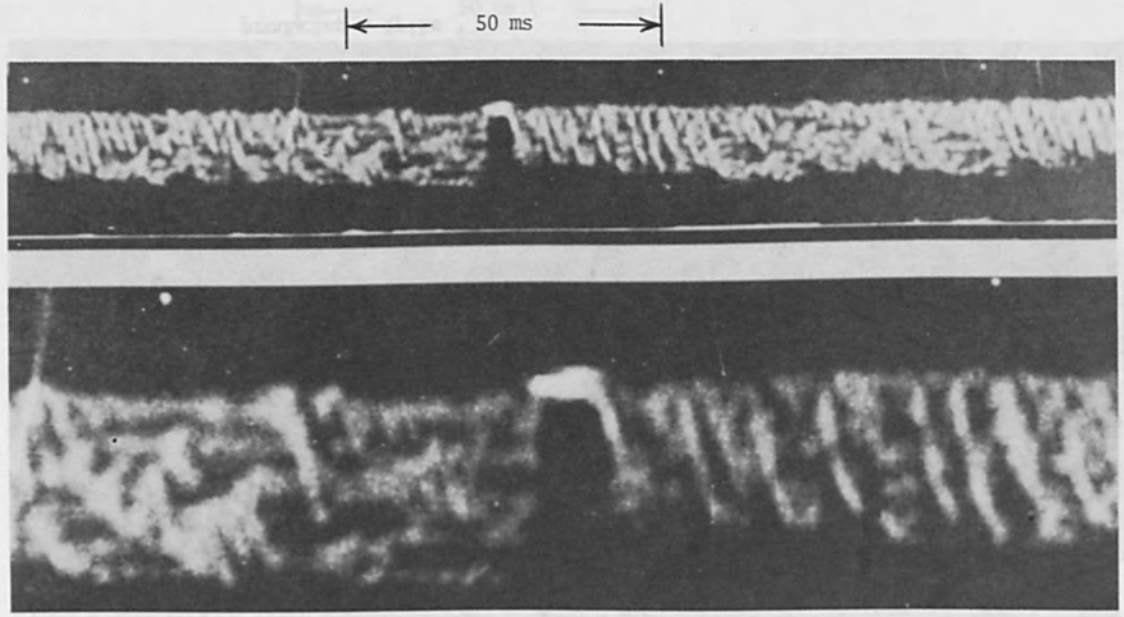

Figure 6 X-ray exposure and enlargement of a weld (126 kv, 10 ma, 21 ipm) on 7075 aluminum showing closure activity and a temporary blockage at the cavity top.[4]

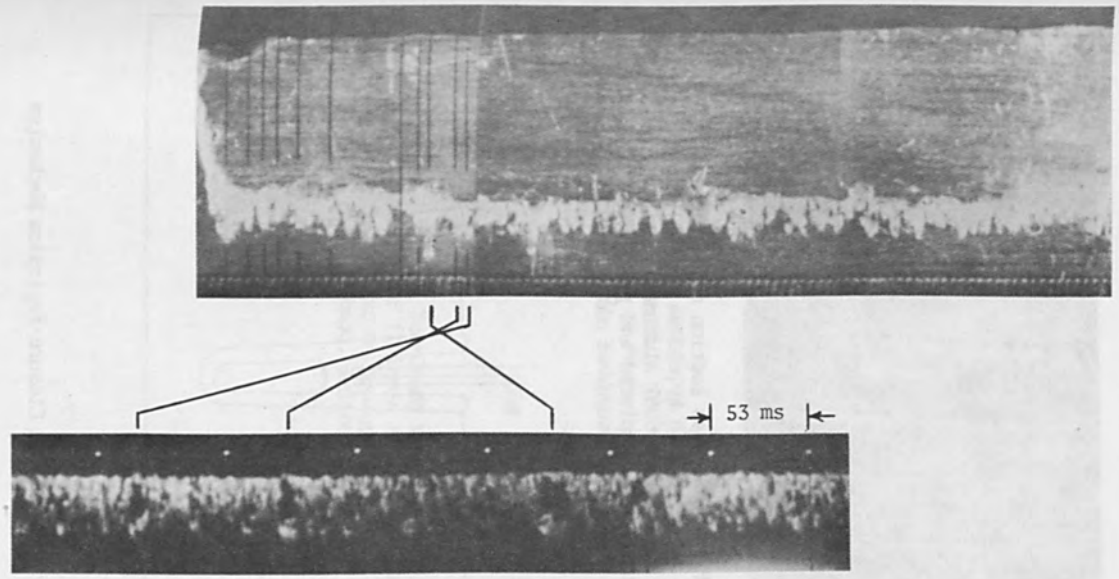

Figure 7 Correlation between longitudinal section and X-ray exposure for a weld (150 kv, 10 ma, 22 ipm) on 6061 aluminum.[3] The absence of closures produced spikes.

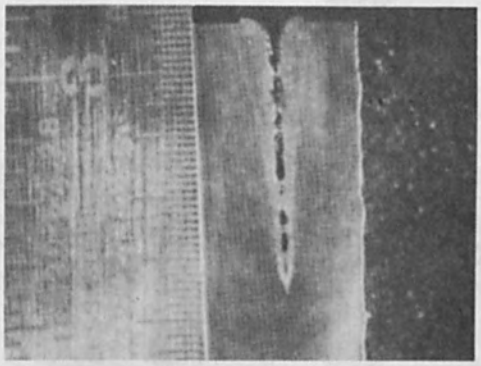

Figure 8 Cross section of a weld (150 kv, 10 ma, 0 ipm) on 6061 aluminum showing completed and pending closures of the cavity.[3]

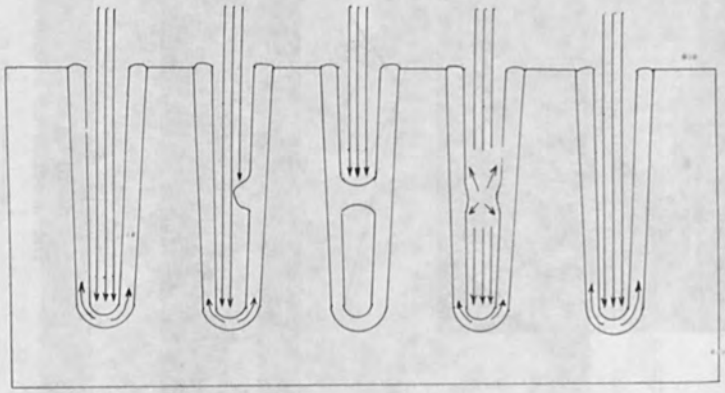

Figure 9 Simulated Closure-Explosion Mechanism

EFFECTS OF ELECTRODE ALIGNMENT OF A PIERCE TYPE GUN ON BEAM CURRENT DENSITY DISTRIBUTION

Henry Tong
Aerotherm Division/Acurex Corporation
Mountain View, California 94040

Warren H. Giedt
University of California
Department of Mechanical Engineering
Davis, California 95616

and

Zuu-Chang Hong
University of Illinois at Chicago Circle
Department of Energy Engineering
Chicago, Illinois 60680

ABSTRACT

Current distributions of an unfocused electron beam emitted from a Pierce gun were qualitatively determined from observations of fluorescent patterns. The fluorescent intensity was compared with current distributions measured with an electron probe and found to be in good agreement. The relative positions and shapes of the Pierce electrodes were varied and the effects of measured current distributions on weld cross-sections were noted.

It is shown that the fluorescent pattern of an unfocused beam can be used as a qualitative indicator to ensure that a consistant electrode alignment is maintained. The fluorescent patterns clearly show that surface irregularities of the filament and emission from the sides of the filament are projected in the beam image. It is also shown that certain distributions are more prone to the formation of weld-root defects.

INTRODUCTION

The purpose of an electron gun is to generate a well-defined stream of high energy electrons. Materials may then be fusion-joined by the bombardment of the interface region with this electron beam. The volume affected by this energy input, the depth of penetration, and the cross-section of the fusion zone depend on the beam characteristics and the material properties. Controllable parameters, such as applied voltage, beam current, gun-to-work distance, and welding speed have been widely investigated and have been related to welding results both in experimental and analytical work (e.g., see Enquist[1]). In addition, Hashimoto and Matsuda[2,3,4] measured the beam diameter and demonstrated that this has a strong influence on the depth of penetration and the bead shape of the weld. Although it has been noted[5] that beam current distribution is also an important parameter, measuring the current distribution in a high energy-density electron beam is a difficult experimental task.

As an alternative to determining the distribution in a focused beam, it is possible to observe the distribution in an unfocused beam which is larger and has a substantially lower energy density. If the beam were para-axial and were passed through a Gaussian optics system, the focused beam would be an image of the unfocused beam. Unfortunately, in many beams used for electron beam welding, neither the para-axial nor Gaussian optics conditions are satisfied so that it is not possible to relate directly the distribution of the unfocused beam to that of the focused beam. However, certain qualitative features, which will affect the welding characteristics, are expected to prevail.

The current distribution of an unfocused electron beam is a function of the shape and position of the electrodes in the electron gun. Depending on the arrangement of these electrodes, the gun may be classified as of the Pierce type or telefocus type; both are currently in use in electron beam welding equipment and each has its limitations. Similar guns are used in microwave and cathode ray tubes and in this context a notable amount of analytical and experimental effort has been expended. For instance, Kirstein[6] discussed the beam distribution near the cathode and Ashkin[7] used a beam analyzer and measured the current distribution in a magnetically shielded electron beam for application of electron flow in microwave tubes.

Any welding process will, of course, depend on the materials being joined and the welding conditions (e.g., power, gun-to-work distance, welding speed, etc.) but it has also been observed that disassembly and reassembly of the gun may noticeably affect the dimension of the fusion zone. It is believed that this may be the result of small variations in the alignment of the electrodes which have significant effects on the beam current distribution. A research program was therefore initiated to observe the effects of electrode alignment on the beam current distribution; particular emphasis was placed on the relationship between the cathode and the bias cup. It was found that certain simple techniques may be applied to determine qualitatively whether or not the electrodes of a Pierce type gun are properly aligned.

The experimental method to be described is presently applicable only to low power conditions; it would be expected that at high power, i.e., high beam current, there would be some shift in the current distribution, although the primary features should remain very much the same. The shift would be due to interaction effects such as space charge repulsion or nonsymmetric defocusing, due to passage of the beam through the aperture of the anode. Furthermore, due to the nonideal nature of the beam and its optics, the focused beam will not be an exact image of the unfocused beam; but again it is expected that certain predominant features will be preserved. In any event, if the electrodes of the electron gun can always be adjusted so as to yield a prescribed unfocused beam pattern, then one possible cause for the lack of reproducibility of electron beam welders is minimized or eliminated.

To obtain information about the effects of beam current distribution on welding characteristics several representative beam shapes were chosen and the weld fusion zone profile which each produce observed.

EXPERIMENTAL METHOD

Two independent techniques were used to study the electron current distribution in an electron beam - the first being qualitative but very

simple to apply and the latter being quantitative but by no means routine in application. To gain a qualitative knowledge of the current distribution, a thin coating of common flat black paint was applied on the upper surface of a copper plate. This plate was then placed in the path of the beam which in turn formed a fluorescent pattern. The black paint provided a high contrast between the fluorescent and non-flourescent regions on the plates. It was then possible to obtain clear photographs of the luminous pattern with the arrangement shown in Figure 1.

A simple electron collection probe was used to obtain quantitative measurements of the current distribution which could be compared with the fluorescent pattern to verify that the luminescent intensity was indeed related to current density. The current flow through the probe was recorded on an oscillograph and probe scans across the beam at 1/16-inch intervals yielded three dimensional plots of the current distribution in the beam.

Due to the high heating rate of an electron beam, the maximum total beam current was limited to 5 to 7 milliamperes. This low beam current and the small entrance area (1/16-inch in diameter) of the electron probe required a high gain amplifier in order to obtain measurable outputs. Hence it was necessary to carefully shield, electrically, components so as to obtain an acceptable signal-to-noise ratio.

The electron gun employed in these studies (Figure 2) is made up of three active components, the cathode, bias cup and anode. The cathode is a ribbon filament with a 1/16-inch square emission area and was of the same type for all experiments. Two different bias cups were used, one had a spherical field shaping surface and the other a conical surface; the dimensions of each are shown in Figure 3. Four different anodes were used; their dimensions are given in Figure 4.

The distance P from the filament surface to a reference position on the bias cup was measured with a depth-dial-indicator to an accuracy of $\pm$0.0005 inch. (Positive P denotes displacement towards the anode and negative P displacement away from the anode.) The distance P was varied systematically over a range of about $\pm$0.015 inch.

Measurements of the position of the filament relative to the bias cup were made under room temperature conditions and it is of importance to assess the change in position due to thermal expansion. During the experiment the maximum beam current was approximately 10 milliamperes, which, from the emission properties of tungsten[8], would require a filament temperature between 2000° and 2500°C. This temperature change was estimated to cause the filament to move toward the anode approximately 0.001 inch. Because this dimensional change is small, it was more practical to record only the room temperature measurements and ignore the thermal expansion. This causes no difficulty since identical techniques

are used to align the gun and the resultant beam patterns are associated with a particular room temperature alignment.

EXPERIMENTAL RESULTS

Conical Bias Cup

A representative fluorescent pattern and the corresponding three-dimensional representation of the measured current distribution for a conical cup are shown in Figure 5. It is clear from this figure that for this particular gun configuration there is a high current density ridge parallel to the y axis. Although the current probe provides quantitative information, it samples a finite area of the beam. On the other hand, the fluorescent pattern records, in essence, an infinite number of points. As a result, it shows much more detail. For example, near the edge of the beam, it can be seen that there are regions in which there is virtually no current flow.

From this and other fluorescent patterns, it was apparent that the AC current in the filament caused the beam to deflect slightly and cause a "ghost" image effect. Although the three-dimensional representation exhibited irregularities in the current density distribution, the ghost effect is not apparent in this representation. The fluorescent pattern also showed that there were regions of the filament that were apparently poisoned so that the local electron emission was virtually zero. It is, of course, not known if these regions persist at high beam currents.

Figures 6 and 7 show the effect of filament position, for the conical bias cup, on the fluorescent pattern and the electron current density distribution respectively. It was observed from this sequence of patterns that the qualitative shape of the pattern changes gradually as the filament is moved towards the anode but retains its basic characteristics. (i.e., The beam shape remains essentially rectangular.) It was also noted from the electron probe data that as the filament was displaced towards the anode, the maximum or peak current density increased, and that the beam pattern shifted from a fairly uniform distribution over a square surface to a distribution concentrated along a line.

Spherical Bias Cup

In marked contrast with the conical bias cup, variation of the position of the filament in the spherical bias cup caused noticeable changes in the beam fluorescent pattern. This change in beam pattern is shown in the fluorescent patterns of Figure 8 and the current distributions in Figure 9. It can be seen from these figures that the current density distribution has a characteristic ridge when the filament is deep in the negative position region and becomes diffused as the filament is moved towards the anode up to about the P = -0.004-inch position

where the beam appears to be fairly uniform. Further displacement toward the anode caused the ridge to form at 90 degrees from the original position. This change in the characteristic ridge of the beam pattern suggests that the filament-bias cup relationship is much more critical for a spherical cup than for a conical cup.

Welding Results

To investigate the possible effects on the quality of the fusion zone representative bead-on-plate welds using 6061 aluminum were made with several different gun configurations and their corresponding beam current density distributions. As previously mentioned, no detailed information about the focused beam was obtained in these experiments, but for consistency, all welds were run with the electron beam focused on the surface of the plate. The focusing was performed by adjusting the focus current so as to obtain the most intense spot. The samples were then welded, sectioned, and etched to show macroscopic details.

Typical welding results are shown in Figure 10 for the spherical bias cup and Figure 11 for the conical cup. From observations of the fusion zones, it appears that the smaller (or more concentrated) beam size has a deeper penetration as might be expected. From these figures it is noted that for a spherical cup, the fusion zone becomes progressively sharper as the filament is moved from the P = -0.015 inch position towards the anode, whereas there is very little qualitative change for the conical bias cup.

Fusion Zone Profiles

In order to use the electron beam for welding purposes, it must be focused at or near the workpiece surface. During this focusing process, due to imperfect electron optics, the beam current distribution distorts gradually as the degree of focusing is increased. Since the present experiments provide no direct information about the current distribution of the focused beam, no firm conclusions can be drawn regarding the effects of current density distribution on the fusion process. However, if it is assumed that the focused beam retained the characteristics of the unfocused beam (i.e., a sharp peaked beam would focus to the same kind of beam), then some useful information relating welding results to beam current distribution can be obtained. In the welding results to be discussed, the beam was visually focused on the surface of the workpiece. All welds were made at the same gun-to-work distance and were run in the same direction. It can be readily appreciated that a beam which focuses to an elongated spot would have different fusion zone features depending on the direction of the weld pass. It can also be expected that smaller and more concentrated beams produce larger depth-to-width ratios.

One might then conclude that the best welding beam is a small and highly concentrated one (i.e., high power concentration), but it has been

observed that this is the condition which is conducive to the formation of welding defects such as porosity, cold shuts, or spiking. A typical set of weld macrosections for different positions of the filament is shown in Figure 12. The spherical bias cup was used for all cases, the beam parameters were set at 30 kV and 135 ma and a welding speed of 37 in/min was used. It can be observed from Figure 12, that the P = -0.010 inch position produced a very uniform weld cross-section, whereas the P = +0.001 inch position produced a wedge shaped cross-section. The former condition has a uniform root and the latter shows evidence of spiking. Referring to Figure 8, it can be seen that the current distribution would be more uniform in the P = -0.010 inch position than at the P = +0.001 inch position. In all cases the visually observed dimensions of the focused spot did not change noticably so that the average power density was approximately constant. Thus, it becomes apparent that the specification of average power density is not sufficient; it is also necessary to specify how this power is distributed in the beam.

DISCUSSION

The experimental results show that the beam current distribution changes with variations in the cathode-bias cup alignment. For any given anode-bias cup relationship, the beam current distribution changes as the filament is moved along the beam axis, the changes being more dramatic for a spherical cup than for a conical cup. The size of the beam, measured from edge-to-edge of the fluorescent pattern, also changes as the filament is displaced as shown in Figures 6 through 9. For the conical bias cup (Figures 6 and 7) the beam size is approximately constant when the filament is in the negative position region, increases in the region of P = 0 inch and decreases back to an approximately constant size at about P = +0.007 inch. For a spherical cup, (Figures 8 and 9), there is a pronounced "hot" zone and the dimensions of this zone vary widely. It can be seen from these figures that the spherical cup has a filament position which causes a minimum size of the beam pattern, the position of the minimum condition being slightly dependent on the choice of anodes.

It should be noted that the edges of the fluorescent pattern are determined somewhat by the characteristics of the fluorescent surface. Further, the total energy in the fringes of the beam appear to be small and may not have a significant influence on the welding characteristics of the beam.

It is not as yet clear which beam current distributions yield the most acceptable fusion zones. However, a parameter which is probably more important than the size of the beam is the peak current density. As this peak increases, for a given total beam current, the beam can be said to be sharper. With a conical cup, the results in Figure 10 show that the peak current density increases rapidly when the filament is moved from the zero position towards the anode. Whereas, when it is

moved from the zero position away from the anode, the peak current density does not change significantly. The reason for this is that the accelerating field in the gun region between the opening of the bias cup and the anode is much stronger than the field above the opening. Thus, the electric field distribution at the emitter will be changed to a greater extent when the filament position is in this region than when it is above the bias cup.

Although the basic characteristics of the fluorescent pattern for a gun with the conical bias cup did not change significantly due to the position of the filament, the same could not be said for the spherical bias cup. When the filament is in the negative position region, the beam current distribution has a high current density ridge which coincides in orientation with the temperature distribution of the filament (Figures 8 and 9). As the filament is moved towards the anode the length of the ridge decreases and its width increases until about the P = -0.004 inch position where the pattern resembles a square. Further advancement of the filament causes the ridge to form again except that its orientation is 90° from the original ridge. This effect is probably due to the fact that, although the spherical cup satisfies the spherical diode condition, the presence of a column of electrons modifies the electric field. Thus, it is shown by Pierce[9] that the electron beam should form an angle of about 67 degrees with the bias cup. The conical cup apparently satisfies this condition and the spherical cup does not. Paradoxically, the peak current density for the spherical cup appears to be more uniform over a wider range of filament positions as shown in Figure 9. This is probably due to a compensating effect caused by the change in characteristics which are observed in the fluorescent patterns. As already stated, the pattern for the spherical cup is most uniform at about the P = -0.004 inch position. As the filament is advanced from this position the peak current density increases until P = +0.004 inch and then begins to decrease. This decrease appears to be the result of a considerable portion of the emitted electrons striking the anode and hence reducing the true beam current.

The anodes used in these experiments did not have a significant effect on the beam current distribution except that anode A_4 (Figure 4) caused a slightly larger beam. This is because this anode is 0.25 inch closer to the filament so that the field gradient is greater. This greater gradient causes the anode, which is effectively a defocusing lens, to have a greater effect on the beam and causes it to have a larger divergence angle. In terms of the basic characteristics of the beam, it is concluded that the geometry of the anode is not as important as the relative position of the filament and bias cup in controlling the beam current distribution.

It is apparent from the above discussion that the conditions near the emitter (i.e., the electric field distribution and possibly the temperature distribution of the filament) are important in establishing

the current distribution on the beam. Other factors, such as the magnetic field induced by the filament current, space charge, and thermal velocity were found to be less important. These are discussed in Reference 10.

CONCLUSIONS

1. An experimental method for determining relative beam current distributions of an electron beam gun by observation of fluorescent patterns formed by impingement of the beam on a painted copper plate was presented. The consistency of these fluorescent patterns with distributions measured by an electron probe demonstrate that the technique is a reliable indication of the current density distribution of the beam.

2. Observation of the fluorescent patterns of an unfocused electron beam can be used to determine whether or not the electrodes of the gun are properly aligned. The patterns can also be used to detect locally poisoned cathodes.

3. For a convergent Pierce type gun, the electric field distribution near the emitter has a strong effect on the current density distribution.

4. The unfocused current density distribution can be related to the resulting weld fusion-zone characteristics. In general a beam with a large current density peak forms a wedge shaped cross-section with large curvature at the root. The greater the curvature, the the greater the base porosity; also such peaked beams are conducive to the formation of spikes.

5. For consistent and repeatable welding results it appears to be insufficient to specify only average power density of the beam. Rather, it is also necessary to specify the current density distribution within the beam.

ACKNOWLEDGMENT

The authors wish to express their appreciation to the Lawrence Livermore Laboratory of the University of California for supporting this investigation.

REFERENCES

1. R. D. Enquist, "Parameters Affecting Electron Beam Welding," Metal Engineering Quarterly, American Society for Metal (Nov. 1968).

2. T. Hashimoto, F. Matsuda, and H. Suzuki, "On the Characteristics of Electron-Beam Current in Electron-Beam Welding," Trans. of National Research Institute for Metals, 6, 1 (1964).

3. T. Hashimoto and F. Matsuda, "Unique Feature of Bead Shape and Its Formation Process in Electron-Beam Welding," Trans. of National Research Institute for Metals, 7, 1 (1965).

4. T. Hashimoto and F. Matsuda, "Effect of Welding Variables and Materials upon Bead Shape in Electron Beam Welding," Trans. of National Research Institute for Metals, 7, 3 (1965).

5. Private Communication with D. J. Sandstrom, Los Alamos Radiation Laboratory, Los Alamos, New Mexico.

6. P. T. Kirstein, "On the Effects of Thermal Velocities in Two Dimensional and Axially Symmetric Beams," Trans. IEEE, Vol. ED-10 (1963).

7. A. Ashkin, "Dynamics of Electron Beams from Magnetically Shielded Guns," J. Appl. Physics, 29, 1594-1604 (Nov. 1958).

8. Kohl, W. H., Handbook of Materials and Techniques for Vacuum Devices, Reinhold Pub. Corp., New York, N. Y. (1961).

9. J. R. Pierce, Theory and Design of Electron Beams, Van Nostrand, Princeton, N. J., (1954).

10. H. Tong, W. H. Giedt, and Z. Hong, "Effects of Electrode Alignment of a Pierce Type Gun on Beam Current Density Distribution," Dept. of Mechanical Engineering, Rept., University of California, Davis, May 1971.

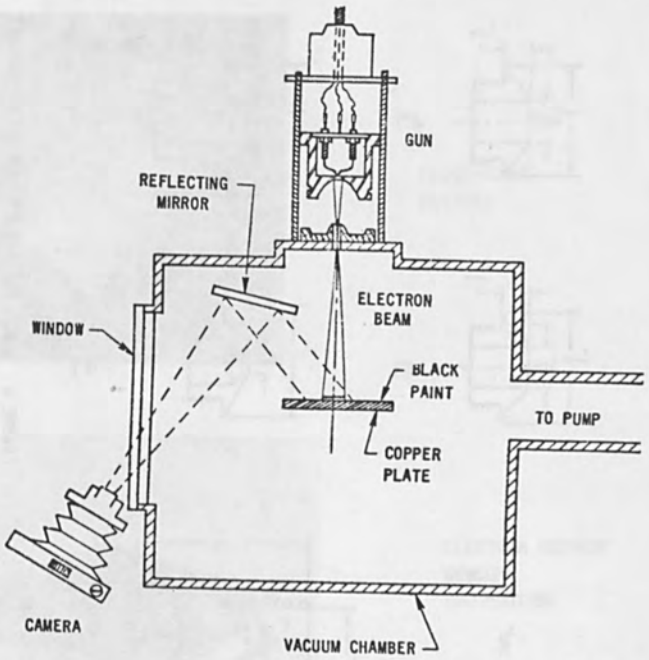

FIGURE 1 PHOTOGRAPHIC PROCEDURE

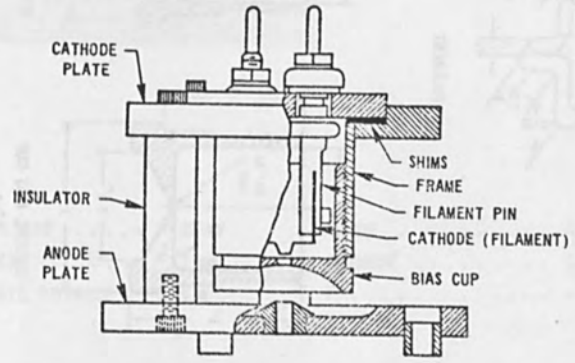

FIGURE 2 ELECTRON GUN

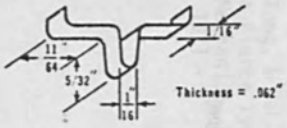

FILAMENT

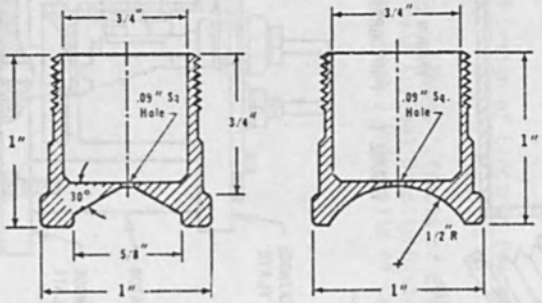

CONICAL BIAS CUP (C_1)

SPHERICAL BIAS CUP (C_2)

FIGURE 3 DIMENSIONS OF FILAMENT AND BIAS CUPS

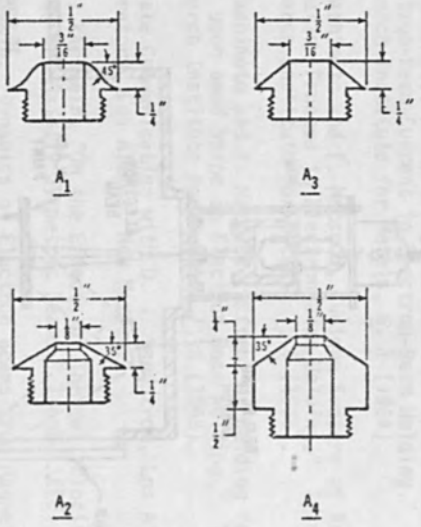

FIGURE 4 DIMENSIONS AND GEOMETRIES OF ANODES

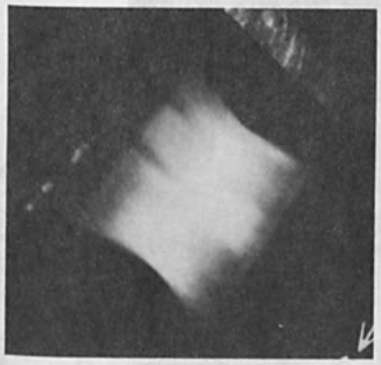

FLUORESCENT
PATTERN

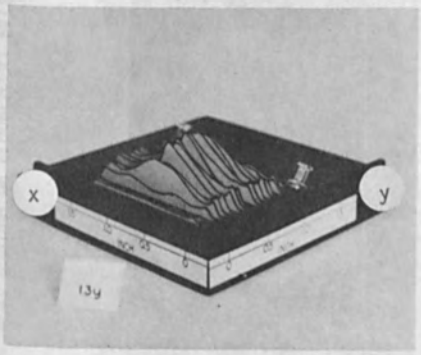

ELECTRON CURRENT
DENSITY
DISTRIBUTION

APPLIED VOLTAGE	30 kV	ANODE	A_1
BEAM CURRENT	7 ma	CATHODE	C_1
GUN-TO-PLATE DISTANCE . . .	9 in.	P	−0.0005 in.

FIGURE 5 BEAM FLUORESCENT PATTERN AND CURRENT-DISTRIBUTION PROFILES

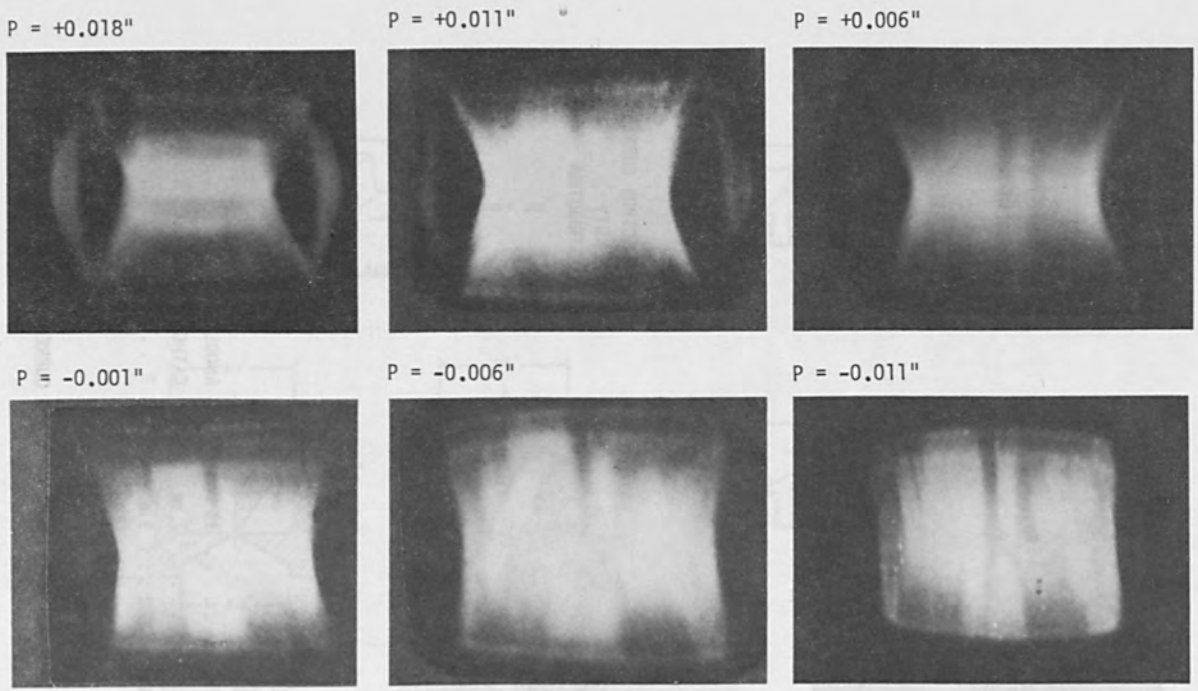

FIGURE 6 EFFECT OF FILAMENT POSITION ON FLUORESCENT PATTERNS WITH CONICAL BIAS CUP

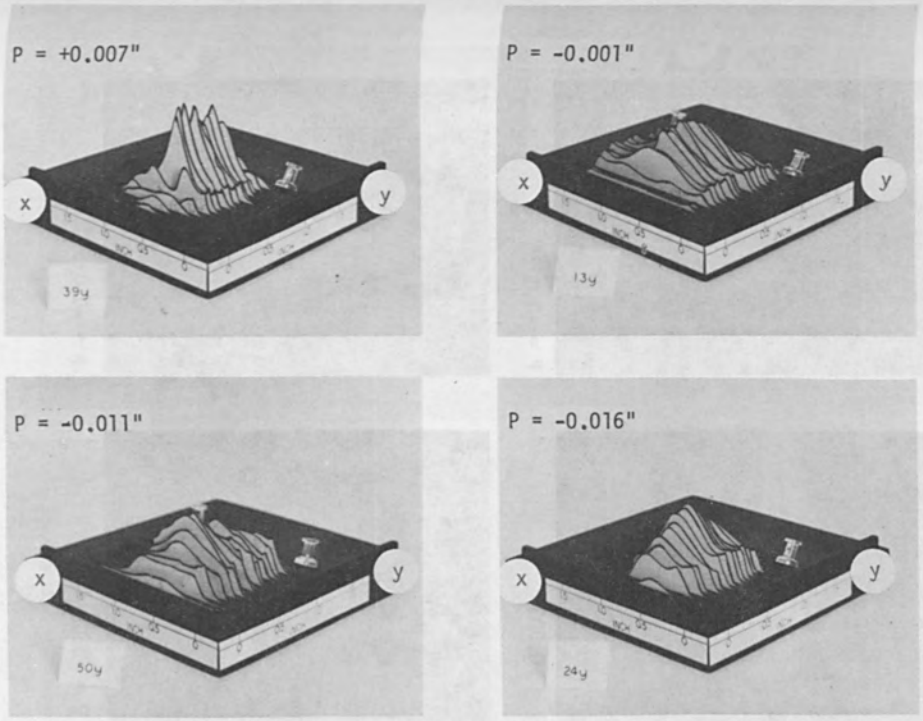

FIGURE 7 CURRENT DENSITY DISTRIBUTION PROFILES FOR CONICAL BIAS CUP

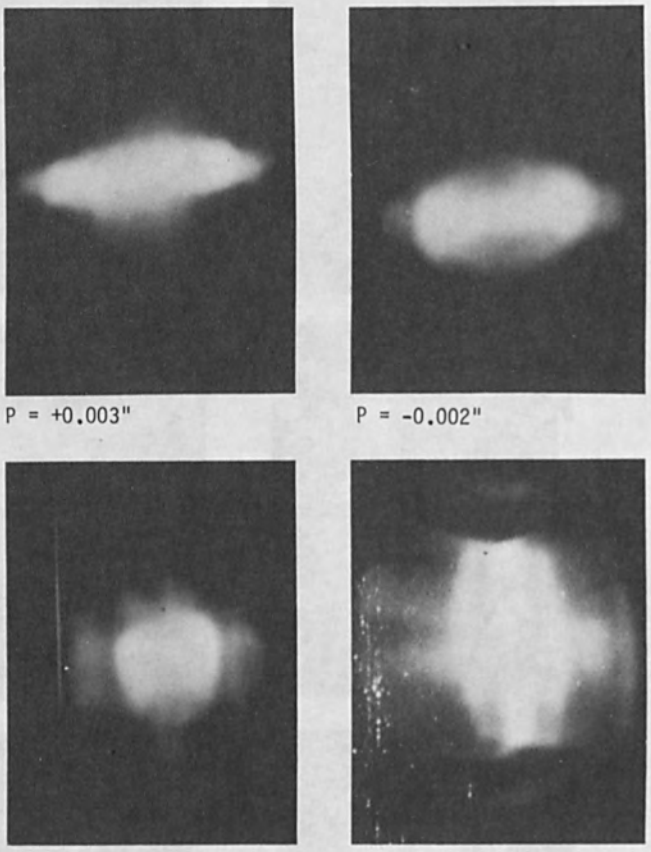

FIGURE 8 EFFECT OF FILAMENT POSITION ON FLUORESCENT PATTERN WITH SPHERICAL BIAS CUP

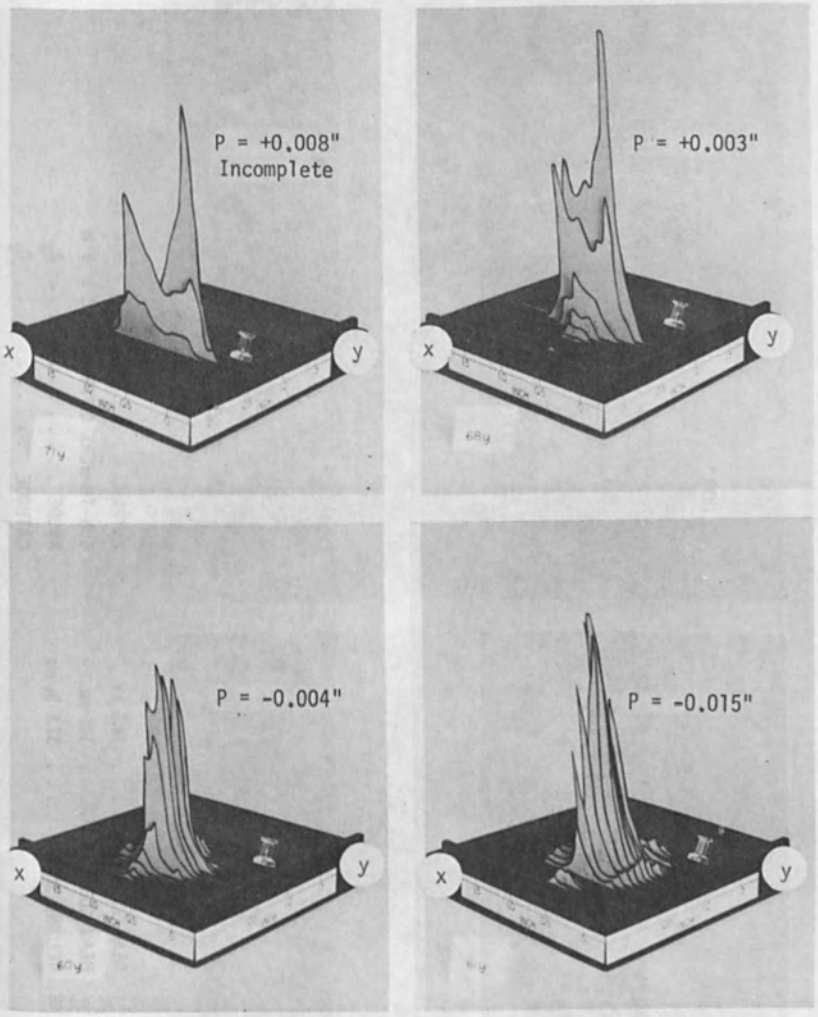

FIGURE 9 CURRENT DENSITY DISTRIBUTION PROFILES FOR SPHERICAL BIAS CUP

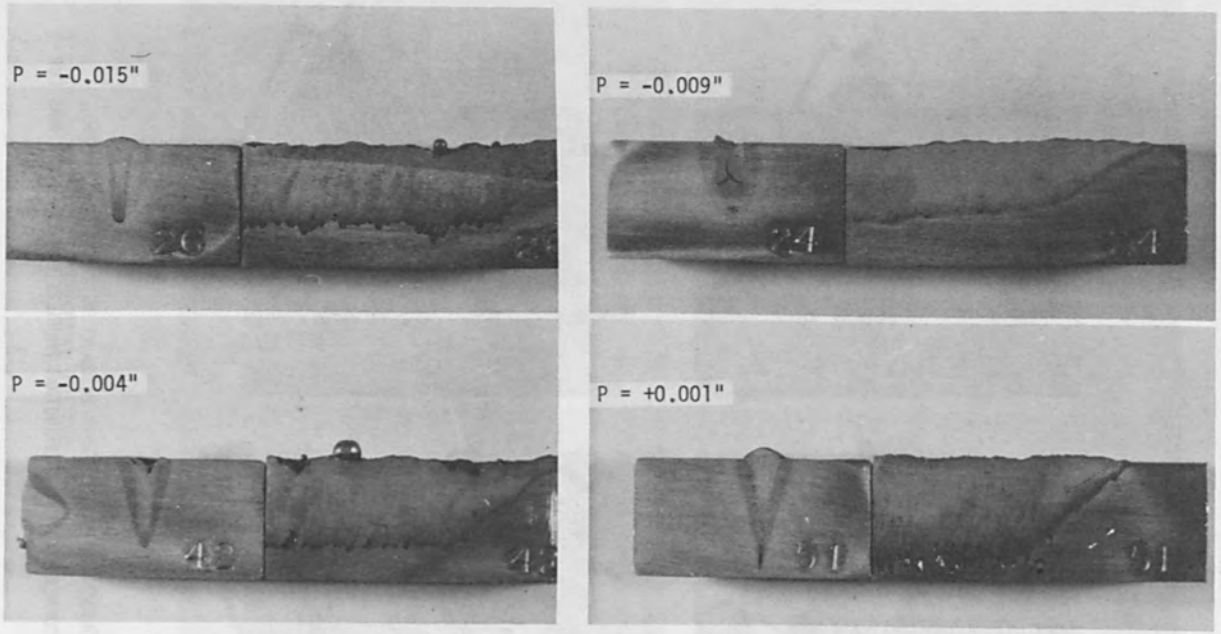

BEAM VOLTAGE	34.5 kV	MATERIAL	6061 Al
BEAM CURRENT	135 ma	GUN-TO-WORK DISTANCE	9 in
WELDING SPEED	37.5 in/min	ANODE	A_3
		CATHODE	C_2

FIGURE 10 EFFECT OF FILAMENT POSITION IN SPHERICAL BIAS CUP ON FUSION ZONE PROFILE

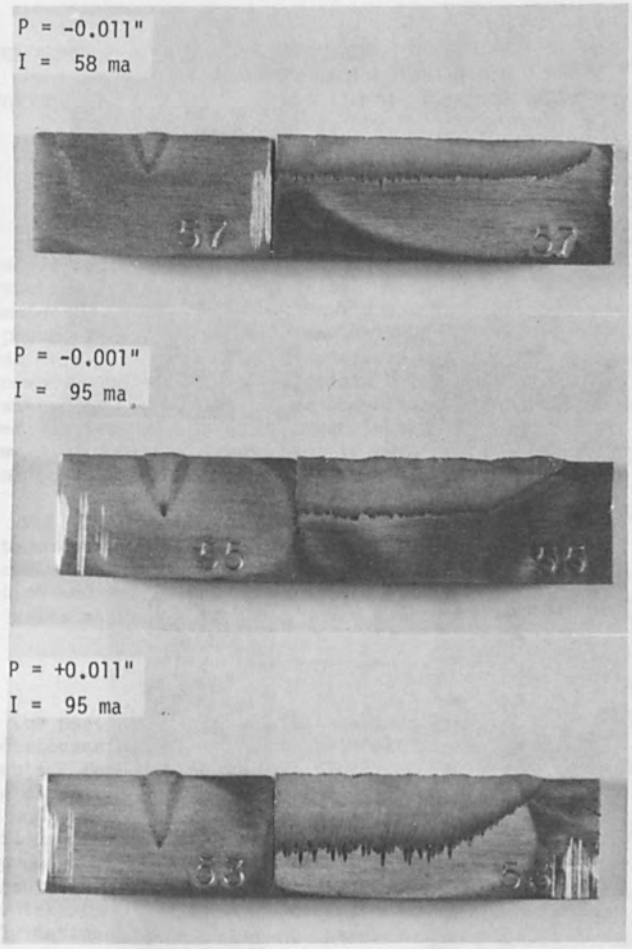

BEAM VOLTAGE	34.5 kV	GUN-TO-WORK DISTANCE	9 in.
WELDING SPEED	40 in/min	ANODE	A_3
MATERIAL	6061 Al	CATHODE	C_2

FIGURE 11 EFFECT OF FILAMENT POSITION IN CONICAL BIAS CUP ON FUSION ZONE PROFILE

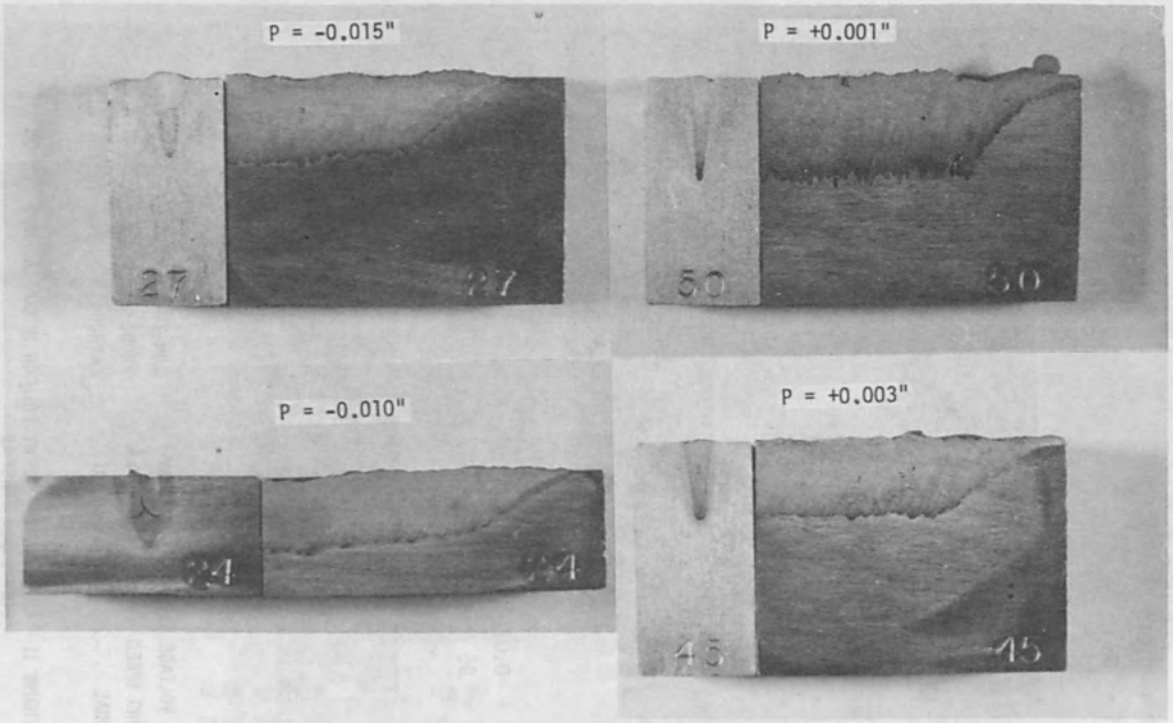

FIGURE 12 FUSION ZONE PROFILES

POWER DENSITY AS A CONTROL PARAMETER IN ELECTRON BEAM WELDING

Donald J. Sandstrom
University of California Los Alamos Scientific Laboratory
Box 1663, Los Alamos, New Mexico 87544

ABSTRACT

Recent experiments have been performed which show that power density should be used as the most important control parameter for electron beam welds. Measurements of the diameter of an electron beam have been made over a variety of power settings and focal lengths in an effort to relate these measurements to weld characteristics. Welds have been made in a variety of materials using various power densities. These studies have shown that the variation in power density at high total power levels has less effect on weld geometry than variation in power density at low total power levels.

Welds have been made on both high voltage and low voltage equipment using power density as the control parameter. These results showed that the weld penetration and weld geometry were essentially identical for welds made at high total power input.

For the past several years the electron beam welding process has been used successfully throughout the world for a variety of joining requirements. Perhaps the initial flurry of activity toward evaluating the characteristics of electron beams as applied to welding has subsided and those of us who must use the process are now left with all of its imperfections and perfidies. Electron beam welding is the kind of process which has an inherent appeal for researchers because it appears to have all of the ingredients necessary for generating data in which some of the usual welding parameters will be very accurately defined. From the pure research point of view this process is probably more controllable than the conventional arc welding processes, however from a users point of view it becomes more obvious that the process presents all of the difficulties usually associated with other joining processes. I dare say that no welding researcher would, a priori, be willing to define the welding parameters necessary to guarantee not more than 95% or less than 90% weld penetration in a 1/2 in. thick stainless steel pressure vessel. Perhaps the request is an unreasonable one, since it seems reasonable that any program requiring this type of weld control would have sufficient mock-up parts to allow for the welding parameters to be sufficiently

well defined to produce the weld. However, as all of those involved in the art and science of welding know, definition of welding parameters without also specifying material cleanliness, joint design and fit-up, and atmosphere is insufficient for the job.

The mechanism of weld penetration has been well described by other investigators[1,2] and I believe is at least conceptually understood. The question under consideration now is how to define the welding parameters for a specific weld in order to take advantage of our knowledge of the mechanism of weld penetration and development. In previous papers,[3,4] I have shown rather conclusively that the mode of melting developed in electron beam welds is dependent upon power density. The threshold power density for cavity penetration occurs at power density greater than 1.2 MW/in.^{2}. At power densities less than this value the melting mechanism occurs by a thermal conductance process.

The work which has been performed at Los Alamos since the early work on beam size measurements has shown that the definition of welding parameters solely in terms of power density is also inadequate for defining weld characteristics. It appears that there is a condition of electron distribution which must be considered in calculations. The distribution of electron density will be strongly dependent upon the type of emitter used in the electron gun and it now appears that the peri-axial electrons, those electrons which are bunched around the very center of the beam, or around a hot spot in the beam may be more important in determining weld conditions than was previously believed. Most beam measuring systems are averaging devices, i.e., they sample a total section of the beam as defined by the probe, and as a result they do not give exact representations of electron densities. Figure 1 consists of the beam measuring device which is routinely used at Los Alamos. This particular device is only 4.0 in. total diameter and is very useful in defining sharp focus of the welding beam. The problem of this being an averaging device still exists and for this reason the distribution of electron densities is not described. The distribution of the electrons in the beam can be described by a Gaussian distribution and a beam trace has been shown in previous papers.[5] The density of electrons in the periphery of the electron beam is lower and there is a greater effect of interaction with foreign atoms and ions on the outer fringe electrons. The effect of the interaction with foreign atoms in the vacuum system can be clearly shown.

Figure 2 consists of a plot of the beam diameter vs. beam current for two different gun-to-work distances at constant voltage. The curves which have been plotted using the open symbols are representative of the electron beam diameters which were measured at the long (4.375 in.) focal length. The behavior of the beam spot at this increased focal length is predictable. Higher accelerating voltage results in a smaller spot. This is probably due to the decreased

electron scatter associated with the high energy electron beam. Increasing beam current causes the beam spot to increase due to repulsion effects in the beam. The effect of increasing gun-to-work distance on the beam spot size is clearly illustrated by this data. The deviation of the spot size from non-linearity with increasing focal length tends to be in better agreement with the data presented by Schwarz.[8] His data indicated that the relationship of beam diameter to beam parameters was described by the equation:

$$d = S\left(\frac{i}{v}\right)^{3/8}$$

where d = beam diameter in inches

i = beam current in ma

v = accelerating voltage

S = constant which is dependent upon electron gun optics

The exponential function described by our curves does not behave according to the above listed equation, however, the results do exhibit exponential deviation.

Additional experiments have been performed in which weld characteristics, i.e., penetration, crown width, etc. were determined as a function of gun-to-work distance. Figure 3 consists of a plot of weld penetration vs. gun-to-work distance for welds in 2219 aluminum which were made at settings which yield constant energy/in. of weld. The data is rather as would be expected. The penetration decreases with increasing gun-to-work distance. Also, the percentage decrease in penetration gets greater as the beam power is decreased. This condition is clearly as would be expected for the condition of lowered beam voltage results in the beam diffusing and spreading out. The broader beam causes the power density of the beam to decrease according to an exponential function which is related to the square of the beam diameter. Figure 4 consists of the same type of plot for 304L stainless steel. The data shown on this set of curves is generally of the same form as was observed for the aluminum samples. The difference in the stainless steel welds is associated with the change in thermal conductivity. When the power density is decreased, the decrease in percent penetration is not as great due to the lower thermal conductivity of the stainless steel. The lower thermal conductivity results in a weld which has a much higher depth-to-width ratio.

The effect of gun-to-work distance for various power settings, on the beam diameter has been plotted and is shown in Figure 5.

The reason for comparing the graph with that of the previous two figures is to show that the percentage change in power density

with increasing gun-to-work distance is much greater than the percentage change in penetration. For example, at 30 kV, 300 mA, the power density at a 1.25 in. gun-to-work distance is ~ 8.0×10^3 kW/in.^{2} while at a 4.375 in. gun-to-work distance the power density is 4.8×10^3 kW/in.^{2}. This corresponds to a 40% change in power density with essentially no change in the resulting penetration. This could mean several things. What appears to be the most important consideration is associated with the distribution of energy densities in the actual electron beam. An analysis of the energy distributions has been made and it appears that the portion of the beam which has the most significant contribution to welding is a very small, highly dense portion in which the electron density is high.

Equations have been determined for the electron distributions in the beam and the standard deviation was determined. It was thought that the beam diameter at the standard deviation might be more useful in calculating power density. This assumption has turned out to be incorrect since the power density as calculated at the standard deviation for a high power beam at short focal length is at least a factor of ten greater than a similar powered beam at a longer focal length. The variation in penetration does not, however, compare with this variation in calculated beam diameter.

Experiments have been performed at Los Alamos and Dow Chemical Companies, Rocky Flats Div. in which an attempt has been made to compare results obtained from welded samples in which identical power densities were used to define the welding parameters. Identical plates of 2219 aluminum alloy were submitted to Rocky Flats and Los Alamos.

The experiments which were performed involved making bead-on-plate welds on the aluminum alloy at two different power density levels. The power densities would correspond to a high voltage weld and a low voltage weld which would deposit the same energy per inch of weld. The weld settings selected on the low voltage, high power density machine at the LASL and the resultant weld geometries are shown in Figure 6. The high power density weld had an average penetration of 0.491 in., however, there was considerable weld "stitching" which resulted in 100% penetration in the plate at various sections. The horizontal section through the weld shows how this penetration has occurred. The power density used for this weld was 3.4×10^3 kW/in.^{2} while the average energy per inch of weld was 8.5 kJ/in. The actual beam parameters for the weld were 25 kV, 170 mA, 30 IPM with a beam diameter of 0.040 in. The average power/inch of weld in the high power density mode was 20.4 kW/in. of weld. The average weld penetration was previously mentioned and a very minor variation in penetration and weld width was observed in the sample independent of position in the welded plate, i.e., the penetration at the start of the weld was essentially identical to the penetration observed at the point of completion.

The low power-density weld was made at a power density of 0.513 x 10^3 kW/in.^{2}. This corresponds to a 6 fold decrease in power density over the high-power-density weld. The actual beam parameters for the low power density weld were 15 kV, 75 mA, 8 IPM, with a beam diameter of 0.053 in. The average energy per inch of weld was, once again, 8.5 kJ/in. whereas the average power per inch of weld is 3.08 kW. The power per inch of weld is 6.6 times less than the average power per inch of weld in the high power density sample. The penetration variation in the low power density weld was from ~ 0.080 in. at the start of the weld to ~ 0.100 in. at the completion of the weld. The variation in penetration appears to have been affected by the preheat which has been supplied to the weld by the low speed, low power density weld. The penetration variation from the start of the weld made at low speed to the high energy density weld is ~ 6.2 times the depth of penetration of the low speed weld.

The longitudinal section of the welded plate shows the characteristic root geometry developed in low power density welds. The root is smooth and free from spiking and other defects. The length of the weld plate was apparently insufficient to obtain the equilibrium depth of penetration, but it appears that a steady state condition has almost been reached.

Table I consists of a summary of the weld penetration results obtained using power density as a defining parameter for weld settings. This experiment was performed using a high voltage machine at Dow Chemical Company - Rocky Flats Div. and a low voltage machine at the Los Alamos Scientific Laboratory.

TABLE I

A SUMMARY OF WELD GEOMETRIES FOR 2219 ALUMINUM ALLOY WELDED AT DOW RF AND LASL

Agency	Voltage kV	Current mA	Beam Dia in.	$\frac{kW}{in.^2}$	Penetration in.	Avg. Width
Dow	120	35.4	0.040	3.4×10^3	0.470	0.225
LASL	25	170	0.040	3.4×10^3	0.490	0.230
Dow	100	11.4	0.053	5.1×10^2	0.088	--
LASL	15	75	0.053	5.1×10^2	0.090	--

This data shows that within some limits, that weld parameters can be specified in terms of power density which will yield similar results despite a difference in the welding equipment. This experiment demonstrates the possibility of exchanging information on welding parameters between agencies and getting some level of reproducibility.

The type of penetration which has been obtained from the weld tests performed thus far suggest the following things.

1. The penetration mechanism of the high power density weld does not appear to be strongly dependent upon a thermal conductivity mechanism. This statement is supported by the fact that the weld penetration appears to be independent of position in the weld, i.e., the measured penetration is essentially identical at the start, in the middle, and at the end of the weld. This suggests that the weld geometry will not be greatly affected by fixturing used on a piece part.

2. The penetration mechanism in low power density welds is dependent upon thermal conductivity affects. This statement is supported by the observed increase in weld penetration in the start, midpoint and end of an electron beam weld.

3. Increasing the gun-to-work distance for any given power setting results in a decrease in power density due to beam broadening. This effect is strongly influenced by accelerating voltage with higher accelerating voltages reducing the effect of beam broadening.

4. The penetration mechanism does not appear to be a simple function of beam power density as determined by beam diameter measurements.

ACKNOWLEDGEMENTS

The author wishes to acknowledge the valuable assistance of the following persons and their contributions to the work reported in this paper: Mr. James M. Taub, Group Leader of the Materials Technology Group, CMB-6, Mr. Gale S. Hanks, Fabrication Section Leader, CMB-6, Messrs. Fred Flick and Victor Vigil, who are electron beam welding machine operators, Mr. Tom Jones for metallographic sample preparation, Mr. John Buchen for the development of beam measuring equipment, Mrs. Jimmie Ellis for preparation of the manuscript and other numerous unnamed people at the Los Alamos Scientific Laboratory who have assisted in this work.

REFERENCES

1. Hashimoto, et al,"Penetration Mechanism of Weld Bead in Electron Beam Welding," Trans. NRIM, Vol. 7, No. 5 (1965).

2. Tong, Henry - "Heat Transfer and Cavity Penetration During Electron Beam Welding," Report No. 69-14 - University of California Davis, June 1969.

3. Sandstrom, D. J., "The Relationship of Beam Parameters to Weld Geometry in Electron Beam Welds," 4th Int'l Conf. Electron and Ion Beam Sci. and Tech., 1970.

4. Sandstrom, D. J., et al, "On the Measurement and Interpretation and Application of Parameters Important to Electron Beam Welding - Welding Journal, July 1970.

5. Sandstrom, D. J., et al, op. cit.

6. Schwarz, H., "Electron Beam Processes at Different Voltages 1961 Trans. of the 8th Vacuum Symposium, Pergamon Press (1962).

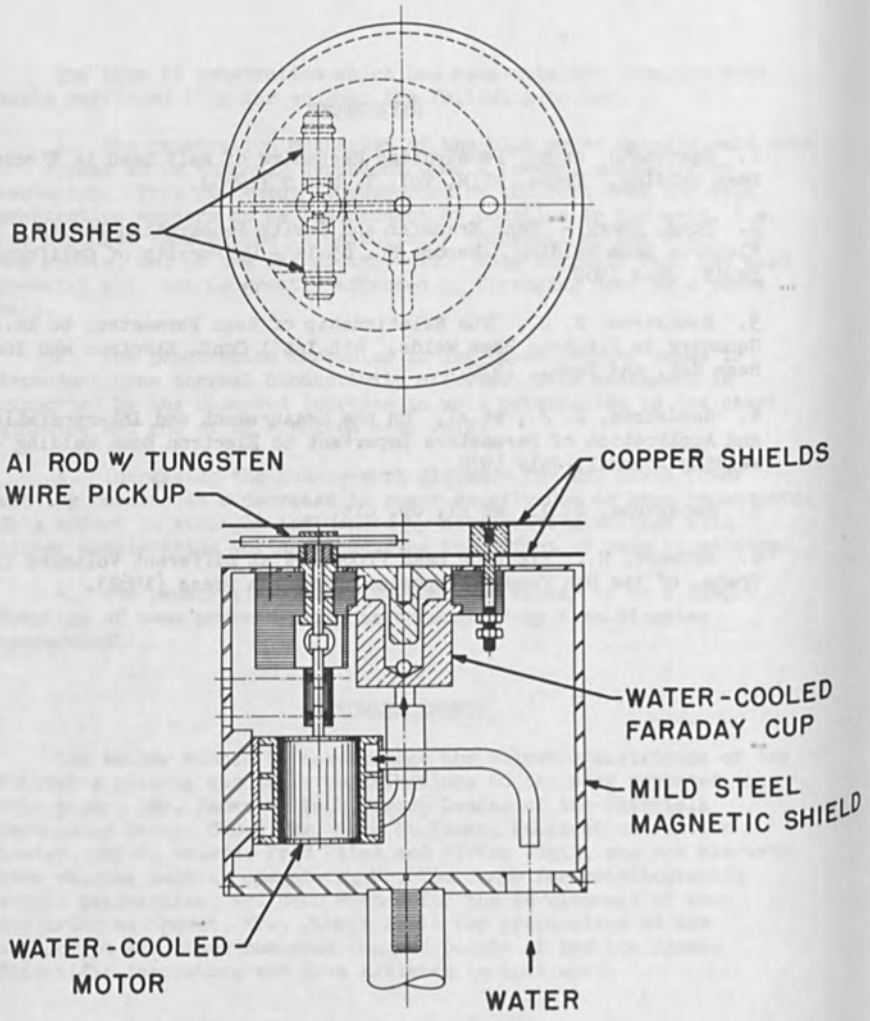

ELECTRON BEAM SCANNER

Figure 1

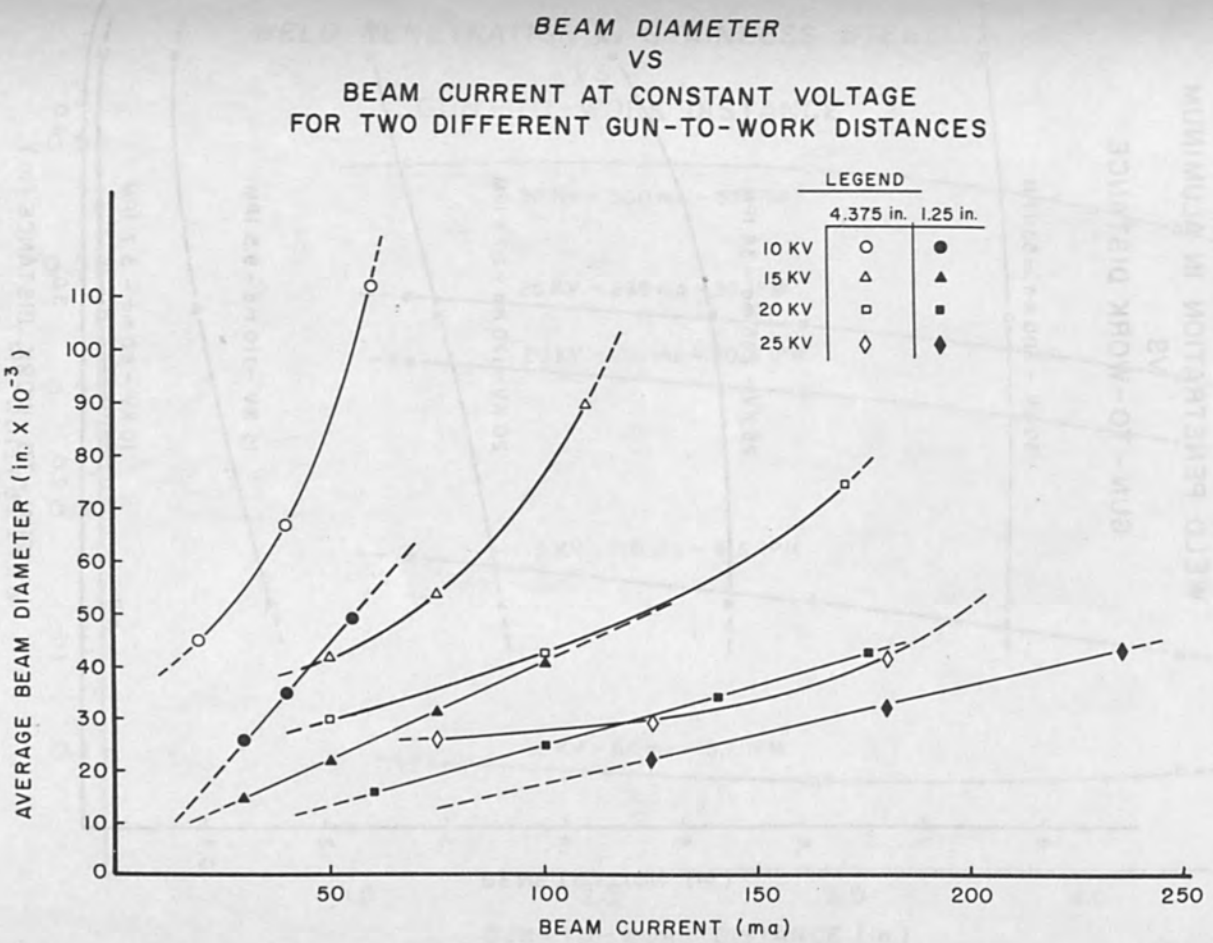
BEAM DIAMETER
VS
BEAM CURRENT AT CONSTANT VOLTAGE
FOR TWO DIFFERENT GUN-TO-WORK DISTANCES
LEGEND
4.375 in.
1.25 in.
10 KV
15 KV
20 KV
25 KV
AVERAGE BEAM DIAMETER (in. X 10⁻³)
0
10
20
30
40
50
60
70
80
90
100
110
50
100
150
200
250
BEAM CURRENT (ma)

Figure 2

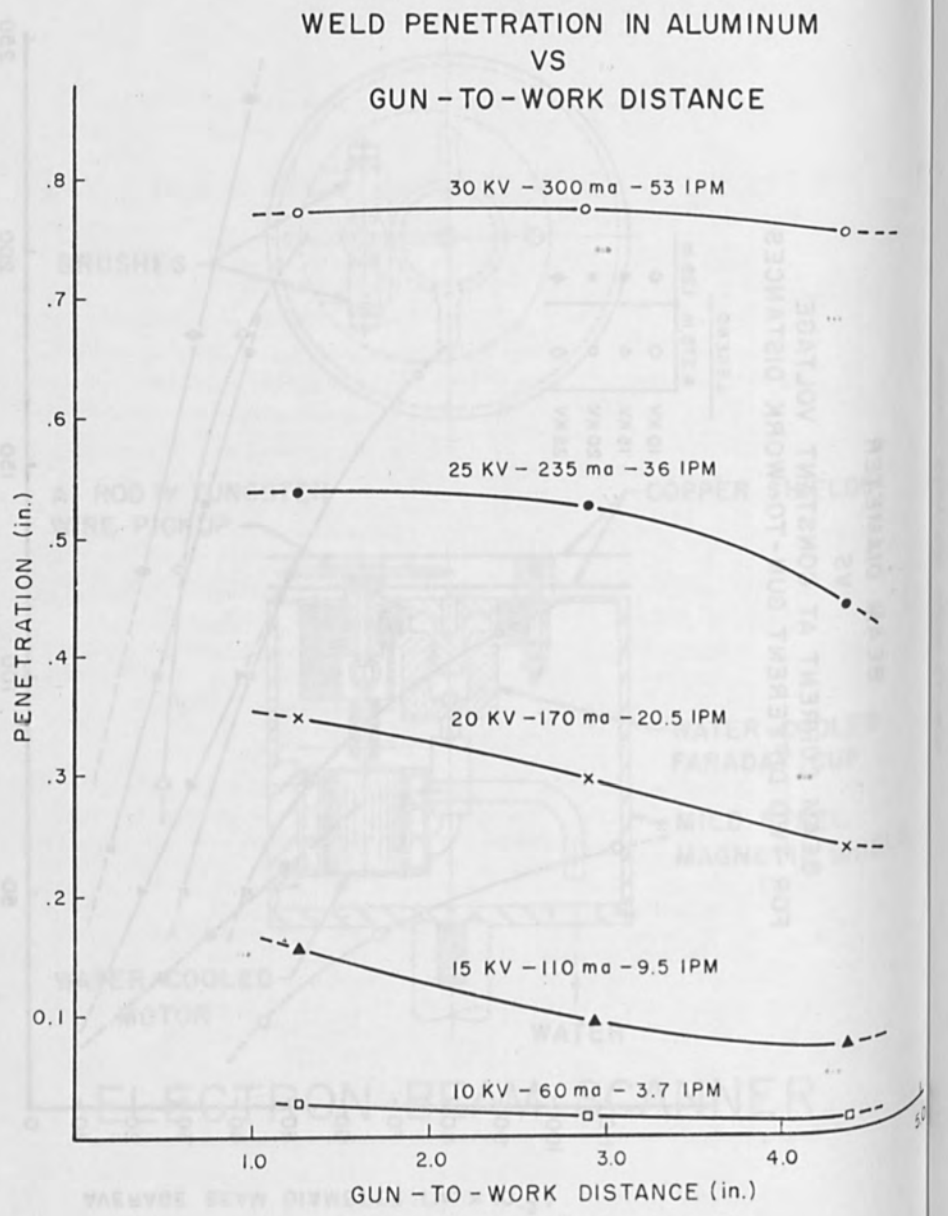
WELD PENETRATION IN ALUMINUM
VS
GUN - TO - WORK DISTANCE
30 KV - 300 ma - 53 IPM
25 KV - 235 ma - 36 IPM
20 KV - 170 ma - 20.5 IPM
15 KV - 110 ma - 9.5 IPM
10 KV - 60 ma - 3.7 IPM
PENETRATION (in.)
.8
.7
.6
.5
.4
.3
.2
0.1
1.0
2.0
3.0
4.0
GUN - TO - WORK DISTANCE (in.)

Figure 3

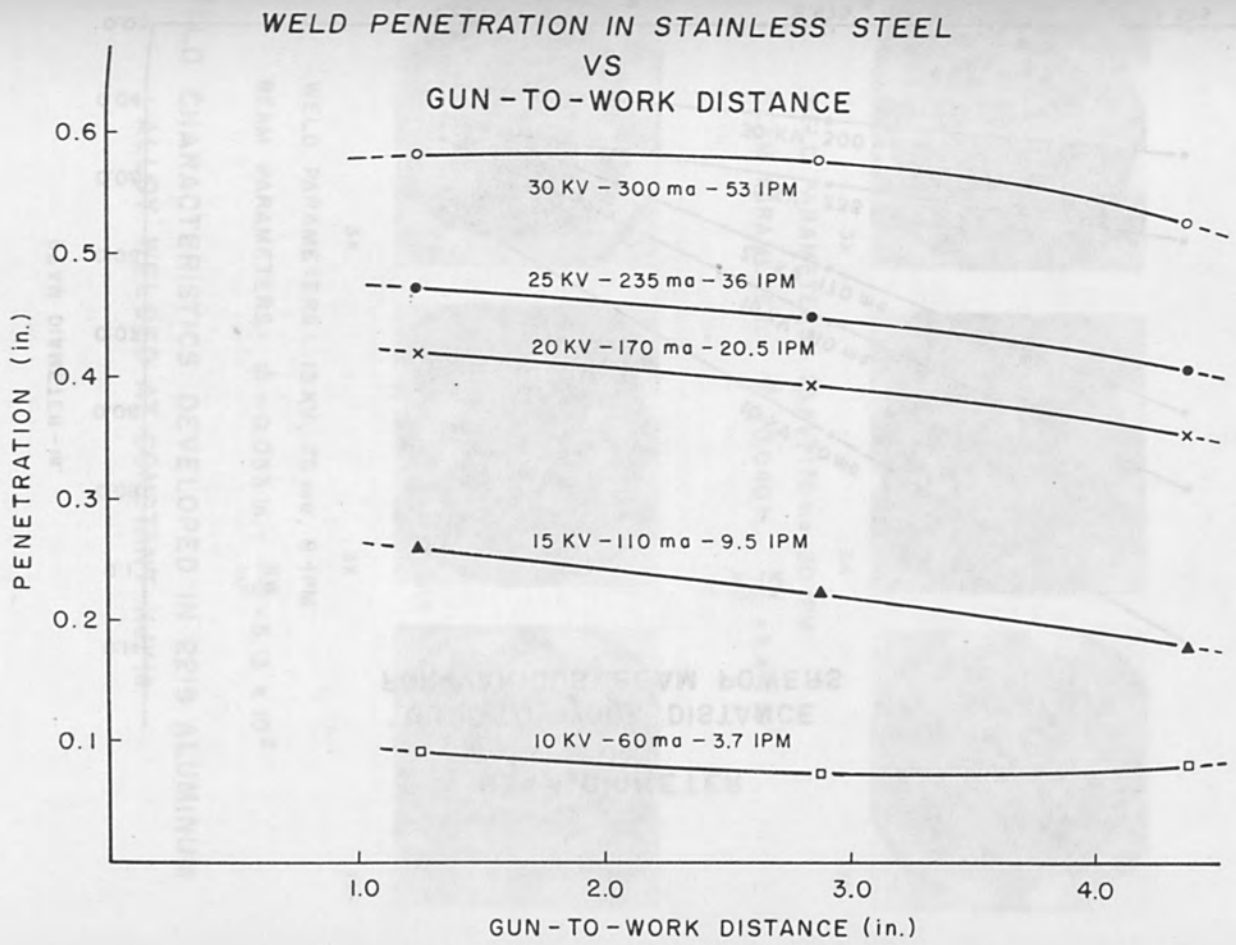
WELD PENETRATION IN STAINLESS STEEL
VS
GUN-TO-WORK DISTANCE
PENETRATION (in.)
0.6
0.5
0.4
0.3
0.2
0.1
30 KV - 300 ma - 53 IPM
25 KV - 235 ma - 36 IPM
20 KV - 170 ma - 20.5 IPM
15 KV - 110 ma - 9.5 IPM
10 KV - 60 ma - 3.7 IPM
1.0
2.0
3.0
4.0
GUN-TO-WORK DISTANCE (in.)

Figure 4

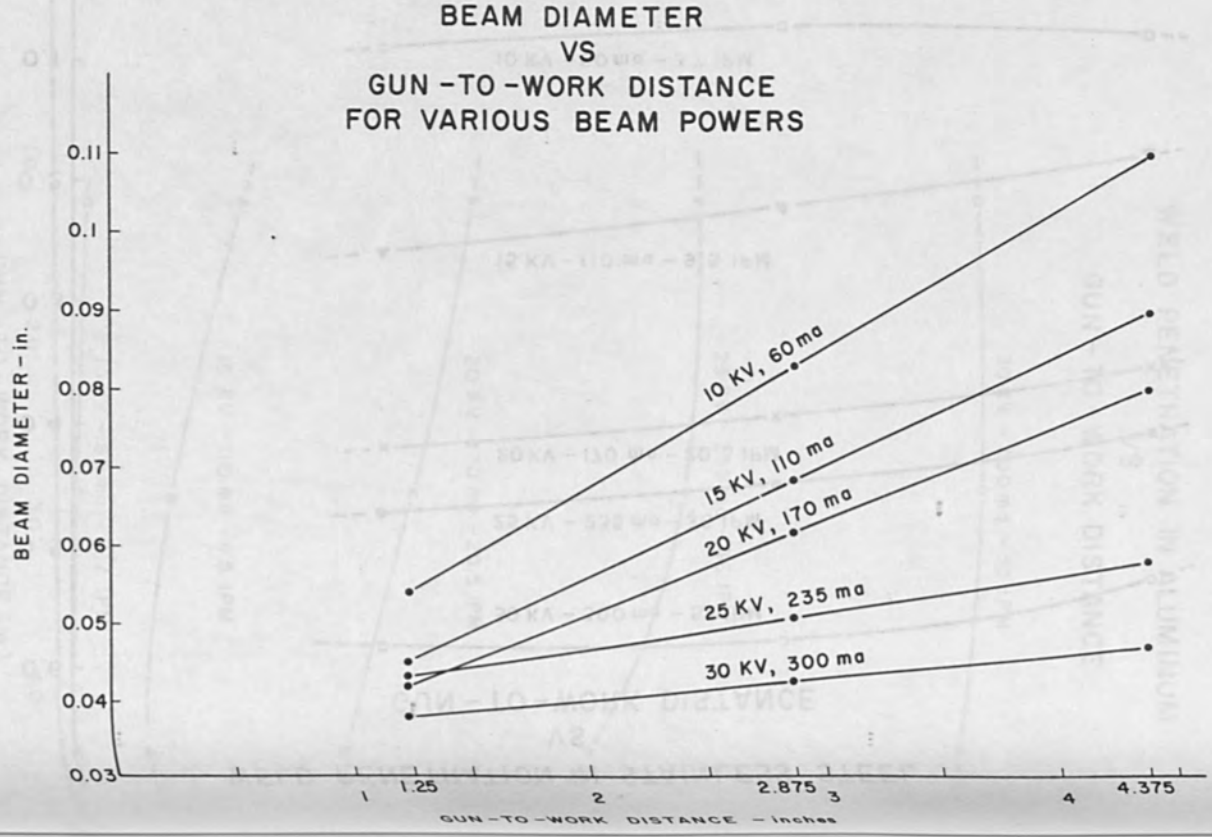
BEAM DIAMETER
VS
GUN-TO-WORK DISTANCE
FOR VARIOUS BEAM POWERS
BEAM DIAMETER - in.
0.11
0.1
0.09
0.08
0.07
0.06
0.05
0.04
0.03
10 KV, 60 ma
15 KV, 110 ma
20 KV, 170 ma
25 KV, 235 ma
30 KV, 300 ma
1
1.25
2
2.875
3
4
4.375
GUN-TO-WORK DISTANCE - Inches

Figure 5
352

GUN-TO-WORK DISTANCE - Inches

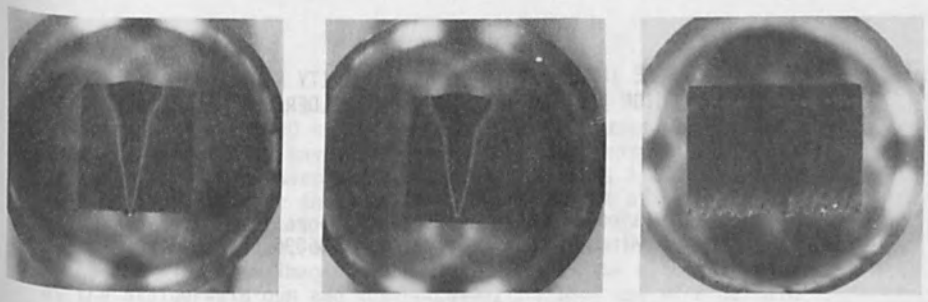

3X 3X 3X

WELD PARAMETERS: 25 KV, 170 ma, 30 IPM

BEAM PARAMETERS: ϕ = 0.040 in.; $\frac{KW}{in.^2} = 3.4 \times 10^3$

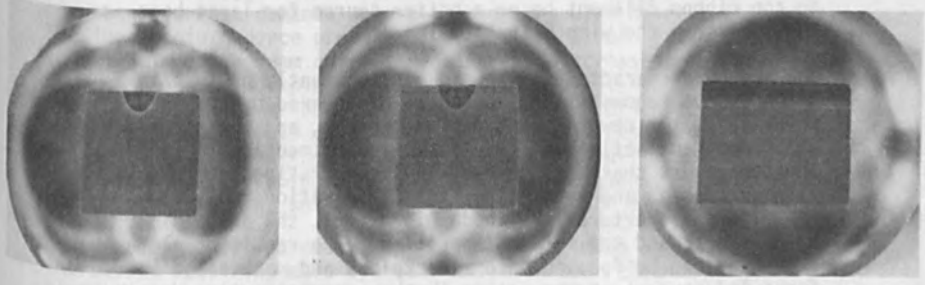

3X 3X 3X

WELD PARAMETERS: 15 KV, 75 ma, 8 IPM

BEAM PARAMETERS: ϕ = 0.053 in.; $\frac{KW}{in.^2} = 5.13 \times 10^2$

WELD CHARACTERISTICS DEVELOPED IN 2219 ALUMINUM ALLOY WELDED AT CONSTANT KJ/in.

Figure 6

SOME IMPROVEMENTS IN BEAM QUALITY FOR HIGH VOLTAGE ELECTRON BEAM WELDERS

Glen S. Lawrence

Hamilton Standard
Division of United Aircraft Corporation
Windsor Locks, Connecticut 06096

ABSTRACT

A new, long life, ribbon filament has been incorporated into a modification of Hamilton Standard's Rogowski electron gun in a manner that enhanced the beam quality and controllability. The improvement in beam controllability is due to the electron gun's capability of producing and maintaining a stationary image. The improvement in beam quality is due to the ribbon filament being a better source for large beam currents than the wire hairpin filament.

The improved characteristics were not inherently present in the previous Rogowski guns, but were discovered by the incorporation of the new filament design concept, and the testing, adjustment and definition of critical gun dimensions. The gun parameters that were changed in incorporating the new filament design and optimizing the gun operation included the filament aperture, the anode pin height, the anode pin to grid gap, and the filament position. The resulting electron beam can be focused onto a workpiece and maintained in focus independent of changes in the beam current.

The beam quality produced by the gun, judged by the welds produced by the machine, were superior to that produced with the old gun assembly. The beam from a wire hairpin filament in a Rogowski gun produces an oval beam spot on the workpiece which causes the weld penetration to be sensitive to the weld direction and can also cause undercutting of the weld bead unless the weld direction is aligned with the oval shape of the beam. The symmetric shape of the ribbon filament essentially eliminates these geometric sources for undercutting and weld penetration variation.

INTRODUCTION

Most high voltage (150 kilovolts) electron guns used in electron beam welders historically have used tungsten wire hairpin filaments as a cathode. The wire hairpin filament has served as a fine approximation to a point source for the relatively small amount of beam current produced by the early welding guns. In addition, they are easily manufactured, inexpensive, and have a reasonable life expectancy of 10 to 20 hours. The beam imaging characteristics of the electron guns, such as the Steigerwald gun and the Rogowski gun that use wire hairpin filaments, are beam current dependent; the beam has to be focused for a given beam current, and refocused for any change in beam current if a sharp focus is to be maintained. The focusing of the beam at low beam powers is not difficult and is easily accomplished by the machine operator using viewing optics that give a "beam's eye" view of the workpiece.

As the electron guns were upgraded to provide higher power levels, more beam current demands were placed on the wire hairpin filaments. The ideal point source provided by the wire hairpin filament became less ideal as the beam current requirements increased; the focused beam spot on the workpiece became decidedly oval. The weld penetration, with an oval beam, is dependent on the orientation of the beam spot and the weld direction, as is clearly reported by P. J. Konkol et al.[1] Making identical welds in two different directions could involve developing two sets of weld parameters, or searching for a compromise setting suitable for welding in both directions.

As the beam power increases, the task of obtaining a sharp focus also increases, requiring more operator skill or the reliance on predetermined focus setting. The need for an improved electron source for high voltage welding systems developed along with the need for improved focusing abilities as the systems operating capabilities were extended into the high power regime.

SUMMARY

We developed a new ribbon filament for use in low voltage electron beam welding systems, and the new ribbon filament demonstrated such remarkable life times that we decided to try it in a high voltage system. We incorporated the ribbon filament into a modification of our high voltage Rogowski guns, and the resulting electron gun demonstrated improvement in the beam quality and beam controllability. The improved beam quality, as demonstrated by improved weld quality, is due primarily to the ribbon filament; the ribbon filament is a better source for large beam currents than is the wire hairpin filament. We obtained the improved beam controllability because the electron gun produces a stationary image, or apparent source of electrons, indepen-

dent of the beam current or accelerating voltage. The improvement in beam characteristics were not inherently present in previously used Rogowski systems but were discovered by the incorporation of the new filament design concept, and the testing, adjustment and definition of critical gun dimensions.

The Rogowski electron gun system can be characterized and defined by the following parameters:

1. The biasing electrode has a concave hemispherical surface with a spherical radius, R_1, and a circular filament aperture of diameter, d_1.

2. The anode is a cylindrical pin centered on the anode plate. The pin has an outer diameter, d_2, an anode aperture with diameter, d_3, and a height above the anode plate, h_1.

3. The bias electrode is positioned above the anode plate a distance h_2, so that a gap, h_3, is obtained between the anode pin and the bias electrode.

4. The filament, or cathode, is centered in the filament aperture of the bias electrode, and it is recessed (-) or projected (+) a distance h_4.

A sketch of the Rogowski gun system, illustrating the above parameters, can be seen in Figure I.

Our basic 25 kilowatt Rogowski electron gun was used and various gun parameters were changed throughout the development tests. The results were used to define the new ribbon filament gun. A tabultion of the modification to the critical parameters is shown below in Table I.

TABLE I

Gun Parameter	Modification for Ribbon Filament Gun
R_1	No change
d_1	Increased
d_2	No change
d_3	No change
h_1	Decreased
h_2	No change
h_3	Increased
h_4	Decreased to recessed position

RIBBON FILAMENT DEVELOPMENT

Wire hairpin filaments have been used in preference to ribbon filaments in high voltage electron guns because they are a better approximation to a point source at low beam currents, and, when they are made of high quality tungsten wire, they have a longer life expectancy than a tungsten ribbon filament. We developed a ribbon filament because we needed one for a low voltage (60 kilovolts) electron gun to be used in low voltage partial vacuum welders, or PVL machines. The electron optics of the PVL machine required the use of a ribbon type filament, as opposed to the wire hairpin type of filament, to function properly. The first ribbon filaments for the PVL machine were made of pure tungsten or pure tantalum ribbon materials. These filaments exhibited lifetimes of two to four hours, if they were properly made and carefully operated. While the optics of the PVL machines required the use of ribbon filaments, the brief lifetimes exhibited by these filaments when manufactured from the common filament materials were hindrances to the introduction of the machine as a production tool.

We initiated the ribbon filament development program with a goal of obtaining useful filament lifetimes of 8 to 10 hours. We decided to make two changes to the filament construction on the initial attempt to improve the expected filament lifetimes. The first change incorporated 10 mil thick ribbon geometry, replacing the 5 mil thick ribbon geometry previously used. Secondly, the material used was a tungsten alloy, instead of pure tungsten or tantalum. The tungsten alloy was selected to give the toughness and erosion resistance of tungsten, but with increased ductility for easier forming of the filaments. Also, the grain structure of the alloy is modified so that the large grain growth and accompanying brittleness that occurs in pure tungsten at operating temperature is avoided. The first filaments were made from 55 mil by 10 mil thick stock. The shape was kept simple to prevent forming stress while presenting a square (55 mil by 55 mil) emitting face. The legs of the filament were brought back at an angle to give more rigid support to the filament face than parallel legs would have done. A testing program was set up to test about ten filaments with up to ten hours of "useful" lifetime.

The test was designed to obtain filament lifetimes under "beam-on" conditions. The beam settings used were 60 kilovolts and 150 milliamps (or 9 kilowatts). Timers were used to monitor the total time the filament was turned on and the total time the beam was turned on. The desired filament lifetime was ten hours of "beam-on" time and not merely "filament-on" time. The beam energy was dissipated during the test by a water-cooled copper workpiece. The pressure in the electron gun area was controlled by adjusting a variable leak in the chamber, and monitoring the pressure in the cathode region with a hot cathode ionization gauge.

For the first filament test, the vacuum was maintained at 2-4 x 10^{-5} torr; this is considered a good vacuum for electron beam welders. The first filament burned out after 58 hours and 20 minutes of "beam-on" time or useful life. The actual length of time the filament was activated was 62 hours and 34 minutes.

The second filament was tested at a higher operating pressure of 0.8-1.0 x 10^{-4} torr. During the first four hours of testing, the vacuum system was shut down by a blown fuse. Since the filament was not protected by an interlock in this particular lab setup, the filament was not shut down until the operator realized what happened and shut it down manually. The filament survived the vacuum failure and continued to operate for a total of 23 hours and 13 minutes of "beam-on" time.

The apparent dependence of filament life on vacuum level disappeared during the testing of the next three filaments. The filament life tests are summarized in Table II. The last three filaments were tested at twice the pressure of the second filament, i.e., 1.8-2 x 10^{-4} torr; all three filaments tested at the higher pressure lasted longer than the second filament. A second vacuum system failure occurred during the testing of the fourth filament, after 27 hours of "beam-on" time. Although not conclusively proven, the loss of vacuum during the testing of the second and fourth filaments must have shortened their life. It should be noted that the three filaments tested without loss of vacuum during the test had lifetime in excess of fifty hours of "beam-on" time; the average life of all five filaments was forty-five hours of "beam-on" time.

TABLE II

Ribbon Filament Lifetime Test

Filament No.	Pressure Torr	Beam On Time	Filament On Time	Comments
1	$2\text{-}4 \times 10^{-5}$	58h 20'	62h 34'	(a)
2	$0.8\text{-}1.0 \times 10^{-4}$	23h 13'	24h 28'	(b)
3	$1.8\text{-}2 \times 10^{-4}$	53h 48'	55h 57'	
4	$1.8\text{-}2 \times 10^{-4}$	42h 8'	44h 29'	(c)
5	$1.8\text{-}2 \times 10^{-4}$	51h 1'	53h 32'	
	Average Life	45h 42'		

(a) Should be upper limit of life.
(b) Had vacuum failure during test.
(c) Had vacuum failure during test.

The life tests were terminated after testing the five filaments because the original goal of 10 hours of useful life had been exceeded by each of the test filaments.

ELECTRON GUN DEVELOPMENT

The long lifetime demonstrated by the ribbon filament prompted the testing of a similar ribbon filament in the high voltage Rogowski electron gun for use in our high voltage welding equipment. The 7 mil thick ribbon filament assembly was made for testing in the high voltage gun. This filament is the same as the filament developed for the PVL machine except that it is formed from 7 mil thick stock instead of 10 mil thick stock. The material was thinned down to allow the ribbon filament geometry to be tested without modification of the ancillary filament power supply within the high voltage power supply.

The machine used for the testing of the new gun with the ribbon filament was a 25 kilowatt, high vacuum electron beam welder equipped with a bent column, viewing optics and magnetic focusing lens. A schematic of the machine is shown in Figure II. The electron beam is formed in the electron gun where electrons are accelerated to near six-tenths the speed of light. The electrons "drift" at this velocity in a narrow pencil of energy into the bend section where the electron beam is deflected by the magnetic fields produced by an electromagnet. The electrons then drift through the viewing optics into the electromagnetic lens. The electromagnetic lens uses electrically generated magnetic fields to focus the electron beam onto the workpiece to be welded.

The action of the magnetic lens is analogous to the operation of an ordinary optical lens. The lenses in our machines act as "thin lenses" as they focus electrons emitted from an object a distance "a" from the lens center into an image at a distance "b" from the lens according to the equation:

$$\frac{1}{f} = \frac{1}{a} + \frac{1}{b} \qquad (1)$$

where "f" is the focal length of the lens. In the thin lens approximation, the measurements of "a", "b", and "f" can be made from the center plane of the pole gap since the principal planes of the lens and the center plane nearly coincide.

The focal length of a magnetic lens is determined by the magnetic field strength and the momentum of the electrons being acted upon. At focal lengths great enough for the lens to be considered weak and in the absence of significant core saturation, the focal length can be expressed as a function of the lens current creating the magnetic field, and the effective relativistic potential of the electron gun,

so that:

$$f \approx \frac{KV^*}{I_L^2} \qquad (2)$$

where I_L is the lens current, V* is the effective relativistic voltage, and K is a constant for any one lens.(2) The relativistic voltage is related to the actual voltage of the electron gun by the following equation:

$$V^* = V + \frac{eV^2}{2m_0c^2} \qquad (3)$$

or

$$V^* \approx V\,(1 + 10^{-6}V) \qquad (4)$$

where V is the accelerating voltage of the electron gun, e is the charge and m_0 the rest mass of an electron, and c is the speed of light.

From equation (1), we can see that the focal length "f" required of the lens to maintain a beam focused on a workpiece at a location "b" is determined by the object distance "a" and that "f" would have to change if any change occurred in "a". The electron gun is an electrostatic lens system that not only extracts electrons from the filament and forms them into a beam, but also produces an image of the source that can be real or virtual. The image of the filament produced by the electron gun is the "object" for the magnetic lens and the location of this image is "a", the object distance for the magnetic lens. Therefore, the image produced by the electron gun must be stationary for there to be no required variation in the focal length of the magnetic lens.

From equation (2), we can see that even for a fixed focal length where the object and image distances are constant, the lens current must reflect changes in the high voltage beam potential.

As we have stated earlier, the high voltage electron guns equipped with wire hairpin filaments produce an image that varies with the gun operating level. Figure III shows typical variations in lens current required to obtain a focused beam using a Rogowski gun with a wire hairpin filament. The curves show that the object location "a" is changing with both beam current and high voltage, making corrections to the lens current necessary for each change in gun operation level. The variation in lens current with high voltage for a fixed beam current deviates from the square root dependence defined by equation (2). This indicates a change in "a" occurs with high voltage. The variation in lens current with beam current for a fixed high voltage is a direct indication of the variation in "a" with beam current.

We installed the ribbon filament in the Rogowski gun with the filament aperture, d_1, enlarged .012 inches. This initial enlargement of the filament aperture was necessary to allow sufficient clearance between the filament and bias electrode for operation of the gun. No other modifications were made to the gun for the first tests with the ribbon filament. The focus obtained with this gun configuration was not well defined at low currents. We could not find a focus for beam currents over about 50 milliamps. Such a condition can be caused by two reasons. First "$\frac{1}{a}$" could go to infinity, or "a" could become undefined, i.e., there may be no distinct image produced by the electron gun.

We modified the anode, reducing the height, h_1, by 0.275 inches which simultaneously increased the anode to grid gap, h_3, by the same amount. The modification was intended to sharpen or improve the focusing characteristics of the electron beam by reducing the strength of the main electrostatic field in the gun. The modification was successful and the operator was able to focus the beam over the full current range. Several tests were made using different filament positions with h_4 changing from +.004 to -.020 inches. The variation in lens current required to maintain focus over the current range is shown in Figure IV. The change in lens current with beam current indicates that the gun image is changing with beam current but is stable with respect to filament position.

We made a further enlargement of the filament aperture, d_1, for a total enlargement of .057 inches. We made a series of focus tests using different filament positions with h_4 changing from +.010 to -.024 inches. The results, seen in Figure V, demonstrate a dependence of the gun image on the filament position, with a marked improvement in performance as the filament is recessed to .024 inches. At this filament position, the lens current needs only about a 3% correction to maintain sharp focus over the beam current range.

The apparent success of the filament aperture enlargement encouraged us to make a final enlargement of the aperture, for a total enlargement of .086 inches. Again, we made a series of tests using different filament positions with h_4 changing from -.017 to -.029 inches. The results, seen in Figure VI, show the lens current to be independent of the beam current for all the filament positions tested. Thus, the image location produced by the electron gun appeared to be stabilized to the point that variations were not detectable at 11-1/4 inches work distance.

The magnification of the object produced by the magnetic lens is determined by the equation:

$$M = \frac{b}{a} \qquad (5)$$

where M is the magnification and "a" and "b" are the image and object distances as stated previously. Since the magnification increases as "b" increases, any motion of the object distance "a" would become more apparent as the work distance is increased.

We ran a series of focus tests at various work distances and with three different filament positions. The results are shown in Figures VII, VIII and IX. With a filament position, h_4, of -.017 inches, lens current variation with beam current started to become evident as the working distance was increased, as demonstrated in Figure VII. By varying the filament position, we found that the lens current variation could be still further reduced by utilizing the more recessed filament positions, as shown in Figure VIII. By recessing the filament until "h_4" was -.025 inches, the variation in lens current with beam current was eliminated over the full range of working distances, as shown in Figure IX.

The elimination of lens current or focal variation with changes in beam current means that the electron optics of the electron gun are now independent of the beam current. We ran focus tests at three different beam potentials to see if the optics of the electron gun were now also independent of the high voltage beam potential. If the electron optics of the electron gun are independent, the focal length of the magnetic lens should be independent of the beam potential; from equation (2), the lens current should be directly proportional to the square root of the relativistic voltage. The results, shown in Figure X, show that the only change in lens current required to maintain constant focus is the square root dependence on the beam potential.

WELD PENETRATION TESTS

For an electron beam welding machine, the effective proof of an improvement in the electron gun is in the welding capabilities of the machine. We ran weld tests with the final configuration of the ribbon filament Rogowski gun to confirm the improved focusing characteristics, and to compare the new gun with the original gun configuration that uses the 20 mil wire hairpin filament. We used 304 stainless steel as the workpiece material throughout the weld tests.

We ran bead-on-plate weld passes at sharp focus and also at several lens current settings higher and lower in value than sharp focus. We ran the welds with full beam power of 25 kilowatts and at a low beam power of three kilowatts for two workpiece locations. The results are shown graphically in Figures XI and XII and pictorially in Figures XIII and XIV. The results clearly demonstrate that the focus, or maximum penetration obtained at low power, occurs at the same lens current setting as the focus at high powers. The results clearly indicate the possibility of obtaining a sharp focus at low power where

the operator can clearly and easily see the beam focused, and then using this focus to make high power welds, thus avoiding the necessity of obtaining a focus under adverse conditions of high power operation.

We made two bead-on-plate weld passes to demonstrate the ability to perform high power welds using a low power level focus. The weld passes were made in four inch thick steel with a beam that had been focused on a target block set two inches lower than the surface of the weld block. One weld pass was made with a beam that had been focused at full power, the other weld pass was made with a beam that had been focused at twenty milliamps, or three kilowatts. The welds, as shown in Figure XV, are equivalent; both welds are just peaking through the four inch thick steel block.(3)

We made bead-on-plate weld passes in both the X and Y axis directions with the new ribbon filament gun and with the original wire hairpin filament gun. The weld passes were made with 60 milliamps of beam current at 60 inches per minute, with 100 milliamps of beam current at 100 inches per minute, and with 167 milliamps of beam current at 150 inches per minute; the energy input per inch of weld is 9 to 10 kilojoules. We see, from the results of the weld passes shown in Figure XVI, that the ribbon filament welds are both more symmetrical in shape and more uniform and consistent in weld penetration from one axis to another.

The wire hairpin weld shows undercutting in the X axis weld at 167 milliamps beam current and possibly a little undercutting in the Y axis. The beam from a wire hairpin filament in a Rogowski gun produces an oval beam spot on the workpiece which causes the weld penetration to be sensitive to the weld direction and can also cause undercutting of the weld bead unless the weld direction is aligned with the oval shape of the beam. The symmetric shape of the ribbon filament essentially eliminates these geometric sources for undercutting and weld penetration variation.

The welds made with 60 milliamps of beam current at 60 inches per minute using the ribbon filament gun were just peaking through one inch of steel with only nine kilojoules of energy per inch of weld; we would have expected to need about 20 to 25 kilojoules per inch to penetrate one inch thick stock.(4)

CONCLUSIONS

1. The development of a ribbon filament with a long life expectancy has made practical the replacement of the wire hairpin filament in high voltage electron beam welders.

2. The use of the ribbon filament in the high power Rogowski electron gun and the adjustment of critical gun parameters have made the electron gun's optics independent of the beam current and beam

potential.

3. The lens current required to focus the electron beam onto a workpiece is no longer dependent on the beam current and is directly proportional to the relativistic voltage. Therefore, an operator may focus the electron beam onto the workpiece at low power where the task is simple and perform the welds at high power.

4. The analytical nature of the lens current dependence on high voltage makes automated focus control a relatively simple task.

5. The new electron gun produces welds more symmetrical in shape, more consistent in weld penetration from one axis to another, and it produces welds with less energy per unit length of weld.

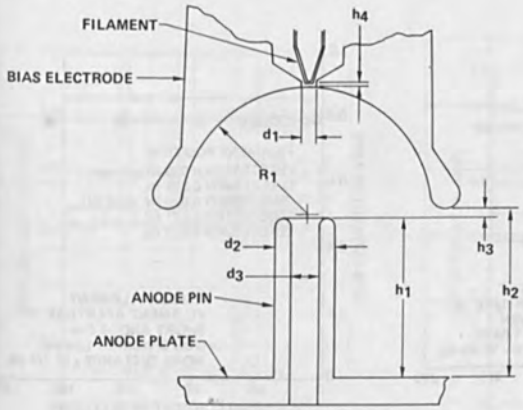

FIGURE I ROGOWSKI ELECTRON GUN

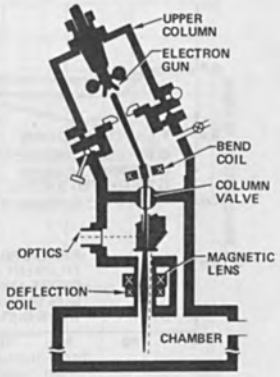

FIGURE II 25 KW WELDING MACHINE SCHEMATIC

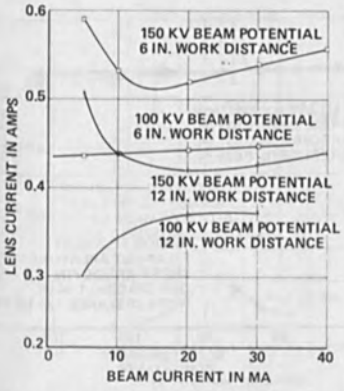

FIGURE III FOCUS VARIATION WITH BEAM CURRENT ROGOWSKI GUN WITH WIRE HAIRPIN FILAMENT

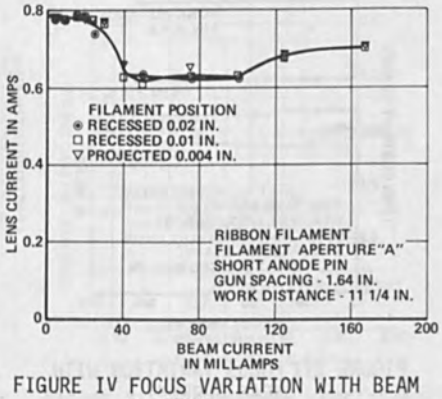

FIGURE IV FOCUS VARIATION WITH BEAM CURRENT AT 150 KILOVOLTS BEAM POTENTIAL

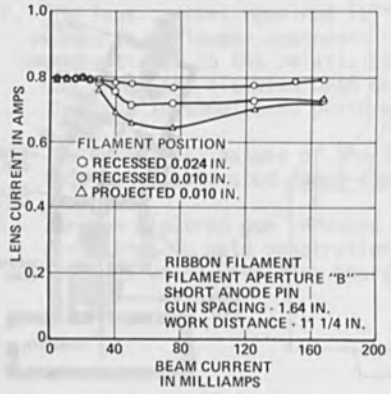

FIGURE V FOCUS VARIATION WITH BEAM CURRENT AT 150 KILOVOLTS BEAM POTENTIAL

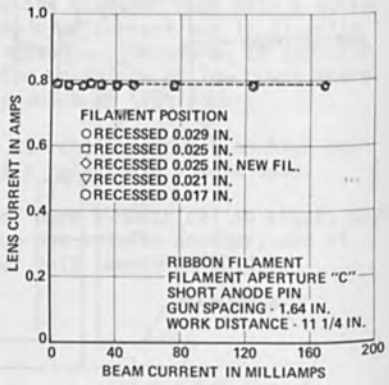

FIGURE VI FOCUS VARIATION WITH BEAM CURRENT AT 150 KILOVOLTS BEAM POTENTIAL

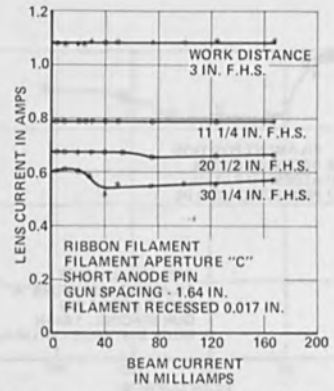

FIGURE VII FOCUS VARIATION WITH BEAM CURRENT AT 150 KILOVOLTS BEAM POTENTIAL

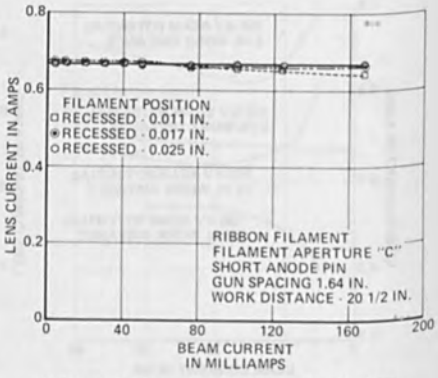

FIGURE VIII FOCUS VARIATION WITH BEAM CURRENT AT 150 KILOVOLTS BEAM POTENTIAL

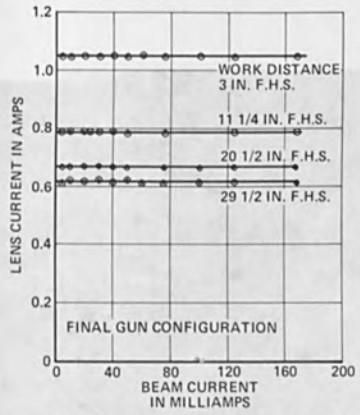

FIGURE IX FOCUS VARIATION WITH BEAM CURRENT AT 150 KILOVOLTS BEAM POTENTIAL

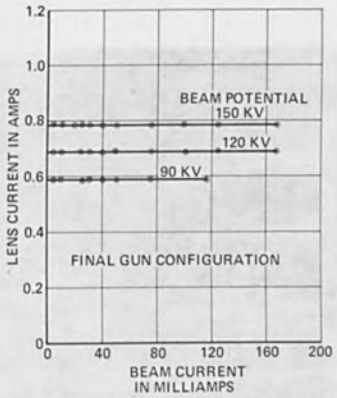

FIGURE X FOCUS VARIATION WITH BEAM CURRENT

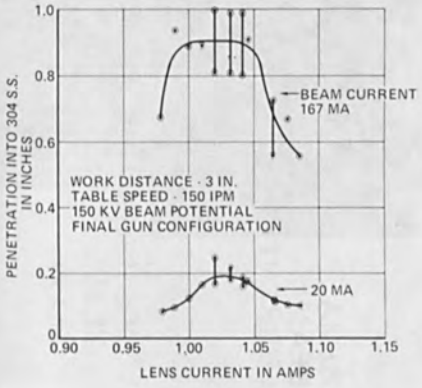

FIGURE XI PENETRATION SENSITIVITY TO LENS CURRENT

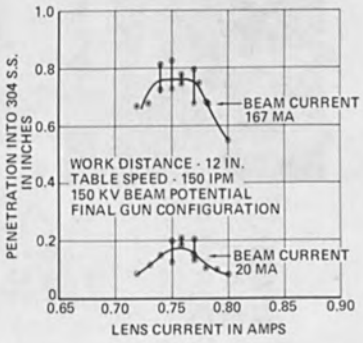

FIGURE XII PENETRATION SENSITIVITY TO LENS CURRENT

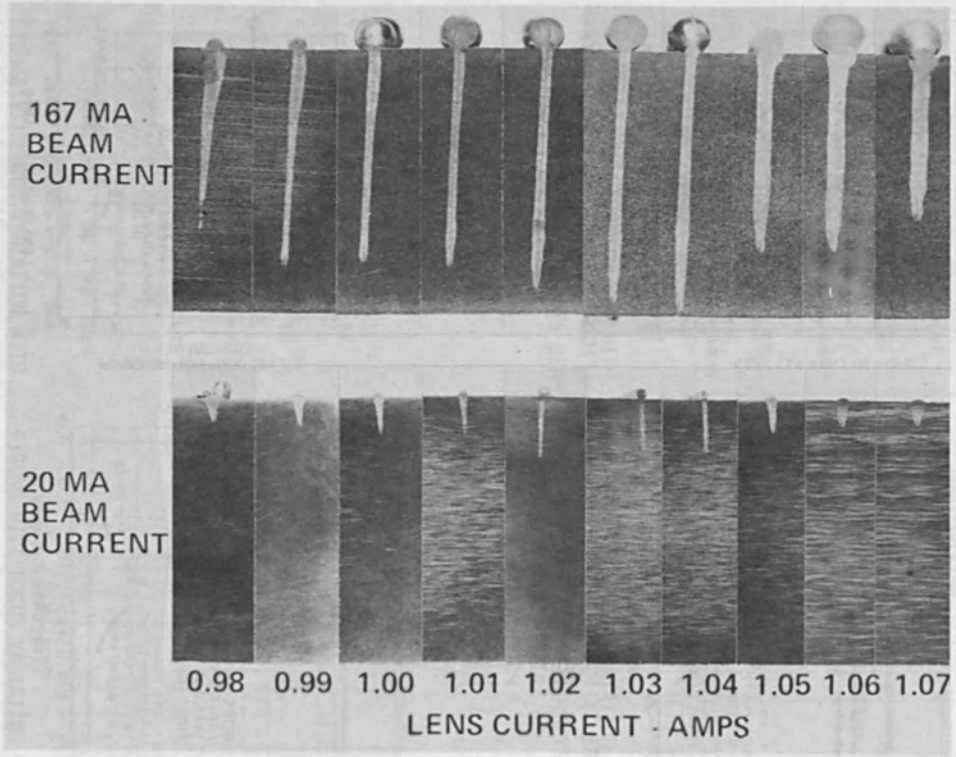

FIGURE XIII PENETRATION VS. LENS CURRENT
3 IN. WORK DISTANCE
150 KILOVOLTS BEAM POTENTIAL

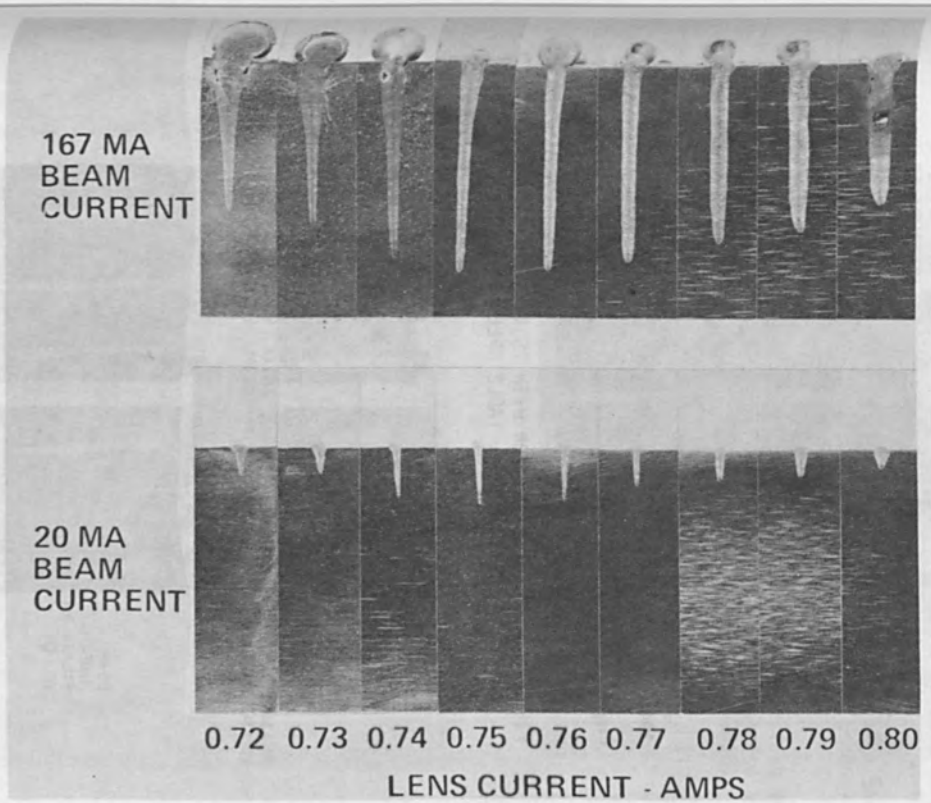

FIGURE XIV PENETRATION VS. LENS CURRENT
12 IN. WORK DISTANCE
150 KILOVOLTS BEAM POTENTIAL

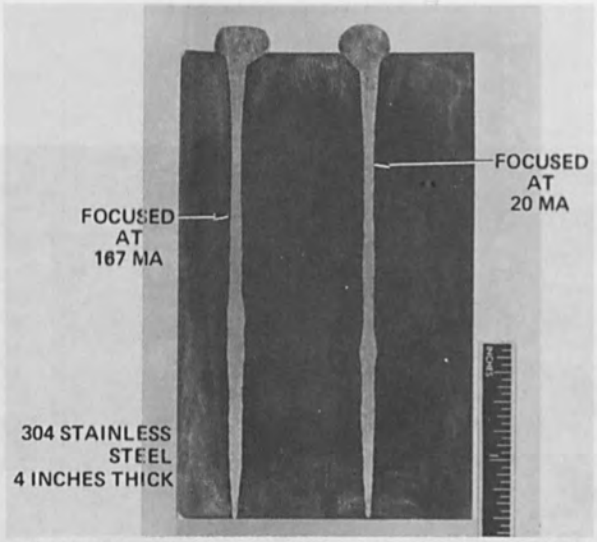

FIGURE XV WELD PENETRATION WITH 25 KW BEAM POWER
AT 7-1/2 I.P.M. TABLE SPEED

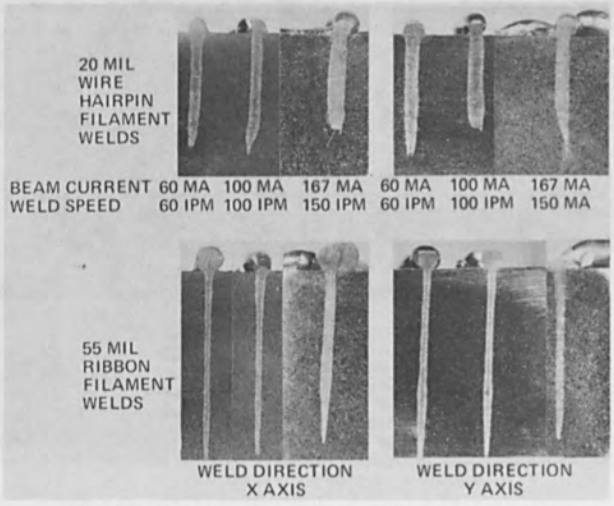

FIGURE XVI COMPARISON OF X AND Y AXIS WELDS
150 KILOVOLTS BEAM POTENTIAL
7 IN. WORK DISTANCE

REFERENCES

1. P. J. Konkol, P. M. Smith, C. F. Willebrand and L. P. Connor, "Parameter Study of Electron Beam Welding", Welding Journal 50, No. 11, 765 (1971)

2. G. Liebmann and E. M. Grad, "Imaging Properties of a Series of Magnetic Electron Lenses", Proc. Phys. Soc. (London) 64, Sec. B, Part 11, 956 (1951)

3. G. K. Hicken and W. G. Booco, "Penetration Variations in Electron Beam Welding", Electron and Ion Beam Science and Technology Third International Conference, 398 (1968)

4. American Society of Metals, "Metals Handbook", 6, 519 (1971)

A SYSTEMS APPROACH TO ELECTRON BEAM PRODUCTION WELDING EQUIPMENT

F. D. Seaman, Beam Technology,
Sciaky Bros., Inc.,
4915 W. 67th St., Chicago, Ill. 60638

ABSTRACT

A production application implies the ability to meet stringent cost and quality objectives while handling the work with due regard to the close association between the electron beam and a vacuum. A systems approach is required to meet these diverse objectives. An electron beam system is described in terms of its subsystems and the contribution each makes to the over-all objective. Particular attention is paid to selection of the work handling subsystem. Methods of minimizing the effect of a vacuum working environment on work flow are discussed along with the constraints of each. As a more effective approach to systems optimization, the objective of balancing the welding operation with nonproductive operations is considered in terms of three fundamental arrangements of vacuum systems and loading stations. The versatility of these three arrangements is demonstrated by calculating their effect on unit costs over a very wide range of production requirements.

INTRODUCTION

The introduction of electron beam welding as a production tool (Photo 1.) makes certain demands of the equipment that is to be used. First, the term "production" implies the existence of highly competitive cost and quality goals. Second, "production" involves a close association with a specific product and implies the efficient handling of this product with due regard for the necessary association between a beam of electrons and a vacuum environment.

Low product cost, high product quality, work handling efficiency, and vacuum are characteristics next to impossible to bring together in one piece of equipment. Accomplishing these objectives requires a systems approach to equipment selection. It is easier to visualize separate pieces of equipment, or subsystems, each charged with meeting a particular portion of the over-all requirement.

THE ELECTRON BEAM WELDING SYSTEM

In its most elementary form, an electron beam system involves three basic subsystems:

Electron beam generation,
Electro-mechanical control,
Work handling.

These basic subsystems are discussed below, along with the prime contribution each makes to the over-all system.

THE BEAM SUBSYSTEM

Although the beam subsystem is the heart of the complete welding system from a technical viewpoint, the user should consider it primarily as the source of system capacity. It provides the power (capacity) necessary to do the job at hand. Beam flexibility is desirable to adjust the power. Triode guns that permit full range current adjustment, and automatically regulated power supplies that have a continuous range of voltages (Sciaky AVR systems) provide this flexibility.

For production, beam reliability, as well as capacity, is required. It is provided in part by making the filaments (that produce electrons when heated) from strips of refractory metal shaped to avoid hot spots and thermal damage. These emitters must hold the beam stable in space and thus must be mounted in composite metallic structures that can compensate for thermal variations during operation.

Beam utility can be enhanced by providing electrically programmed deflection fields that often eliminate tooling. These fields cause the beam to sweep through complex joint patterns on a workpiece that is simply clamped in a fixed position (Drawing 1.). The effect of these fields on the electron paths is automatically held constant, even during programmed changes in accelerating voltage by using circuits such as the Sciaky square root extractor. Reference 1 contains a more detailed discussion of the beam generating subsystem.

THE CONTROL SUBSYSTEM

The level of sophistication of the system controls relates more closely to the use of the equipment as a production tool than do any characteristics of the beam. Automatic, presettable, closed-loop controls with feed back are

recommended in order to assure accuracy and repeatability of the weld cycle. This keeps scrap losses to a minimum. The competitive cost and quality goals, associated with production, suffer if scrap rates are not at a minimum.

Furthermore, competition demands high welding rates. High speed welding procedures require very close control of all of the quantities that go into the making of a weld (Table I). Thus, one set of controls must be dedicated to assuring control over these quantities.

Another set of controls must establish the sequence of events. By way of illustration, a production welding procedure used on the finished details of a gear may require a preweld tacking pass at a low power; a carefully programmed increase to a higher power for the fusion pass, and a final decrease in power at a precise location and rate that assures complete fusion of the joint circumference, but does not overlap the weld start to add useless welding stresses. Clearly, the transitions in this relatively common sequence (moving at several inches per second) must be initiated with a precision and consistency that are beyond the operator's capability. Some of the sequence controlled operations are listed in Table II.

It should be noted that the above typical welding procedure requires that the "quantity" controls be presettable at several operating levels.

Reference 2 contains a further description of controls for beam joint alignment, and of adaptive controls. These adaptive controls measure workpiece variations and use small dedicated computers to accommodate the variations.

WORK HANDLING SUBSYSTEM

The work handling subsystem is most directly related to both production and product. It serves as a bridge between the familiar environment of the shop and the deep vacuum in which the electron beam must form. Moving workpieces between such disparate environments implies some impedance to work flow. Unless careful attention is given to work handling, this impedance may materialize. Should this happen, the productivity of the system would suffer, regardless of the capacity of the beam or the reliability of the controls. For this reason, work handling (and associated tooling) must be elevated to the stature of a subsystem. It cannot be treated as an accessory where production welding is involved.

SYSTEMS APPROACH TO WORK HANDLING

Because a vacuum is alien to the shop environment, it is not surprising that initial attempts to improve work handling (hence the productivity) of the electron beam process, dealt with the elimination of part or all of the original "hard" (one millionth of an atmosphere) vacuum requirement (Drawing 2). Two such schemes have been developed:

Soft Vacuum System - The operating pressure is 100 to 500 times greater than hard vacuum so that air can be made to flow out of the vacuum chamber at a reasonable rate, using mechanical pumps and blowers, with no need to rely on diffusion to remove the last traces. Furthermore, at these pressure levels, several solid materials can be used as seals in schemes that permit the work to pass easily from the manufacturing environment into the vacuum environment without requiring unusual precautions as to the nature and cleanliness of the surfaces involved. (Drawing 3).

Out of Vacuum System - The work is situated at atmospheric pressure, in an enclosure that shields personnel from X-rays. In this enclosure, the work must be positioned within approximately a half inch of the beam exit orifice where the electrons emerge from the vacuum portion of the welder system. (Drawing 4).

However, an improvement in one function of the system does not necessarily result in an over-all improvement of the entire system. In fact, a reduction in over-all attractiveness, as a consequence of bringing the workpiece out of vacuum into air, can be cited for several commonly encountered welding situations.

Many products benefit from full (hard) vacuum. Workpieces made from reactive metals (titanium, for example), or other workpieces which must be sealed in vacuum, illustrate this point well, but these are not very common in commercial applications. On the other hand, many welded parts would benefit if metallurgical effects such as annealing could be kept to a minimum and narrow welds with parallel sides could be produced to avoid distortion. The achievement of these qualities in the ultimate degree requires that pressure at the beam-work interaction be kept as low as possible.

Soft vacuum, to increase productivity, can be applied to the majority of welded products and results in virtually

no compromise of the above basic process characteristics. All of the characteristics which account for the basic attractiveness of hard vacuum electron beam welding are, to a large degree, retained in the soft vacuum process. These include:

- Narrow, fast, low distortion welds, which are similar to those produced in hard vacuum. (Photo 2).
- Projection of the beam of electrons deep into the recesses of a workpiece without the need to provide clearance for any portion of the electron gun.
- Following a complex weld path when directed by an electrically controlled deflection system (as in Drawing 4).
- Defining joint location or even finding and tracking the joint path over its length.

Conversely, while the out-of-vacuum approach may be a large step toward minimizing the work flow impedance, it places severe restraints on other facets of production.

- The energy distribution in the beam is affected by the various gas densities through which the beam must pass, and in some systems, the focus points are adjusted with reference to the orifice location rather than with primary regard for workpiece surface. As a result, the narrow parallel sided character of the weld disappears. (Ref. 3 describes weld shape and its effect on joint property for out-of-vacuum equipment).
- Penetration is limited to about one inch (for large systems).
- Physical arrangement of the orifice nozzle and column is such that only certain, very accessible joints can be reached.
- Eliminating vacuum from the workpiece area does not eliminate the vacuum pumping system. In fact, the vacuum system size of out-of-vacuum equipment approaches that of the hard vacuum equipment in order to accommodate the high thruput associated with the orifice through which the beam must pass as it leaves the vacuum in which it is formed.

Selection of a workpiece handling scheme requires a clear identification of purpose and recognition of constraints. These are elements that go into the selection of any system. In short, workpiece handling is a systems problem and deserves a systems solution. In view of the many products now being considered for electron beam welding, any solution to the work handling problem must be general.

BALANCING OPERATIONS TO IMPROVE PRODUCTION

The basic element of the proposed general solution is the welding operation. The production cycle can never be shorter than the welding cycle, regardless of the approach to work handling. The objective of all production welding systems, however, should be to reduce the difference between the total cycle time (including welding, loading, pumping, and indexing) and the basic welding cycle time to zero within constraints of justifiable cost and technical requirements. Maximum production output will come about only when all nonproductive portions of the cycle can be carried out in parallel with the welding operation. The 1400 part per hour system shown in Photo 1 achieves this objective. But not all products need the maximum output of today's electron beam production welding.

What is required is a range of work handling subsystems with increasing ability to manipulate the difference between nonproductive and productive time toward zero, over a broad spectrum of products and production requirements at a minimum capital investment. Keeping the special benefits of all three working vacuum levels in mind, several approaches to work handling suggest themselves. These approaches fall into readily identifiable categories.

Table III describes the categories in detail and provides illustrations of some variations that have proved themselves in production. A brief description of each category follows.

> One Cycle Systems: The one cycle system produces a workpiece each time a weld (or other productive operation associated with welding) is completed. Drawing 5 shows a schematic of a typical one cycle system. A soft vacuum welder with many small chambers connected together uses durable elastomer seals to let the workpiece move into the low pressure chamber thru an intermediate pumping station. In this way, while each weld is made, one

part is loaded, one is pumped, and one is unloaded. The out-of-vacuum welder is a special one-cycle machine that is capable of handling extensive or continuous workpieces where the necessary compromises in weld shape and workpiece accessibility are acceptable. There is little or no wait for pumping and only a short wait for indexing.

Two Cycle Systems: Two operational cycles can be combined by a modest investment in an alternate loading station. Photo 3 shows a typical two-cycle system with an alternate loading station built onto either side of the vacuum chamber door. The pump-weld operation is carried out during loading. A low cost, fast pumping, soft vacuum system is usually the basis for this approach. When loading time is much shorter than pumping-welding time, slightly increased investment is adviseable to provide two pumping stations so that both loading and pumping can go on during welding.

Three Cycle Systems: The term "three cycle" implies the need to wait until all three operational cycles have been completed before unloading a finished part and starting the process again. This class of machinery is stripped of any extensive work handling subsystem in order to keep cost to a minimum. Productivity can be greatly improved by making several welds in one pump down. Photo 4 shows a conventional hard vacuum welder equipped for "batch loading" to produce several hundred parts each hour. A common approach to multiple welds per load is to make the gun moveable in the chamber.

EFFECT ON ECONOMICS

The establishment of minimum unit costs over a large variety of applications is the goal of any system that attempts to relate equipment to products as effectively as possible. If the proposed method of system selection were perfect, system costs (including operating costs) should increase or decrease exactly with production to produce a minimum and constant unit cost over a large range of productive requirements for a given part.

Drawing 6 shows that unit costs are stable over a large range of annual outputs, suggesting a high degree of flexibility for soft vacuum. Furthermore, as their capacity increases, the selected handling systems increase in

effectiveness more rapidly than they add to total system costs. Thus, unit costs drop a few cents per part even at production rates that could be considered only moderately high. There is a minimum basic investment in controls and the beam subsystem. This investment hardly varies with production and is necessary even for a very limited annual requirement.

In arriving at the costs in Drawing 6, a 100% return on investment, 2 year payback, $16,000 yearly labor cost, 4,000 hour/year and $.01 per KWH utility cost were applied to four systems, each representing a progressively greater production capability. The systems chosen are actually in operation on production applications. Their specifications and price have been modified to make them comparable and contemporary. All are of the type that weld the part in pressure equal to .00005 atmospheres (often termed a soft, semi, or commercial vacuum).

SUMMARY

It would appear that the qualifications of a system worthy of a place in a production line might be summed up as follows —

- Capacity
- Reliability
- Productivity

This paper has described how each portion of the system is a prime contributor to these qualifications.

- The beam generating subsystem must be selected to assure sufficient capacity to produce the most demanding weld.
- Proper controls assure that each weld will duplicate its predecessor. This type of reliability must apply to the quantitative procedure variables as well as the sequence of events necessary to complete each weld. All controls should be presettable.
- Work handling is the key to productivity. As such, it attains the stature of a major subsystem in a production facility.

Optimization of the system means more than elimination of the need to weld at very low pressures. Increasing welding pressure to atmospheric pressure compromises beam quality and system flexibility. Moderate increases in welding pressure retain the qualities and characteristics of the

electron beam, reduce pumping system size, and introduce several means for expediting work flow.

Because product requirements differ, no single system meets all requirements. However, most systems fall into one of three categories:

- One cycle system wherein a part is produced each time a weld is made. Out-of-vacuum welders are a special case. They are useful when the workpiece is large or continuous and when compromises in beam geometry or operating flexibility can be tolerated.

- Two cycle systems for lower production rates balance operations so that a part is produced after two events have taken place. Very simple machines can be made into two cycle welders by the addition of an extra loading station (or, at most, an extra loading-pumping station).

- Three cycle welders require that the vacuum chamber be loaded, pumped and welded before it is available. Nevertheless, the productivity of such machines can be considerable if more than one weld is made in a single cycle. Batch loaded systems and moveable gun systems fall in this category.

When actual costs were used to test the proposed approach to selecting electron beam welding equipment, the following observations were made:

- Consideration of all of the many available schemes for work handling permits a good balance between a system cost and its output.

- The systems illustrated in this paper actually increase in capacity more rapidly than they increased total system cost so that unit costs go down as productivity goes up.

- At all production levels studied, welding costs run only a few cents per part.

REFERENCES

1. H. A. James - "Electron Beam Welding Equipment: Process Parameters, Limitations, And Controls" -- Electron Beam Metallurgical Processing Seminar, Universal Technology Corp., Dayton, Ohio.

2. F. D. Seaman - "Electron Beam Systems For On-Line Production" -- Sciaky Bros., Inc., 4915 W. 67th St., Chicago, Ill. 60638.

3. F. D. Seaman - "Experimental As Welded Properties Of Out-of-Vacuum Welds in 2219 T87 Aluminum Alloys" -- Fourth International Conference, Electron & Ion Beam Technology, Editor R. Bakish, Electro Chemical Society, Inc., New York, New York.

TABLE I

Quantities that should be controlled in a production welding system:

- Beam current
- Accelerating Voltage
- Process speed

TABLE II

EVENTS THAT MAY BE PROGRAMMED BY SEQUENCE CONTROL

EVENT	REMARKS
A. START OF BEAM	
1. Simultaneously with workpiece	Normal welding condition
2. Before workpiece motion starts	Where beam can be started off-work and must be at full power as soon as it reaches the joint (as in massive parts or short joints).
3. After workpiece motion starts	Used on circumferential welds to control quality and appearance of the overlap area.
B. POINT OF INITIAL POWER LEVEL CHANGES	This feature requires presetability of control at two levels as a minimum.
1. Increase	Control weld contour and eliminate defects as work heats up and penetration reaches full depth in circular welds or welds where beam must start on work.
2. Decrease	Used in special applications where thickness decreases after start of weld.
C. POINT OF SUBSEQUENT OR FINAL POWER LEVEL CHANGES	This feature requires presetability of controls at two levels (as a minimum).
1. Increase	Used in special applications where thickness increases after start of weld.

(continued next page)

TABLE II (continued)

EVENT	REMARKS
2. Decrease	Power is decreased after the weld has been completed in circumferential welds or welds where beam must be terminated on work in order to permit the penetration cavity to fill without leaving a depressed area in the weld bead.
D. RATE OF POWER LEVEL CHANGES	This is an important procedure variable when combined with the amount of change specified. Controlling it requires that voltage, current and/or power have closed loop feedback controls so that a variable reference signal can be generated and impressed on the reference of the control.
1. Exponential Rate Change in Power Level	Used for most welds where a power level transition is involved. Two-thirds of the selected power level change is accomplished in the first third of the selected transition period. Rates become more gradual as transition progresses.
2. Linear Rate Change in Power Level (Time Defined)	After initiation of the power level transition, power changes at a constant rate. Thus the initial change is less disturbing to weld solidification. Applied when defects occur in area of initial exponential rate change.
3. Sinusoidal Rate in Power Level	This mode is the reverse of the exponential method and thus causes least disturbance of the weld solidification during the first part of the transition. However, about two-thirds of the change takes place in the final one-third of the selected transition period.
E. POINT OF SPEED CHANGES	Used primarily to jog part from one operation to the next to increase productivity. Not normally used to program power if controls are available for programming voltage, current or their product.

TABLE III

TYPES OF VACUUM ELECTRON BEAM WELDERS FOR PRODUCTION

THREE CYCLE SYSTEMS:	Load — Pump — Make multiple welds — Unload.
Application:	Used where pumping cycle is long because (a) parts are large, or (b) required vacuum level is low.
Principles:	Employs moving gun to keep pumps and chamber as small as possible. Alternatively may place a number of parts in magazines and manipulate them in the beam through automatic work handling devices. May weld two seams with one beam if they are stacked one above the other.
Illustrations:	
System 1 -	Hard vacuum chamber is sized to fit part, and gun is moved on 3 to 5 axis to reach several joints in one pumpdown. (Photo 5).
System 2 -	Soft vacuum is substituted to shorten pump time for given volume. Gun is still moveable on one axis. Workpiece has one axis of movement. (Photo 6).
System 3 -	(Two guns - four welds). Two guns are mounted in chamber to weld opposite ends of assembly. Each makes two joints simultaneously in panel faces displaced 1-1/2" vertically by penetrating upper and lower face in one pass. (Photo 7).
System 4 -	Batch of 300 welds in 30 ft. diameter tube sheet made after pumpdown of frame-like soft vacuum chamber. Top closure provides X and Y axis gun motion of tube. Beam is positioned over nominal center of tube by numerical control. Compensation for variance in individual tube position and diameter is accomplished by fully automated beam scan operation prior to automated two pass welding cycle. Operation is fully automatic. Operator sets up alternate chamber during weld cycle. (Drawing 7A-7B).

(cont'd next page)

TABLE III (cont'd)

(A) TWO CYCLE SYSTEMS:	With alternate work stations to permit simultaneous loading and pumping welding cycles.
Application:	Where soft vacuum is acceptable and length of pumping cycle can be kept low(usually with compact parts) compared to assembly-loading operations.
Principles:	Small chambers and mechanical pumps with blowers keep pumping time to a minimum. Often the chamber enclosure and work station are combined. Gun is moveable during welding, using a sliding seal as a welding motion or for positioning.
Illustrations:	
System 1 -	(Single gun) - More rapid operation obtained by automated work station - closure action combined with minimum size chamber. Emphasis on automated welding justifies use of monitor to check all pertinent welding variables (including joint location). (Photo 8).
System 2 -	(Single gun) - (Two beams) Rapid deflection splits beam and permits parallel welds to be made. (Photo 9).
(B) TWO CYCLE SYSTEMS:	With alternate vacuum systems and chambers that can be loaded and pumped during the welding cycle.
Application:	Where soft vacuum is acceptable and length of pumping time approaches welding cycle. Separate vacuum systems permit loading and evacuation to take place while single gun moves from chamber to chamber using a sliding seal.
Principle:	Motion of conventional sliding gun seal is extended to cover two chambers. Transfer is accomplished by closed loop control operating in the position mode.
Illustration:	
System 1 -	(Two chambers-single gun) (Photo 10).

(cont'd next page)

TABLE III (cont'd)

(C) ONE CYCLE SYSTEMS:	Individual workpieces move continuously under electron beam in vacuum environment.
Application:	Where beam freedom is desirable and soft vacuum acceptable, this type of system is applied when the load, pump and weld cycles are of about same duration and approach the length of time required for venting or for work station, or gun to index. Loading or welding can be broken into several steps in order to balance cycle.
Principle:	Based on a further extension of the sliding, elastomeric seals used to provide gun motion in all soft vacuum systems in above illustration.
Illustration:	
System 1 -	Dial feed principle used to index work stations. Each work station is also part of vacuum chamber. Vacuum system consists of an inner and outer zone serviced by separate pumps. Work moves under sliding seal into outer zone and is pumped while welding, loading, gauging, venting, and unloading take place. Then, moves to weld station. Loading is automatic. Parts are handled with vibratory bowl feeders. (Photo 1 and Drawing 5).

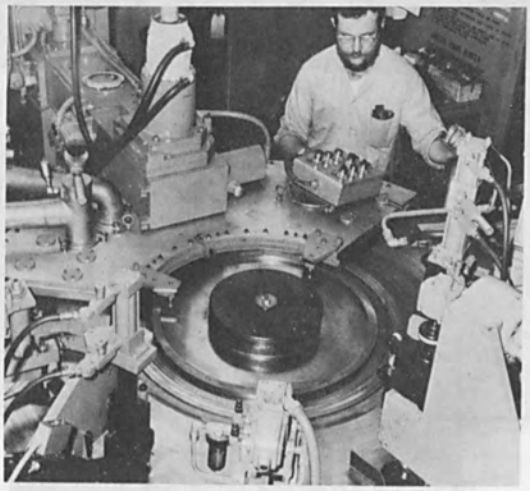

Photo 1 - Automotive destributor cam details and the production electron beam welding system used to assemble them at approximately 1,400 parts per hour.

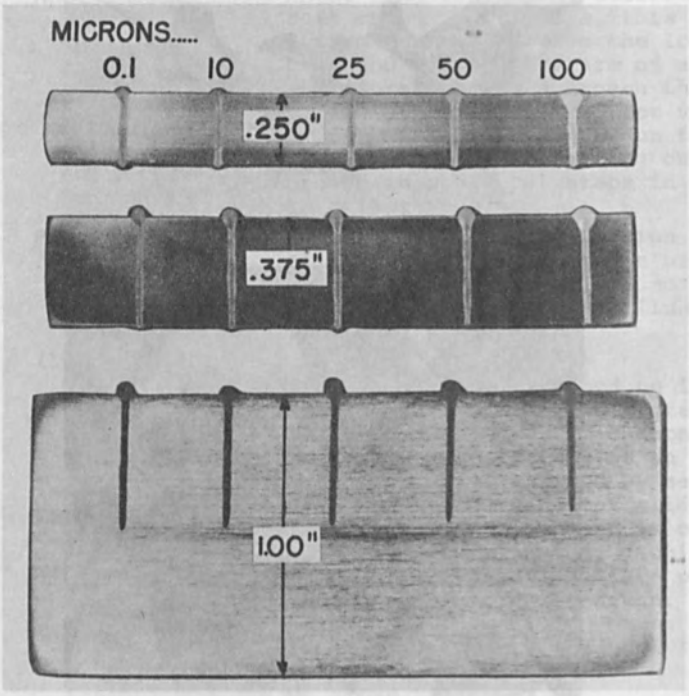

Photo 2 - Effect of pressure on welds.

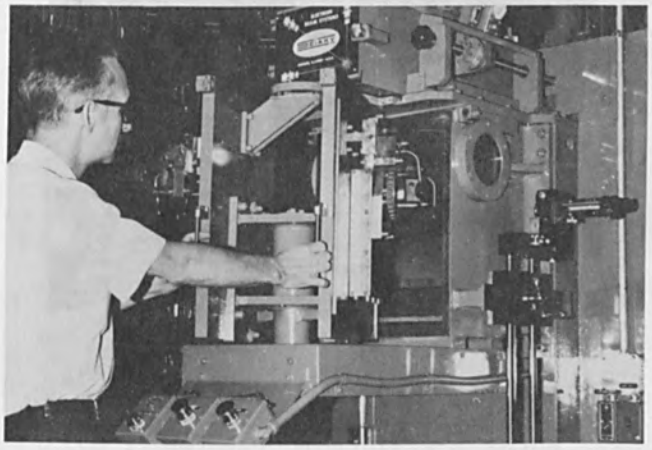

Photo 3 - An efficient Two-Cycle machine was made in this application from a Three-Cycle machine by putting alternate loading stations on either side of pivoted door.

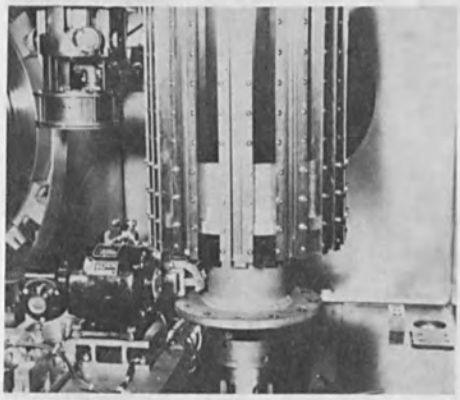

Photo 4 - Magazine and manipulator are used to weld a "batch" of parts in each load, greatly increasing productivity in this Three-Cycle system.

Photo 8 - Productivity of a Two-Cycle machine can be increased by automating the work stations. The work station flange serves as the door to a minimum size chamber. Chamber can be set up with gun on top or side to accommodate parts with downhand or horizontal welds.

Photo 9 - Cylindrical loading station arrangement of this unusually productive Two-Cycle machine moves part under long overhead welding station. Square wave deflection spits beam to form parallel weld paths as single gun slides on seals down the length of the chamber. Cylindrical assembly lifts to close chamber.

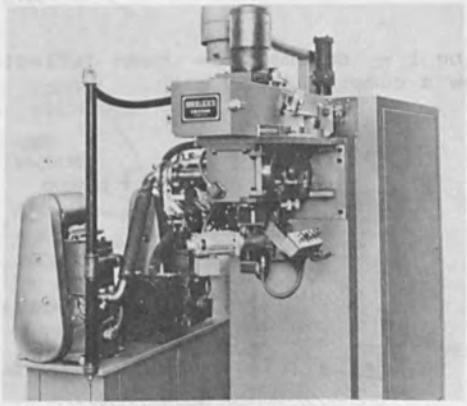

Photo 10 - When combined loading and pumping time approaches welding cycle, the Type B Two-Cycle machine is applied by adding a separate vacuum system to each loading station. Single sliding gun serves both chambers, to minimize capital investment.

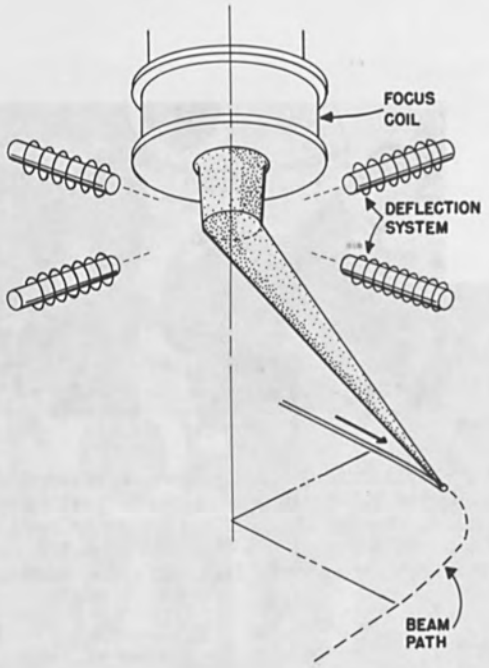

Drawing 1 — Schematic — beam deflection to follow a complex joint path.

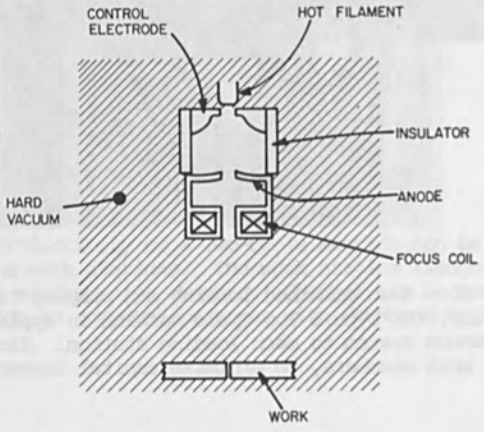

Drawing 2 — Schematic — hard vacuum welding.

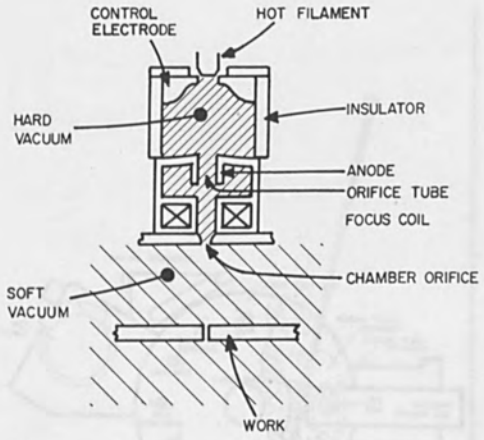

Drawing 3 — Schematic — soft vacuum welding.

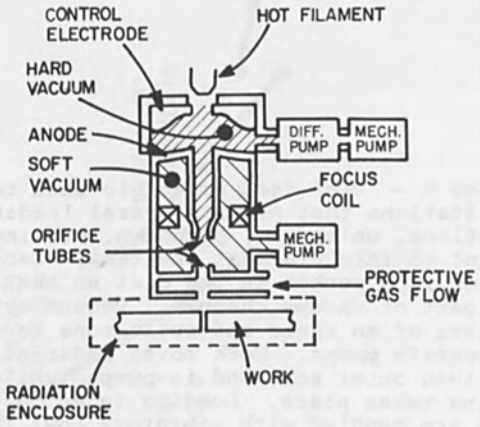

Drawing 4 — Schematic — out-of-vacuum welding.

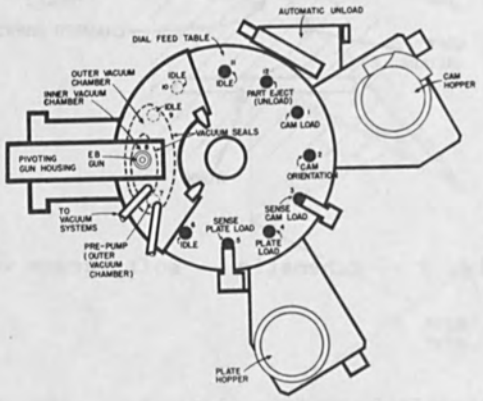

Drawing 5 — Dial feed principle used to index work stations that permit several loading operations, unloading, pumpdown, venting, and welding to take place at one time. Each work station is a pocket in the dial so that it is also part of vacuum chamber. Vacuum system consists of an inner and outer zone serviced by separate pumps. Work moves under sliding seal into outer zone and is pumped while welding takes place. Loading is automatic. Parts are handled with vibratory bowl feeders.

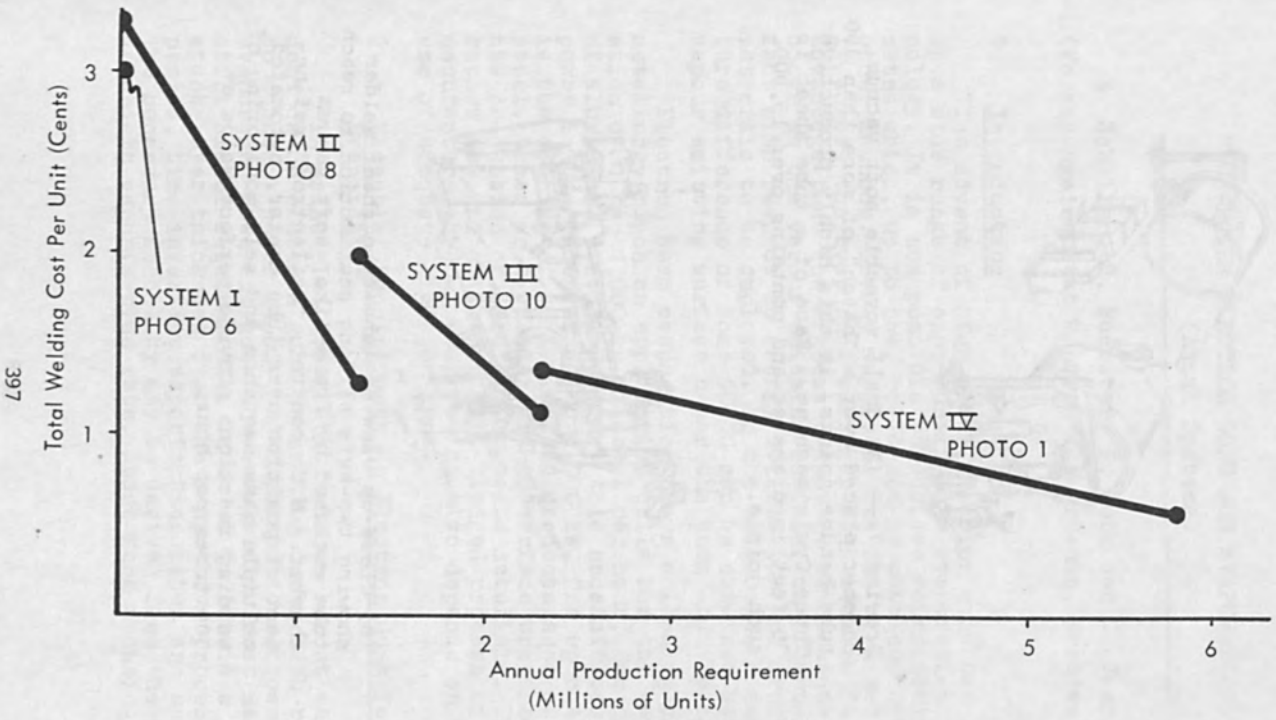

6-COST PRODUCTION RELATIONSHIP FOR SELECTED SYSTEMS

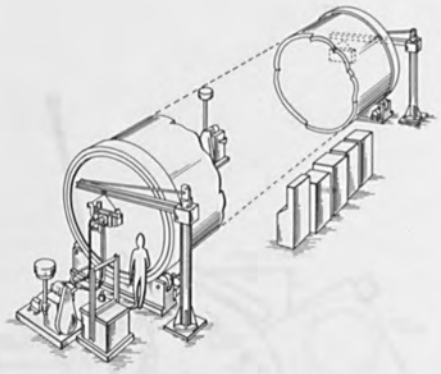

Drawing 7 — (A) Small moveable soft vacuum chamber placed over a "batch" of more than 300 tube-header joints, in this highly productive Three-Cycle machine. Face of a tube sheet is 30 feet in diameter and contains over 15,000 such joints.

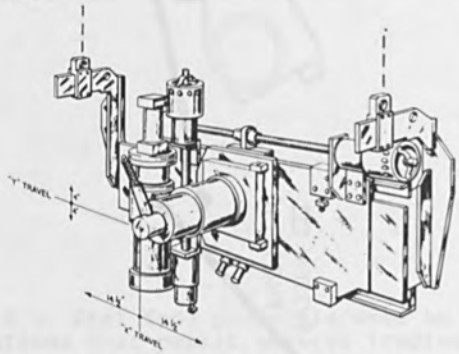

(B) Close-up view of tube-tube sheet welder showing two-axis sliding seal motion to reach tube enclosed by frame-like, soft vacuum chamber. N.C. control, "Reflectron" refinement of position over tube center, automated multiple pass sequence and self-monitoring of welding functions provide perfect welds at 300 tubes per hour.

HIGH-POWER ELECTRON GUNS FOR EVAPORATION
(Axial Systems)

S. Schiller, H. Foerster, P. Lenk and G. Jaesch
(Forschungsinstitut Manfred von Ardenne, Dresden/GDR)

1. Introduction

The advent of high-power electron guns has opened up a wide range of opportunities in evaporation technology. It is now possible to achieve vaporization rates which, up to now, could not be obtained with other methods. Energy supply is via the beam and directly across the evaporant surface. This results in the advantage that the highest evaporant temperature will occur at the vapour emitting surface; an important fact with respect to energy utilization and crucible materials to be employed. In the evaporant, a temperature difference of some 100°C can be obtained between vapour emitting surface under the beam and the crucible.

Electron beam evaporation plays a leading role in metallurgy. Such an application calls for the vaporization of 10 to 1,000 kg of metal per hour, for example, of aluminium [1,2,3]. However, this necessitates a gun power in the order of 50 to 5,000 kw. One special field is the coating of semi-finished products such as strip steel, tubes or wires for either surface treatment or the production of special composite materials. The rather new and still not full-fledged process of foil manufacture through evaporation also depends on the use of adequate electron guns.

2. Essential Requirements on Electron Guns for Evaporation

In principle, evaporation places almost the same demands on electron guns as melting does. With respect to constant power supply and distribution across the evaporant, however, guns for evaporation must meet still higher requirements. In order to obtain a constant layer thickness over the respective processing period, time invariant vaporization rates are a must. The necessary stability may be derived from the power dependent vaporization rate. Apart from securing a

stable amount of evaporated metal it is essential to eliminate any pronounced spread of directional distribution. Thus the vapour beam characteristic must be kept almost constant. Owing to the high vapour density and the resulting small free path, however, considerable 'blurring' effects have to be taken into account.

Generally, evaporation in the previously mentioned fields of application is from the liquid phase and it will therefore be of advantage to arrange the material to be processed directly above the evaporant. For this reason, gun design should permit either horizontal bombardement or beam injection from below, with a follow-up deflection of 90° and almost 180°, respectively.

Based on the high deposition rates, metal vapour pressure above the evaporant reaches a level of up to 10 torr. Hence it is essential to warrant adequate beam generation and guidance under these conditions. Moreover, the accelerating voltage should be high enough, permitting the beam to penetrate the vapour cloud. It has been found that an acceleration voltage of 20 to 30 kv will guarantee proper function in such a very dense vapour cloud even if the beam has to travel through a distance of, say, 500 mm.

There are many applications where the material to be coated is passed across the evaporant at a speed of several metres per second. It is therefore necessary to avoid even short-term fluctuations of power and power density distribution in the seconds range.

Especially in metallurgy, highly efficient production lines call for adequate measures to keep gun maintenance, operation and control as simple as possible.

3. Axial Gun Designs for Evaporation

A great number of companies have developed guns of various design and it is only the axial system which shall be dealt with here.

More than 10 years ago, axial systems - initially intended for melting - were developed in the Manfred von Ardenne Research Institute [4]. To meet the ever increasing demand, axial guns had to be derived from these systems and adapted to the various coating applications. Now they cover a power range of 5 to 600 kw and most of them are actually used in practice [3].

In the following sections, the term 'electron gun' will include the entirety of electron-optical components for beam generation and beam guidance; i.e., focusing system, pressure stages as well as beam deflection and turning systems.

3.1 Cathode

The most suitable cathodes for use in electron guns are solid bolt- or plate-type tungsten cathodes. Heating is by electron bombardement from a primary cathode. Solid cathodes combine a long service life with the advantage of a high emission current density which ranges from 5 to 10 A cm^{-2}. Essentially, the service life will be limited by ion bombardement and the design of a cathode system must warrant proper function even after many working hours.

Fig. 1 shows axial system cathodes of different power after various hours of melting steel or titanium. Electron bombardement is vertically from above and the reversed ion flow has caused considerable attrition especially in the cathode centre. Despite the pronounced wear, cathodes of this type still remain fully operative as far as current density and total current are concerned.

Primary cathodes have to be arranged in a way that they cannot be hit by the ion current. Thus their service life will be almost the same as that of gun cathodes. Cathodes for a beam power of 1,200 kw have been provided with a bore already prior to utilization so as to come to further improvements with reference to the constancy of beam generating conditions.

Solid cathodes have a service life of 100 to 500 hours. Nevertheless their design should permit easy replacement. When used in large production lines, the cathode will be preheated in a special device to prevent it from warping during operation. Beam generating systems are to be dimensioned in such a way that the beam current is space charge limited. This is why small heating power alterations and the resulting gun cathode temperature fluctuations have no bearing on the beam current. In addition, provision has been made to keep the heating power of the gun cathode almost constant.

3.2 Beam Formation.

Beam formation takes place in the beam generating system which consists of cathode, control electrode and anode. Fig. 2 gives a schematic representation of the beam generating system for ratings greater than 50 kw. Bolt-type cathodes will be used in the power range of 20 to 50 kw whilst disk-type tungsten cathodes with curved emitting surface predominate with still higher ratings. System dimensioning is according to the theoretical foundations established by Pierce [6]. The diameter of the control electrode is somewhat greater than the cathode diameter and, referred to the control electrode, the cathode has been shifted back by some millimetres. This configuration serves to shield the beam contribution which comes from the cathode edge.

Apart from its geometry it is especially the intrinsic space charge of the developing beam which is of importance for beam formation. Owing to the interaction of the various effects, a minimum beam diameter, d_m, is obtained near the anode. Generally, d_m will be smaller than the cathode which permits to use anode bore diameters in the same order as the cathode diameter. But it is not the geometry in the accelerating region alone which determines the aperture of the formed beam. Other influencing parameters are the intrinsic space charge in the vicinity of the smallest beam cross-section and the dispersing lens action of the anode. The virtual image of the smallest beam cross-section with the aperture $\overline{r'}$ then serves for representation in the follow-up electron-optic system.

With the high-power guns ($p \geqq 50$ kw) under discussion, the control electrode is on cathode potential. At present, power control or adjustment therefore takes place exclusively through a change in accelerating voltage.

Attempts are under way to set the power level by selecting adequate negative control potentials, aiming at a power level alteration independent of the accelerating voltage. This offers the advantage that adjustment of focusing, beam deflection and turning systems remains independent of power control. Generally, however, power control via control voltage alteration will only be

possible within narrow limits. Otherwise a too pronounced decrease in perveance has to be taken into account.

Fig. 3 gives the schematic sectional view of a high-performance system with a beam power of 1,200 kw. The smallest beam cross-section will be formed near the anode and the aperture - located about 100 mm away from the anode bore - amounts to 5×10^{-1}.

3.3 Beam Focusing

The focusing system serves for the loss-free transmission of the formed beam to the working site and to adjust the beam diameter on the surface of the evaporant. Metal-clad coils are employed as focusing lenses. They are protected by water-cooled copper tubes which simultaneously act as flow resistance. The inner tube diameter has been matched to the respective beam diameter. Two pressure stages with associated flow resistance and vacuum pump warrant proper operation in the working chamber even at a residual gas pressure of 10^{-2} torr.

In close proximity of the vapour source the pressure may reach a level of up to 10 torr. Focusing must be performed with due consideration of space charge compensation caused by ions generated in the beam. Actually, this effect is used in practice for dimensioning [4]. In production plants with gun ratings of up to 250 kw the beam power loss will be kept on a level of $\leq 1\ \%$.

3.4 Beam Deflection and Turning

Beam injection between evaporant and the material to be coated takes place almost horizontally. Programmed deflection then serves to distribute the beam power across the evaporant which also permits to obtain a particular power density distribution required for a maintained uniform coating thickness across the width of the moving substrate.

The selected deflection frequencies must be so high that coating thickness fluctuations are entirely avoided. With reference to deflections transversely to the direction of substrate motion, the following relation holds true for the frequency f :

$$f_x \geq k \cdot \frac{v_{(mm \cdot s^{-1})}}{l_{(mm)}} \; (s^{-1})$$

where

f_x = deflection frequency transversely to belt movement (x-direction)

v = belt speed

l = length of evaporation zone

k = form factor .

Generally, k will be equal to or greater than 5 and is a quantity that depends on the required constancy of layer thickness.

Programmed deflection toward the moving substrate reduces especially the mean power density on the evaporant whilst the length of the evaporation zone, l , is increased.

The selected deflection frequency in y-direction, f_y , is generally small as compared to f_x .

Programmed deflection in x- and y-direction then results in a surface evaporator with programme dependent different yield at the individual points.

At a belt speed of $v = 1$ to 2 $m \cdot s^{-1}$ and a width of $b = 500$ mm, frequencies of $f_x = 300$ Hz and $f_y = 50$ Hz will be found in practice. With $P = 100$ to 200 kw, this gives layers in the µm-range characterized by a thickness tolerance of $\frac{\Delta d}{d} \approx 10\ \%$. In such cases, sine deflections will be adequate for both directions.

Fig. 4 shows a principal arrangement where the beam is injected horizontally in the direction of belt motion.

Periodic deflection in x- and y-direction at a frequency of f_x and f_y , respectively, is by means of system 1 ; a system that is directly attached to the gun. System 2 then serves to turn the beam. The angle of impact on the evaporant surface is in a range of 50° to 80°. Smaller angles should be avoided

because this would markedly increase the portion of reflected electrons.

4. Actual Gun Design

There is hardly any difference in the basic design of guns for melting, heat treatment and evaporation. Fig. 5 shows the sectional view of guns with ratings of 60 kw, 250 kw and 1,200 kw. The auxiliary magnetic lens serves to guide the beam through the pressure stages. Located at the beam exit is another magnetic lens which permits to set the beam diameter to requirement. After that the beam will pass the deflection systems.

Thanks to the differential pumping system and the horizontal arrangement, beam generation will remain free from detrimental effects with a metal vapour pressure of up to 10 torr.

Fig. 6 shows an actual 250 kw gun design.

References

[1] Smith, H.R.; Hunt, Ch.D.A.:
Advances and the Future of Electron Beam Processes, in Bakish, R. "Electron and Ion Beam Science and Technology", New York 1966, Vol.1, 277 - 300 .

[2] Reichelt, W.; Dietrich, W.; Hauff, A.:
Das großtechnische Aufbringen von Schutzschichten auf Stahlbändern durch Bedampfen im Vakuum,
Metalloberfläche 20 (1966), 474 - 478 .

[3] Schiller, S.; Förster, H.; Lenk, P.; Kühn, G.; Kunack, W.: Zur Anwendung der Bedampfungstechnik in der Metallurgie,
Neue Hütte 13 (1968), 705 - 711 .

[4] Ardenne, M.v.; Schiller, S.; Lenk, P.:
Elektronenkanonen mit Leistungen von 5 kW bis 1200 kW und ihre technischen Anwendungen,
Kernenergie 11 (1968), 81 - 90 .

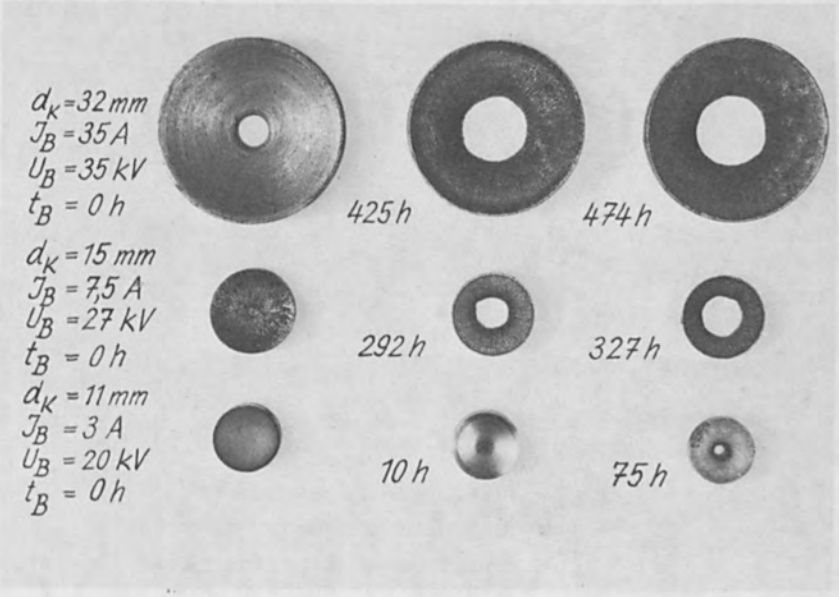

Fig. 1 : Practical cathodes in the initial state and after various operating time

d_k = cathode diameter

t_B = operating time

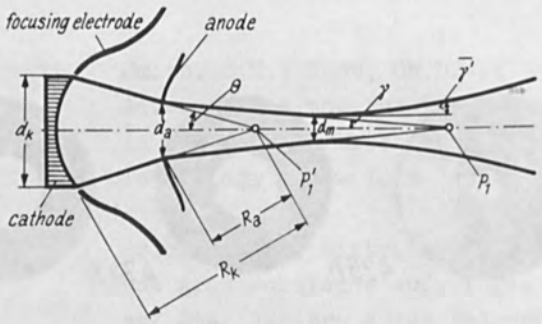

Fig. 2 : Cross section of a spherical beam generation system of Pierce-type (schematically)

d_k = diameter of cathode

d_a = diameter of anode bore

Θ = aperture angle of the beam generator = convergence angle of marginal rays in the beam generator

γ = aperture angle of marginal rays behind the anode considering scattering effect

P_1' , P_1 = convergence points

d_m = smallest diameter of the beam considering the intrinsic space charge

$\bar{\gamma}$ = aperture of marginal ray at the position of the smallest beam cross section

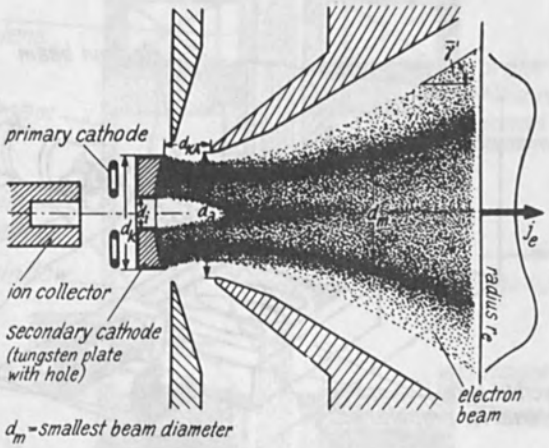

Fig. 3 : High performance beam generation system (schematically)

Geometrical arrangement and schematic current density distribution in the range after the anode

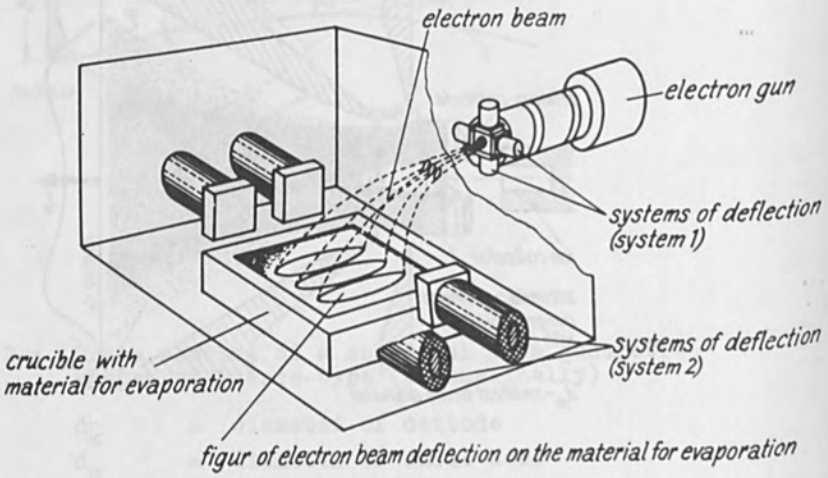

Fig. 4 : Schematic arrangement of systems of electron beam deflection

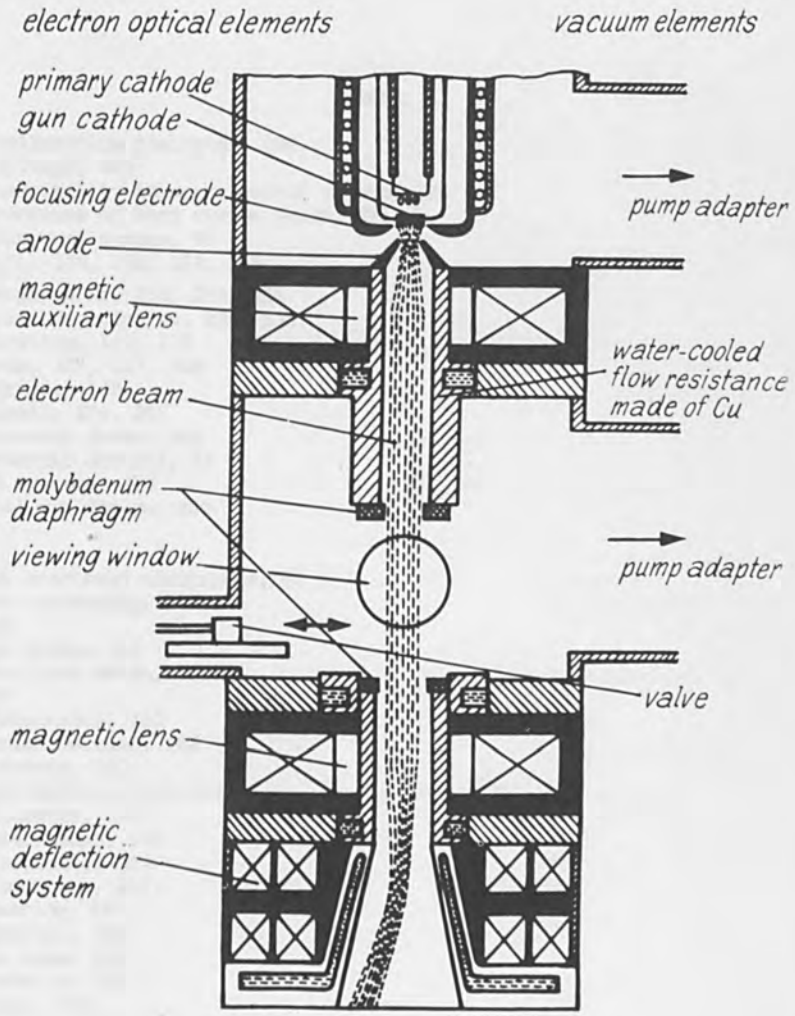

Fig. 5 : Schematic representation of the fundamental principles of guns with high beam power for

P = 1200 kW, U_B = 35 kV

P = 250 kW, U_B = 30 kV

P = 60 kW, U_B = 20 kV

Forschungsinstitut Manfred von Ardenne

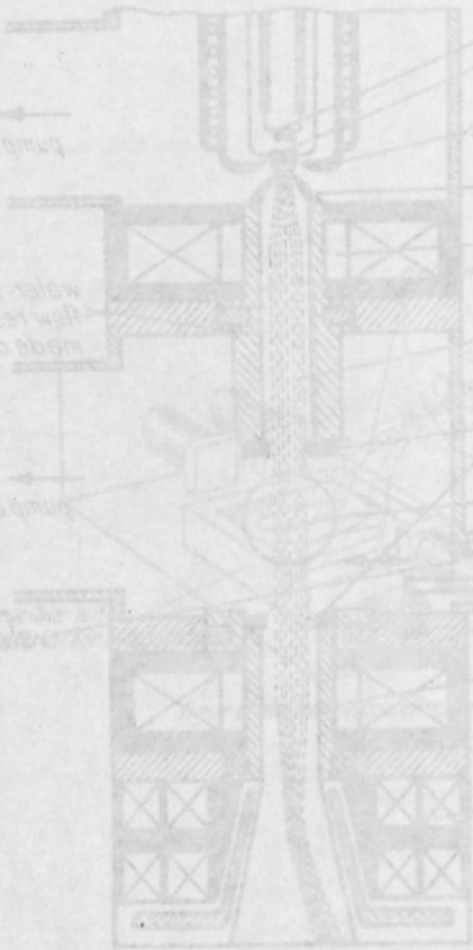

INDEX

Accelleration Electrode, 184
  Voltage, 343
Accessibility to work, out-of vacuum, 376
Advantages of hard vacuum welds, 375
Allignment system, 95
Al_2O_3, 148, 150, 154, 156
Amorphous Si, 254, 255, 256
Amplitude hologram, 134, 135
Annealing, 148, 153
Anode, 325, 327, 329
Apertude, 188
Arsenic, 254, 262
Automated focus, 364
Automatic control, 92
AVR systems, 373
Axial gun design, 400

Back scattered electrodes, 61
Back scattering, 55
Bead
  on plate, 344
  on plate welds, 363
Beam
  Attenuator, 163
  cross-section, 162
  current, 343
  deflection, 173, 403
  diameter, 343
  divergence, 187
  focussing, 403
  formation, 402
  heating, 165
  monitor, 184
  on time, 358
  profile, 181
  spot, 342
Bias cup, 324, 325, 328, 329
Biasing electrode, 356
Bias temperature stress, 148, 152
Binary hologram, 135
BN furnace, 227
Bubble propagation, 124

Calibration curve, 202

Capacitance voltage characteristics, 104
Carbon analysis, 202
Cathode, 401
Cathodic sputtering, 199
Cavity, 295, 307, 310
Chain reaction, 106
Channel, 292
Characteristic X-Rays, 82
Chemical etching, 84
Chemical etching process, 73
Chevron, 123
Chromium mask, 69, 72, 136, 137
Chromium matrices, 136
Closure, 310, 311
Collapse, 401
Computer
  controlled electron beam, 69
  generated hologram, 134
Concentration profile, 190, 254, 257
Conduction band, 281
Conical, 324, 325, 328, 329
Controls, closed loop, 374
          presentable, 374
Cross-linking, 105
CRT, 162
Current density, 185
Current density distribution, 164

Deflection coil, 125
Device
  fabrication, 52
  instability, 103
Diffraction, 81
  efficiency, 137
Diffusion, 254, 257, 243
  barries, 102
  mask, 117
Diode , 270
Distribution maps, 203
Domain wall, 123
Duoplasmatron ion source, 198
Duplicator, 35

ECL, 31
Economics of electron beam production welding, 378
Electric field, 329
Electrode alignment, 322
Electron beam
  analyser, 324

current distribution, 323, 325, 328
defined phosphosilicate glass, 106
defined siliceous patterns, 104
drafting machine, 135
effect of PVS, 115
exitation, 281, 282
lithography, 51, 123
machine, 162
pattern generator (EBPG), 34, 35, 38, 92, 265
processing plant, 171, 180
recording, 51, 134
techniques, 103
technology, 34
welders, 355, 359
welding, 307, 341
welding process (out of vacuum), 375
welding process (soft vacuum), 375
Electron
density, 342
electron interaction, 167
energy, 26
gun, 172, 356
electron gun, Pierce type, 323, 324
hole pairs, 284
irradiation, 148
micrography, 91
optics, 96
penetration, 312
probes, 3, 326
range, 82, 89, 295
sensitive resists, 106
Electronically programmed beam deflection, 373
Einzel lens, 182
Emission density, 7
Energy dissipation, 26
profiles, 27, 28, 29, 51, 54
Energy input, 363
loss, 54
Epitaxial, 123
Etch resist, 116
Exposure profile, 83, 86
Extraction electrode, 184
Extractor length, 189

Fast fourier transformation, 135
Field emission cathode, 3, 7, 9, 11
Filament, 327, 355, 356, 361, 373
materials, 357
position, 328, 329
ribbon, 325

Film lift off, 86
Fluorescent pattern, 323, 325, 326, 329
Focus, 186, 323, 327
  length, 359, 360
  out of vacuum, 376
  sharp, 355
  test, 362
Fusion zone profile, 324, 327

Gallium, 254, 258, 261
Gap distance, 187
Garnet, 123
Gaussian image, 4
Generation of shapes, 93
Ge Se, 281
Ghost image, 326

Halo, 188
High power evaporation guns, 399, 402
Hologram, 134
  recording, 134
Hybrid circuits, 172

IC, 265, 267
  performance, 31
Implant, 225, 229
Image, 355, 356, 361
Immersion lens, 182
Implantation systems available, 219
  mask, 117
  target chambers, 223
  variables, 220
Impurities, 254, 257
Increasing production, 377
In depth analysis, 203
Integrated
  circuit, 31, 68, 225
  machining, 176, 179
Integrator, 281, 283
Interferometer, 96, 100
Ion
  beam techniques, 222
  beam micro fabrication, 15
  beam technology, 34
  beam techniques, 222
  implantation, 40, 86, 190, 217, 221, 225, 235, 236,237, 243, 265, 268, 272
  implanted, 254

etching, 268
mass spectra, 223
microanalyser, 196
probes, 3
sources, 218, 219, 221, 222, 183
Irradiation dose, 151
Isography display, 166
Isotope separator, 229

JFET, 124, 225, 265, 266

Kinoform, 138
KPR, 71
KTFR, 71

Lantanum hexaboride, 3, 6, 7
Lens
current, 359
magnetic, 359
Lifetime test, 358
Lift off, 150
process, 68
Luminescence, 281

Magnetic bubble, 123
Manufacturing equipment, 241
Mask fabrication, 85
Masking operation, 95
Master mask, 92
Membrane, 84
Metallization, 125, 126
Merit factor, 32
Microanalysis, 13
Micro fabrication, 13
Microscopy, 3
Minimum basis investment in electron beam welding systems, 379
Mis capacitors, 148
Monte Carlo calculation, 26
MOS, 31
capacitors, 104
Mosfet, 266, 269

NaI Scintillation counter, 292
NANO, 265, 267
circuit, 38

electronic circuit, 36, 38, 40
electronics, 31, 37
New processing, 277

One cycle work handling system, 377
Oxydation layers, 204

Passivating layers, 102
P band, 281, 284
Penetration, 341, 346
mechanism, 307, 310, 311, 347
out of vacuum, 376
Penumbra, 81
Perfect conductor, 297
Permalloy, 123, 126, 127, 130
Phase hologram, 136
Phosphosilicate glass, 103
Phosphorous, 256
Photographic, 92
Photolithography, 33, 180
Pico Joules, 31
Pierce gun, 322, 402
Pierce type gun, 323, 324
Pinhole, 307, 308
Pinhole camera, 307, 308
Planar technology, 148
Plasma boundary, 183
Plasma debsity, 185
PMMA, 52, 59, 124, 128
Polyatomic ions, 202
Polycharged ions, 200, 202
Polymer, 82
Polymer film, 51
Polymer resist, 91
Polymethyl methacrylate, 70, 90
Polymethyl cyclosiloxane, 104
Polyvinysiloxane (PVS), 112
Postbaking, 71, 72
Power density, 341
Production line, 228
Production machine, 235, 236
Production welding (EB), 372
Production welding system (EB), 373
Profile distortion, 187

Quartz spacer, 70

Radiation decay, 285
Radiation dose, 83
Random positioning mode, 70
Rate meter, 293
Reconstructed image, 136
Relativistic voltage, 360
Resistor, 173, 177, 235
Resolution, 51
RF sputter ion source, 198
Ribbon filament, 354, 357, 358
Rogowski gun, 354, 356

Safety, 245, 247, 248
Scanning electron beams, 180
Scanning electron microscopy, 28, 69, 73, 85
Secondary electrons, 175
SEM, 3, 4, 271
Semiconductors, 241
Semiconductor processing, 102
Sheath thickness, 186
SIC, 230
Silica conversion, 116
Siliceous film patterns, 102
Silicon, 84, 254, 261, 149
Silicon wafer, 92
S_1O_2, 148, 150, 154, 156
Soft X-Rays, 87
Sodium contamination, 103
Spherical, 329
Spiking, 311, 328
Sputtered atom yield, 199
Sputter etching, 85
Square root extractor circuits, 373
Stock, 294
Surface, 123
Submicron line-width, 68, 69
Submicron replication, 180
Surface analysis, 196
Surface wave transducer, 72
Synthesis of PVS, 113
Symmetric shape, 364

T-bar, 123
Telefocus ion gun, 181
Thermal electron beam machining, 171
Thermal electron sources, 4
Thin films, 171

Thin films analysis, 204
Thompson Widdington law, 56, 57
Three cycle work handling systems, 378
Transducer, 86, 91
Trapezoidal profile, 189
Threshold shift, 236
Trimming, 173, 177
Tris-(dimethylsilylene) diphosphate, 105, 106
TTL, 31
Tungsten cathode, 3, 6, 12
Two cycle work handling system, 378

Ultra high resolution, 87
Undercut profile, 58
Undercutting, 363
Unfocused, 323

Vaporization rate, 400

Wehnelt geometry, 5
Weld characteristics, out of vacuum, 376
Weld characteristics, soft vacuum, 376
Weld geometry, 341
Welding guns, 356
Welding parameter, 341
Welding procedure, gears, 374
Weld penetration, 362
Widdington, 291
Wire hairpin filament, 357
Work distance, 362
Work handling subsystems, 374

Xenon, 260
X-Ray, 308
  absorption, 84
  Attenuation, 89
  lithography, 80, 89
  micro analyser, 3, 12
  resist, 82
  source, 81
  mask, 83, 90